Inherent strength and stiffness anisotropy of laminated rocks

To the Faculty of Geosciences, Geoengineering and Mining
of the Technische Universität Bergakademie Freiberg
approved

THESIS

to attain the academic degree of
Doctor of Engineering
Dr.-Ing.
submitted

By Dipl.-Ing. Mohamed Ahmed Ismael
Born on May 25, 1987 in Cairo, Egypt

Reviewer: Prof. Dr. habil. Heinz Konietzky, Freiberg

Date of award: 19.11.2018

Acknowledgment

This thesis marks the end of a research period that has been fruitful, successful and valuable for me at the Geotechnical Institute of TU Bergakademie Freiberg. I cannot express the possible thanks to all generous individuals, whose support have been greatly appreciated.

I would like first and foremost to express my sincere gratitude to my PhD advisor, Prof. Heinz Konietzky, for his consistent guidance and mentorship over the period of this research. All the gained academic achievements and personal progress during my doctoral study are owed to his insight, guidance, meticulous review, understanding, enthusiasm and continuous encouragement. I am very blessed to have such an excellent supervisor, who will always be appreciated.

I am very grateful for the funding scholarship program number: 57030312 and named (*GERLS – German Egyptian Research Long-Term Scholarship*) fully supported by the Egyptian ministry of higher education (MoHE) and the German academic exchange service (DAAD). Also, a special word of thanks to TU Bergakademie Freiberg for funding my research for further 3 months. I am grateful to professors from Cairo University, especially Prof. Mohamed Elwageeh and Prof. Ayman El-Midany, who encouraged me to pursue this scholarship.

I would like to thank Prof. Jorge Castro Gonzales for reviewing this work, the effort and valuable comments are very appreciated. I would like to take the chance to thank Prof. Hani Mitri, McGill University, for introducing me to rock mechanics field and his continuous encouragement. Special thanks to Mrs. Angela Griebsch for her friendly help whenever needed and to Dr. Martin Herbst for his consistent consultation and suggestions which improved my work, Mr. Gerd Münzberger and Dr. Thomas Frühwirt for their assistance during the lab experiment, Mr. Fabian Weber and Mr. Lifu Chang. Dr. Martin Herbst and Mr. Lifu Chang have helped me in the improvement of the literature survey presented in chapter 2. I would like to acknowledge the generous encouragement I have received from Prof. Arno Zang and Prof. Ove Stephansson of GFZ Helmholtz Center, Potsdam. Also, I wish to express my gratitude to my fellow colleagues at the Geotechnical Institute for their kind support.

Finally, I would like to thank my wife, Engy, for her support, encouragement and love throughout this journey. I owe all my success to my dear parents (my father, mother and brother) and my family who always prayed for me and wished me the best of luck. Special thanks to my in-laws:

Magda, Eid and Esraa. Also, I would like to dedicate this work to my kids, Abdallah and Ammar, who will hopefully read these words in the very near future.

Abstract

This thesis aims to deepen the understanding of the anisotropic nature of the laminated rock masses. Such nature is governed by the primary and secondary structures generated during the formation stages. Thus, the variation of rock strength and stiffness, as known as mechanical anisotropy, is expected at different scales: large- or small- scale. For most sedimentary and metamorphic rocks, the anisotropic nature is characterized as inherited at which no main discontinuities (i.e. major faults or cracks) could be distinguished. For engineering applications built either on or in the anisotropic rock masses, the investigation of the strength and deformation behavior is essential. To achieve this goal, two different continuum-based constitutive models named 'Transubi model' and 'Jhoek model' are presented and implemented into FLAC for the analysis of inherent anisotropic rocks. Both models are adequate for laminated rocks whose inherent planes of anisotropy could not be explicitly simulated.

Using the Jhoek model, the strength anisotropy could be described within the rock matrix by applying rock material parameters which vary with the orientation of the inherent planes of anisotropy. This model combines the Hoek and Brown failure criterion with the ubiquitous joint plane approach to capture both non-sliding and sliding failure modes, respectively. On the other hand, the Transubi model captures the stress-strain behavior of laminated rocks using a bi-linear yield surface consisting of the Mohr-Coulomb yield criterion to check the failure of the rock matrix and the weakness planes. This Transubi model behaves as strain hardening/softening by which the strain hardening in the pre-peak region and the strain softening in the post-peak region for bedded argillaceous rocks could be simulated.

Experimental investigations and numerical simulations, using Transubi model, mainly focus on the influence of the mechanical anisotropy on the development of plastic zones around excavated openings in laminated rocks. Later, the Transubi model is applied to a tunnel driven in a shaly facies formation of bedded argillaceous Opalinus clay in an URL (FE-tunnel) to obtain short-term stability insights. The simulation results are compared with data from in-situ measurements showing good agreements and indicating that the consideration of stiffness anisotropy is as important as the strength anisotropy. Overall, the research outcomes may have a prospective impact regarding the understanding of anisotropy of laminated, bedded and foliated rocks which

improves the prediction of deformation behaviour using continuum-based numerical modeling tools.

Table of Contents

List of Figures

List of Tables

Notation

a	Hoek-Brown material constant
a_{ij}	microstructure tensor
A_{ij}	traceless symmetric tensor
A_{ijkl}	transformation matrix
b	layering effect on the displacement
C_{ijkl}	fourth order elastic compliance tensor
$\{C\}$	elastic compliance matrix
c_a	apparent cohesion
c_1, c_1^{res}	peak and residual cohesion values of first failure surface for rock matrix
c_2, c_2^{res}	peak and residual cohesion values of second failure surface for rock matrix
c_{j1}, c_{j1}^{res}	peak and residual cohesion values of first failure surface for joint plane
c_{j2}, c_{j2}^{res}	peak and residual cohesion values of second failure surface for joint plane
dd	dip direction angle, in chapter 7 *jdd* is similar to *dd*
dip	dip angle, in chapter 7 *jdip* is similar to *dip*
E	isotropic Young's modulus
E_1, E_2, E_3	orthotropic Young's moduli
$E_{//}$	Young's modulus in direction parallel to bedding plane, sometimes E
E' or $E_{\perp}$	Young's modulus in direction normal to bedding plane
$E_{t\text{-}50}$ or $E_{0.2\%}$	secant or tangent Young's modulus
$f_1^{\,s}$, $f_2^{\,s}$	shear failure envelops for first and second yield surfaces, respectively
f^t	tensile failure envelop
$F(\sigma)$	yield surface
$g(\sigma)$	plastic potential
$g_1^{\,s}$, $g_2^{\,s}$	shear plastic potential for first and second yield surfaces, respectively
g^t	tensile plastic potential
G	shear modulus
G_1, G_2, G_3	orthotropic shear moduli
GSI	Geological Strength Index
G, λ	Lame's constants

G'	shear modulus in direction normal to bedding plane
h	layer thickness
h, h_1, h_2	diagonal functions to separate the failure envelopes
$I\alpha_{(50)}$	point load strength anisotropy index
$I_{s(50)\perp,//}$	point load strength normal and parallel to the foliation planes, respectively.
k_v, k_h	permeability in vertical and horizontal directions, respectively.
k_{ni}, k_{si}	joint normal stiffness and shear stiffness for i^{th} joint set
k_h	hardening parameter
k^s, k^t	shear and tensile hardening parameters for rock matrix
k_j^s, k_j^t	shear and tensile hardening parameters for joint plane
k	elastic anisotropic ratio
k_I	degree of strength anisotropy
K	bulk modulus
l_i, l_j	normal components of the plane where a_{ij} is projected
m	Hoek-Brown rock parameter, refers to particles interlocking
m_i	Hoek-Brown parameter for intact rock
m_β	anisotropic Hoek-Brown parameter
MR	Modulus Ratio
n_x, n_y, n_z	normal unit vector of the joint plane
P_i	internal pressure
r	radius of circular opening
Rc	strength anisotropy classification
R_σ	transformation matrix for second order stress tensor
R_ε	transformation matrix for second order strain tensor
R	radial distance from the opening
s	Hoek-Brown rock parameter, refers to rock quality
$space_i$	spacing between joints for i^{th} joint set
$\{S\}$	elastic stiffness matrix
$\{S^P\}$	elastic stiffness matrix in principal coordinates (x^P, y^P, z^P)
$U_{x'}$, $U_{y'}$, $U_{z'}$	displacement components in local coordinate system x', y′, z′
U_X, U_Y, U_Z	displacement components in global coordinate system X, Y, Z

URL	Underground Rock Laboratory
ν	isotropic Poisson's ratio, also refers to Poisson's ratio parallel to bedding
ν_1, ν_2, ν_3	orthotropic Poisson's ratios
ν'	Poisson's ratio in direction normal to bedding plane
α	bedding plane orientation angle, in 2-dimensional α equals *dip*
β	loading orientation, angle between loading direction and joint plane
ε_{XYZ} , $\varepsilon_{x'y'z'}$	strain state in global and local coordinates, respectively.
ε, ε^e, ε^p	total, elastic and plastic strains, respectively.
$\varepsilon_1, \varepsilon_2, \varepsilon_3$	principal strains
$\varepsilon^s{}_p$	accumulated plastic shear strain
$\Delta\varepsilon_i{}^{p,s}$	shear plastic strain increments
$\Delta\varepsilon_i{}^{p,t}$	tensile plastic strain increments
$\Delta\varepsilon_m{}^{p,s}$	volumetric plastic shear strain increment
ϕ_a	apparent friction angle
ϕ_{f1}, $\phi_{f1}{}^{res}$	peak and residual friction angles of first failure surface for rock matrix
ϕ_{f2}, $\phi_{f2}{}^{res}$	peak and residual friction angles of second failure surface for rock matrix
ϕ_{fj1}, $\phi_{fj1}{}^{res}$	peak and residual friction angles of first failure surface for joint plane
ϕ_{fj2}, $\phi_{fj2}{}^{res}$	peak and residual friction angles of second failure surface for joint plane
ψ	foliation angle, bedding planes direction or *dd*
ψ_1, $\psi_1{}^{res}$	peak and residual dilation angles of first failure surface for rock matrix
ψ_2, $\psi_2{}^{res}$	peak and residual dilation angles of second failure surface for rock matrix
ψ_{j1}, $\psi_{j1}{}^{res}$	peak and residual dilation angles of first failure surface for joint plane
ψ_{j2}, $\psi_{j2}{}^{res}$	peak and residual dilation angles of second failure surface for joint plane
λ	plastic multiplier
σ_c	compressive strength
σ_{ci}	Hoek-Brown rock parameter, unconfined isotropic compressive strength
$\sigma_1 - \sigma_3$	deviatoric stress
$\sigma_1, \sigma_2, \sigma_3$	principal stresses
$\sigma_{i+1}{}^{trial}$	trial stress
σ^t, $\sigma^{t\,res}$	peak and residual tensile strength for rock matrix
$\sigma_j{}^t$, $\sigma_j{}^{t\,res}$	peak and residual tensile strength for joint plane

$\sigma_{3'3'}$	normal stress component acting on the joint plane
σ_{pp}	undisturbed pore pressure
$\Delta\sigma^{P,C}$	obtained plastic shear corrections for principal stresses
σ^{O} ,σ^{N}	old and new corrected stress component
τ	shear stress component acting tangential to the joint plane
Ω_0	principal coefficient of the spatial distribution second order tensor
η	anisotropy parameter, while $\bar{\eta}$ is the mean value of η.

1. Introduction

1.1. Scope and research strategy

Rocks are generally jointed and naturally anisotropic. The stability of engineering applications built on or in the rock masses are related to the strength and deformation behavior of those masses. Thus, their strength and deformation behavior under different and complicated stress conditions have to be analyzed in order to solve stability problems related to slopes, tunnels and underground excavations. Rock anisotropy is not only caused by the existence of major faults, remarkable cracks or secondary structures in general, it also depends on the nature of the host rock. For example, intact sedimentary or metamorphic rocks show remarkable orientation dependent variations in strength and elastic moduli. In other words, even massive rocks possess anisotropic nature without the presence of natural or induced discontinuities. This nature is caused by the so-called primary structures: bedding planes, schistosity, fissility etc.

Through the past decades, various analytical, numerical and empirical methods are developed to consider the mechanical anisotropy of rock masses. Nowadays, it is possible to incorporate more aspects of rock mass behavior into the analysis using numerical simulation tools. Continuum based numerical methods are one of the best tools to provide both, accurate estimations and efficient computations.

In this thesis, two new continuum-based constitutive models named ‘Transubi model’ and ‘Jhoek model’ are presented and implemented into FLAC for the analysis of inherent anisotropic rocks. Both models are adequate for interlayered rock masses whose inherent planes of anisotropy could not be explicitly simulated. The Transubi model aims to capture the stress-strain behavior of transverse isotropic rocks, while a bi-linear yield surface consisting of the Mohr-Coulomb yield criterion is used to check the failure of the rock matrix and the weak planes. The Transubi model is validated and calibrated against a series of triaxial tests conducted on well-known inherent anisotropic rock samples such as Tournemire shale and Opalinus clay. The scope of the formulation of the Transubi model is to improve predictions of the deformational behavior of underground excavations in inherent anisotropic rocks. On the other hand, the Jhoek model considers inherent anisotropic rocks by applying a Hoek and Brown failure criterion for intact rock, and a Mohr-Coulomb yield criterion for weak planes.

1.2. Structure of thesis

This dissertation is subdivided into eight chapters as follows:

The first chapter (Introduction) (current chapter) introduces the scope the of the research and provides the major contributions of the thesis.

The second chapter (State-of-art) based on a literature review considers the main geological features which cause rock anisotropy. It provides a theoretical review of anisotropy based on elastic and inelastic concepts. Besides, a detailed overview of continuum-based approaches for anisotropic rocks is given. Advantages and limitations of different approaches are discussed.

The third chapter (Transubi model) describes the formulation of this new model and delivers a validation via uniaxial and triaxial tests and a comparison with the ubiquitous joint and the Caniso model.

The fourth chapter (Tournemire shale and Opalinus Clay) presents detailed numerical investigations of the mechanical anisotropy of bedded argillaceous rocks (Tournemire shale and Opalinus clay). Data from literature of triaxial tests and direct shear tests are used to calibrate the numerical simulations using the Transubi model.

The fifth chapter (Physical tests) investigates the significant influence of the transverse isotropic elastic constants on the plastic zone around excavated openings. Thus, a special laboratory test with a slate block containing a circular hole was designed. Cyclic loading is applied on the sample while the opening perimeter is continuously observed. Then, the experiment is numerically simulated using the Transubi model and results are compared against the lab measurements.

The sixth chapter (FE-Tunnel in Opalinus clay) presents numerical simulations of the excavation of the FE-Tunnel in Opalinus clay using the Transubi model. The tunnel is modelled with and without consideration of pore water pressure. The simulation results are compared with the in-situ measurements. Special attention is paid to the short-term deformation behavior around the excavated opening.

The seventh chapter (Jhoek model) introduces a new constitutive model based on a combination of the Hoek model and the ubiquitous joint approach. The Jhoek model is validated by using literature data of triaxial tests. In addition, simulation of a true triaxial test is presented.

The eighth chapter (Conclusions) summarizes the work presented. Conclusions and an outlook are given in which achievements and new finding are summarized. Recommendations for future research work are specified.

1.3. Major contributions of the thesis

This thesis focuses on capturing both, the strength and the stiffness anisotropy of inherent laminated rocks such as sedimentary and metamorphic rocks. Such study is important to predict the deformational behavior around openings excavated in those rocks using numerical simulation tools. The main findings of the thesis are:

(1) Normally, continuum-based models are suited for inherent laminated rocks with small thickness of interlayers (< 1cm). Also, most of those rocks show pronounced anisotropy in both, strength and stiffness.

(2) Considering only anisotropy in strength will lead to under-prediction of final strain values and therefore the estimated deformations.

(3) Usually, the compressive strength values are plotted as U-shaped with shoulders as assumed by Jaeger and Cook (1979) showing constant strength values for the rock matrix, while in reality there is anisotropy in the intact rock as well as the joint plane.

(4) A review on the various developed continuum-based approaches for anisotropic rocks is given. These approaches were compared with each other. Based on this review two new approaches are proposed.

(5) A transverse isotropic elasto-plastic model called Transubi-model was developed and implemented which considers stiffness and strength anisotropy as well as strain hardening/softening of weak planes and rock matrix.

(6) The proposed Transubi model is applied to simulate the behavior of bedded argillaceous rocks (Tournemire shale and Opalinus clay). Simulation results show very good agreement with the lab results. Direct shear tests of Opalinus clay are firstly simulated using continuum-based tools.

(7) In-depth going investigations are performed on the dilation behavior of Opalinus clay using the Transubi model. Realistic values for the dilation angles are proposed.

(8) Exploring the plastic zone and the deformation behavior around a loaded slate rock block containing a circular hole documents that the Transubi model is able to predict measurements and observations quite well.

(9) Numerical simulations of the short-term deformational behavior during the excavation of the FE-Tunnel in Opalinus clay (Mt. Terri) showed that – compared to measurements - considering the pore water pressure is necessary especially in respect to volumetric strain.

(10) For strain softened material like Opalinus clay, grid structure and resolution play an important role. Strain localization and formation of shear bands are highly grid dependent. Best results are found for radial symmetric grids.

(11) An elasto-perfect-plastic model called Jhoek model is proposed using the Hoek and Brown failure criterion to simulate the rock matrix, while ubiquitous joint approach is proposed for the weak planes. The H-B parameters m_β, σ_{ci0} and σ_{ci90} for rock matrix reflect the strength anisotropy of the matrix.

2. State of the art: Continuum-based modelling of anisotropic rocks

2.1. Features causing rock anisotropy

Rocks are characterized by mechanical bonding of grains of one mineral (mono-mineral rocks) or more than one mineral (poly-mineral rocks). The mechanical bonding depends on the origin of the rock, whether it is of igneous, metamorphic or sedimentary type. During the formation of rocks different processes takes place which cause primary and secondary rock structures. In the following the main geological features which cause rock anisotropy are discussed. The mechanical anisotropy of rocks is already widely investigated through the last few decades. The anisotropic behavior is influenced by micro and macro scale characteristics. Anisotropy can be subdivided into inherent and induced anisotropy (Casagrande and Carillo (1944)). Inherent mechanical anisotropy of rocks can be interpreted very well and is common for all metamorphic rocks and some sedimentary rocks as well. As seen in Fig. 2-1, the naturally inherent anisotropy planes result in variations in both, rock strength and stiffness with respect to the loading direction (Saroglou and Tsiambaos 2008). The anisotropic nature of metamorphic rocks is caused by the natural orientation of flat and long minerals or banding phenomena which can be found in schists, gneisses and slates (Ismael et al. 2014; Oda and Nakayama 1989; Bagheripour et al. 2011). The inherent anisotropy of sedimentary rocks is caused by the stratification of the bedded layers.

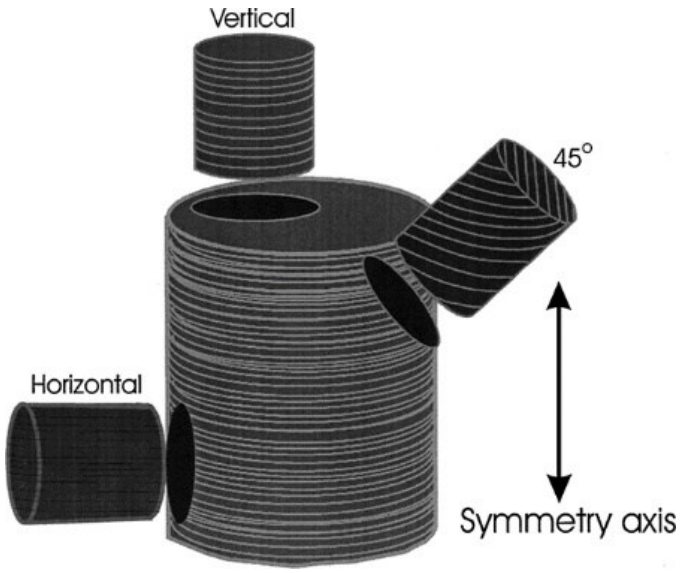

Fig. 2-1 Orientation of inherent planes as function of plug direction, (Wang 2002)

The induced anisotropy appears at the inelastic stage but can be illustrated by the fabric scale as well as the inherent anisotropy which has been explained for granular material by Oda (1993). He found that during a plastic deformation the particles reform continuously and create new contact planes. Such planes can be considered as planes of anisotropy which influence the following stage of plasticity (i.e. hardening or softening). At the macro scale, induced anisotropy can be generated in originally isotropic rock masses due to extremely non-hydrostatic stress states (Wu and Hudson 1991; Shao et al. 1994). Usually the investigation of induced anisotropy is associated with rock masses and is related to engineering applications, such as excavation of tunnels (Wang and Huang 2014) or borehole stability (Fang et al. 2013; Wang et al. 1993). Here we concentrate mainly on the mechanical inherent anisotropy, although to some extent induced anisotropy is also discussed.

2.1.1. Primary structures

Micro geological features are named also primary structures generated during the formation stage of rocks. These features influence the rock anisotropy by rock fabric anisotropy, texture, schistosity and fissility. They are mainly found at the micro scale and related to the grain size. In general, the anisotropic behavior of the rocks mainly depends on the texture and fabric of the principal rock forming minerals, the so-called microscopic fabric (Ullemeyer et al. 2006). According to the anisotropic nature of rocks Bagheripour et al. (2011) stated:

1. Most foliated metamorphic rocks, such as schists, slates, gneisses and phyllites, contain a natural orientation in their flat/long minerals or a banding phenomenon which results in anisotropy in their mechanical properties. Fig. 2-2.a shows a sample of metamorphic fabric in which a coarse-grained band-textured gneiss interlocks with different feldspar minerals.
2. Stratified sedimentary rocks like sandstone, shale or sandstone-shale alteration often display anisotropic behavior due to the presence of bedding planes. The major reason for the anisotropy of sedimentary rocks is the sedimentation processes of the different layers (strata) or different minerals with various grain sizes. Fig. 2-2.b shows a sample of bedding which is found in graded bedded sedimentary rock. Fissility is a special geological feature of sedimentary rocks in which grains are deposited forming parallel sets of planes and the rock unit fails by slipping along these planes. However, the fissility of laminated rocks is considered as a structure related mostly to sedimentary rocks such as siltstone and it is metamorphosed into the foliation (Van Hise 1896).

3. Anisotropy can also be exhibited by igneous rocks having flow structures as may be observed in porous rhyolites due to weathering (Matsukura, Hashizume, and Oguchi 2002). Generally, igneous rocks have only seldom fabric anisotropy. But in some cases, anisotropy may be found due to layering when lava flows and moves as highly viscous masses immediately before the consolidation (Walhlstrom 1973).

Here, we have to point out the difference between terminologies, such as: layering, bedding, lamination and foliation. Basically, sedimentary rocks are formed by the deposition of grains and particles. The default is a horizontal stratum which usually turned to graded bedded layers based on the size of grains (coarse grains settle faster and before fine grains). Non-horizontal sedimentation is called cross bedding deposition. Generally, the undisturbed formation of sedimentary rocks takes place as follows: bedding as macro-scale labeling, layering which can be found within the same bed indicating the variation of the deposition rates, and at the finest scale, there is lamination with small thickness (< 1cm).

(a) (b)

Fig. 2-2 Samples of primary styructures (a) Metamorphic texture of coarse-grained foliated gneiss (Weinberg, 2007); and (b) Graded bedded sedimentary rock, one strata consists of various layers due to discontinuity of the depostion.

Metamorphic rocks are formed by subjecting the original rocks to the conditions of high temperature and high pressure. One of the main metamorphic fabric is called foliation in which the realignment of the long and flat minerals such as mica causes repetitive layering which could be very thin like a sheet of paper or reach a thickness of several meters. Schistose rocks are categorized as coarse grained foliated metamorphic rocks. Foliation is a common fabric and can be found in several metamorphic rocks such as slate, gneiss, schist and phyllite.

2.1.2. Secondary structures

Secondary structures are macro scale features also called "discontinuities". They are defined as: (i) cracks and fractures, (ii) bedding planes and (iii) shear planes and faults (Salager et al. 2013). Such features' influence is significant and associated with three distinct issues (Bobet et al. 2009):

i. The scale: which effects the modelling of these planes implicitly or explicitly,
ii. Stress and/or displacement conducted: these planes significantly reduce the rock strength, and
iii. Relative motions of rock blocks: the discontinuity limits the elastic behavior of the rock material.

Hoek (1983) has developed a criterion to express the strength of the jointed rock mass:

i. The rock strength of jointed rock depends completely on the degree of interlocking of rock blocks,
ii. Rocks with a single joint set behave highly anisotropic, and
iii. The strength behavior of rock masses having three, four or five intersecting joint sets are considered approximately homogenous and isotropic.

2.2. Observation and measurement of rock anisotropy

For the characterization of rock anisotropy most of all the following parameters are used.

2.2.1. Strength anisotropy

Anisotropy of rock strength means that the rock strength is a function of the angle between loading direction and orientation of the anisotropy planes. For simplicity and due to the fact that this constellation is often met in engineering practice and lab testing, let us consider uniaxial loading of a rock sample with one plane of weakness. In that case the minimum strength value will be found usually between β_{min} = 30° and 45° (β is the angle between loading direction and plane of

weakness). The magnitude of the strength changes according to the orientation of the inherent planes of weakness. Saroglou and Tsiambaos (2008) have tested different types of metamorphic rock. Fig. 2-3 shows the obtained uniaxial compressive strength (UCS) as function of orientation angle β. This diagram shows, that some rocks show pronounced anisotropy in strength, others not or only marginal.

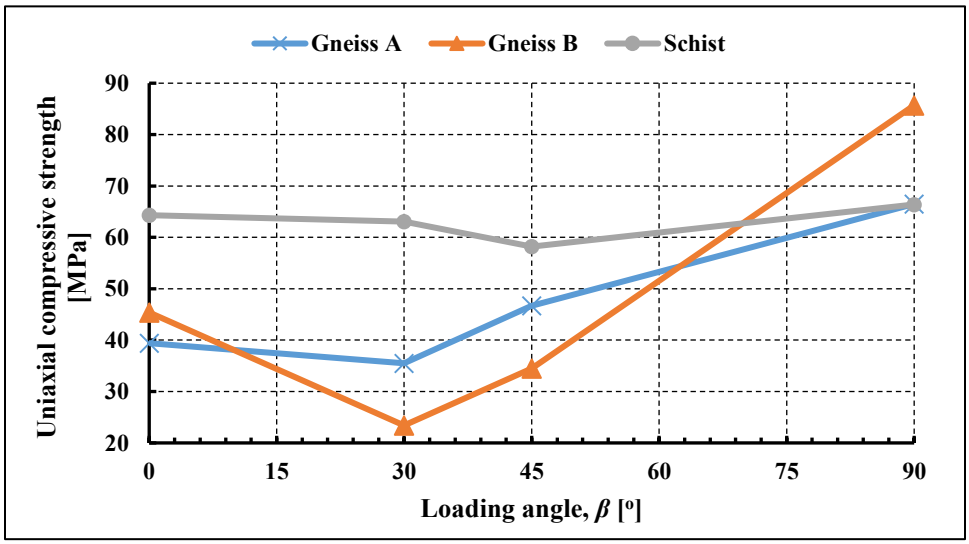

Fig. 2-3 Uniaxial compressive strength versus orientation angle β (modified after Saroglou and Tsiambaos (2008))

Anisotropy in strength is also observed under tensile loading. Fig. 2-4 shows results for Brazilian indirect tensile tests carried out on Leubsdorfer Gneiss (Le.Gs) at fixed value of bedding dip direction (ψ = 0°, bedding planes direction is parallel to loading). It is indicated that the loading orientation plays also a significant role in characterizing the tensile strength anisotropy. Also, the dip direction has significant influence on the results.

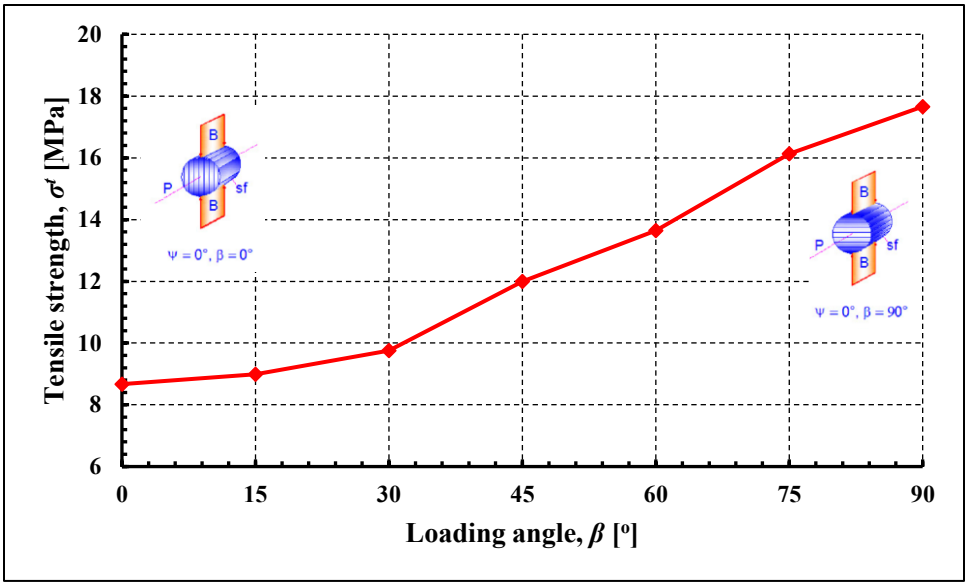

Fig. 2-4 Tensile strength versus orientation angle β of Leubsdorfer Gneiss (Le.Gs) at dip direction $\psi = 0^{o}$, after von Dinh (2011).

2.2.2. Stiffness anisotropy

Besides strength anisotropy, there exists also an anisotropy in stiffness, namely in terms of elastic constants like Young's modulus E or Poisson ratio v.

Table 2-1 Elastic constants of Mayen-Koblenz slate (Nguyen 2013)

Matrix Parameters	**Unit**	**Min. – Max. Value**	
		∥	⊥
Young's modulus	[GPa]	71 – 75	40 – 43
Poisson's ratio	[-]	0.25 – 0.3	0.23 – 0.3

∥ - Parallel to schistosity plane. ⊥ - Perpendicular to schistosity plane

Table 2-1 shows the elastic properties of a slate measured parallel and perpendicular to the plane of anisotropy (schistosity plane). Stiffness parallel to the schistosity planes is much higher than those perpendicular to the schistosity planes. Kim et al. (2012) as well as Park and Min (2015) have studied anisotropic characteristics of the elastic moduli of Asan (As) gneiss and Yeoncheon (YC) schist. The YC schist shows stronger anisotropy in stiffness than the AS gneiss as presented in Fig. 2-5.

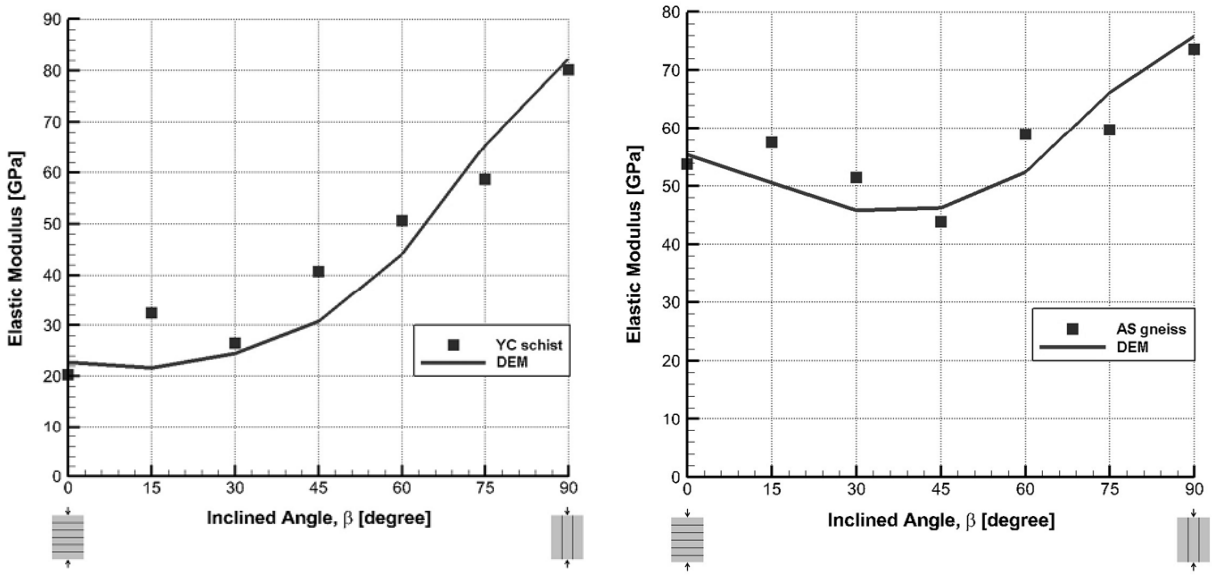

Fig. 2-5 Young's modulus for AS gneiss and YC schist as function of angle β (Park and Min 2015)

2.2.3. Other types of anisotropy

Anisotropy of rocks is also observed in respect to permeability and seismic properties. Permeability anisotropy can be caused by bedding, schistosity, fractures, damage, loading etc. A rock material is considered to be quasi-isotropic when the permeability ratio in two perpendicular directions (k_v) to (k_h) is >= 0.7 (Meyer 2002). Mokhtari et al. (2013) investigated the permeability of Mancos shale in respect to the orientation of the bedding planes and the confining pressure. Fig. 2-6 shows the permeability values of six vertical, one inclined (45°) and one horizontal core samples subjected to different confining pressures ranging from 1130 psi (≈7.79 MPa) to 3390 psi (≈ 23.37 MPa).

On the other hand, seismic anisotropy means that the wave propagation velocity depends on the propagation direction of the waves through the rock. The wave speed is maximum (Vfast) in the direction parallel to the anisotropy plane and minimum (Vslow) perpendicular to this direction. It can be distinguished between P- and S-wave velocities (compressional and shear wave velocities) (Inks et al. 2014). In addition, shear wave splitting or damping can be used to characterize anisotropy.

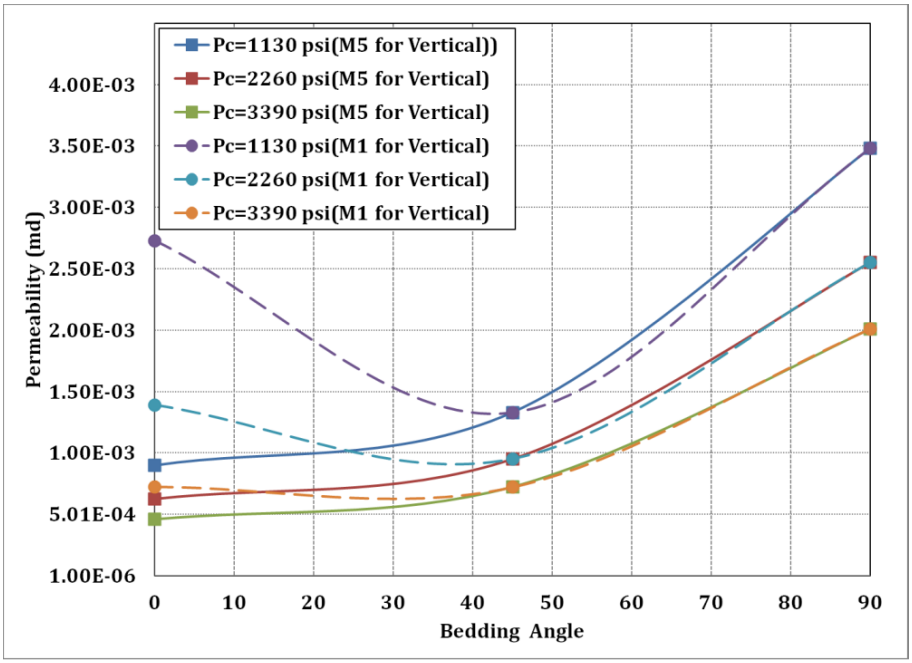

Fig. 2-6 Permeability anisotropy of Mancos shale core samples (Pc: confining pressure; 1 psi = 0,0069 MPa), Mokhtari et al. (2013).

2.3. Theoretical research background

2.3.1. Elastic stiffness/compliance matrix of rocks

The classical continuum mechanical constitutive models for anisotropic rock masses are mostly based on the elasto-plastic theory, but with special consideration of joint effects. An increment in total strain (ε) can be decomposed into an elastic part ε^e and a plastic part ε^p.

$$\varepsilon = \varepsilon^e + \varepsilon^p \tag{2.1}$$

The first deformation stage is characterized by linear elasticity. A review of the generalized Hooke's law considering different types of anisotropy are provided in Table 2-2 and Fig. 2-7. The incremental strain-stress equation in the elastic stage can be written in tensorial form as follows:

$$\Delta\varepsilon_{ij} = C_{ijkl}\Delta\sigma_{kl} \tag{2.2}$$

where, C_{ijkl} is the elastic compliance tensor, which has 36 elastic constants (6 x 6 matrix).

Table 2-2 Overview about anisotropic elastic rock models

Anisotropy type	**Representation of joints**	**Independent parameters for compliance tensor**	**Scope of application**	**Model type**
Isotropic	None	E, v	Hard rocks or heavily-fractured rocks	Elastic / Elasto-plastic
	One joint set	E, v	Thinly bedded bedrock	Elasto-plastic
	Several joint sets	$E, v + \sum (kn_i, ks_i, space_i)$	Fractured rock mass	Elasto-plastic
Transverse isotropic	None	E_1, E_2, v_1, v_2, G_2	Layered rock	Elastic / Elasto-plastic transverse isotropic
	Parallel to inherent joint orientation	E_1, E_2, v_1, v_2, G_2		
Orthotropic	Two or three orthogonal joint sets	$E_1, E_2, E_3, v_1, v_2, v_3, G_1, G_2, G_3$	Perpendicular joint sets	Elastic/ Elasto-plastic orthotropic

2.3.1.1 Intact rock as an isotropic material

The model of linear elasticity is the most widely used one to describe the mechanical behavior of hard brittle rocks. In this case the compliance matrix of the constitutive law is simply characterized by two independent material properties: Young's modulus E and Poisson's ratio v, or the corresponding Lame's constants, G and λ.

Elasto-plastic models which use the Mohr-Coulomb or Hoek-Brown failure criteria have been developed and applied for fractured rocks since the 1970s (e.g. Hoek and Brown 1980; Owen and Hinton 1980). Intact rock masses in those elastic/elasto-plastic models are all regarded as an isotropic material are shown in Fig. 2-7.a. Mohr-Coulomb plasticity is suitable for rocks with negligible bedding (thick sandstone), while for the thinly bedded bedrock several anisotropic models are used (Barton et al. 2005) which embedded joints inside an intact rock (see Fig. 2-7.b). In the above mentioned models, influence of joint parameters and joint spacing are not considered in the elastic compliance matrix.

2.3.1.2 Intact rock as isotropic material combined with joint parameters

For a jointed rock mass, the mechanical behavior is influenced by joints (Zhang and Lei 2013). More sophisticated constitutive models (Fig. 2-7.c, .d) for a jointed rock mass can be derived using the equivalent continuum method which considers the spatial, stiffness and strength characteristics of up to three joint sets (Sitharam and Verma 2005; Sitharam et al. 2007; Jiang et al. 2009; Wang and Huang 2014). The established equivalent elastic compliance matrix of the rock mass can be determined by superposing the compliance of all components (Agharazi et al. 2011), as follows:

$$C_{eq} = C^{I} + \sum_{i=1}^{n} C_{j}^{i} \tag{2.3}$$

where:

C_{eq}: equivalent compliance matrix of the rock mass,

C^{I}: intact isotropic rock compliance matrix,

C_j: joint compliance matrix represented by joint stiffness and space parameters.

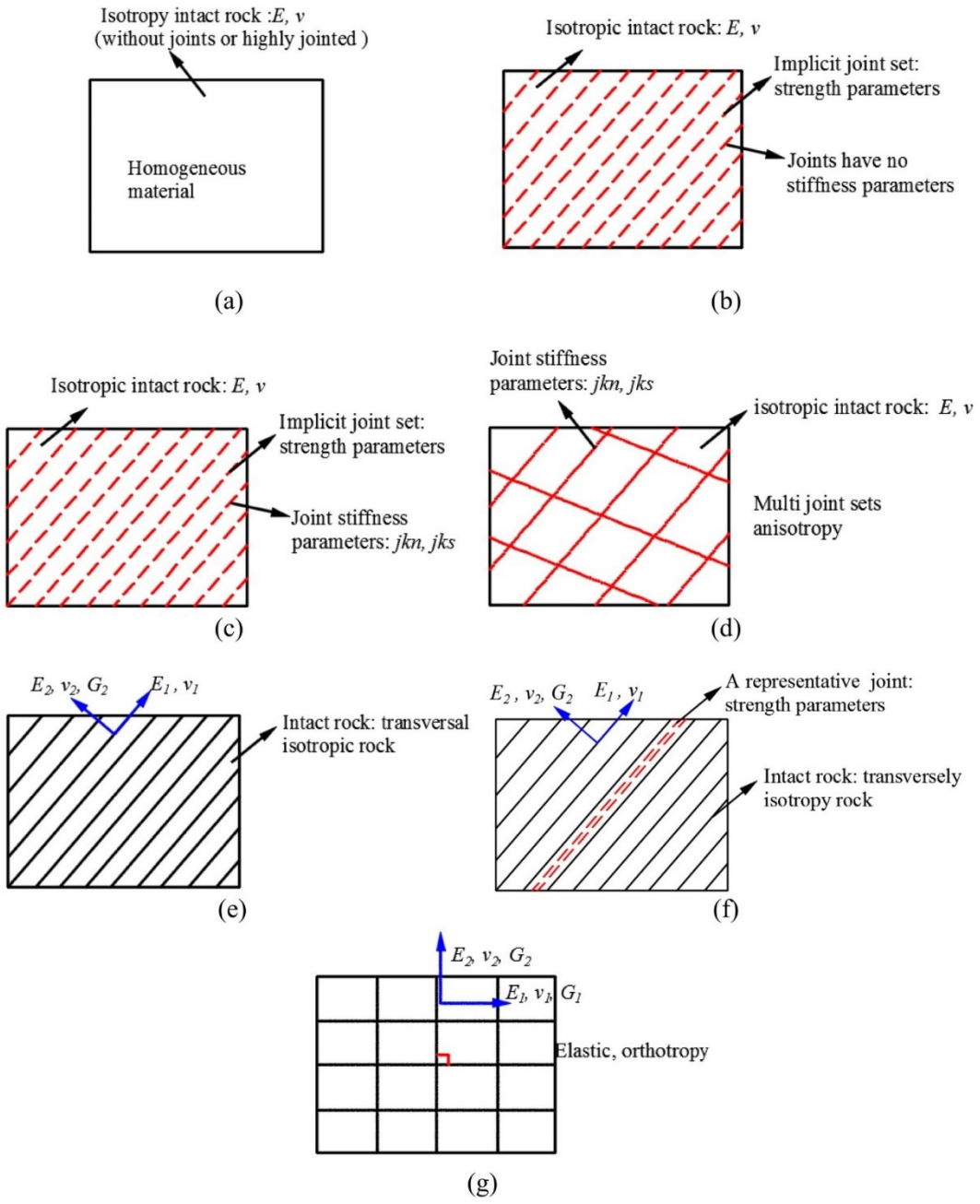

Fig. 2-7 Schematic for anisotropic models: (a) isotropic model (elastic/elasto-plastic: two independent elastic parameters), (b) anisotropic model composed by isotropic intact rock and one implicit joint set without joint stiffness, (c) anisotropic model consisting of isotropic intact rock and implicit joint with joint stiffness parameters, (d) anisotropic model consisting of several joint sets with joint stiffness parameters, (e) elastic transverse isotropic model (five independent elastic parameters), (f) anisotropic model consisting of transvers isotropic intact rock with a representative joint orientation, (g) elastic orthotropic model (nine independent elastic parameters)

2.3.1.3 Intact elastic anisotropic rocks

Models based on the concept of isotropic intact rock cannot fully describe the behavior of typical layered rock masses due to the preferred joint orientations or the subsistent of non-random joints (Tien and Kuo 2001). Several anisotropic models were deduced by considering alternative elastic symmetry conditions, such as transverse isotropy (Fig. 2-7.e) or continuum intersected by two orthogonal sets of joints (Jing 2003). The elastic transverse isotopic compliance matrix has five independent constants. For the past few years, some developed models combine the transverse isotopic intact rock with the joint strength parameters to consider the stiffness anisotropy influence of the layered rocks. These models (Fig. 2-7.f) have a single plane of weakness, which matches the orientation of the plane of isotropy. Similar developments are also noticed by Schoenberg and Muir (1989) who added additional joint elements into the homogeneous medium equivalent to a heterogeneous set of layers. Johnson and Rasolofosaon (1996) characterized the stress-induced behavior of transverse isotropic rocks.

Extensive research work has been carried out to formulate appropriate models for orthotropic materials (Fig. 2-7.f). An orthotropic rock has nine independent elastic constants. Layered sedimentary rocks intersected with perpendicular tension joints are examples of orthotropic rock masses. Crook et al. (2002) used an orthotropic elasto-plastic model to analyze the principal characteristics of weak shales, while Xin-pu et al. (2001) introduced an orthotropic damage tensor into the Mohr-Coulomb criterion through homogenization.

2.3.2. Various anisotropic rock failure criteria

A failure criterion is a governing equation or framework which predicts the value of the maximum loading and its conditions, i.e. loading rate and loading orientation, causing the rock to fail. Both, Duveau et al. (1998) and Kwasniewski (1993) published a review about anisotropic rock failure criteria, while a most recent classification can be found in (Ambrose 2014). In these reviews, anisotropic rock failure criteria are classified into continuous and discontinuous based on the representation of the anisotropy or the discontinuities within the material.

Mathematical continuous approaches

A continua is modelled as a solid body having a continuous variation in strength depending on direction. Usually the main linkage in the formulation is the loading angle β or the foliation angle ψ or both of them (Ambrose 2014). Pei (2008) and Semnani et al. (2016) summarized different mathematical based failure criteria for anisotropic rocks.

Based on the von Mises approach, Hill (1950) proposed the first anisotropic failure criterion for frictionless material (i.e. metals) which has been extended for fiber reinforced composites by Tsai and Wu (1971) and for anisotropic rocks by Pariseau (1968) in which a relationship between the deviatoric stress (= σ_1 - σ_3) and β has been formulated. Another way to consider the anisotropy was proposed by Boehler and Sawczuk (1977) based on the invariants of stress and structure tensors. Allirot and Boehler (1979) applied this criterion on samples of diatomite. In the same context, Pietruszczak and Mroz (2000) formulated a failure criterion incorporating an anisotropy parameter within the microstructure tensor. The third and the final type of those approaches is the transformed stress tensor technique by which the Mohr-Coulomb isotropic failure criterion has been extended to both, transverse isotropic and orthotropic materials (Boehler and Sawczuk 1977). Later one Nova (1986a) provided an extended Cam-Clay model for soft anisotropic rocks by rotating the fourth-order tensor in reference to the principal stress directions.

Although those mathematical approaches have a strong basis and background, there are some challenges facing them: (i) most of those models are complex and do not provide a clear physical meaning of the material parameters, (ii) when those models are applied to anisotropic rocks, several constants have to be determine experimentally, and (iii) the introduced terms of the stress state require well understanding of the behavior of the studied anisotropic rocks (Riahi 2008).

Empirical continuous approaches

These approaches are mainly an extension of isotropic failure criteria, mostly the Mohr-Coulomb or the Hoek-Brown failure criteria, which are altered by adding some empirical parameters to predict the strength anisotropy regarding the loading angle β. A good review of these empirical criteria for both, isotropic and anisotropic rocks has been provided by Sheorey (1997). Although this approach is more direct, easy to handle and applicable, there are some drawbacks: (i) sound physical and mathematical basis are missing, (ii) formulations depend on curve fitting techniques of experimental datasets which require a large data base, and (iii) deduced criteria are restricted to rocks on which experimental testing was conducted.

One of the first empirical formulation is known as the variational cohesion theory by Jaeger (1960) in which the strength is defined empirically as a function of β. This criterion was extended by McLamore and Gray (1967) to account also for the variation of the friction coefficient. A non-linear regression of triaxial lab data was conducted by Ramamurthy et al. (1993). Hoek and Brown (1980) proposed an indirect modification on their original failure criterion which defined empirical

formulations for the variation of rock parameters *m* and *s* in reference to the maximum principal loading orientation (Fig. 2-7.a). Another modification was proposed by Colak and Unlu (2004) for rock parameter *m* and its variation with the orientation of the anisotropy plane, assuming *s* = 1 for intact rocks. Also, distribution functions were formulated for both, *m* and *s* in terms of a second-order tensor to predict those parameters for transverse isotropic rocks (Lee and Pietruszczak 2008). On the other hand, Saroglou and Tsiambaos (2008b) and Bagheripour et al. (2011) proposed a direct modification in order to consider the rock anisotropy for inherent anisotropic intact rocks direct in the Hoek-Brown failure criterion. A review about different empirical approaches extending the Hoek-Brown failure criterion for anisotropic rocks can be found in (Ismael et al. 2015; Shi et al. 2016).

Discontinuous criteria (plane of weakness approach)

Such criteria distinguish between non-sliding (isotropic) failure in the intact rock and sliding (anisotropic) failure along the plane of weakness. One of the pioneering discontinuous criteria is Jaeger's theory of single plane of weakness (Jaeger 1960; Jaeger 1964). Later, this approach has been embedded into the Mohr-Coulomb isotropic failure criterion to model the failure of jointed rocks (Jaeger and Cook 1979). Later, Duveau and Shao (1998) extended the single weakness plane approach by the non-linear Barton's criterion. Hoek (1964) as well as Walsh and Brace (1964) used Griffith's fracture criterion to follow the crack propagation through inherent anisotropic rocks. Generally, this approach assumes that the strength of the anisotropic rocks varies due to the existence of the discontinuous plane. Thus, it is no longer considered as a continuous approach. Also, those discontinuous criteria usually prescribe rocks having one single plane of weakness.

2.3.3. Classifications of rock anisotropy

Anisotropy of rocks can be quantified and classified (degree of anisotropy). Two often used systems are: the point load index and the strength anisotropy index.

Point load index

Tsidzi (1990) proposed a scheme for foliated rocks to classify the degree of foliation as well as the degree of anisotropy. A fabric index was introduced first to classify metamorphic rocks (Tsidzi 1986). It has been noted that there is a strong relation between the degree of foliation and the point load strength anisotropy index $I\alpha_{(50)}$ according to Eq. (2.4) which is proposed by the ISRM (1985).

$$I\alpha_{(50)} = {I_{s(50)\perp}}\Big/{I_{s(50)\parallel}} \tag{2.4}$$

$I_{s(50)\perp}$ and $I_{s(50)//}$ are the point load strength measured perpendicular and parallel to the foliation planes for a samples of diameter equal to 50 mm. According to the observations, the minimum point load value is found when the loading is parallel to the foliation causing splitting along the weakness planes (Saroglou and Tsiambaos 2007). Table 2-3 shows the proposed classification of foliated rocks based on the point load strength anisotropy index.

Table 2-3 Classification of foliated rocks based on point load anisotropy index (Tsidzi 1990)

Nature of rock	**Point load anisotropy Index,** $I\alpha_{(50)}$	**Descriptive term**	**Examples**
Very strongly foliated	> 3.5	Very highly anisotropic	Slate
Strongly foliated	3.5 – 2.5	Highly anisotropic	Quartz mica schists
Moderately foliated	2.5 – 1.5	Moderately anisotropic	Mica gneisses
Weakly foliated	1.5 – 1.1	Fairly anisotropic	Granitic gneisses
Very weakly foliated or non-foliated	< 1.1	Quasi-isotropic	Quartzite

Strength anisotropy classification (*Rc*)

Ramamurthy (1993) defined the anisotropy strength (*Rc*). Eq. (2.5) quantifies the *Rc* value as the ratio between strength of the intact rock with loading angle perpendicular to bedding (β=90º) and the minimum strength of the same intact rock at β_{min}.

$$Rc = \frac{\sigma_{c(90)}}{\sigma_{c(\min)}} \qquad (2.5)$$

The strength anisotropy classification *Rc* for various rock types is shown in Table 2-4. *Rc* is essentially based on the uniaxial compressive strength of rocks. However, reports on the strength anisotropy in confined compression state have shown that the degree of anisotropy for a specific rock is not constant (Zhang 2006).

As the effect of strength anisotropy is reduced when the confining pressure is increased, a newly introduced experimental criterion for discontinuous rock defines a specific level of confining pressure above which the jointed weak sandstone ceased to behave as anisotropic rock

(Bagheripour et al. 2011). This specific level of confining pressure σ_3 was evaluated in terms of the uniaxial compressive strength of the corresponding intact rock as $\sigma_3 = 0.58\sigma_{ci}$ which is in close agreement with the value reported by Ramamurthy and Arora (1994).

Table 2-4 Anisotropy strength ratio *Rc* (Zhang 2006)

Anisotropy ratio *Rc*	**Class**	**Rock Types**
$1.0 < Rc < 1.1$	Isotropic	Sandstone
$1.1 < Rc < 2.0$	Low anisotropy	Sandstone, Shale
$2.0 < Rc < 4.0$	Medium anisotropy	Shale, Slate
$4.0 < Rc < 6.0$	High anisotropy	Slate, Phyllite
$6.0 < Rc$	Very high anisotropy	

2.3.3. Analysis using different numerical methods

The stress-strain behavior has a non-reversible part which refers to the plastic nature of the rock material. The description of the elasto-plastic behavior under multiaxial stress conditions demands the definition of the following terms:

Yield surface (F) is the stress state at which yielding starts (failure criterion). The yield condition including an interface with β as the orientation of applied load with respect to state of stress, σ and the hardening parameter, k_h, is given by Eq. (2.6).

$$F(\sigma, k_h, \beta) = 0 \tag{2.6}$$

The plastic potential (g) as given in Eq. (2.7) determines the direction of plastic strain.

$$g(\sigma) = const. \tag{2.7}$$

If yield function and plastic potential are identical the flow rule is called associated, otherwise non-associated (Vermeer and de Borst 1984).

Continuum versus discontinuum approach

There are two major approaches that can be used for the same aim: the continuum or the discontinuum approach. Table 2-5 shows the main differences between them.

Table 2-5 Comparison between continuum and discontinuum approaches

Continuum approach	**Discontinuum approach**
Benefits and usability: 1) Numerical discretization is independent of the joints. 2) Reduced model size. 3) Increased computational efficiency.	*Benefits and usability:* 1) Explicit simulation of micro- or macro-scale discontinuities. 2) Allows finite displacements and rotations of discrete bodies including complete detachment and generation of new contacts automatically.
Drawbacks: 1) Geometry of discontinuities is restricted. 2) For every time-step, especially when significant displacement is noticed along the discontinuity, remeshing is required for the entire model which can lead to numerical instabilities.	*Drawbacks:* 1) Demand of huge computational power. Run times are quite long. 2) Reliability of results is highly dependent on input parameters which are difficult to determine.
Most popular methods: - Finite Element Method (FEM) - Boundary Element Method (BEM) - Finite Difference Method (FDM) - Extended Finite Element Method (XFEM).	*Most popular methods:* - Distinct Element Method (DEM) - Discontinuous Deformation Analysis (DDA) - Finite Element Method with interface model (FEM*)

2.4. Continuum-based constitutive approaches for anisotropic rocks

A comprehensive consideration of the directional dependence of rock strength demands the usage of constitutive models with following characteristics: (i) capture the full path of stress-strain response such as: post-peak and hardening/softening behavior, (ii) analyze large scale behavior of geo-structures (Salager et al. 2013), and (iii) consider the stiffness anisotropy besides the strength anisotropy.

2.4.1. Ubiquitous joint approach

In continuum based models, the joints are regarded as smeared cracks which are implicitly used. The term 'ubiquitous joint' which was introduced by Goodman (1967) implies that the joint set may occur at any point in the rock mass without a fixed location, and the orientation of the joint set is precisely defined (Manh et al. 2015). The ubiquitous joint model is a conventional equivalent continuum approach where a layered material can be substituted by a homogeneous anisotropic medium. The behavior of the interfaces is governed by various yield criteria (Hsiung et al. 1995).

The two commonly used joint types are the Mohr-Coulomb and Barton-Bandis joint models. Failure may occur in either the rock matrix or along the joints, or both, according to the stress state, the orientation of the weak planes and the material properties of the matrix and the joint.

Both, Amadei (1996) and Park and Min (2015) indicated that the overall Young's modulus (elastic modulus) of an anisotropic rock can be expected to vary widely if the uniaxial compressive test is performed under different joint directions (Fig. 2-8.c). There are numerous studies on the mechanical behavior of a single joint or a set of ubiquitous joints. This approach is widely used for the numerical investigation of underground excavations and for slope stability (e.g Cartney 1977; Coulthard and Dutton 1988; Bye and Bell 2001; Jiang et al. 2009; Zhu et al. 2009).

Plenty of researches on the fluid flow and hydraulic conductivity were carried out to study the ubiquitous discontinuity effects on the hydraulic properties and the conductivity of rock masses (e.g. Hakami and Barton 1990; Coli and Pinzani 2014). Within the framework of elasto-plasticity and taken into account the time-dependent behavior by degrading the strength of rock with time, a model with ubiquitous joints was developed by Wang and Huang (2011). A new anisotropic time-dependent constitutive model was proposed by Manh et al. (2015) including ubiquitous joints of specific orientation embedded in an isotropic visco-plastic medium to simulate the anisotropic closure of the Saint-Martin-la-Porte gallery.

2.4.1.1. Original ubiquitous joint model

The original ubiquitous joint model (Fig. 2-8.b) behaves elastic-perfect-plastic and has some restrictions in respect to the simulation of fractured rock masses. First, the rock mass is simulated using only one set of joints in a Mohr-Coulomb material (Riahi 2008); second, the joints are considered to be persistent at the zone level and very closely spaced. Under 1-dimensional loading the angle β is the angle between the applied vertical stress and the joint (Fig. 2-8.a). The anisotropy behavior of the uniaxial compressive strength is shown in Fig. 2-8.b. Uniaxial compressive test results based on the original ubiquitous joint model with various joint orientations are shown in Fig. 2-8.d in which the compressive strength varies with the loading angle but the slope of the stress-strain curve inside the elastic stage is the same because the elastic phase is isotropic.

2.4.1.2. Strain-hardening/softening ubiquitous joint model

The strain hardening/softening ubiquitous-joint model (subiquitous) is a generalization of the ubiquitous-joint model in which the failure envelopes for the intact rock and the joint are formed by multi surface yield functions (Mohr-Coulomb failure criterion) with a tension cut-off part. This

model has the advantage that the strength parameters of the matrix and joint may harden and soften after the onset of plastic yield (Itasca 2016). Based on a calibration for a Synthetic Rock Mass (SRM), Sainsbury et al. (2008) developed a Ubiquitous Joint Rock Mass (UJRM) model and showed that a calibrated subiquitous model can reproduce accurate failure mechanisms and strength anisotropy of jointed rock masses. The stress-strain curves of the subiquitous joint model which contains one joint set are shown in Fig. 2-8.e. Like the original ubiquitous joint model, the stress-strain curves of the subiquitous joint model have a constant slope in the elastic stage for different joint orientations.

2.4.1.3. Intrinsic anisotropic ubiquitous joint model

The above mentioned models, the original ubiquitous and the subiquitous joint models, do not consider the intrinsic anisotropy of the rock matrix. In order to simulate the behavior of layered material and to account for slip along the direction of layering, some new constitutive models have been developed by Itasca (2016), Rahmati (2016) or Ismael and Konietzky (2017). The intrinsic anisotropic ubiquitous joint model combines the logic of an elastic transverse isotropic material with that of the ubiquitous joint model. A local Mohr-Coulomb yield criterion with tension cut-off is used as failure criterion on the weak planes. The rock matrix is treated as an elastic material. To include anisotropy characteristics for the rock matrix, several models are proposed. The Modified Ubiquitous Joint (MUJ) model (Ismael and Konietzky 2017) describes the elastic and plastic behavior of a transverse isotropic rock mass considering rock matrix and one joint set. Another model presented by Rahmati (2016), called Anisotropic Ubiquitous Joint (AUJ) model, treats the intact rock as an intrinsic anisotropic material and the ubiquitous joint method is adopted to account for the influence of weak planes which induce structural anisotropy. In order to describe the intrinsic anisotropy of the intact rock, the Mohr-Coulomb criterion with variable cohesion and friction (McLamore and Gray 1967) is used as shear yield criterion to describe the intrinsic anisotropy behavior of the rock matrix. A tension cut-off is adopted as tensile yield criterion. Non-associated and associated flow rules are adopted in the shear and tensile constitutive models, respectively (Rahmati 2016).

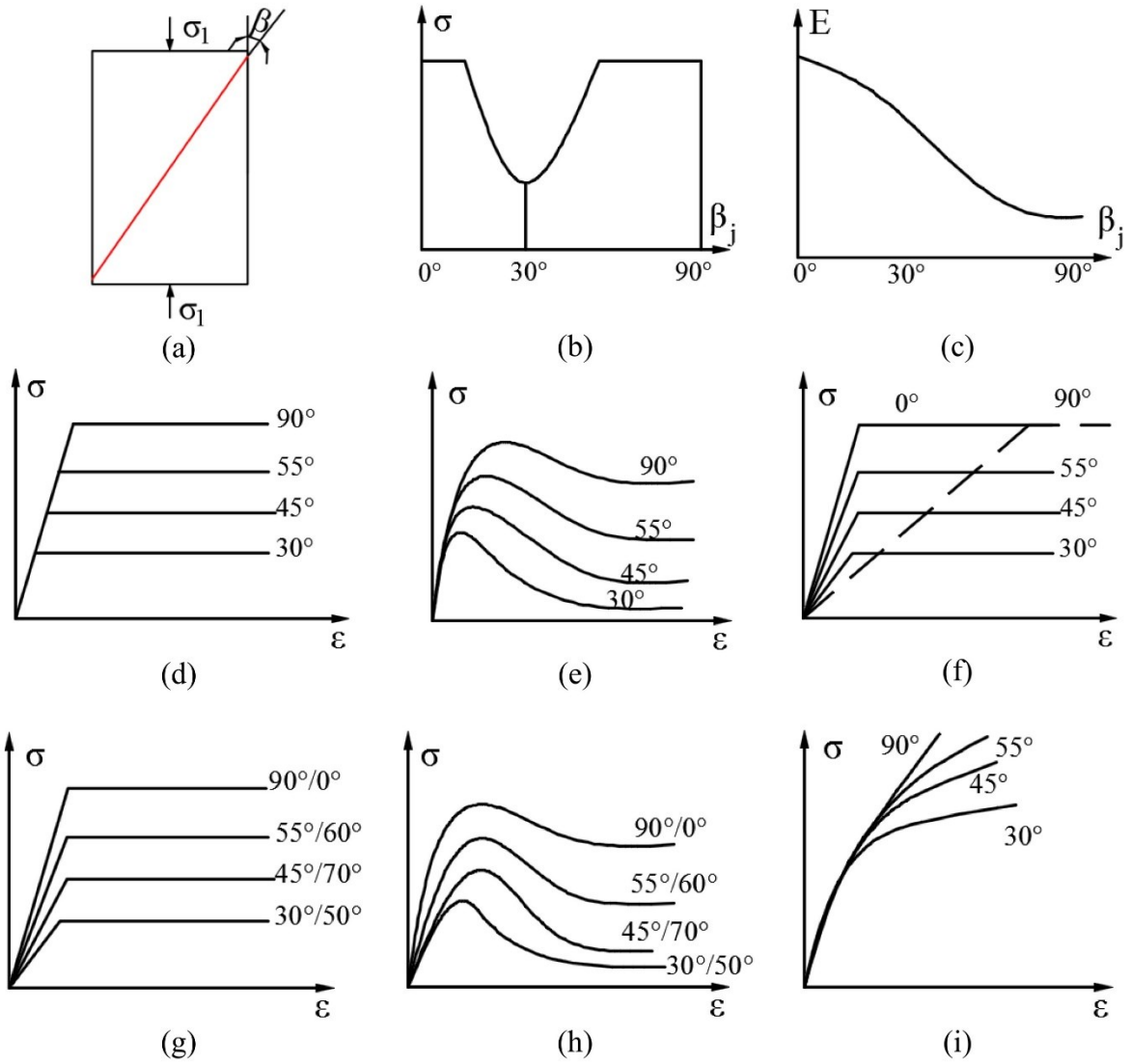

Fig. 2-8 Uniaxial compressive test results for ubiquitous joint models: (a) test configuration, (b) uniaxial compressive strength versus loading orientation, (c) general trend of elastic modulus versus loading orientation, (d) elastic-perfect-plastic stress-strain curve for several loading angles of a single joint considering no stiffness anisotropy, (e) elasto-plastic stress-strain curve with strain softening for several loading angles of a single joint considering no stiffness anisotropy, (f) elastic-perfect-plastic stress-strain curve for several loading angles of single joint considering stiffness anisotropy due to transverse isotropy, (g) elastic-perfect-plastic stress-strain curve for several loading angles of multi-joints (two joints) considering stiffness anisotropy due to spacing and stiffnesses of joints, (h) elasto-plastic stress-strain curve with strain softening for several loading angles of multi-joints (two joints) considering stiffness anisotropy due to spacing and stiffnesses of joints, (i) elasto-plastic stress-strain curve with strain hardening for several loading angles of single joint considering no stiffness anisotropy.

These different models consider not only the strength anisotropy but also the elastic stiffness anisotropy related to the joint orientations. The slope of the stress-strain curves are influenced by the joint angle. The stress-strain curves of the intrinsic anisotropic ubiquitous joint model with various joint orientations are shown in Fig. 2-8.f. The stiffness anisotropy has a major influence on the rock mass deformation behavior.

2.4.1.4. Ubiquitous multi-joint models

A rock mass often contains several sets of discontinuities. Therefore, more sophisticated modelling techniques based on the ubiquitous/subiquitous joint concept have emerged over recent years. A three-dimensional equivalent continuum model (Jointed Rock model) containing up to three persistent joint sets was developed by Agharazi (2013). There are two limitations of the Jointed Rock model: first, joint strength parameters are given for the first (most critical) joint set and only this joint set can fail; second, the multi-surface plasticity is not considered. To overcome such limitations, a two-dimensional multi-joint model was developed by Chang (2017). In this multi-joint model, each joint set has independent strength and stiffness parameters which downgrade the mechanical parameters of the rock matrix for the equivalent continuum. Each joint is considered and failure incl. plastic corrections are considered for the joint at critical angle. Both, Joined Rock model and Multi-joint model are elastic-perfect-plastic models. Fig. 2-8.g describes the stress-strain curves for different joint angle combinations. The stiffness parameters and the spatial distribution of joint sets can also influence the slope of the stress-strain curves.

2.4.1.5. Subiquitous multi-joint models

A non-linear constitutive model and an associated numerical implementation for rock masses with regularly distributed subiquitous joint sets was proposed by Wang and Huang (2009) and Wang and Huang (2014) so that the complete pre-and post-peak deformation of the rock mass can be obtained. The shear strength in this model is estimated by the Barton empirical formula and this model combines the mechanical behavior of intact rock with the spatial configuration and strength parameters of joint sets. The slope of the stress-strain curves are different for various joint orientations resulting in stiffness and strength anisotropy as shown in Fig. 2-8.h and Fig. 2-8.i. A new constitutive model combining orthotropic elastic behavior with the presence of up to four arbitrary subiquitous joints has been proposed to simulate the behavior of columnar basalt with non-isotropic elastic matrix (Detournay et al. 2016).

2.4.2. Cosserat-based approach

Constitutive models based on the Cosserat approach (Cosserat and Cosserat 1909) have recently witnessed a significant development especially for capturing the mechanical behavior of anisotropic materials, i.e. layered or laminated rocks. The original theory has been generalized by Mindlin (1964) to consider a 3-dimensional elastic continuum. The Cosserat approach conceptualizes the continua as infinite number of layers and considers an internal length scale parameter. Therefore, the micro-moments are introduced into the governing equations. On the other hand, Cosserat theory is known also as micropolar theory, i.e. a theory of asymmetrical elasticity, in which the micro-moments vary along the continua and consequently the stress tensor *[σ]* is asymmetric (Riahi and Curran 2009). Fig. 2-9 shows the placement of the Cosserat based models in the classification scheme of continuum based models.

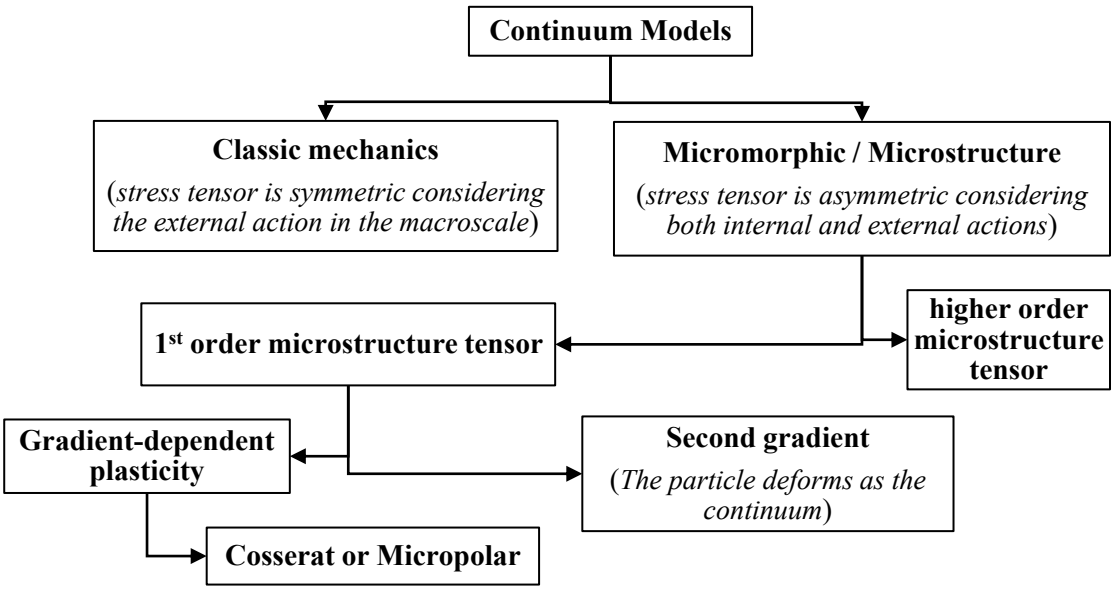

Fig. 2-9 Clasification scheme for continuum based models with special consideration of Cosserat models (Germain 1973; Godio et al. 2015; Madeo 2015).

2.4.2.1. Cosserat based constitutive models for layered materials

The first trials to adopt the lamination concept of the Cosserat approach can be noticed in (Mühlhaus and Vardoulakis 1986; Mühlhaus 1990), where the influence of the bending stiffness *[μ]* of layers was inserted into the micro-tensor. The bending stiffness term stands for the effect of the layer thickness, i.e. the internal lengths, as illustrated in Fig. 2-10. Thus, the Cosserat based

constitutive models use a [9 x 9] stiffness matrix which relates the stress and bending stress components with the strain and curvature components in local coordinates.

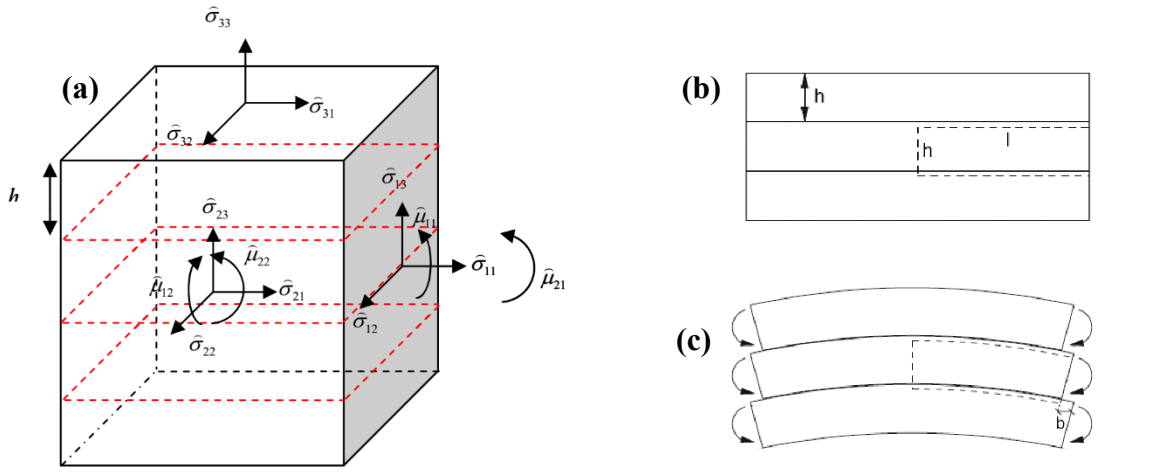

Fig. 2-10 Schematic view of a Cosserat layered continuum (a) 3D representative stress *[σ]* and bending stress *[μ]* components, (b) unloaded layered continuum, and (c) layered continuum after deformation (Riahi 2008), *b* stands for the layering effect on the displacement (Kolymbas 2007).

Due to the assumptions that length scale of the layer thickness plays a significant role at the macroscopic scale, the effects of bending and buckling of the layers had to be considered in the elasto-plastic framework (Mühlhaus 1995). This effect can be neglected if the length of modelled continua is much larger than the thickness of the layers, and consequently in that case the result is similar to the ubiquitous joint model (h=0). Riahi (2008) studied the effect of the internal length scale on the deformation pattern for stratified rocks, where it has been depicted by Adhikary and Dyskin (1997) that the larger the thickness, the more the results differ. In fact, the bending of the layers is triggered when slipping along the joints takes place. A detailed review about the Cosserat plasticity for generalized continua is presented in (Forest and Sievert 2003; Riahi 2008). However, these papers focus mainly on the development of the Cosserat based elasto-plastic formulations for layered rocks.

Considering the equivalent continuum approach, the Cosserat based elasto-plastic governing framework for layered rocks was introduced firstly by Cundall and Dawson (1992) using Finite Difference Method implemented in FLAC. It was simplified later by Alehossein and Korinets (1999) and Alehossein and Korinets (2000) utilizing the gradient dependent plasticity approach.

In parallel Mühlhaus (1995) developed a Finite Element formulation for an elasto-plastic Cosserat model applied for the interface only. As an example a beam under a point load was analyzed. Then, a generalized 2D Cosserat elasto-plastic model was presented by Adhikary and Dyskin (1997) and Adhikary and Dyskin (1998) in which a large number of layer parameters is considered. The Finite Element formulation procedure of this model is briefly presented by Adhikary, Dyskin, and Jewell (1996). However, the intact layers are assumed to be rigid and possess no plastic behavior. Later, the 2-dimensional elasto-plastic model was extended by adding yield possibility of the intact layers (Adhikary and Guo 2002). Both, intact layers and smeared joints are described by the Mohr-Coulomb law with tension cut-off.

A 3-dimensional extended Cosserat based constitutive model for an equivalent continuum with multi-surface plasticity approach was introduced by Riahi and Curran (2009). Based on this model, the buckling analysis of the layered rocks was studied (Riahi et al. 2009). Because of the difference in rotation between 2D and 3D, it was difficult to extend the Cosserat based constitutive model to 3D (Riahi and Curran 2008). Most of above mentioned models assume a layered rock mass as an equivalent continuum where the interface between the layers has its own stiffness and therefore the thickness of the layers are inserted into the stiffness matrix. Recently, an elastic transverse isotropic model in the framework of the Cosserat approach for layered soils has been introduced by Hu and Tang (2013). This model is elastic and does not show any plastic yield.

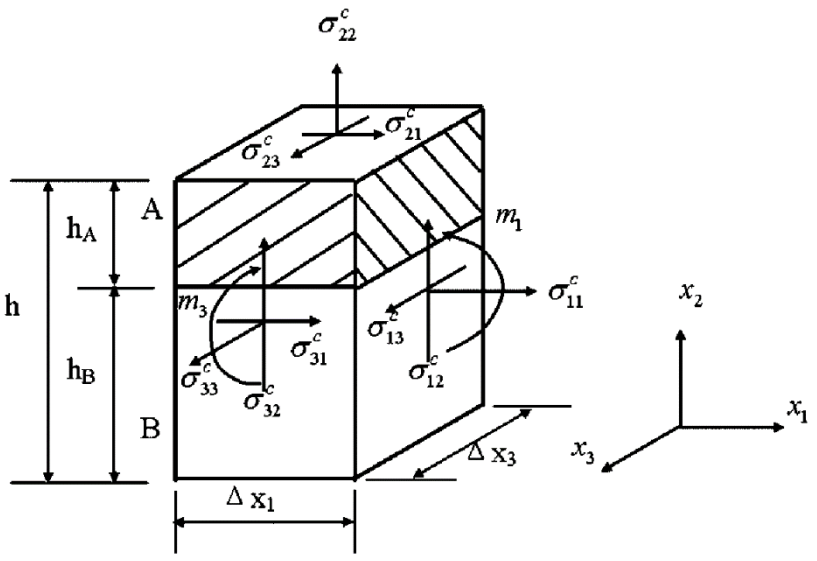

Fig. 2-11 Model set-up for the salt interlayered rock mass (Li et al. 2009)

All of the above discussed Cosserat models assume that the layers of the intact rock have a constant thickness (h=constant) and all layers have the same mechanical properties and therefore the same elasto-plastic behavior. A 3-dimensional Cosserat like elasto-plastic constitutive model was introduced for bi-laminated salt rocks as a composite of anhydrite-halite or mudstone-halite (Li et al. 2009). This model assumes that bedding is horizontal and each layer has its own thickness and mechanical properties. As shown in Fig. 2-11, this model assumes that both layers (layer A and layer B) are bonded in a perfect way which prevents opening or sliding and this is in agreement with the experiments on anhydrite interlayers. However, the numerical implementation in FLAC3D neglects the influence of the bending effect. Each zone in the model has the thickness (h) and the volume fractions of the two layers are represented by: $\alpha_A = h_A/h$ and $\alpha_B = h_B/h$.

2.4.2.2. Cosserat-based constitutive models for blocky (masonry-like) materials

Sometimes rock masses are formed in a brickwork pattern or in orthotropic fabric as shown in Fig. 2-12.a (Mühlhaus 1993). The Cosserat approach was utilized extensively to capture such behavior of regular blocky structures. A simple 2-dimensional kinematic concept with two adjacent blocks was firstly introduced by Mühlhaus (1993), as shown in Fig. 2-12.b. The block dimension was assumed as length = $2a$ and height = b. Masiani and Trovalusci (1996) presented a study conducted on brick masonry structures comparing Cosserat and Cauchy continuum models. The Cosserat based model showed an advantage over the Cauchy model as it considers the internal length scale and showed also better results compared to the rigid Discrete Element model.

Later, based on (Mühlhaus 1993), a 2-dimensional Cosserat based elasto-plastic framework was implemented by Sulem and Mühlhaus (1997) in which the model can be adjusted for square bricks (b=$2a$) and a columnar (orthotropic) structure as shown in Fig. 2-12.c. However, this model assumed rigid blocks having no yield condition and plasticity acts only for the interfaces. Sulem and Cerrolaza (2000) presented various failure modes (e.g. sliding and tilting) of a blocky slope where the rock blocks behave as rigid material. Based on another approach, Schlegel et al. (2005) introduced a continuum based model to simulate masonry structures considering different block dimensions ($2a$ x b). The parameters of the elasto-plastic model were calibrated based on the modelled block dimension, the block format (masonry structure as shown in Fig. 2-12.b or orthogonal as in Fig. 2-12.c) and if the blocks are cemented by mortar or not. An extensive review of Cosserat based continuum models for the masonry like structures can be found in (Casolo 2006; Salerno and de Felice 2009; Baraldi et al. 2016).

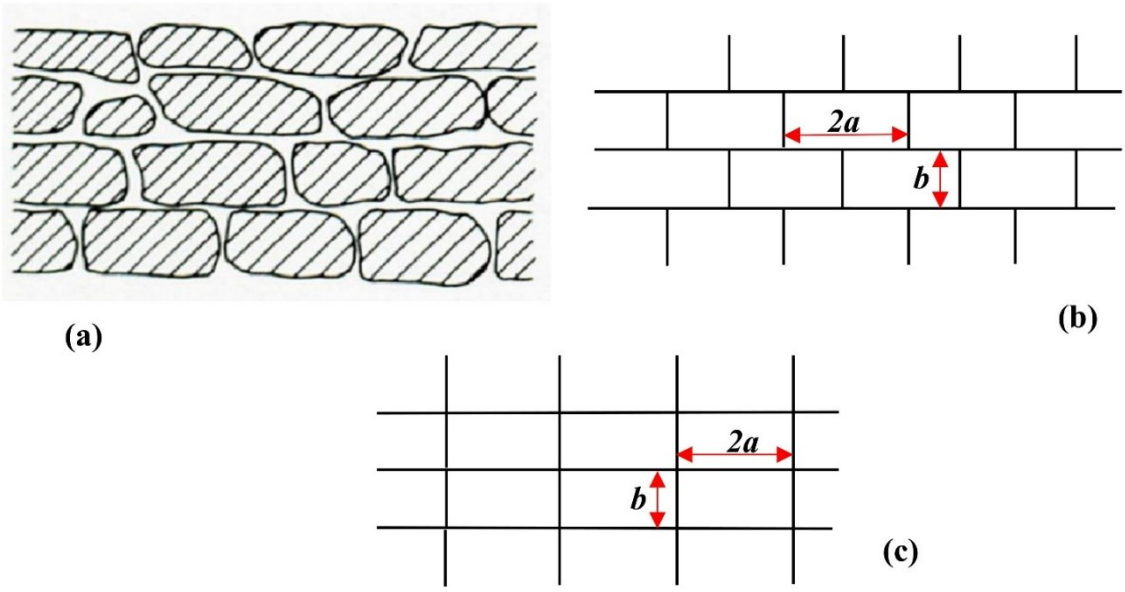

Fig. 2-12 Blocky (masonry-like) fabric: (a) natural broken rock mass, (b) modelled masonry structure, and (c) orthotropic structure after (Mühlhaus 1993), *2a* stands for the length and *b* is the height or thickness.

2.4.2.3. Comparison between Ubiquitous Joint and Cosserat models

Adhikary (2010) and Riahi (2008) defined the shortcomings of ubiquitous joint models as follows: (i) the local stress tensor is symmetric due to the assumptions of partially equal shear stresses, (ii) there is no consideration of rotation of the layers and thus there is also no representation of the internal moment components, and (iii) the existence of joints have no anisotropy influence on the elastic properties. On the other hand, Sainsbury and Sainsbury (2017) illustrated that although the Cosserat based constitutive models showed an advanced representation of the layered rocks by containing additional rotational degrees of freedom, there are some technical complications to be commercially released. Those complications arise because of: (i) adjusting the meshing to allow the rotational degrees of freedom, (ii) updating the equations of motion for each grid point according to the additional stress components related to the moments and coupling of each layer. Due to the rotational degrees of freedom, some new phenomena can be duplicated, i.e. buckling and deflection. The discussion of these two models raised important questions: to which extend is the conventional beam theory – the reference of Cosserat based models – capable to predict elastic deflection of stratified rock masses ? Can the ubiquitous joint model simulate the buckling mechanism of layered rocks ?

For underground openings in horizontal bedded anisotropic rocks as shown in Fig. 2-13.a, a deflection is observed in the roof because of the lamination partings (Diederichs and Kaiser 1999). Although the conventional beam theory could work to predict the deflection of the roof for horizontally stratified rocks, there might be various intersecting joint sets within the roof causing difficulties to work based on the beam theory. In such conditions, the conventional beam theory tends to underestimate the stability (Diederichs and Kaiser 1999).

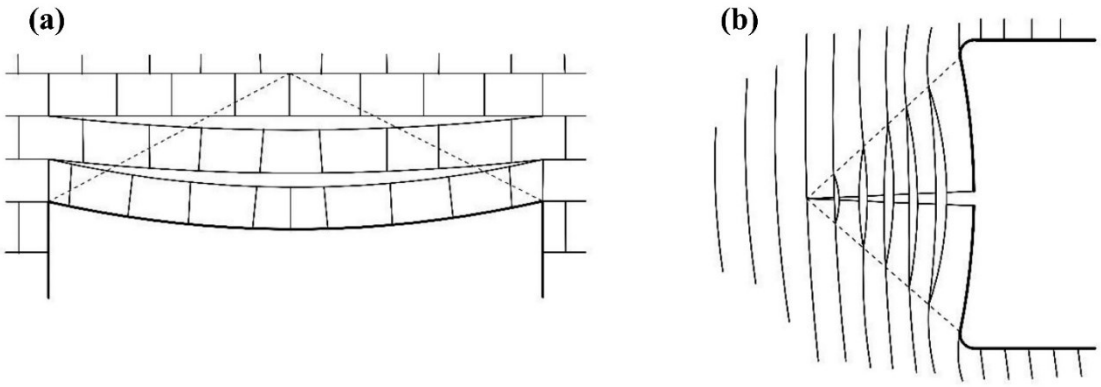

Fig. 2-13 Schematics of different underground openings having (a) a deflection of a horizontal bedded jointed roof, and (b) a buckling of the sidewall of a steeply bedded rocks, the doted lines show the highly deformed zones (Diederichs and Kaiser 1999; Yun-mei et al. 1984).

When the foliation angle is steep, there is a buckling mechanism within the layered (laminated, foliated or stratified) rocks which is a significant characteristic. Failure modes are specified such as buckling at sidewalls and the related squeezing of steeply bedded rock masses as shown in Fig. 2-13.b (Yun-mei et al. 1984). Karampinos et al. (2015) studied the non-linear anisotropic response of steeply hard foliated rocks in deep underground openings. The continuum based models could not fully simulate the buckling of foliated rocks. Therefore a Discrete Element approach was adopted (Karampinos et al. 2015). Concerning the Cosserat based models, Riahi et al. (2009) applied a 3-dimensional Cosserat continuum based approach to model the buckling phenomenon of layered structures. On the other hand, the ubiquitous joint model alone cannot simulate such behavior because of the above mentioned reasons. Sainsbury and Sainsbury (2017) developed a new strategy to overcome the ubiquitous joint model shortcomings by combining continuum and discontinuum approaches. In this new strategy, Distinct Element model software (UDEC and

3DEC) was applied to model explicitly the major joints by using their advantages to consider joint spacing, length and stiffness. In addition, the modelled blocks in between those explicit joints were simulated as a continuum based ubiquitous or subiquitous joint model.

Up to now, layered rocks cannot fully be assessed using continuum based approaches especially by the ubiquitous joint model. However, there are trials by Sainsbury and Sainsbury (2017) but their strategy had some limitations concerning the scale effect. On the other hand, Cosserat based models show promising advance in relation to the simulation of deflection and buckling phenomena, but some limitations related to the meshing and the usage of beam theory exist as well.

2.4.3. Approaches based on critical plane and microstructure tensor

2.4.3.1. Critical plane approach

According to experimental data of Donath (1964), the orientation of the critical (failure) plane is a function of the orientation of the weakness planes, as shown in Fig. 2-14. It is obvious that for the strength anisotropy, the experimental data and numerical values fit well especially for loading angle β between 20° and 80° (failure plane = weakness plane). There are also discrepancies between the experimental and simulation results for β between 0° to 15° and 80° to 90° where failure takes place inside the matrix and not along the weakness planes.

According to Pietruszczak and Mroz (2001), an anisotropic failure criterion extended from the Coulomb criterion was proposed to consider a spatial distribution of strength parameters. The failure function is defined through a traction component which acts on a physical plane. This critical plane approach has been successfully applied to the analysis of masonry structures (Pietruszczak and Ushaksaraei 2003). The performance of the critical plane approach is especially suited for rocks with evenly spaced homogeneous layers. Lee and Pietruszczak (2008) used the critical plane approach to depict the strength properties of transverse isotropic rocks combined with the Hoek and Brown failure criterion. Hoek-Brown rock parameters m and s are used to define rock masses anisotropy with the symmetric traceless tensors which describe the spatial distribution of strength parameters.

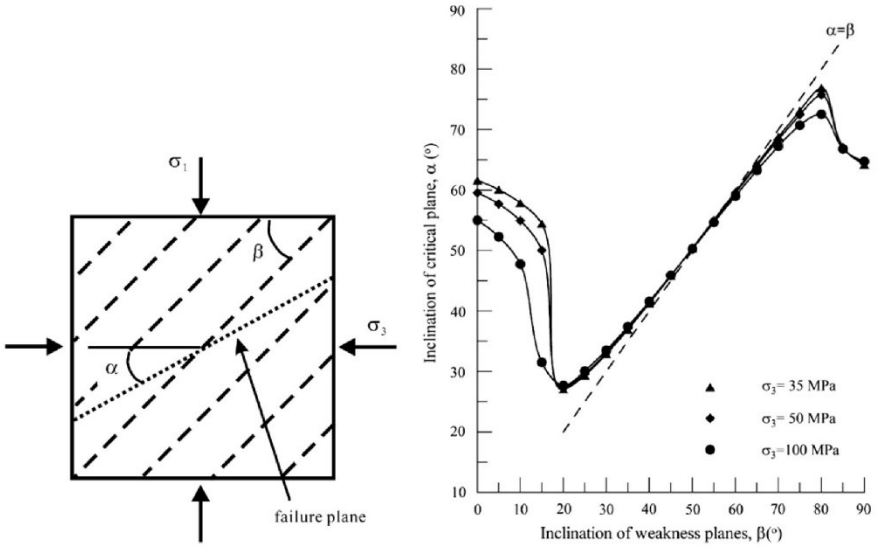

Fig. 2-14 (a) Definition of failure plane for anisotropic material under triaxial compression and (b) corresponding simulation results for slate (Lee and Pietruszczak 2008).

The purpose of the critical plane approach is to find out the orientation of a failure plane which satisfied the maximum of the failure function. The failure of the rock is then identified as failure along this critical plane but it should be noticed that the critical plane approach does not fit well the intact rock failure pattern. It is also not inconvenient to implement different failure criteria for the numerical analysis because the specification of the critical plane orientation is obtained from a maximization procedure (Pietruszczak and Mroz 2001). More detail information for the specific corresponding failure criterion can also be found in (Pei 2008).

This approach was incorporated in a constitutive model based on the multi-laminate framework which will be discussed later in section 2.4.4.

2.4.3.2. Microstructure tensor approach

A non-linear failure criterion was introduced to consider directly the anisotropy based on the microstructure tensor approach (Pietruszczak and Mroz 2000). This approach defines explicit functions in which the stress invariants and microstructure tensors are incorporated in connection with material parameters. The result of this failure criterion is a scalar parameter called anisotropy parameter (η) which is a function of higher degree tensors and quantifies the load orientation

influence in terms of the material axes. The general formulation of η can be expressed as follows according to Pietruszczak et al. (2002).

$$\eta = a_{ij} l_i = \hat{\eta}[1 + A_{ij} l_i l_{ij} + b_1 (A_{ij} l_i l_j)^2 + b_2 (A_{ij} l_i l_j)^3 + ...] \qquad (2.8)$$

η physically means the projection of the microstructure tensor a_{ij} on the direction of l_i. l_i and l_j are the normal components of that plane where a_{ij} is projected, $\hat{\eta}$ is the mean value of η. A_{ij} is the traceless symmetric tensor describing the bias in the spatial distribution and is the deviatoric part of the microstructure tensor a_{ij}. b_1 and b_2 are material parameters. A_{ij}, b_1 and b_2 are determined by curve fitting of simple tests, i.e. uniaxial compression tests.

In order to specify Eq. (2.8) in a sample having arbitrary planes of anisotropy with angle α in respect to the bedding planes (bedding orientation angle), Haghighat et al. (2015) provided a simple example (Fig. 2-15) based on the assumptions of Pietruszczak et al. (2002) for a sample under compressive loading σ_y ($\sigma_y = \sigma_1$) and constant confining pressure p_o ($p_0 = \sigma_2 = \sigma_3 =$ constant).

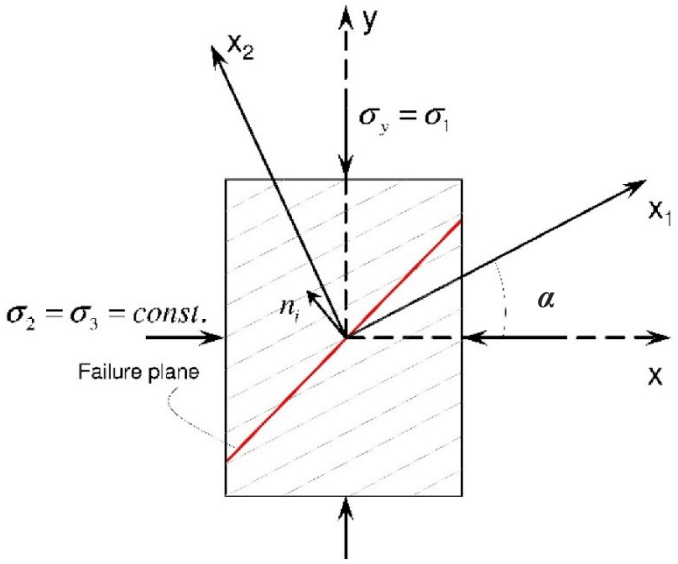

Fig. 2-15 Schematic of a failure plane and inherent planes of anisotropy (Haghighat et al. 2015).

In case of non-confining compression Eq. (2.8) can be expressed as follows:

$$\eta = a_{ij} l_i = \hat{\eta}[1 + A_1 (1 - 3\cos^2 \alpha) + b_1 A_1^2 (1 - 3\cos^2 \alpha)^2 + ...] \qquad (2.9)$$

The first full elasto-plastic constitutive model based on this failure criterion was introduced by Pietruszczak et al. (2002). In this model, a non-associated plasticity framework for brittle plastic anisotropic sedimentary rocks is used. It is based on a continuum elasto-plastic constitutive model

for concrete (Pietruszczak et al. 1988), in which the transition mechanisms from brittle to ductile behavior is conceptualized using an appropriate hardening/softening parameter. However, this framework is restricted to strain hardening only. The constitutive model by Pietruszczak et al. (2002) was the motivation of a simpler elasto-plastic model for argillite rock by Xu et al. (2013). That model uses a return mapping scheme created by Krieg and Krieg (1977) and Huang and Griffiths (2008). Xu et al. (2013) introduced a linear elastic-perfect-plastic constitutive model with associated flow rule based on the nonlinear constitutive model of Pietruszczak et al. (2002).

Recently, the microstructure tensor approach was adopted to formulate an elasto-plastic constitutive model based on the Mohr-Coulomb failure criterion (Haghighat et al. 2015). Similar to the previous model (Pietruszczak et al. 2002), the strength parameters (i.e. the cohesion and friction angle) were extended to consider the effect of load orientation. This elasto-plastic framework simulates exclusively strain hardening, but no softening. Haghighat et al. (2015) developed this framework based on a simple linear approximation of the Mohr-Coulomb failure criterion introduced in (Pietruszczak and Mroz 2000) which is applicable for low confinement. Abdi and Evgin (2013) and Haghighat et al. (2015) altered Eq. (2.9) to directly describe the anisotropic behavior of the Mohr-Coulomb rock parameters. In fact, the anisotropy parameter η is normalized to predict the value of friction angle ϕ_f in respect to the orientation angle while the cohesion c is assumed to be constant.

Table 2-6 and Fig. 2-16 show a comparison between the previously discussed three elasto-plastic models in which the microstructure tensor approach is used. The microstructure tensor approach was incorporated into a Mohr-Coulomb strain hardening/softening constitutive model by Nguyen and Le (2015) in which cohesion (initial and residual) and friction angle (interlocking and residual, initial friction angle is assumed to be zero) are orientation dependent. Their values can be predicted according to Eq. (2.9). The constitutive model assumes transverse isotropy where the elastic regime is linear applying Hooke's law while the plastic flow rule is non-associate. Regardless the time dependency of the Young's modulus, we focus here on the plastic part of this model and the consideration of the microstructure tensor approach. This model predicts well the hardening before yielding. The friction angle varies based on a square root function starting from zero to a maximum value (i.e. interlocking friction angle). By applying this model to simulate the behavior of Opalinus clay under triaxial test conditions, the simulations show good agreement with the lab results especially for higher confinement.

Table 2-6 Summary of microstructure tensor models and their applications

Model	**Pietruszczak et al. (2002)**	**Xu et al. (2013)**	**Haghighat et al. (2015)**
Modelled rock type	Transverse isotropic Tournemire shale (Niandou et al. 1997) E_1= 22 GPa, E_2 = 7 GPa, υ_1 = 0.12, υ_2 = 0.14 and G_2 = 4 GPa	Transverse isotropic argillite rock E_1= 5.619 GPa, E_2 = 4.129 GPa, υ_1 = 0.213, υ_2 = 0.187 and G_2 = 0.885 GPa	Transverse isotropic Tournemire argillite E_1= 12.5 GPa, E_2= 21 GPa, υ_1 = 0.16, υ_2 = 0.08 and G_2 = 4.57 GPa
Parameters used in Eq. (2.9)	$\hat{\eta}$ =22 MPa, A_1=0.017025, b_1=515.49, b_2=61735.3, b_3=2139820	$\hat{\eta}$ =26.885 MPa, A_1=0.17034, b_1=0.214, b_2=−0.563	$\hat{\eta}$ =1.0725 MPa, A_1=0.17034, b_1=5.4957
Used elasto-plastic framework	Framework for brittle plastic material by Pietruszczak et al. (1988) considering hardening only	Elastic-perfect-plastic framework based on Pietruszczak et al. (1988) and return mapping schemes	Linear approximated (Mohr-Coulomb) elasto-plastic framework.

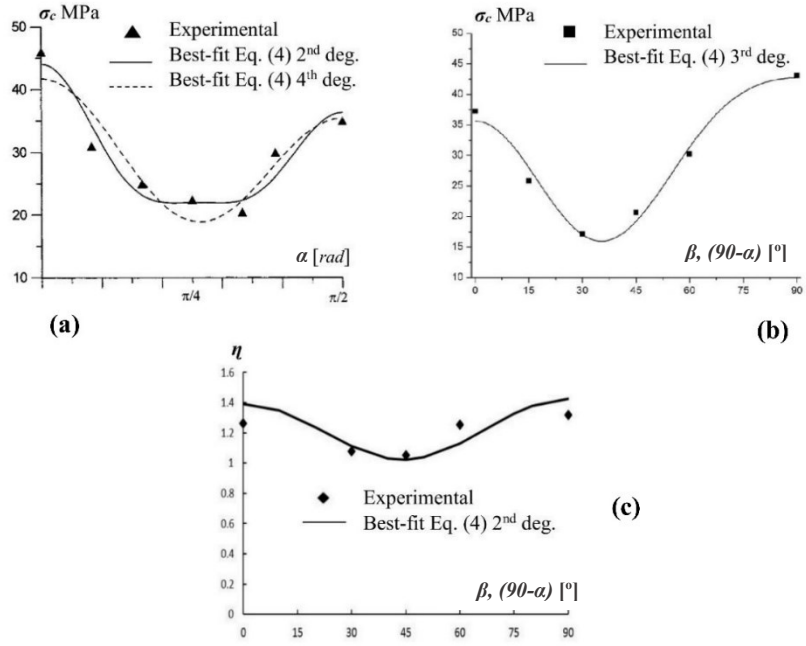

Fig. 2-16 Illustration of anisotropy behavior according to (a) Pietruszczak et al. 2002, (b) Xu et al. 2013, and (c) Haghighat et al. 2015.

2.4.4. Multi-laminate and micro-polar related approach

The multi-laminate approach is one of the most commonly used methods for equivalent continuum based models originally introduced by Zienkiewicz and Pande (1977) to simulate rock mass behavior based on the theory of elasto-visco-plasticity. The multi-laminate framework for modelling rock masses and soils is given by Pande and Yamada (1994). Sánchez et al. (2008) used the multi-laminate framework to predict the behavior of the geomaterials by considering several "integration planes" (Fig. 2-17).

The slip theory of plasticity was first introduced into a multi-laminate model for clay by Pande and Sharma (1983) not considering the rotation of the principal stress axes during plastic flow. The plasticity formulation of a multi-laminate isotropic hardening model for soil was presented by Pietruszczak and Pande (1987). A multi-laminate model for soft clays incorporating bonding anisotropy was developed by Cudny and Vermeer (2004) using the framework of rate independent plasticity. Within the past few years, sophisticated multi-laminate constitutive models incorporating anisotropy behavior for soils were developed by Schweiger et al. (2009).

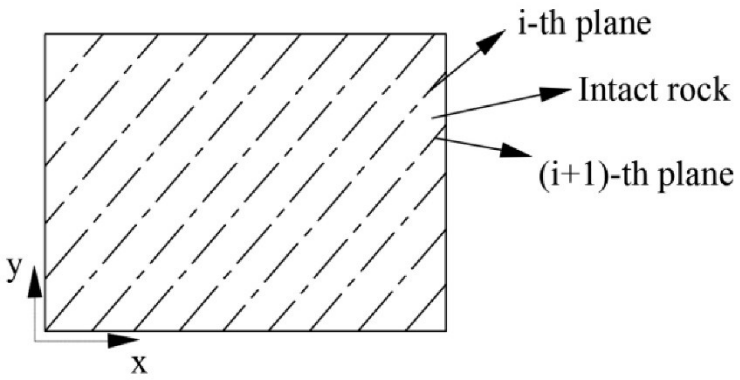

Fig. 2-17 Schematic for multi-laminate model

An improved multi-laminate model which uses the Coulomb criterion as yield condition on the i-th plane for clays were developed by Pietruszczak and Pande (2001). Cohesion and friction angle are orientation dependent. A set of second-order symmetric traceless tensors were used to describe the distribution of the Coulomb parameters. The multi-laminate model may be considered as a simple version of the critical plane approach (Pietruszczak and Mroz 2001), see also chapter 2.4.3.1.

A constitutive model similar to the multi-laminate framework was proposed to simulate the behavior of reinforced rock masses with rock bolting (Chen and Pande 1994). The intact rock was

treated as an isotropic material and yielding according to the Drucker-Prager failure criterion. The flow rule of the rock matrix is associate, while it is non-associate for the joint sets. The yield surface is based on the Mohr–Coulomb failure criterion (Chen and Egger 1999). Later, Chen et al. (2009) extended the original Chen model to consider spacing, normal and shear stiffness of the joints. On the other hand, Roosta et al. (2006) proposed a multi-laminate model which accounts for strain hardening/softening behavior to simulate jointed rock masses. The Mohr-Coulomb failure criterion with tension cut-off was used for both, the joint planes and the intact rock. Intact rock behaves elastic-perfect-plastic and the joint planes show strain hardening and softening. In these multi-laminate model simulations, the peak shear strength values are reproduced in a correct manner but the expected residual shear strength revealed larger deviation compared to test results.

2.4.5. Approaches based on Boehler's theory of stress transformation

As previously discussed, Boehler and Sawczuk (1977) defined the concept of stress tensor transformation as a straightforward failure criterion in which the stress tensor is dependent on the orientation of the inherent planes of anisotropy. In case of transverse isotropic rocks, a fourth order transformation tensor A_{ijkl} is defined according to the existing planes of anisotropy, while this tensor is a function of three independent parameters α, β and γ. These parameters are defined from curve fitting with lab test results.

$$\hat{\sigma}_{ij} = A_{ijkl}\sigma_{kl} \tag{2.10}$$

$\hat{\sigma}$ is the anisotropic stress tensor. This approach is a very effective way to extend most of the isotropic elasto-plastic constitutive models to anisotropic models.

2.4.5.1. Stress history model of Oka

Oka et al. (2002) introduced an extension to an isotropic elasto-plastic constitutive model which considers the strain hardening/softening behavior of soft rocks proposed by Adachi and Oka (1995). The original isotropic model has the ability to consider the stress and strain history tensors and the plastic deformation is governed by a non-associated flow rule. To extend such an isotropic model, Oka et al. (2002) considered both, the elastic and the plastic anisotropy assuming that the tested soft rock is transverse isotropic. For the elastic part five elastic independent moduli are specified and the stress incrementation is applied using the generalized Hooke's law (linear elasticity).

The stress tensor transformation approach is applied in the plastic regime to adapt the anisotropic characteristics within the plastic stress tensor. The plastic strain increment in the original isotropic

constitutive model is replaced by the transformation tensor proposed by Boehler and Sawczuk (1977) within the yield function and the plastic potential function. By applying this modified model to simulate triaxial tests on a weak rock, a slight overestimation of the residual strength and underestimation of the volumetric strain is observed. This overestimation is explained by Fu et al. (2012) as there is no consideration of the intermediate principal stress dependency.

2.4.5.2. The inherent anisotropic soft sedimentary rock model

Fu et al. (2012) added mechanical anisotropy to an existing elasto-visco-plastic constitutive model proposed by Zhang et al. (2005). This model is complicated as it is formulated in order to describe not only the mechanical anisotropy but also to include strain hardening/softening, stress dilatancy and the influence of the intermediate principal stress. Like the work of Zhang et al. (2005), the anisotropic model assumes that the elastic part has no stiffness anisotropy, but a hypo-elastic relation between the Young's modulus and the mean principal stress exists. The anisotropic plastic deformation follows an associated flow rule. The plasticity framework of Zhang et al. (2005) considers the transformation of the equivalent isotropic stress tensor into the generalized stress space called t_{ij}-concept according by Nakai and Mihara (1984). However, Fu et al. (2012) altered the equivalent isotropic stress tensor according to the Boehler's theory of stress transformation by introducing a modified anisotropic model with two stages of transformations: first transferring the isotropic stress tensor into the anisotropic state and then describing the anisotropic stress tensor in the t_{ij} space. By applying this model to triaxial tests of two soft rocks, the predicted stress behavior and the volumetric strain almost met the lab test results for different applied confining stresses. As advantage over the Oka model, Fu et al. (2012) considered the dependency on the intermediate principal stress. On the other hand, the model of Fu has no stiffness anisotropy, the applied flow rule is associated and it requires a significant number of parameters.

2.4.5.3. The Cam-Clay based constitutive model by Nova

First versions of Cam-Clay based anisotropic rock-like models for soft rocks and bonded soils was presented by Nova (1986a,b). Based on the technique of Boehler (Boehler and Sawczuk 1977), an elasto-plastic constitutive model with associated flow ruled was introduced which captures strain hardening of soft rocks (Nova 1986b). By applying this model to triaxial lab tests on diatomite (Allirot and Boehler 1979), it was found that the simulations did not give good agreement with the lab results and the model tends to overestimate the hardening behavior of the tested rock with increasing confining pressure (Attaia et al. 2015).

2.4.5.4. Crooke's 3D orthotropic model

The modified Cam-Clay model was extended to account for stiffness and strength anisotropy of orthotropic soft rocks such as shales by Crook et al. (2002). The developed yield surface is orthotropic pressure dependent. In other words, all three principal stresses are included into the constitutive model. The elastic behavior of this model is linear and the post peak behavior shows strain hardening/softening based on the evolution of volumetric plastic strain (Crook, Yu, and Willson 2002). The complexity of this model arises in the post peak region where compaction or consolidation of soft rock appears. The Crooke model adopts the Hoffman yield criterion (Hoffman 1967) and the return mapping algorithm developed by Hashagen and de Borst (2001). The detailed numerical implementation of the Crooke model is introduced in (Attaia et al. 2015), although the procedure is slightly different than the original model where only the first derivatives of the yield criterion are used. Crook et al. (2002) has noticed the stiffening of the Young's modulus with increasing applied confinement, but the constitutive model neglects this. The calibration of Crooke's model for different confining pressures on horizontal bedded shale samples showed a significant agreement especially in the post peak range for axial and radial strains. This model has been extended by Søreide et al. (2008) to include thermal effects. However, there is significant mismatch between numerical simulation and lab testing for undrained samples (Søreide et al. 2008) and this might be due to the lack of the implementation of the local strain effects at large deformation.

2.4.5.5. Extended Drucker-Prager model

An elasto-plastic constitutive model was developed for anisotropic weak rocks which considers strain hardening/softening post peak behavior based on the Drucker-Prager failure criterion (François et al. 2011). The elastic regime is linear transverse isotropic. The simulation of the post peak hardening/softening behavior is based on the technique of mobilized friction and cohesion via a hyperbolic variation of the internal variables as a function of the Von Mises equivalent plastic strain (Barnichon 1998). The plasticity framework is non-associate. The plastic strain at each time step is corrected according to computed values of friction angle and cohesion, which vary between the initial and the critical values. Assuming hardening behavior, the critical value of both, cohesion and friction are greater than the initial values, while it is the opposite in case of softening. This model was successfully applied by François et al. (2014) to estimate the Excavation Damaged Zone (EDZ) around saturated overconsolidated Boom clay.

3. Transubi model

3.1. Introduction

This chapter introduces a modified bi-linear strain hardening/softening ubiquitous joint constitutive model (Transubi model) which describes the mechanical behavior of layered rock masses by smeared joints across the rock mass. This modified model considers not only the strength anisotropy but also the elastic stiffness anisotropy (transverse isotropic stiffness matrix). Thus, new elastic stress increments and the plastic corrections have to be included. The Transubi model is applied to simulate the behavior of transverse isotropic rock samples under uniaxial compression and triaxial loading. Simulation results using the Transubi model are compared with the analytical solution from Jaeger and the Caniso model available in FLAC 8.0.

3.2. Elasto-plastic modeling of inherent anisotropic rocks

3.2.1. Transformation of coordinates

Usually, stress state and stiffness tensors of the rock mass are defined with respect to a fixed global coordinate system (X, Y, Z). In order to transform tensors from a global to another coordinate system, for example (x', y′, z′), series of transformation rules are applied. The composition of the rotation matrix for strain tensor is explained as following. Consider a strain state in both local and global coordinate systems $\varepsilon_{x'y'z'}$ and ε_{XYZ}, respectively. Thus, this relation could be expressed as follows:

$$\varepsilon_{x'x'} = \frac{\partial U_{x'}}{\partial x'} \quad \text{and} \quad \varepsilon_{XX} = \frac{\partial U_X}{\partial X} \tag{3.1}$$

where, $U_{x'}$ and U_X are the displacement components in x' and X directions, respectively. By applying chain rule of differentiation, Eq. 3.1 is obtained as follows.

$$\begin{aligned} \frac{\partial U_X}{\partial x'} &= \frac{\partial U_X}{\partial X}\frac{\partial X}{\partial x'} + \frac{\partial U_X}{\partial Y}\frac{\partial Y}{\partial x'} + \frac{\partial U_X}{\partial Z}\frac{\partial Z}{\partial x'} \\ \frac{\partial U_X}{\partial x'} &= l_x \frac{\partial U_X}{\partial X} + l_y \frac{\partial U_X}{\partial Y} + l_z \frac{\partial U_X}{\partial Z} \end{aligned} \tag{3.2}$$

Similarly,

$$\frac{\partial U_Y}{\partial x'} = l_x \frac{\partial U_Y}{\partial X} + l_y \frac{\partial U_Y}{\partial Y} + l_z \frac{\partial U_Y}{\partial Z}$$
$$\frac{\partial U_Z}{\partial x'} = l_x \frac{\partial U_Z}{\partial X} + l_y \frac{\partial U_Z}{\partial Y} + l_z \frac{\partial U_Z}{\partial Z} \quad (3.3)$$

Generally, the displacement component $U_{x'}$ is written in respect to the global system as follows.

$$U_{x'} = l_x U_X + l_y U_Y + l_z U_Z \quad (3.4)$$

By differentiating Eq. 3.4 with respect to x', the following relation results.

$$\frac{\partial U_{x'}}{\partial x'} = l_x \frac{\partial U_X}{\partial x'} + l_y \frac{\partial U_Y}{\partial x'} + l_z \frac{\partial U_Z}{\partial x'} \quad (3.5)$$

By the substitution of Eqs. 3.2 and 3.3 in Eq. 3.5, $\varepsilon_{x'x'}$ is obtained in reference to (X, Y, Z).

$$\varepsilon_{x'x'} = l_x^2 \varepsilon_{XX} + l_y^2 \varepsilon_{YY} + l_z^2 \varepsilon_{ZZ} + l_x l_y \varepsilon_{XY} + l_x l_z \varepsilon_{XZ} + l_y l_z \varepsilon_{YZ} \quad (3.6)$$

Similarly,

$$\varepsilon_{y'y'} = m_x^2 \varepsilon_{XX} + m_y^2 \varepsilon_{YY} + m_z^2 \varepsilon_{ZZ} + m_x m_y \varepsilon_{XY} + m_x m_z \varepsilon_{XZ} + m_y m_z \varepsilon_{YZ}$$
$$\varepsilon_{z'z'} = n_x^2 \varepsilon_{XX} + n_y^2 \varepsilon_{YY} + n_z^2 \varepsilon_{ZZ} + n_x n_y \varepsilon_{XY} + n_x n_z \varepsilon_{XZ} + n_y n_z \varepsilon_{YZ} \quad (3.7)$$

Proceeding in a similar way, the second-order strain tensor (6x1 matrix) is rotated from global to local coordinates using the following transformation rules:

$$\varepsilon_{x'y'z'} = R_\varepsilon \varepsilon_{XYZ} \quad (3.8)$$

where, R_ε is 6x6 rotation tensor which is defined by the direction cosines of local coordinates in terms of the global coordinates. R_ε is formed based on the above mentioned procedure as follows.

$$R_\varepsilon = \begin{bmatrix} l_x^2 & l_y^2 & l_z^2 & l_x l_y & l_x l_z & l_y l_z \\ m_x^2 & m_y^2 & m_z^2 & m_x m_y & m_x m_z & m_y m_z \\ n_x^2 & n_y^2 & n_z^2 & n_x n_y & n_x n_z & n_y n_z \\ 2l_x m_x & 2l_y m_y & 2l_z m_z & l_x m_y + l_y m_x & l_x m_z + l_z m_x & l_y m_z + l_z m_y \\ 2l_x n_x & 2l_y n_y & 2l_z n_z & l_x n_y + l_y n_x & l_x n_z + l_z n_x & l_y n_z + l_z n_y \\ 2m_x n_x & 2m_y n_y & 2m_z n_z & m_x n_y + m_y n_x & m_x n_z + m_z n_x & m_y n_z + m_z n_y \end{bmatrix} \quad (3.9)$$

Same procedure is utilized to form the transformation matrix R_σ for the second-order stress tensor. Similar to Eq. 3.8, the stress state is transformed from global system to local coordinates as follows.

$$\sigma_{x'y'z'} = R_\sigma \sigma_{XYZ} \quad (3.10)$$

As noticed from Eqs. 3.8 and 3.10, the rotation tensor defined for second order strain tensor R_ε is slightly different from the second order stress rotation tensor R_σ. As the rotational matrix is orthogonal, both tensors R_ε and R_σ could be linked to each other as follows:

$$R_\varepsilon^T = R_\sigma^{-1} \tag{3.11}$$

The transformation of the elastic stiffness matrix $\{S\}$ is more complicated and is given as follows:

$$\{S_{XYZ}\} = R_\varepsilon^T \{S_{x'y'z'}\} R_\varepsilon \tag{3.12}$$

3.2.1. Algorithms of anisotropic material

According to elasto-plasticity theory: if a material is subjected to a load, two types of deformations are expected: reversible deformations ε^e (elastic) and irreversible deformations ε^p (plastic). Plastic deformations occur when the stress state reaches the yield condition.

$$\varepsilon = \varepsilon^e + \varepsilon^p \tag{2.1}$$

A yield surface [$F(\sigma) = 0$] has to be defined as plastic limit. If the stress state does not violate the yield surface, the total strains are elastic. Once the yield surface is violated, a correction of the stress state is required. Plastic corrections for granular materials (i.e. rocks, soils, cement or concrete) are based on the plastic potential [$g(\sigma) = \text{const.}$] as the flow rule is non-associated. For more details about the plasticity of granular material, see Vermeer and de Borst (1984). Depending on the defined number of yield surfaces, the techniques for the plastic corrections differ.

3.2.1.1. Single surface plasticity

For stress-based plastic algorithms, the new trail stress value is predicted as follows:

$$\sigma_{i+1}^{trial} = \sigma_i + S d\varepsilon_{i+1} \tag{3.13}$$

Then, the stress state is tested against the defined yield surface:

$$\text{if} \begin{array}{ll} F(\sigma_{i+1}^{trial}) < 0 & \text{elastic domain} \\ F(\sigma_{i+1}^{trial}) > 0 & \text{plastic domain} \end{array} \tag{3.14}$$

If the stress state reaches the plastic domain, the corresponding yield function and flow rule are mobilized as shown in Fig. 3-1.

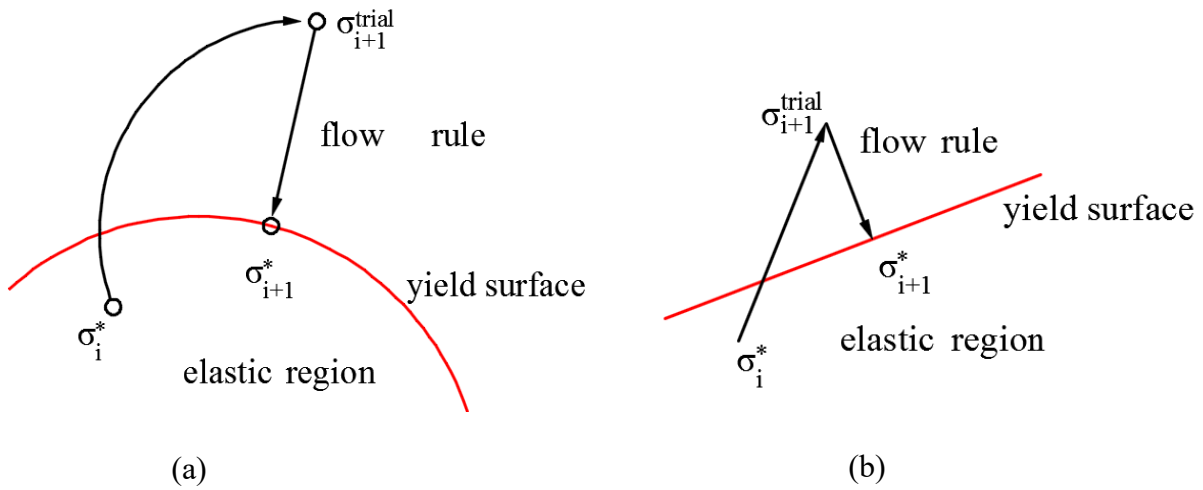

Fig. 3-1 Schematic showing the return mapping procedure for (a) a smooth non-linear yield surfaces, and (b) a linear yield surfaces.

3.2.1.2. Multi surface plasticity

If the yield surface is more complex like for the Transubi model, a more sophisticated procedure should be considered. Each yield surface of this model has its own strength parameters. Generally, the shape of the yield surface is either convex or linear, see Fig. 3-2.

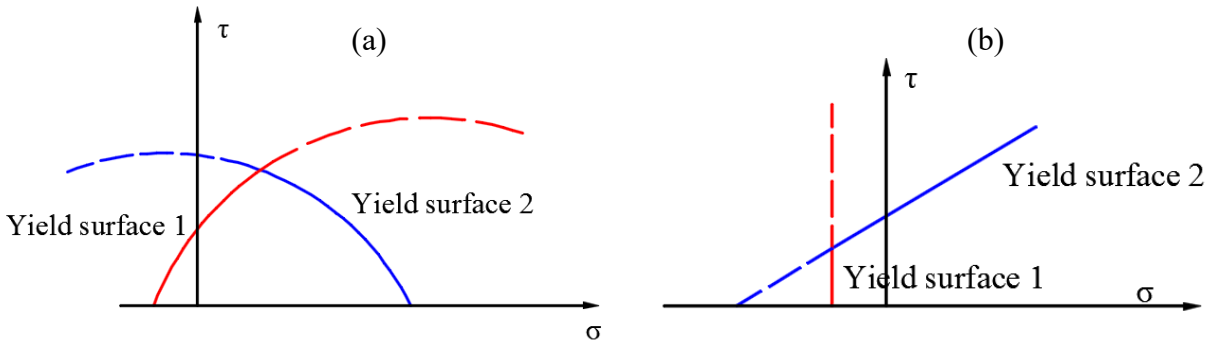

Fig. 3-2 Schematic of interaction of two yield surfaces (a) two convex yield surfaces, and (b) two linear yield surfaces

The intersection between a M-C shear failure criterion and a tension cut-off criterion is shown in Fig. 3-3.

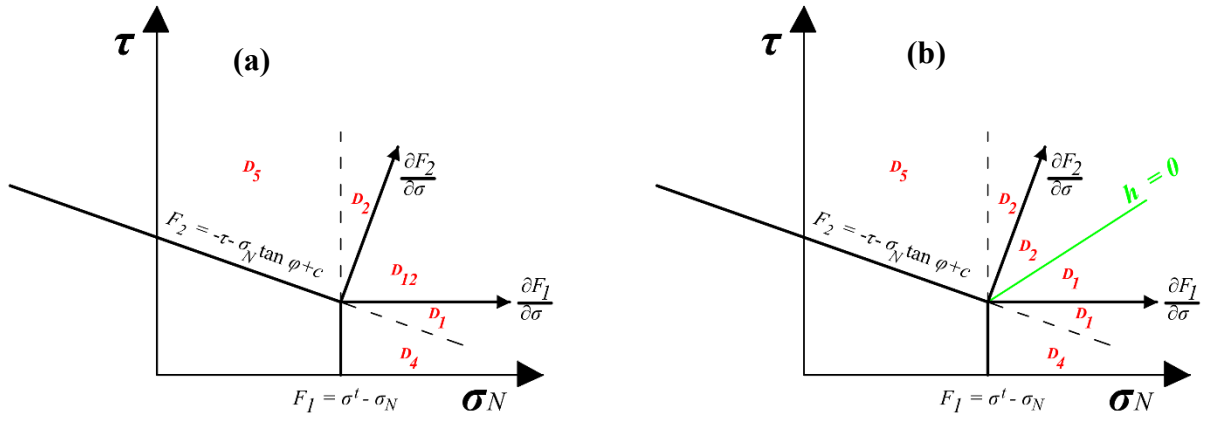

Fig. 3-3 Active surface detection of a multi yield surface composed of a M-C criterion and tension cut-off (a) general solution, and (b) proposed solution by Itasca (2016) applied to the ubiquitous joint model

The total plastic strain increments are given by the sum of the plastic strains of all active plasticity surfaces.

$$\varepsilon^p = \sum_{i=1}^{n} \lambda_i \left(\frac{\partial g_i}{\partial \sigma}\right) \qquad (3.15)$$

where, i represents the number of yield surfaces and λ is defined as the plastic multiplier for the activated yield surface i (see section 3.3.2). According to Fig. 3-3.a, the detection of the active yield-surface is complex. Thus, several different situations have to be considered (Ortiz and Simo 1986).

Case I: when only one yield surface is violated (domains D4 or D5), plastic corrections are processed based on the corresponding functions F_i and g_i.

Case II: when more than one yield surface is violated, the situation can be categorized as:

(a) If $F^{trial}(\sigma) > 0$ and $\lambda_i > 0$ for surfaces i =1 and 2 (domain D12): both surfaces are active.

(b) If $F^{trial}(\sigma) > 0$ and $\lambda_i < 0$, for surfaces i =1 or 2 (domains D1 or D2): only one of the surfaces is active.

Another solution has been proposed by Itasca (2016) which is used for example for the ubiquitous joint model (Fig. 3-3.b). For case II, two yield functions F_1 and F_2 are separated by a diagonal function named (h = 0):

$$h = c + \sigma^t \tan\phi - \tau - (\sqrt{1+\tan^2\phi} - \tan\phi)(\sigma^t - \sigma_N) \qquad (3.16)$$

If $h < 0$ means surface i =2 is active (domain D2). On the other side, if $h > 0$, surface i =1 is active (domain D1). Later in section 3.3.3, a detailed discussed regarding the plastic corrections and detection of multi-surface failure criterion is presented.

3.2.3. Existing upgrades for ubiquitous joint model

Modelling of layered rock mass can be performed by implicit consideration of joints (i.e. ubiquitous joint model) or by explicit representation of the discontinuities (i.e. discrete element approach) (Davila and Schubert 2014). However, computational power and time consumption limits the use of discrete approaches. The accuracy of implicit joint models and the Cosserat approach has been investigated by Riahi (2008) and Dawson (1995). This chapter considers the continuum-based implicit approach (i.e. smeared joints).

The elasto-perfect-plastic ubiquitous joint model is one of the numerical models used to analyze jointed rock masses (Wang and Huang 2009). It is found in the FLAC software package as "an anisotropic plasticity model that includes weak planes of specific orientation embedded in a Mohr-Coulomb (M-C) solid" (Itasca 2016). This model can predict the strength anisotropy for a rock mass containing weak planes reasonably accurate. However, the presence of the joints is taken into account for the plastic corrections but has no effect on the elastic behavior and the model is restricted to one set of joints only (Azadeh Riahi 2008). A modified ubiquitous joint model (Comba model) has been presented to simulate the behavior of columnar basalt with the presence of up to four arbitrary orientation of weak planes. The elastic stiffness matrix in the Comba model is anisotropic due to the orientation of the joint sets and spacing and stiffness are considered. However, it is difficult to set values for joints orientation and stiffness that equalize the elastic stiffness matrix of the transverse isotropy for a specific orientation (Detournay, Meng, and Cundall 2016).

First implementations considered the jointed rock mass without considering the elastic stiffness anisotropy (i.e. cross anisotropy), such as: the elasto-perfect-plastic ubiquitous joint model (Itasca 2016). Then, the elastic transverse isotropic stiffness was implemented without consideration of strain softening. Such models were developed incorporating one or several anisotropy planes with softening but without considering the rock matrix (e.g. Wittke (1990); Caniso model in (Itasca 2016) or Jointed Rock model in (Plaxis 2016). Other approaches considered the anisotropy of the rock matrix without incorporating the softening of both, the rock matrix and the joint plane (Rahmati 2016) and (Ismael and Konietzky 2017). On the other hand, Blümling and Konietzky

(2003) introduced a bi-linear elasto-plastic strain hardening/softening ubiquitous joint model which was improved later by Konietzky and te Kamp (2004) as well as Konietzky and te Kamp (2006) by coupling of two different mechanical constitutive models: the elastic transverse isotropic model and the bi-linear subiquitous joint model. This model was successfully used to simulate the mechanical behavior of Opalinus clay.

To overcome these partial limitations a transverse isotropic elasto-plastic model called Transubi-model with stiffness and strength anisotropy and strain hardening/softening of weak planes and rock matrix is proposed. The "Transubi" model has several advantages: (i) the elastic matrix is transverse isotropic with 5 independent parameters, (ii) pre- and post-yielding behavior can be non-linear: for example, the pre-yielding region can show hardening and the post-yielding region can show softening, (iii) strength anisotropy is considered, and (iv) the bi-linear concept is adapted for both, the rock matrix and the joint planes to allow up to two M-C failure envelopes describing the plasticity of the material. Thus, the Transubi model is known as a transverse isotropic bi-linear strain/hardening ubiquitous joint constitutive model developed for 2D continua.

3.3. Theoretical background of the Transubi model

In principle, the Transubi model is using the same methodology as the original subiquitous joint model. Symmetry characteristics and corresponding properties are illustrated in Fig. 3-4. A zone represents both, a transverse isotropic elasto-plastic rock matrix (RM) and a joint plane (JP), which can fail in tension or shear. Mohr-Coulomb parameters are given for the rock matrix and the joint plane as well in addition to the transverse isotropic matrix. The angle α refers to the orientation of the joint plane which equals (90-β). For a general 3-dimentional case, the orientation is given either by the dip (*dip*) and the dip direction (*dd*) or by specifying the three components (n_x, n_y, n_z) of the normal unit vector of the joint plane. In our study, a 2-dimentional case is applied. The *dd* is assumed as 90^o while the *dip* equals therefore the inclination angle α (Fig. 3-4).

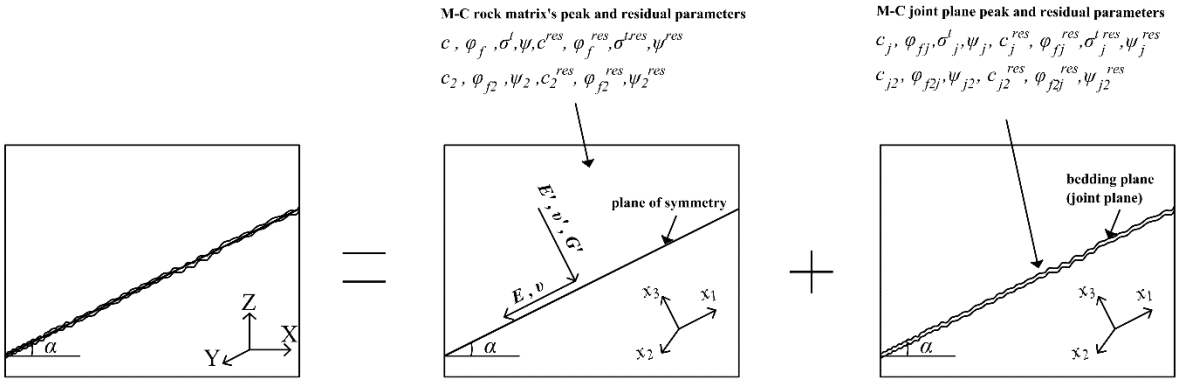

Fig. 3-4 Transubi-model: illustration of a single zone with anisotropy plane and corresponding material parameters

3.3.1. Elastic increments

The elastic stiffness matrix $\{S\}$ is described in local coordinates (x_1, x_2, x_3) of the joint plane. It is simpler to provide the compliance matrix $\{C\}$ which is the inverse of the stiffness matrix. Five independent elastic stiffness parameters have to be given parallel or normal to the joint plane, respectively. The independent elastic properties in the plane parallel to the joint plane are Young's modulus E and Poisson's ratio υ, while the other elastic properties are in the plane normal to the joint plane (E', υ' and G'), as indicated previously in Fig. 3-4. Based on the orientation of the joint plane, a transformation of the elastic stiffness matrix from local coordinates the global coordinates (X, Y, Z) is implemented (Eq. 3.17) as discussed in section 3.2.1. The calculation scheme of the elastic increments is always performed in global coordinates.

$$\{C\} = \begin{bmatrix} \frac{1}{E} & \frac{-\nu}{E} & \frac{-\nu'}{E'} & 0 & 0 & 0 \\ \frac{-\nu'}{E'} & \frac{1}{E} & \frac{-\nu'}{E'} & 0 & 0 & 0 \\ \frac{-\nu'}{E'} & \frac{-\nu'}{E'} & \frac{1}{E'} & 0 & 0 & 0 \\ 0 & 0 & 0 & \frac{2(1+\nu)}{E} & 0 & 0 \\ 0 & 0 & 0 & 0 & \frac{1}{G'} & 0 \\ 0 & 0 & 0 & 0 & 0 & \frac{1}{G'} \end{bmatrix} \tag{3.17}$$

According to Amadei (1996), there are several restrictions in respect to the elastic parameters.

$$\left.\begin{array}{l} E > 0 \\ E' > 0 \\ G' > 0 \\ \nu^2 \le 1 \\ \nu'^2 \le 1 \\ (1-\nu) - \frac{2E\nu'^2}{E'} \ge 0 \end{array}\right\} \tag{3.18}$$

3.3.2. Yield surfaces and input parameters

The rock matrix is defined as bi-linear M-C solid with two intersecting shear failure envelops. First envelop has the strength parameters: cohesion c, friction angle ϕ_f, dilation angle ψ and a tension cut-off with value σ^t as a tensile strength. The second shear yield surface has parameters cohesion c_2, friction angle ϕ_{f2} and dilation angle ψ_2. Residual strength parameters could be assigned for both yield surfaces except tensile strength which is exclusively defined for the first surface. Similar, a bi-linear strength surface is defined for the joint plane. Fig. 3-5 introduces the bi-linear M-C yield surface for both, the rock matrix and the joint plane.

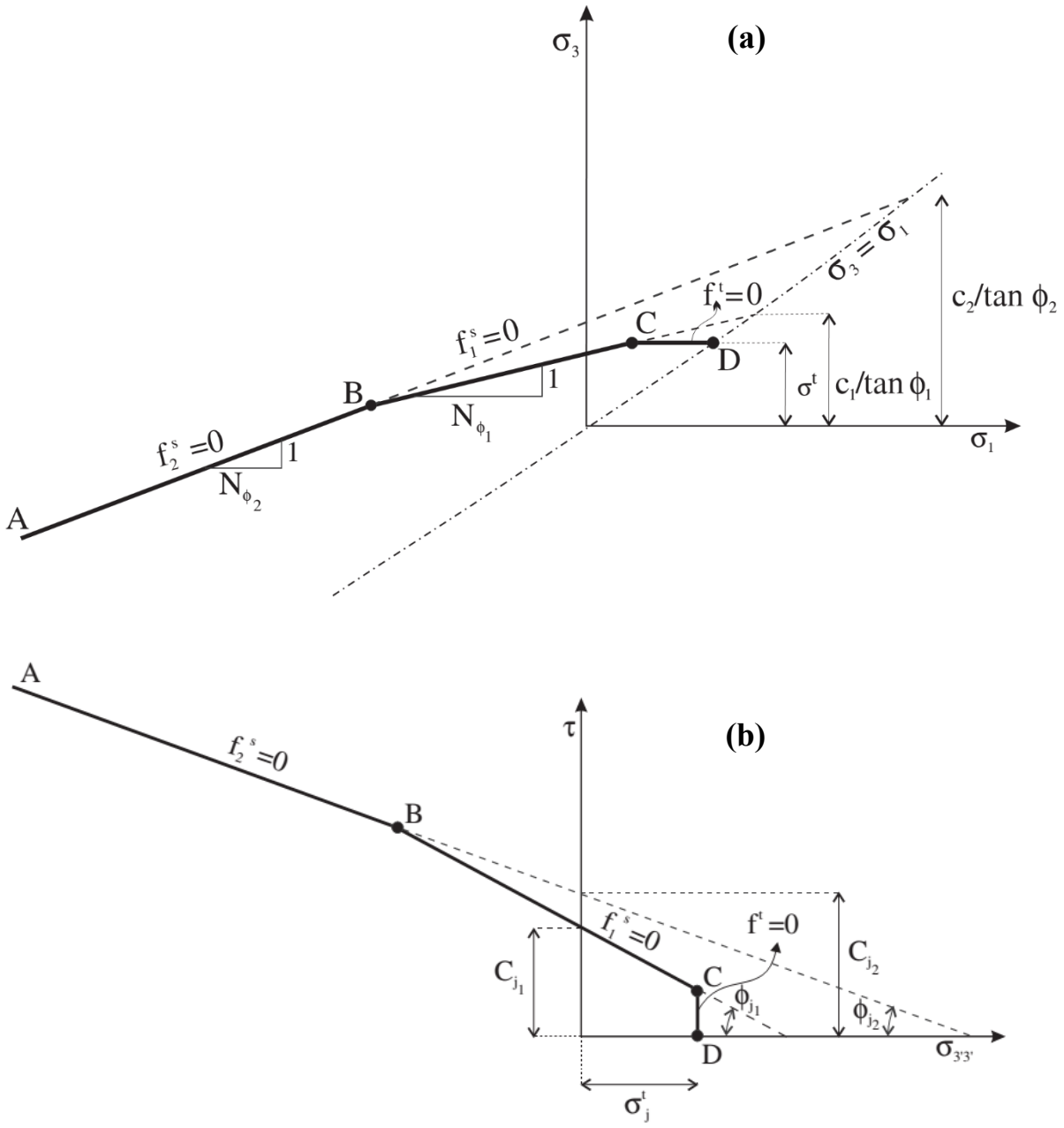

Fig. 3-5 Schematics showing the bi-linear failure criterion for (a) rock matrix in the principal stress space , and (b) joint plane in local stress coordinates (Itasca 2016).

During the elastic stress incrementation, the yield condition is always monitored for both, the rock matrix and the joint plane. For checking the failure condition inside the rock matrix, the global stress state is transformed into the principal stress state as shown in Eq. 3.19. Also, the stiffness matrix is transformed into the principal coordinates (x^P, y^P, z^P) leading to $\{S^P\}$.

$$\left.\begin{aligned}\sigma_1 &= S_{11}^P\varepsilon_1 + S_{12}^P\varepsilon_2 + S_{13}^P\varepsilon_3\\ \sigma_2 &= S_{21}^P\varepsilon_1 + S_{22}^P\varepsilon_2 + S_{23}^P\varepsilon_3\\ \sigma_3 &= S_{31}^P\varepsilon_1 + S_{32}^P\varepsilon_2 + S_{33}^P\varepsilon_3\end{aligned}\right\} \tag{3.19}$$

As shown in Fig. 3-5.a, segments B-C and B-A are two intersected M-C failure surfaces at point B. The segments are defined by $f_1{}^s = 0$ and $f_2{}^s = 0$; respectively. The segment D-C is the tension cut-off part and represented by $f^t = 0$. Thus, the yield functions in the principal stress plane are defined as follows:

$$\left.\begin{aligned}f_1^s &= \sigma_1 - \sigma_3 N_{\phi 1} + 2c_1\sqrt{N_{\phi 1}}\\ f_2^s &= \sigma_1 - \sigma_3 N_{\phi 2} + 2c_2\sqrt{N_{\phi 2}}\\ f^t &= \sigma_3 - \sigma^t\end{aligned}\right\} \tag{3.20}$$

where

$$N_\phi = \frac{1+\sin\phi_f}{1-\sin\phi_f} \tag{3.21}$$

For the intersection point between the shear yield surfaces at point B, the corresponding value of the minimum principal stress defined as $\sigma_3{}^I$ is given by:

$$\sigma_3{}^I = \frac{2c_2\sqrt{N_{\phi 2}} - 2c_1\sqrt{N_{\phi 1}}}{N_{\phi 2} - N_{\phi 1}} \tag{3.22}$$

The plastic shear potential for rock matrix corresponds to a non-associated flow rule by using dilation angles (ψ_1 and ψ_2) instead of the friction angles (Eq. 3.20), while the tensile plastic potential follows an associated flow rule.

$$\left.\begin{aligned}g_1{}^s &= \sigma_1 - \sigma_3 N_{\psi 1}\\ g_2{}^s &= \sigma_1 - \sigma_3 N_{\psi 2}\\ g^t &= \sigma_3\end{aligned}\right\} \tag{3.23}$$

where

$$N_\psi = \frac{1+\sin\psi}{1-\sin\psi} \tag{3.24}$$

After checking the failure state of the rock matrix in the principal stress plane, the corrected stress state (discussed later in chapter 3.3.3.1) is returned back into the global system. Then, the global stress state is transformed to the joint plane local coordinates using the joint inclination angle α. The local stress state is decomposed into two stress components: tangential stress component τ and normal stress component $\sigma_{3'3'}$ acting on the joint plane. The stress components at local coordinates are obtained by the following relations:

$$\left.\begin{aligned}
\sigma_{1'1'} &= S_{11}\varepsilon_{1'1'} + S_{12}\varepsilon_{2'2'} + S_{13}\varepsilon_{3'3'} \\
\sigma_{2'2'} &= S_{12}\varepsilon_{1'1'} + S_{11}\varepsilon_{2'2'} + S_{13}\varepsilon_{3'3'} \\
\sigma_{3'3'} &= S_{13}\varepsilon_{1'1'} + S_{13}\varepsilon_{2'2'} + S_{33}\varepsilon_{3'3'} \\
\sigma_{1'2'} &= \frac{E}{(1+\nu)}\varepsilon_{1'2'} \\
\sigma_{1'3'} &= 2G'\varepsilon_{1'3'} \\
\sigma_{2'3'} &= 2G'\varepsilon_{2'3'}
\end{aligned}\right\} \qquad (3.25)$$

where; S_{11}, S_{12}, S_{13} and S_{33} are elastic stiffness components obtained from the inversion of Eq. 3.17.

$$\left.\begin{aligned}
S_{11} &= E\frac{E'-\nu'^2 E}{(1+\nu)[(1-\nu)E'-2\nu'^2 E]} \\
S_{12} &= E\frac{\nu E'-\nu'^2 E}{(1+\nu)[(1-\nu)E'-2\nu'^2 E]} \\
S_{13} &= E\frac{\nu' E'}{[(1-\nu)E'-2\nu'^2 E]} \\
S_{33} &= E'\frac{(1-\nu)E'}{[(1-\nu)E'-2\nu'^2 E]}
\end{aligned}\right\} \qquad (3.26)$$

The acting normal stress component on the joint plane $\sigma_{3'3'}$ is obtained from Eq. 3.25. The tangential shear stress component τ is computed as follows:

$$\tau = \sqrt{\sigma_{1'3'}^2 + \sigma_{2'3'}^2} \qquad (3.27)$$

Similar to the above mentioned yield surface of the rock matrix, the joint plane failure surface consists of segments B-C and B-A which are two intersected Mohr-Coulomb failure criteria surfaces at point B. Each segment is defined $f_1^s = 0$ and $f_2^s = 0$; respectively. D-C is the tension cut-off part and is represented by $f^t = 0$.

$$\left.\begin{aligned} f_1^s &= \tau - \sigma_{3'3'} \tan\phi_{j1} + c_{j1} \\ f_2^s &= \tau - \sigma_{3'3'} \tan\phi_{j2} + c_{j2} \\ f^t &= \sigma_{3'3'} - \sigma_j^t \end{aligned}\right\} \tag{3.28}$$

Similar to the rock matrix, the plastic shear potential for joint plane follows a non-associated flow rule by using dilation angles (ψ_{j1} and ψ_{j2}) instead of the friction angles (Eq. 3.28), while the tensile plastic potential follows an associated flow rule.

$$\left.\begin{aligned} g_1^s &= \tau - \sigma_{3'3'} \tan\psi_{j1} \\ g_2^s &= \tau - \sigma_{3'3'} \tan\psi_{j2} \\ g^t &= \sigma_{3'3'} \end{aligned}\right\} \tag{3.29}$$

3.3.3. Plastic corrections for rock matrix and joint plane

Once the stress state exceeds the yield conditions for either the rock matrix or the joint plane ($f_1^s > 0$ or $f_2^s > 0$ or $f^t > 0$), a series of plastic corrections are performed to return the stress state to the defined yield surface.

3.3.3.1. Plastic corrections of rock matrix for yielding in shear and tension

The flow rule for plastic yielding has the following form:

$$\Delta\varepsilon_i^p = \lambda \frac{\partial g}{\partial \sigma_i} \tag{3.30}$$

where, i = 1 to 3; λ corresponds to the plastic multiplier for both, shear and tension. In the case of shear failure, the plastic strain increments ($\Delta\varepsilon_i^{p,s}$) are given as follows:

$$\begin{aligned} \Delta\varepsilon_1^{p,s} &= \lambda^s \\ \Delta\varepsilon_2^{p,s} &= 0 \\ \Delta\varepsilon_3^{p,s} &= -\lambda^s N_\psi \end{aligned} \tag{3.31}$$

Thus, the obtained plastic shear corrections $\Delta\sigma^{P,C}$ for the principal stresses in Eq. 3.19 are given by Eq. 3.32.

$$\left.\begin{aligned}\Delta\sigma_1^{P,C} &= -\lambda^s(S_{11}^P - S_{13}^P N_\psi)\\ \Delta\sigma_2^{P,C} &= -\lambda^s(S_{21}^P - S_{23}^P N_\psi)\\ \Delta\sigma_3^{P,C} &= -\lambda^s(S_{31}^P - S_{33}^P N_\psi)\end{aligned}\right\} \tag{3.32}$$

where, λ^s represents the shear plastic multiplier which is calculated as follows:

$$\lambda^s = \frac{\sigma_1^O - \sigma_3^O N_\phi + 2c\sqrt{N_\phi}}{(S_{11}^P - S_{13}^P N_\psi) - (S_{31}^P - S_{33}^P N_\psi)N_\phi} \tag{3.33}$$

The superscript O is used to represent the old corrected value. The obtained strength parameters within the corrections for the principal stresses and the shear plastic multiplier depend on the yield surface on which the corrections are executed. For each computational step, the bi-linear shear surfaces are tested to figure out the active surface based on the given value of principal stresses (σ_1 and σ_3).

Similar, the plastic strain increments for tensile failure $\Delta\varepsilon_i^{p,t}$ are given as follows:

$$\begin{aligned}\Delta\varepsilon_1^{p,t} &= 0\\ \Delta\varepsilon_2^{p,t} &= 0\\ \Delta\varepsilon_3^{p,t} &= -\lambda^t\end{aligned} \tag{3.34}$$

The stress corrections for tensile failure are computed as follows:

$$\left.\begin{aligned}\Delta\sigma_1^{P,C} &= -\lambda^t S_{13}^P\\ \Delta\sigma_2^{P,C} &= -\lambda^t S_{23}^P\\ \Delta\sigma_3^{P,C} &= -\lambda^t S_{33}^P\end{aligned}\right\} \tag{3.35}$$

where, λ^t represents the tensile plastic multiplier which is calculated as follows:

$$\lambda^t = \frac{\sigma_3^O - \sigma^t}{S_{33}^P} \tag{3.36}$$

Thus, the new principal stress state is given by Eq. 3.37, whether it is corrected due to shear or tensile or simultaneously combining shear and tensile yielding.

$$\left[\sigma^{P,N}\right] = \begin{bmatrix}\sigma_1^{P,O} + \Delta\sigma_1^{P,C}\\ \sigma_2^{P,O} + \Delta\sigma_2^{P,C}\\ \sigma_3^{P,O} + \Delta\sigma_3^{P,C}\end{bmatrix} \tag{3.37}$$

The superscripts (^{O} and ^{N}) denote the principal stresses values obtained just before detection of failure and the new corrected values, respectively.

3.3.3.2. Plastic corrections on the joint plane for yielding in shear and tension

Checking the failure on the joint plane is executed directly after the correction of the principal stress state for the matrix returned back to the global system. Then, the updated global stress state is transformed to the local joint plane space. Excluding the shear component on the plane normal to the joint plane, the stress components at local coordinates specified in Eq. 3.25 can be rewritten as follows:

$$\left.\begin{aligned}
\sigma_{1'1'} &= S_{11}\varepsilon_{1'1'} + S_{12}\varepsilon_{2'2'} + S_{13}\varepsilon_{3'3'} \\
\sigma_{2'2'} &= S_{12}\varepsilon_{1'1'} + S_{11}\varepsilon_{2'2'} + S_{13}\varepsilon_{3'3'} \\
\sigma_{3'3'} &= S_{13}\varepsilon_{1'1'} + S_{13}\varepsilon_{2'2'} + S_{33}\varepsilon_{3'3'} \\
\tau &= 2G'\gamma
\end{aligned}\right\} \tag{3.38}$$

where,

$$\gamma = \sqrt{\varepsilon_{1'3'}^2 + \varepsilon_{2'3'}^2} = \left|\varepsilon_{1'3'}\right| \tag{3.39}$$

Based on the flow rule for plastic yielding given by Eq. 3.30 and the potential functions specified in Eq. 3.29, the shear plastic strain increments $\Delta\varepsilon_i^{p,s}$ are given as follows:

$$\begin{aligned}
\Delta\varepsilon_{1'1'}^{p,s} &= \Delta\varepsilon_{2'2'}^{p,s} = 0 \\
\Delta\varepsilon_{3'3'}^{p,s} &= \lambda^s \tan\psi_j \\
\Delta\gamma^{p,s} &= \lambda^s
\end{aligned} \tag{3.40}$$

Thus, the obtained shear plastic corrections for the local stress state are given by Eq. 3.41.

$$\begin{aligned}
\Delta\sigma_{1'1'}^{C} &= \Delta\sigma_{2'2'}^{C} = -\lambda^s S_{13}\tan\psi_j \\
\Delta\sigma_{3'3'}^{C} &= -\lambda^s S_{33}\tan\psi_j \\
\Delta\tau^{C} &= -\lambda^s 2G'
\end{aligned} \tag{3.41}$$

While the shear plastic multiplier λ^s is obtained as follows:

$$\lambda^s = \frac{\tau^O - \sigma_{3'3'}^O \tan\phi_j - c_j}{2G' + S_{33}\tan\psi_j \tan\phi_j} \tag{3.42}$$

The tensile failure follows an associated flow rule. The tensile plastic strain increments $\Delta\varepsilon_i^{p,t}$ are given as follows:

$$\begin{aligned}
&\Delta\varepsilon_{1'1'}^{p,t} = \Delta\varepsilon_{2'2'}^{p,t} = 0 \\
&\Delta\varepsilon_{3'3'}^{p,t} = 1 \\
&\Delta\gamma^{p,t} = 0
\end{aligned} \tag{3.43}$$

The stress corrections for tensile failure on the joint plane are computed as follows:

$$\begin{aligned}
&\Delta\sigma_{1'1'}^{C} = \Delta\sigma_{2'2'}^{C} = -\lambda^{t} S_{13} \\
&\Delta\sigma_{3'3'}^{C} = -\lambda^{t} S_{33} \\
&\Delta\tau^{C} = 0
\end{aligned} \tag{3.44}$$

where, λ^t represents the tensile plastic multiplier which is calculated as follows:

$$\lambda^{t} = \frac{\sigma_3^{O} - \sigma_j^{t}}{S_{33}} \tag{3.45}$$

The new local stress state given by Eq. 3.38 is updated, whether it is corrected due to shear or tensile or simultaneously combined shear and tensile yielding as follows:

$$\left.\begin{aligned}
\sigma_{1'1'}^{N} &= \sigma_{1'1'}^{O} + \Delta\sigma_{1'1'}^{C} \\
\sigma_{2'2'}^{N} &= \sigma_{2'2'}^{O} + \Delta\sigma_{2'2'}^{C} \\
\sigma_{3'3'}^{N} &= \sigma_{3'3'}^{O} + \Delta\sigma_{3'3'}^{C} \\
\tau^{N} &= \tau^{O} + \Delta\tau^{C}
\end{aligned}\right\} \tag{3.46}$$

The superscripts (^{O} and ^{N}) denote the principal stress values obtained just before detection of failure and the new corrected values, respectively. After the local stress state has been updated, it will be transformed back into the global system for checking large-strain up-date of joint orientation. In large strain, the orientation of the weak plane is adjusted per zone to account for rigid body rotations and rotations due to deformations (Itasca 2016).

3.3.3.3. Bi-surface plasticity inside the Transubi model

Similar to the original Subiquitous joint model (Itasca 2016), the yield functions in the Transubi model are linear for matrix and joint. The activation of the second yield shear surface for either the rock matrix or the joints or both is done by setting the properties *bimatrix* and/or *bijoint* to 1. For the rock matrix, the application of the plastic corrections are extremely complex due to the obtained composite yield surface. Thus, new functions, *c*, are introduced in the σ_1- σ_3-space in order to solve the multi-surface plasticity problem. Function h_1 represents the diagonal between $f_1^{\,s} = 0$ and $f^t = 0$, while function h_2 represents the diagonal between $f_1^{\,s} = 0$ and $f_2^{\,s} = 0$. The active

yield surface is detected according to the diagonal functions, h_1 and h_2, and the yield functions of each surface. After the detection of the active surface, the plastic corrections are performed.

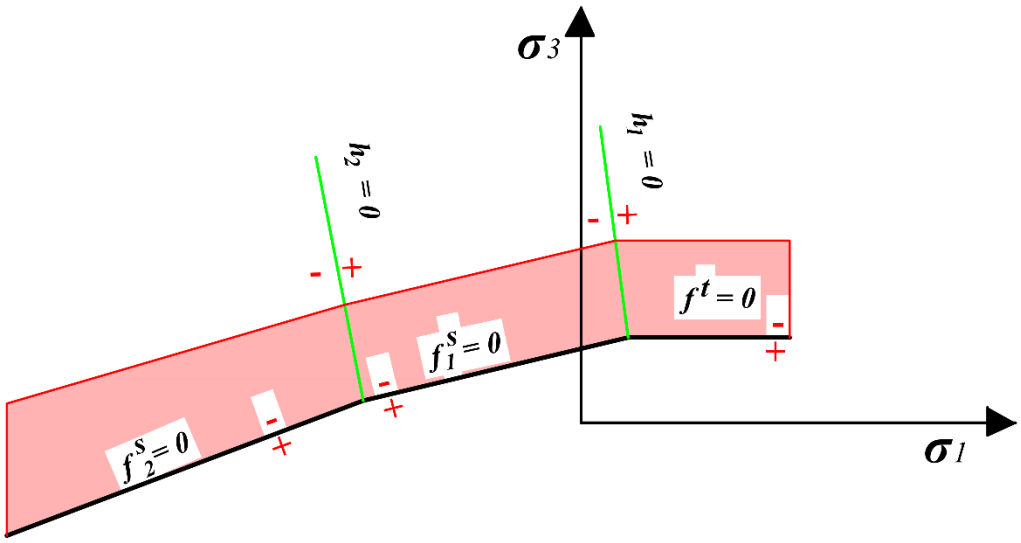

Fig. 3-6 Multi-surface plasticity of rock matrix in principal stress space

As shown in Fig. 3-6, when the composed failure surface is violated, the elastic guess could be located either in domains of $f_2{}^s$ or $f_1{}^s$ or f^t, corresponding to negative or positive domains ($h_1 = 0$ and $h_2 = 0$), respectively. The diagonal functions are defined as follows:

$$h_1 = \sigma_3 - \sigma^t + \alpha^p(\sigma_1 - \sigma^p) \tag{3.47}$$

where

$$\begin{aligned} \alpha^p &= \sqrt{1+N_{\phi 1}^2} + N_{\phi 1} \\ \sigma^p &= \sigma^t N_{\phi 1} - 2c_1\sqrt{N_{\phi 1}} \end{aligned} \tag{3.48}$$

The second diagonal function h_2 is defined as follows:

$$h_2 = (\sigma_3^I - \sigma_3) + \zeta^p(\sigma_1 - \sigma_1^I) \tag{3.49}$$

where, $\sigma_3{}^I$ represents the minimum principal stress at the intersection point of the shear yield surfaces at point B as shown in Fig. 3-5.a and Eq. 3.22.

$$\zeta^p = \frac{\left\{\left[(\sqrt{1+N_{\phi 1}^2}-N_{\phi 1})x(\sqrt{1+N_{\phi 2}^2}-N_{\phi 2})\right]-1\right\}}{(\sqrt{1+N_{\phi 1}^2}-N_{\phi 1})+(\sqrt{1+N_{\phi 2}^2}-N_{\phi 2})}$$
$$\sigma_1^I = \frac{\left[(2c_1\sqrt{N_{\phi 1}}N_{\phi 2})-(2c_2\sqrt{N_{\phi 2}}N_{\phi 1})\right]}{N_{\phi 1}-N_{\phi 2}} \qquad (3.50)$$

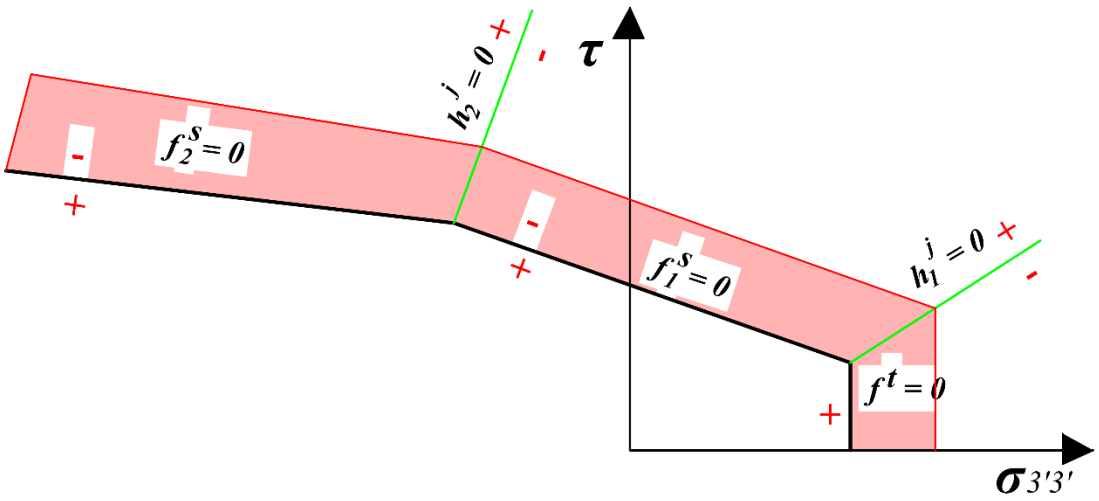

Fig. 3-7 Multi-surface plasticity of joint plane in τ- $\sigma_{3'3'}$ coordinate system

Similar to the rock matrix, the multi-surface plasticity of the joint plane is tackled as shown in Fig. 3-7. However, the composed yield surface is introduced in local coordinates (τ- $\sigma_{3'3'}$ space). Two diagonal functions, $h_1{}^j$ and $h_2{}^j$, are used for detection of the active yield surface. The diagonal functions for the joint plane are defined as follows:

$$h_1^j = \tau - \tau_j^p - \alpha_j^p(\sigma_{3'3'} - \sigma_j^t) \qquad (3.51)$$

where

$$\tau_j^p = c_{j1} - \tan\phi_{j1}\sigma_j^t$$
$$\alpha_j^p = \sqrt{1+\tan\phi_{j1}^2} - \tan\phi_{j1} \qquad (3.52)$$

The second diagonal function $h_2{}^j$ is defined as:

$$h_2 = (\tau - \tau_j^I) - \zeta_j^p(\sigma_{3'3'} - \sigma_{3'3'}^I) \qquad (3.53)$$

where, τ_j^I and $\sigma_{3'3'}{}^I$ represent the stress values in tangential and normal direction to the joint plane, respectively, at point B as shown in Fig. 3-5.b.

$$\zeta_j^p = \frac{1}{\tan(\frac{\phi_{f1j} + \phi_{f2j}}{2})}$$
$$\tau_j^I = \frac{(c_{j2}\tan\phi_{f1j} - c_{j1}\tan\phi_{f2j})}{\tan\phi_{f1j} - \tan\phi_{f2j}} \qquad (3.54)$$
$$\sigma_{3'3'}^I = \frac{(c_{j2} - c_{j1})}{\tan\phi_{f2j} - \tan\phi_{f1j}}$$

3.3.4. Hardening/Softening parameters

In the proposed Transubi model, strength parameters for rock matrix and joint plane (i.e. cohesion, friction angle and dilation angle for bi-linear yield surfaces and tensile strength) could be assigned as tables. For each strength parameter, the table data consist of pairs of these strength parameters and the corresponding hardening parameter. Such hardening parameters are computed directly from the accumulated plastic strains for the rock matrix and the joint. The evaluation of the plastic strains for the rock matrix is implemented in the principal stress space, while is computed in local coordinates for the joint. Four independent hardening parameters are assigned (k^s, k^t, k_j^s and k_j^t). First parameter is k^s which specifies the rock matrix plastic shear strain to update the matrix cohesion c, matrix friction angle ϕ_f and matrix dilation ψ. These parameters can be assigned for both shear yield surfaces to update corresponding strength parameters. The incremental value of this parameter Δk^s is computed as the square root of the second invariant of the incremental plastic shear strain deviator.

$$\Delta k^s = \frac{1}{\sqrt{2}}\sqrt{(\Delta\varepsilon_1^{p,s} - \Delta\varepsilon_m^{p,s})^2 + (\Delta\varepsilon_m^{p,s})^2 + (\Delta\varepsilon_3^{p,s} - \Delta\varepsilon_m^{p,s})^2} \qquad (3.55)$$

where, $\Delta\varepsilon_m{}^{p,s}$ is defined as the volumetric plastic shear strain increment.

$$\Delta\varepsilon_m^{p,s} = \frac{1}{3}(\Delta\varepsilon_1^{p,s} + \Delta\varepsilon_3^{p,s}) \qquad (3.56)$$

The second parameter is k^t which specifies the rock matrix plastic tensile strain to update the matrix tensile strength σ^t. The tensile-hardening increment for the rock matrix is the plastic volumetric tensile strain increment, given as follows:

$$\Delta k^t = \Delta\varepsilon_3^{p,t} \qquad (3.57)$$

Similar, the joint plastic shear strain is specified by the third hardening parameter k_j^s. It updates the joint strength parameters (cohesion c_j, friction angle ϕ_{jf} and dilation ψ_j) for both shear yield surfaces. The incremental value of this parameter Δk_j^s is computed as follows:

$$\Delta k_j^s = \sqrt{\frac{1}{3}(\Delta\varepsilon_{3'3'}^{p,s})^2 + (\Delta\gamma^{p,s})^2} \tag{3.58}$$

where

$$\Delta\gamma^{p,s} = \left|\Delta\varepsilon_{1'3'}^{p,s}\right| \tag{3.59}$$

On the other hand, the fourth hardening parameter k_j^t which updates the joint tensile strength is defined as incremental value as follows:

$$\Delta k_j^t = \Delta\varepsilon_{3'3'}^{p,t} \tag{3.60}$$

The use of these hardening/softening parameters is demonstrated in chapter 4.

3.3.5. Flowchart of Transubi model

Similar to the original Ubi model, the calculations in the Transubi model start first in the matrix followed by the joint plane, see Fig. 3-8. This calculation sequence could be considered as a limitation especially because failure is checked in rock matrix prior to the joint plane. According to Bahrani and Hadjigeorgiou (2018), the joints are much weaker than the rock matrix in reality, therefore failure should always be detected first along these planes. This limitation is widely overcome by applying the time stepping technique in FLAC called the explicit time scheme. The used timestep is always smaller than the critical time step; therefore no failure inside the rock matrix or joint plane will be missed.

Another limitation has been addressed by Bahrani and Hadjigeorgiou (2018) regarding the assigned elastic parameters. If the given elastic parameters are evaluated from tested rock matrix (intact rock samples) and not from a jointed samples (rock mass), the computed deformation will be underestimated. Thus, the elastic moduli in this constitutive model should consider the scale effect.

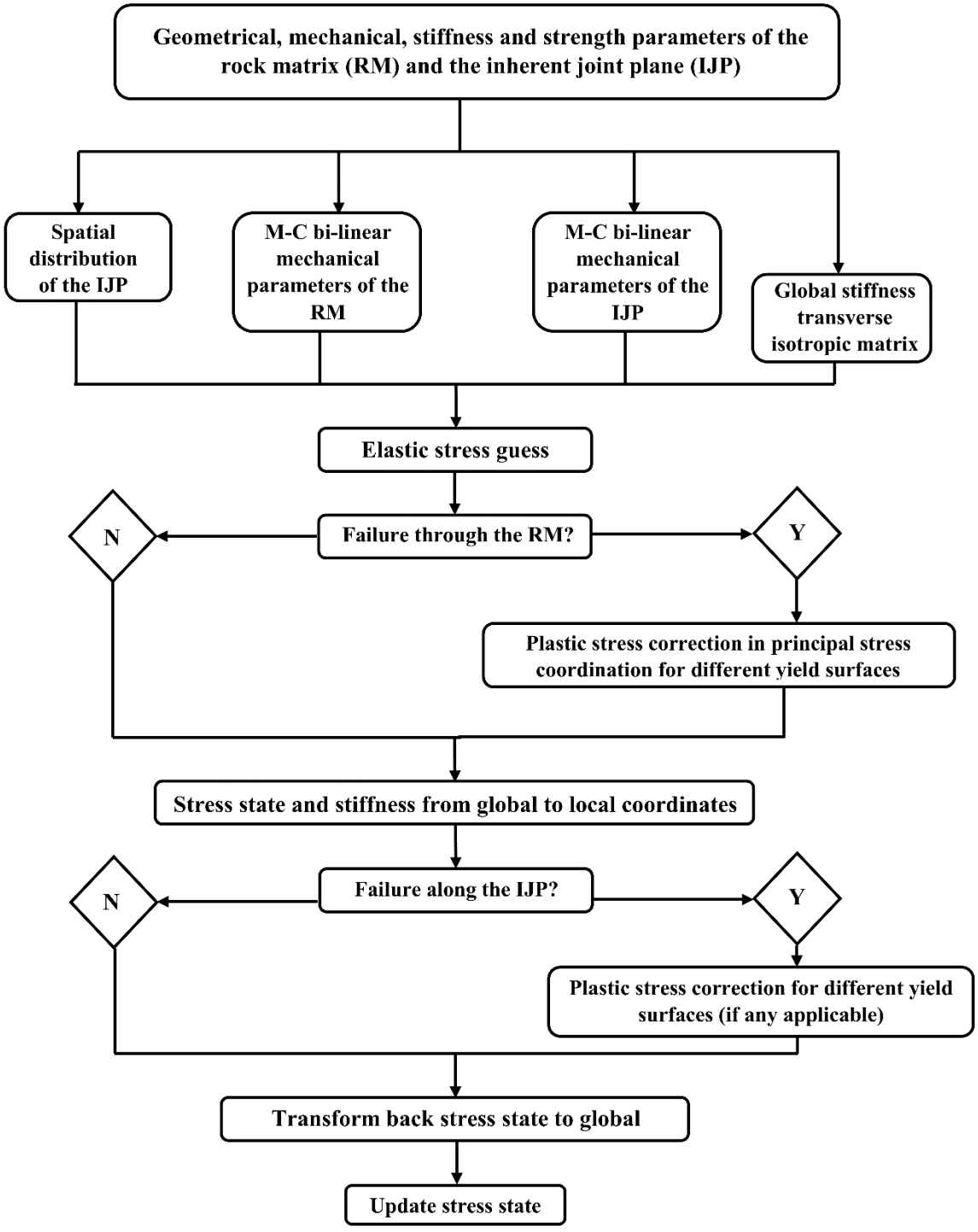

Fig. 3-8 Flowchart of Transubi model

3.4. Model verifications

The verifications discussed within this chapter assume a lineal elastic-perfect-plastic case. These applications are presented to compare the simulated strength anisotropy behavior with the analytical solution of Jaeger and Cook (1979), the original Ubi model and the Caniso model (Itasca 2016). Later (see chapter 4) strain hardening/softening, bi-linear yield surfaces and stiffness anisotropy are introduced to simulated the mechanical behavior of bedded argillaceous rocks (Tournemire shale and Opalinus Clay).

3.4.1. Single joint in an isotropic matrix

For verification, the Transubi model is used to predict the compressive strength of a rock sample with inherent anisotropy planes. The elastic stiffness matrix is isotropic which results in a bulk modulus K of 100 MPa and a shear modulus G of 70 MPa (Table 3-1). The simulation results are compared with the analytical solution from Jaeger and Cook (1979), where the uniaxial compressive strength is calculated by Eq. 3.61. This example is a good verification as the failure mode in a sample having ubiquitous joints is similar to the failure mode of a sample with single plane of weakness (Kazakidis and Diederichs 1993).

$$\sigma_c = \begin{cases} \min\{2c\sqrt{N_{\phi f}}, 2c_j / (1-\tan\phi_{fj}\tan\beta)\sin 2\beta & \text{if } (1-\tan\phi_{fj}\tan\beta) > 0 \\ 2c\sqrt{N_{\phi f}} & \text{if } (1-\tan\phi_{fj}\tan\beta) < 0 \end{cases} \tag{3.61}$$

Table 3-1 Properties of the tested rock sample (Itasca 2016)

Elastic stiffness matrix components					*Rock matrix M-C input*			*Joint M-C input*		
E*=*E'	***υ*= *υ'***	***G*= *G'***	***K***	***G***	***c***	ϕ_f	σ^t	c_j	ϕ_{fj}	σ^t_j
170 MPa	0.22	70 MPa	100 MPa	70 MPa	2 KPa	40°	2.4 KPa	1 KPa	30°	2 KPa

Transubi model and analytical solution show nearly identical results with error less than 1% for all values of β as documented in Fig. 3-9. In the case of rock matrix failure, the uniaxial compressive strength σ_c is limited to 8.58 KPa. For this constellation both approaches give identical results.

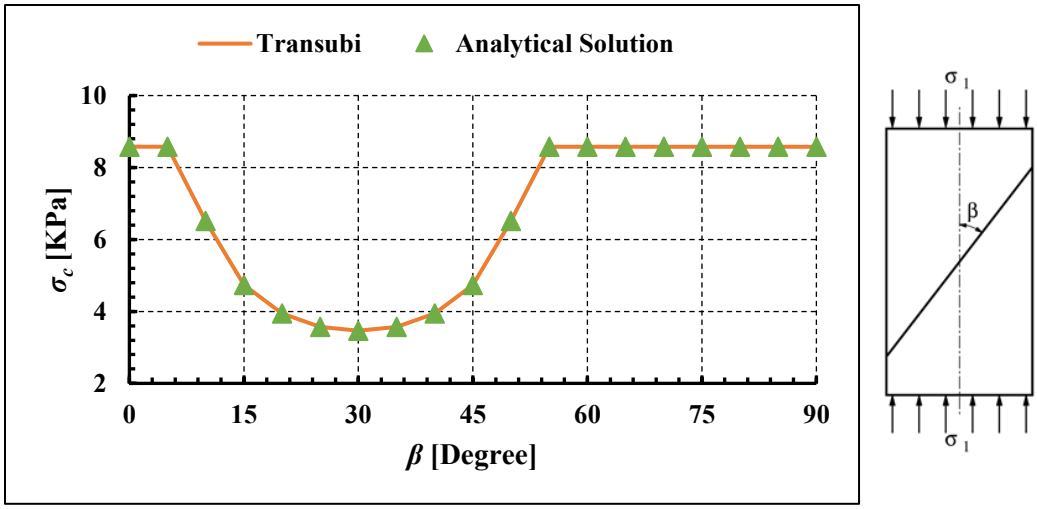

Fig. 3-9 Comparison between analytical and numerical solution using Transubi model.

3.4.2. Single joint plane in a transverse isotropic matrix

Simulations have been conducted to check the applicability of the Transubi model under uniaxial and triaxial loading conditions. Results are compared with the Caniso model and the analytical solution from Jaeger.

3.4.2.1. Uniaxial compression test: Bossier shale

Used input data are based on experimental results of Bossier shale presented in Table 3-2 (Ambrose 2014). This shale is a reservoir rock, highly laminated with organic-filled weak planes. The maximum possible tensile strength is determined by Eq. 3.62. However, realistic tensile strength values are much lower.

$$\sigma^t_{\max} = c \big/ \tan\phi_f \qquad (3.62)$$

The value for G' is estimated based on laboratory results as suggested by Lekhnitskii (1981) and Itasca (2016).

$$G' = \frac{E'E}{E(1+2\nu')+E'} \qquad (3.63)$$

Table 3-2 Parameters for Bossier shale (Ambrose 2014)

Elastic stiffness matrix components					*Rock matrix M-C input*			*Joint M-C input*		
E [GPa]	E' [GPa]	υ	υ'	G' [GPa]	c [MPa]	ϕ_f	σ^t [MPa]	c_j [MPa]	ϕ_{fj}	σ^t_j [MPa]
29.65	15.2	0.2	0.22	5.86	26	29°	7.9	14	24°	4.4

Results for Bossier shale are presented in Fig. 3-10. The Transubi model shows the same behavior as the modified analytical solution. However, the Caniso model can only detect joint failure and not yielding in the rock matrix.

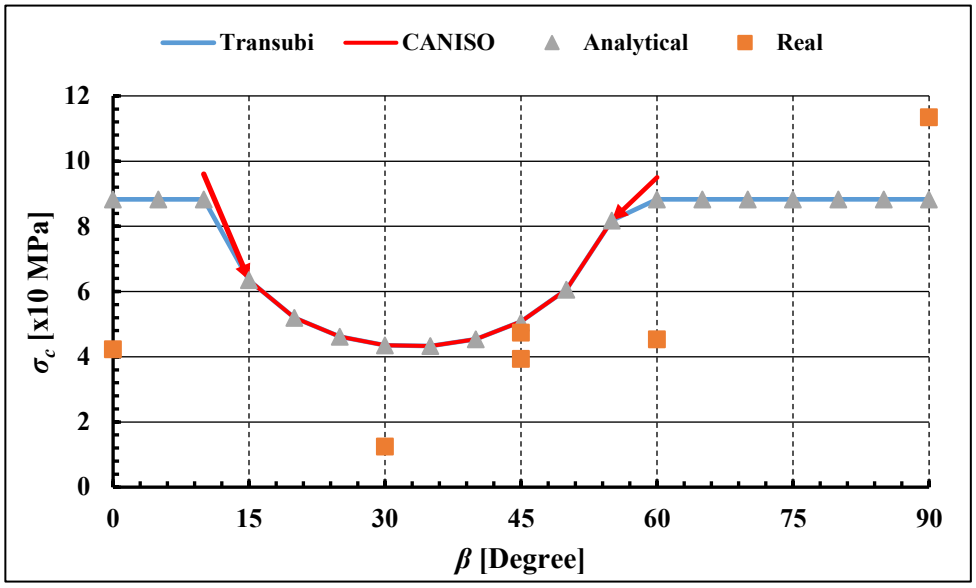

Fig. 3-10 Uniaxial compression tests: Numerical and analytical solutions for Bossier shale compared with lab test results.

3.4.2.2. Triaxial compression test: Martinsburg slate

Both, the Transubi and the Caniso model are used to simulate triaxial tests (confining pressure σ_3=3.5 and 10.5 MPa, respectively) on Martinsburg slate (Donath 1964). This rock behaves like a transverse isotropic rock. E, E', σ^I and σ^I_j are estimated under triaxial stress conditions for β = 0° and 90° using RocLab (Rocscience 2007), assuming GSI=95 and MR=450. Shear modulus G' is computed by Eq. 3.63, while υ and υ' are assumed to be 0.22. M-C parameters for rock matrix and joints are given by Tien and Kuo (2001) and Ambrose (2014). Table 3-3 shows the data applied in the numerical simulations and Jaeger's analytical solution. Results obtained from numerical simulations and the analytical solution are shown in Fig. 3-11.

Table 3-3 Parameters for Martinsburg slate

Elastic stiffness matrix components				*Rock matrix M-C input*				*Joint M-C input*		
E [GPa]	E' [GPa]	υ	υ'	G' [GPa]	c [MPa]	ϕ_f	σ^I [MPa]	c_j [MPa]	ϕ_{fj}	σ^I_j [MPa]
69.7	43.6	0.22	0.22	23	25	45°	8.8	9	21°	4.5

As Fig. 3-11 shows, the Caniso model behaves elastic considering the rock matrix. Thus, a maximum driving strain (ε_{max}) must be assigned. However, the failure in the rock matrix is limited to the Mohr-Coulomb matrix failure surface and corresponds therefore to the modified analytical solution of Jaeger. Generally, both numerical models and the analytical solution show the same behavior in case of joint yielding.

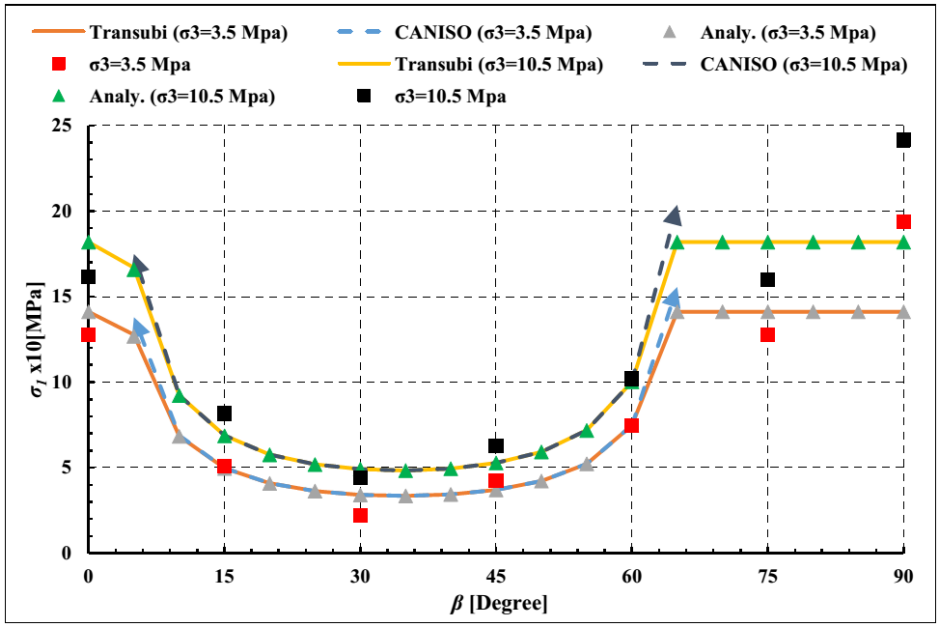

Fig. 3-11 Numerical vs. analytical results for triaxial testing of Martinsburg slate (σ_3=3.5 and 10.5 MPa)

3.5. Conclusion

The stiffness anisotropy of transverse isotropic rock matrix has been integrated into the subiquitous joint model. The mathematical formulations for the plastic corrections for the rock matrix and the joint plane were introduced for both, shear and tension yielding. Numerical simulations on the basis of uniaxial compression tests were carried out to verify this model and results were compared to the modified analytical solution of Jaeger. Furthermore, the Transubi model and the Caniso model were tested under uniaxial and triaxial compression using lab data of two different rocks. Results indicate that the Transubi model is able to reproduce the elastic as well as the plastic behavior for both, joint and rock matrix. The stiffness anisotropy has a major influence in the elastic range. Finally, the new proposed model is an interesting alternative to describe anisotropic rock behavior and is advantageous in case of potential matrix failure.

4. Numerical simulation of laboratory investigations of bedded argillaceous rocks (Tournemire shale and Opalinus Clay)

4.1. Introduction

This chapter presents a detailed investigation of the mechanical anisotropy of bedded argillaceous rocks (Tournemire shale and Opalinus clay). Due to its anisotropic nature, these types of rocks are considered as a good case study to apply the proposed Transubi model, also this rock shows strain hardening in the pre-peak region and strain softening in the post-peak region. In order to verify the proposed model, an experimental dataset of Tournemire shale (Niandou et al. 1997) for different confining pressure applied to three different orientations is used. Later, the laboratory investigations conducted on Opalinus clay are modelled using the proposed constitutive model. Unlike the Tournemire shale, the Opalinus clay behaves bilinear in both, the rock matrix and the bedding planes. Triaxial lab testing and direct shear testing performed in direction parallel to the bedding planes, are numerically simulated and the results are compared against experimental datasets (Popp and Salzer 2007).

4.2. Tournemire shale

4.2.1. Strength and stiffness anisotropy of Tournemire shale

Based on the lab results obtained by Niandou (1994) and Niandou et al. (1997) on a shale taken from a French site in the Massif Central, the mechanical behavior shows significant anisotropy in strength and stiffness. Tournemire shale is a transverse isotropic material because of the presence of the bedding planes. Fig. 4-1 shows the variation of the strength for different confining pressures versus the bedding plane dip angle (Niandou et al. 1997).

Besides the strength anisotropy, the elastic modulus of the Tournemire shale varies with the bedding plane orientation which also indicates that it behaves as a transverse isotropic rock. The corresponding elastic stiffness matrix is defined by 5 independent elastic parameters (E, E', υ, υ' and G'). As previously mentioned, E and υ are working in the direction tangential to the bedding plane, while E', υ' and G' are working in the direction normal to the bedding plane. The lab testing on Tournemire shale revealed that the elastic parameters are highly dependent on the applied confining pressure (Fig. 4-2). The remarkable increase in the elastic parameters - especially the elastic modulus in the direction normal to the bedding planes E' - with increasing confining pressure can be explained by the progressive closure of these planes (Chen et al. 2012).

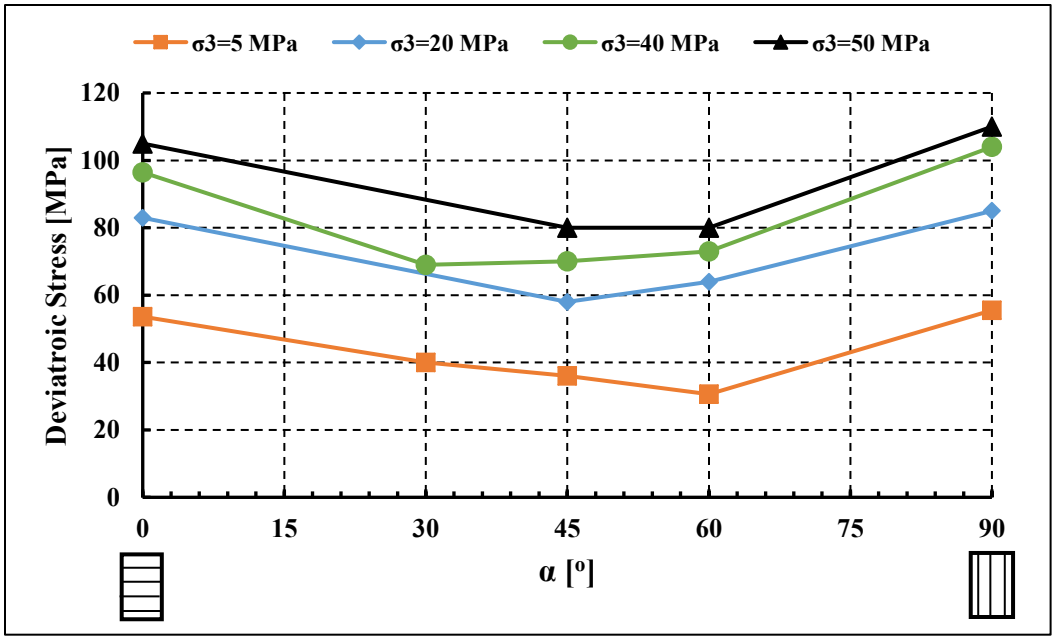

Fig. 4-1 Variation of the deviatoric stress [σ_1 - σ_3] values vs. bedding plane dip angle [α] after (Niandou et al. 1997)

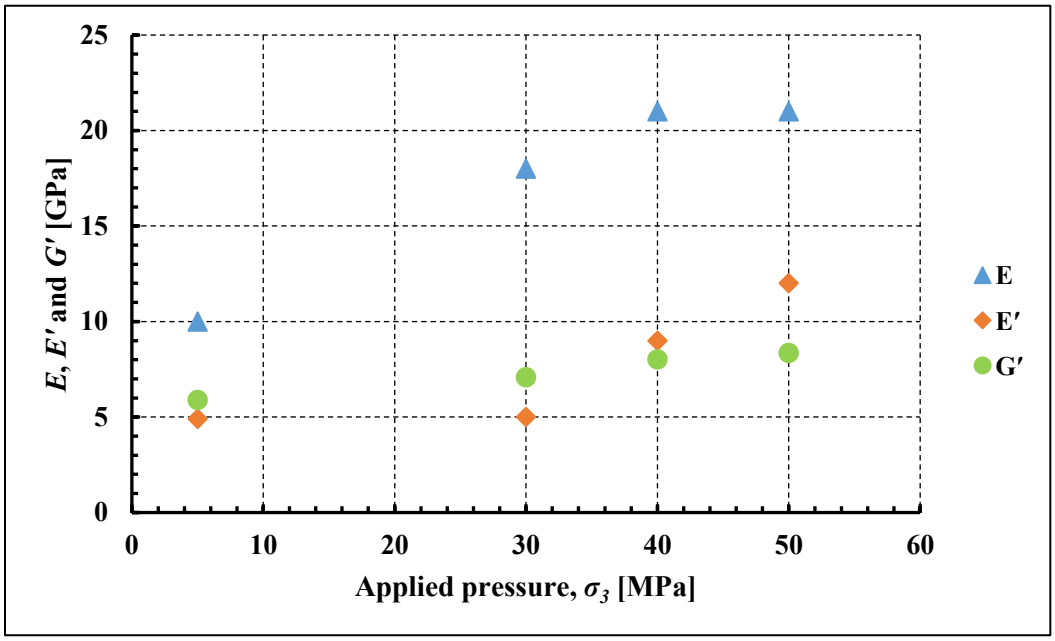

Fig. 4-2 Variation of elastic parameters (E, E' and G') of Tournemire shale under different confining pressures, after (Niandou 1994; Niandou et al. 1997 and Chen et al. 2012).

4.2.2. Parameters identification

In order to identify the parameters for numerical simulation, the mechanical behavior of Tournemire shale under loading has to be identified. Experimental results show elasto-plastic behavior, noticeable hardening in the pre-yielding phase and softening in the post-yielding phase. As indicated in Fig. 4-3, Abdi et al. (2015) specified that the stress-strain curve shows non-elasticity already in earlier stages due to the closure of the existing fissures and bedding planes, and they suggested a mobilization of the strength parameters (cohesion and friction angle) as shown in Fig. 4-3b. The region between points A to B describes the initial inelastic phase due to closure of existing fissures which is not content of this research.

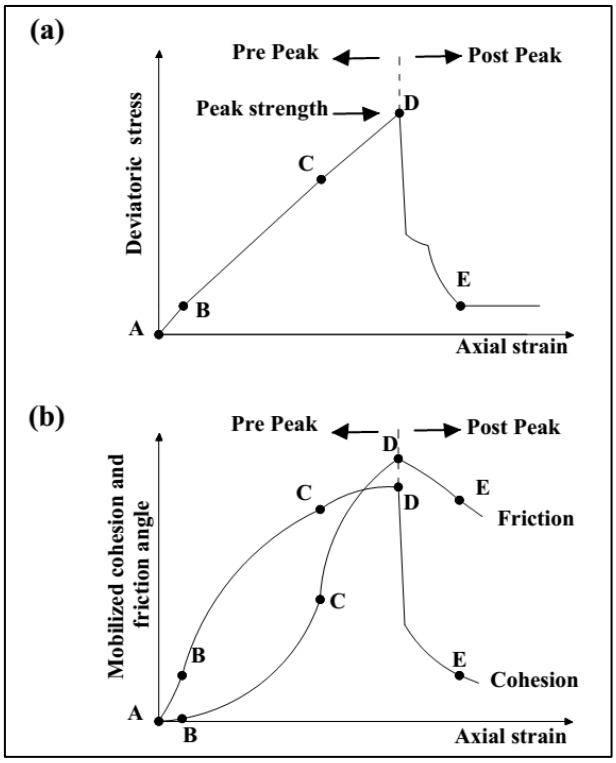

Fig. 4-3 Schematics of (a) stress–strain curve of Tournemire argillite, and (b) the mobilization of the strength parameters, after (Abdi et al. 2015)

Similar to the framework of hardening/softening introduced by Vermeer and De Borst (1984), a rapid increasing rate of the mobilized cohesion is applied in the pre- peak stage especially between points B and C to simulate the hardening in this stage, while in the post-peak region the cohesion decreases to its residual value or almost vanishes as the tested sample is heavily cracked (Abdi et al. (2015)). On the other side, the applied friction angle in the post-peak region becomes the main

component of the post-peak strength of the specimen. Generally, the applied mobilization of the strength parameters according to Abdi et al. (2015): (i) showed a complicated behavior, (ii) did not clarify the basic function to perform such a mobilization, and (iii) has taken the entire rock sample into consideration without differentiation between the mobilization of the rock matrix and the planes of weakness.

In order to apply the Transubi model, a fixed dataset of the independent elastic parameters is assumed for the rock samples, as the proposed constitutive model does not consider the stress-dependent non-linear elasticity. The assumed elastic parameters are given in Table 4-1. The bulk density of the shales is set to 2450 kg/m^3 (Niandou 1994).

Table 4-1 Elastic parameters for Tournemire shale

E [GPa]	E' [GPa]	ν [-]	ν' [-]	G' [GPa]
18.0	7.0	0.22	0.12	2.5

The mechanical observations indicated anisotropy in strength and deformation. The post-peak strain softening behavior is sharp (brittle) at lower confinement and more gentle for higher values of confining pressure. Although, as indicated in Fig. 4-1, there are small differences between the measured peak strength at direction parallel to joint planes (α = 0°) and perpendicular to the joint planes (α = 90°) under different confinement, fixed strength parameters are applied for the rock matrix of the Tournemire shale. This assumption has been investigated also by Abdi et al. (2015) by evaluating the degree of the strength anisotropy (k_1) which is found nearly equal to one.

$$k_1 = \frac{(\sigma_1 - \sigma_3)_{\alpha=0}}{(\sigma_1 - \sigma_3)_{\alpha=90}} \qquad (5.1)$$

Based on the remarks of Niandou (1994) and Abdi et al. (2015), the proposed peak and residual strength parameters for rock matrix and bedding planes are given in Table 4-2.

The M-C peak and residual strength envelops with tension cut-off for rock matrix and bedding planes are shown in Fig. 4-4 and Fig. 4-5, respectively. Constant dilation angles for rock matrix and bedding planes are assumed, although it has been found that the volumetric strains and therefore the dilation angle are influenced by the bedding plane orientation (α) and the applied confining pressure (σ_3).

Table 4-2 Strength parameters of Tournemire shale.

Rock matrix parameters					
c_1 [MPa]	φ_{f1} [°]	σ^t [MPa]	ψ_1 [°]	c_1^{res} [MPa]	φ_{f1}^{res} [°]
11	27	6	2	8.5	21
Inherent joint plane parameters					
c_{j1} [MPa]	φ_{fj1} [°]	σ^t_j [MPa]	ψ_j [°]	c_{j1}^{res} [MPa]	φ_{fj1}^{res} [°]
7.5	20	4.5	0	6.5	18

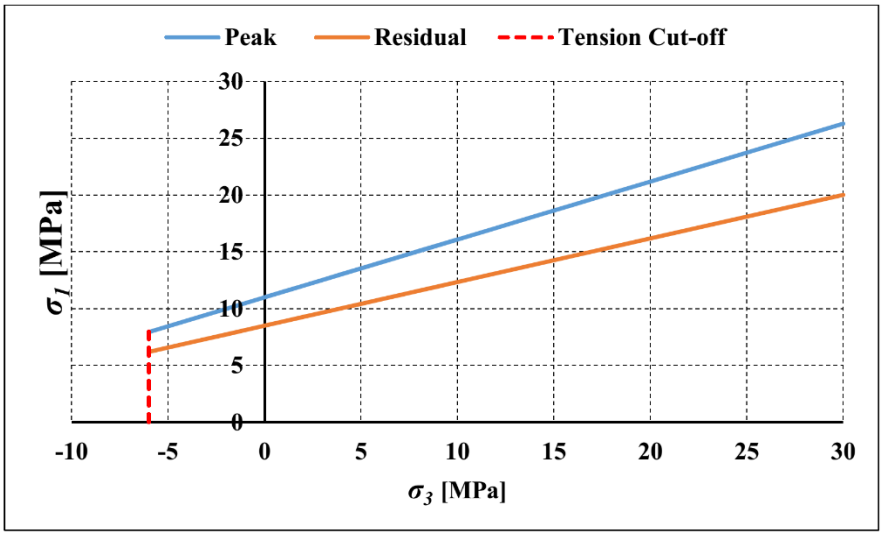

Fig. 4-4 M-C peak and residual failure envelops for Tounemire shale rock matrix

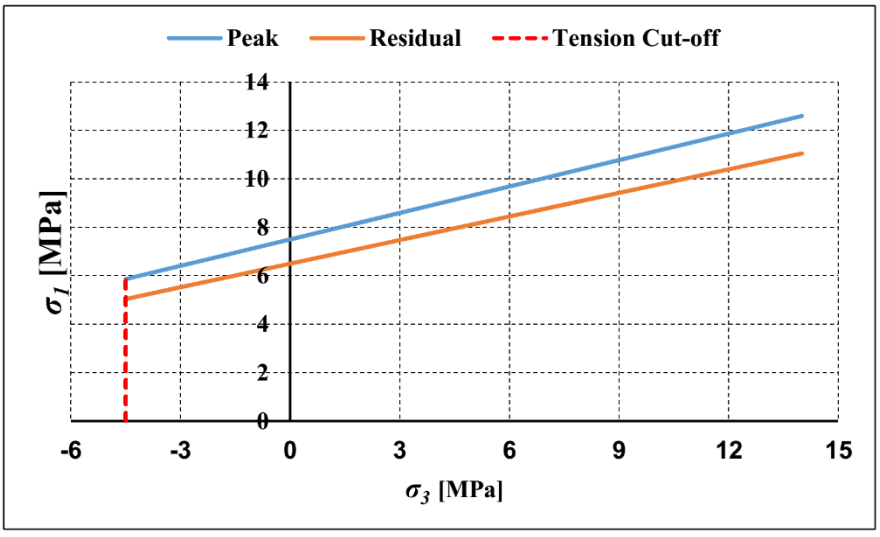

Fig. 4-5 M-C peak and residual failure envelops for Tounemire shale bedding planes

4.2.3. Mobilization of the strength parameters

For the simulation of the Tournemire shale, nonlinear behavior in the pre- and the post-peak regions are assumed. The strength parameters (cohesion, friction angle and tensile strength) for the rock matrix and the bedding planes are mobilized from the first step of the simulation. As previously explained, the Transubi model allows that these parameters are assigned by tables as a function of the accumulated plastic shear and tensile strains. Cohesion, friction angle and tensile strength are mobilized for rock matrix and bedding planes, while the dilation angles are constant although mobilization of the dilation angle is also recommended (Zhao and Cai 2010; X. Zhao, Cai and Cai 2010; Walton et al. 2015).

The inserted tables describing the variation of the strength parameters are divided into two parts: first part describes the pre-yielding hardening and the second part is for the softening. Regarding the pre-peak region, the following analytical approach is applied for cohesion and friction angle (Konietzky, Blümling and te Kamp 2003).

$$c^{actual} = c^{in} + \frac{2\sqrt{(\varepsilon_p^s . \varepsilon_{p,\max}^s)}}{\varepsilon_p^s + \varepsilon_{p,\max}^s} c^{peak} \tag{5.2}$$

$$\Delta_{actual} = \frac{2\sqrt{(\varepsilon_p^s . \varepsilon_{p,\max}^s)}}{\varepsilon_p^s + \varepsilon_{p,\max}^s} \sin(\phi_f^{peak}) \tag{5.3}$$

$$\phi_f^{actual} = \arctan\sqrt{\frac{\Delta^2_{actual}}{1-\Delta^2_{actual}}} \tag{5.4}$$

where:

c^{actual} = actual applied cohesion [MPa],

c^{in} = initial cohesion, mostly very small and nearly zero [MPa],

c^{peak} = maximum value of cohesion at peak strength [MPa],

$\varphi_f{}^{actual}$ = actual applied friction angle [°],

$\varphi_f{}^{peak}$ = maximum value of friction angle at peak strength [°],

ε^s_p = actual value of accumulated plastic shear strain [-],

$\varepsilon^s_{p,max}$ = maximum plastic shear strain at which the maximum values of cohesion and friction angle are achieved [-].

On the other hand, the strain softening behavior starts directly after the strain hardening and the first value of the plastic shear strain ε^s_p is set equal to $\varepsilon^s_{p,max}$ from the hardening stage. Inspired by the analytical functions from Vermeer & De Borst (1984), cohesion and friction angle are gradually reduced as follows:

$$c^{actual} = c^{res} + \exp\left[-\left(\frac{\varepsilon^s_p}{\varepsilon^c}\right)^2\right].(c^{peak} - c^{res}) \qquad (5.5)$$

$$\phi_f^{actual} = \phi_f^{res} + \exp\left[-\left(\frac{\varepsilon^s_p}{\varepsilon^f}\right)^2\right].(\phi_f^{peak} - \phi_f^{res}) \qquad (5.6)$$

where

c^{res} = residual value of cohesion [MPa],

$\varphi_f{}^{res}$ = residual value of the friction angle [°],

ε^c = accumulated plastic shear strain at which c_{actual} reaches c_{res} , this parameter controls the degree of softening [-],

ε^f = accumulated plastic shear strain at which $\varphi_{f.actual}$ reaches $\varphi_{f.res}$ [-].

Applying these functions to adapt the hardening-softening behavior of the Tournemire shale is not as simple as it seems, as the plastic strain is depending on the applied confining pressure and the bedding plane orientation as well (Abdi et al. 2015). The other constraint is that utilizing these functions as failure criterion for the rock matrix does not mean that it works proper also for failure at the bedding planes. The best fit result of Eq. 5-2 to 5-6 for rock matrix and bedding planes are given in Fig. 4-6, Fig. 4-7 and Fig. 4-8 for applied confining pressures of 5, 30 and 50 MPa.

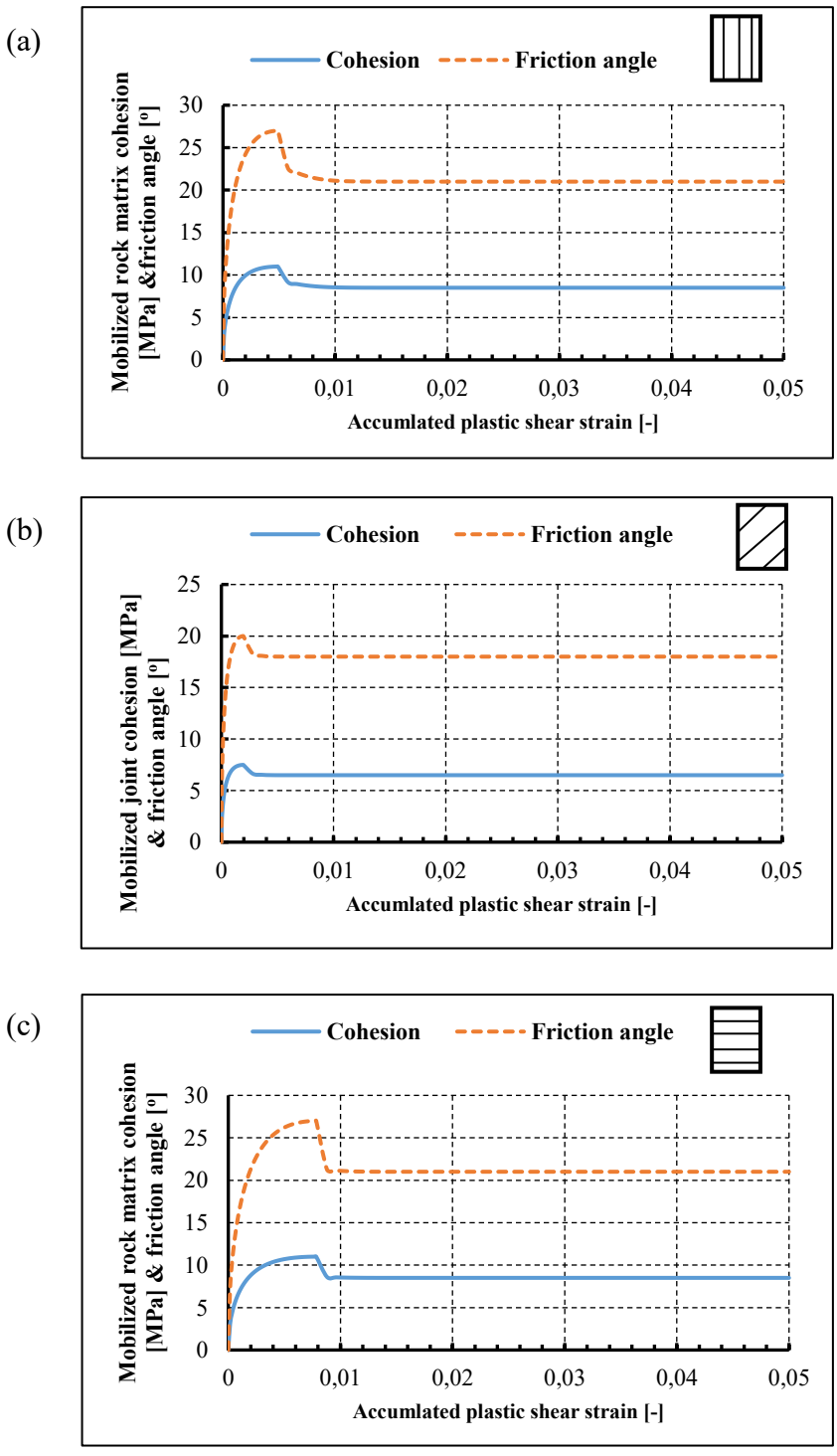

Fig. 4-6 Applied mobilization of strength parameters (cohesion and firction angle) at σ_3 = 5 MPa for (a) rock matrix, loading parallel to joint planes, (b) joint planes, and (c) rock matrix, loading normal to joint planes

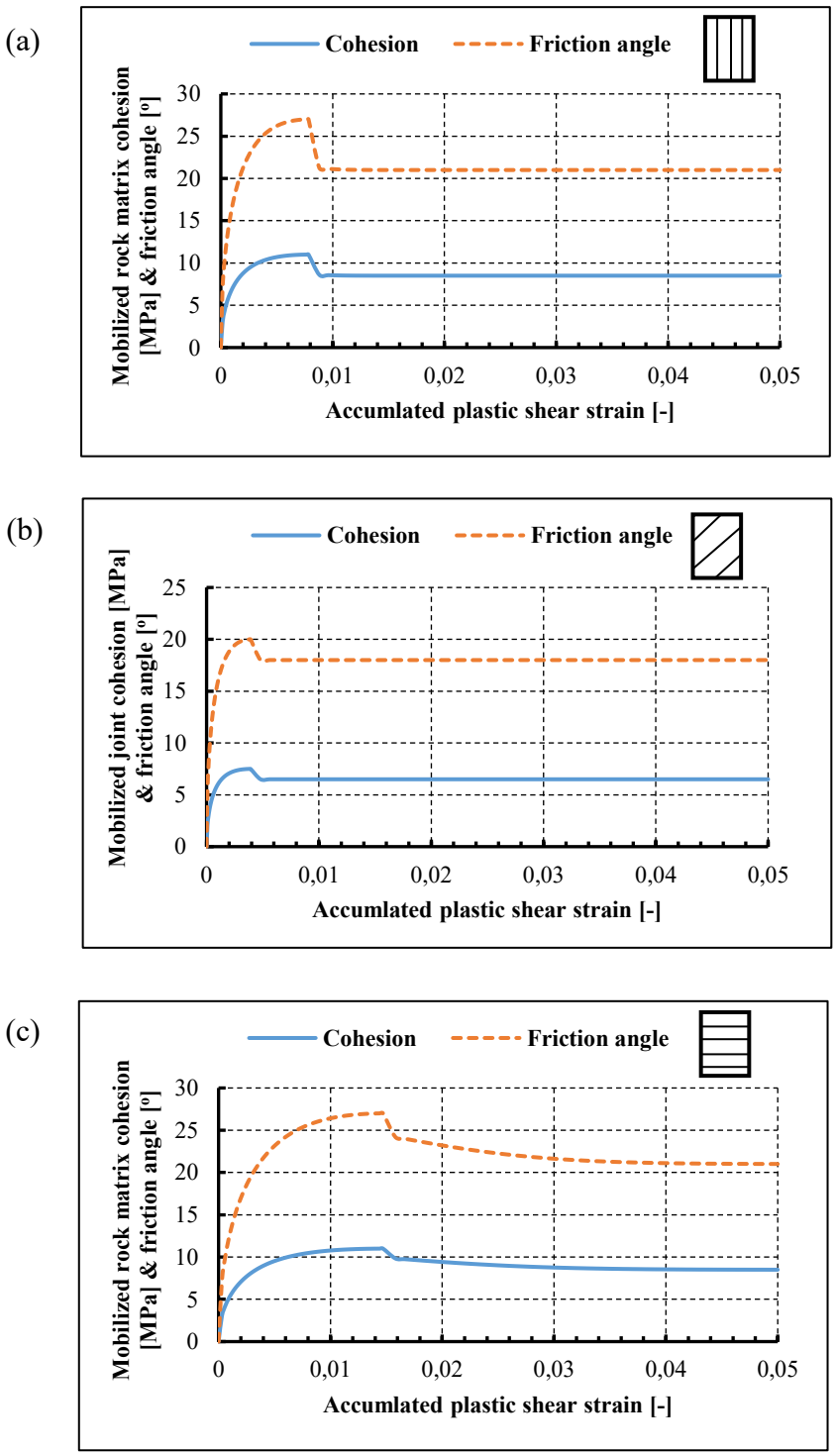

Fig. 4-7 Applied mobilization of strength parameters (cohesion and firction angle) at σ_3 = 30 MPa for (a) rock matrix, loading parallel to joint planes, (b) joint planes, and (c) rock matrix, loading normal to joint planes

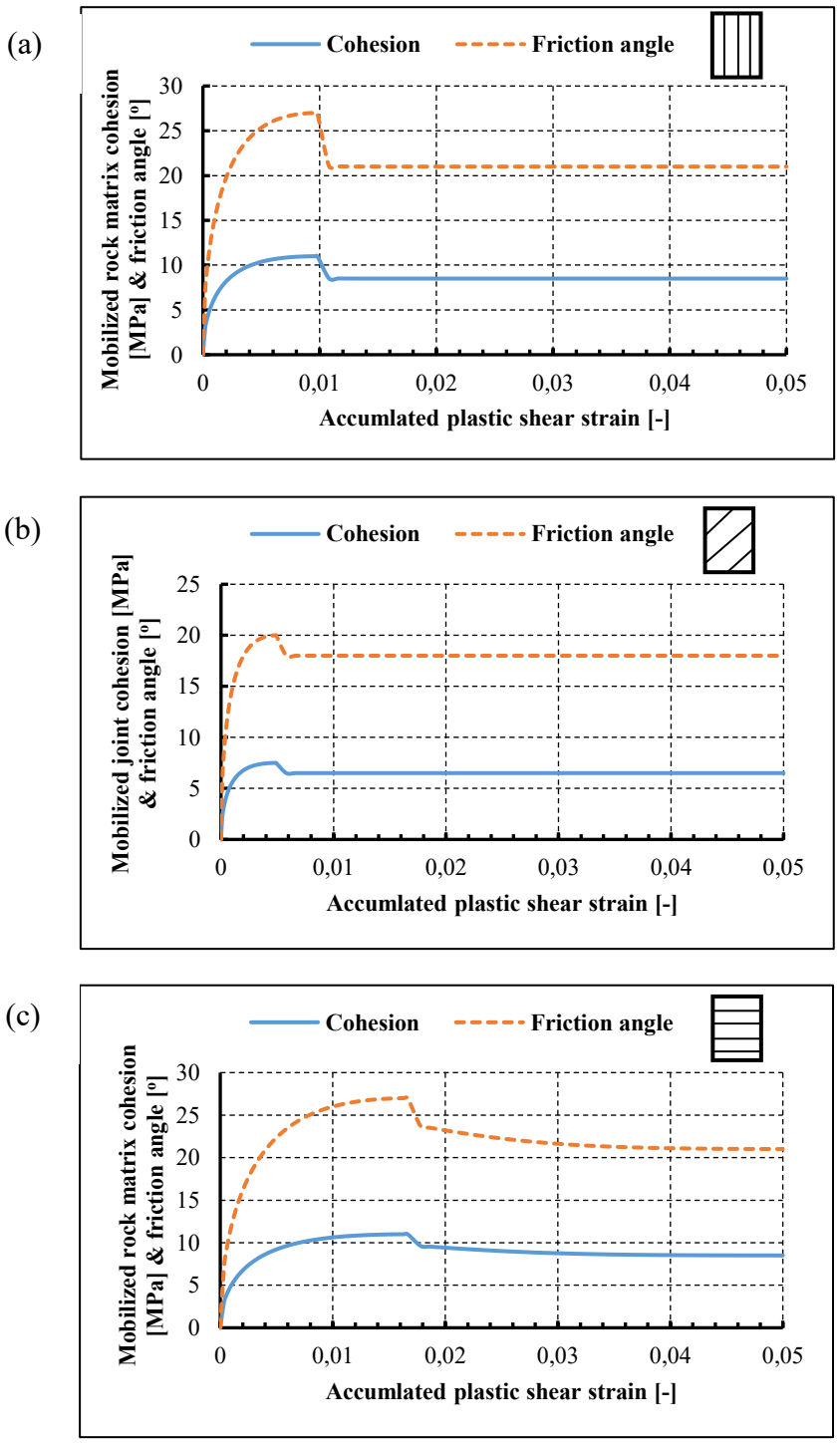

Fig. 4-8 Applied mobilization of strength parameters (cohesion and firction angle) at σ_3 = 50 MPa for (a) rock matrix, loading parallel to joint planes, (b) joint planes, and (c) rock matrix, loading normal to joint planes

The mobilization of the strength parameters is orientation and pressure dependent. For loading in direction normal to the bedding planes, the region of the hardening in the pre-peak stage for $\alpha = 0^o$ is wider than the same for $\alpha = 90^o$. For the same orientation both, hardening and softening behavior are more pronounced with increasing applied confining pressure σ_3.

4.2.4. Numerical modelling of triaxial tests

A series of triaxial tests on Tournemire shale are documented by Niandou (1994) and Niandou et al. (1997). These tests were performed with three different orientations (parallel to bedding planes $\alpha = 90^o$, normal to bedding planes $\alpha = 0^o$ and inclined to bedding planes with angle $\alpha = 45^o$). Also, different confining pressures were applied ($\sigma_3 = 5$, 30, 40 and 50 MPa). Strains in orthogonal directions were measured which allowed the determination of volumetric strains.

Numerical modelling of these tests are carried out using the previously identified strength parameters and the mobilizing functions. Fig. 4-9, Fig. 4-10 and Fig. 4-11 show a comparison between numerical and lab results for loading parallel ($\alpha = 90^o$), inclined ($\alpha = 45^o$) and perpendicular to the bedding planes ($\alpha = 0^o$). This comparison documents, that the Transubi model is able to simulate the strength and the stiffness anisotropy of the Tournemire shale. The volumetric compaction could not be well reproduced because the constitutive model does not consider this effect in detail. The significant difference in volumetric strain behavior for samples loaded parallel and perpendicular to the bedding has been extensively investigated by Abdi et al. (2015). As the volumetric strain is an indicator of crack propagation, the failure mode of samples loaded perpendicular to the bedding ($\alpha = 0^o$) shows strong fracturing and thus higher values of volumetric strain.

Fig. 4-10.b and Fig. 4-11.b document that greater values of dilation angle for rock matrix and bedding ($\psi = 15^o$ and $\psi_j = 5^o$) at higher confining stresses could approximately duplicate the volumetric response of Tournemire shale.

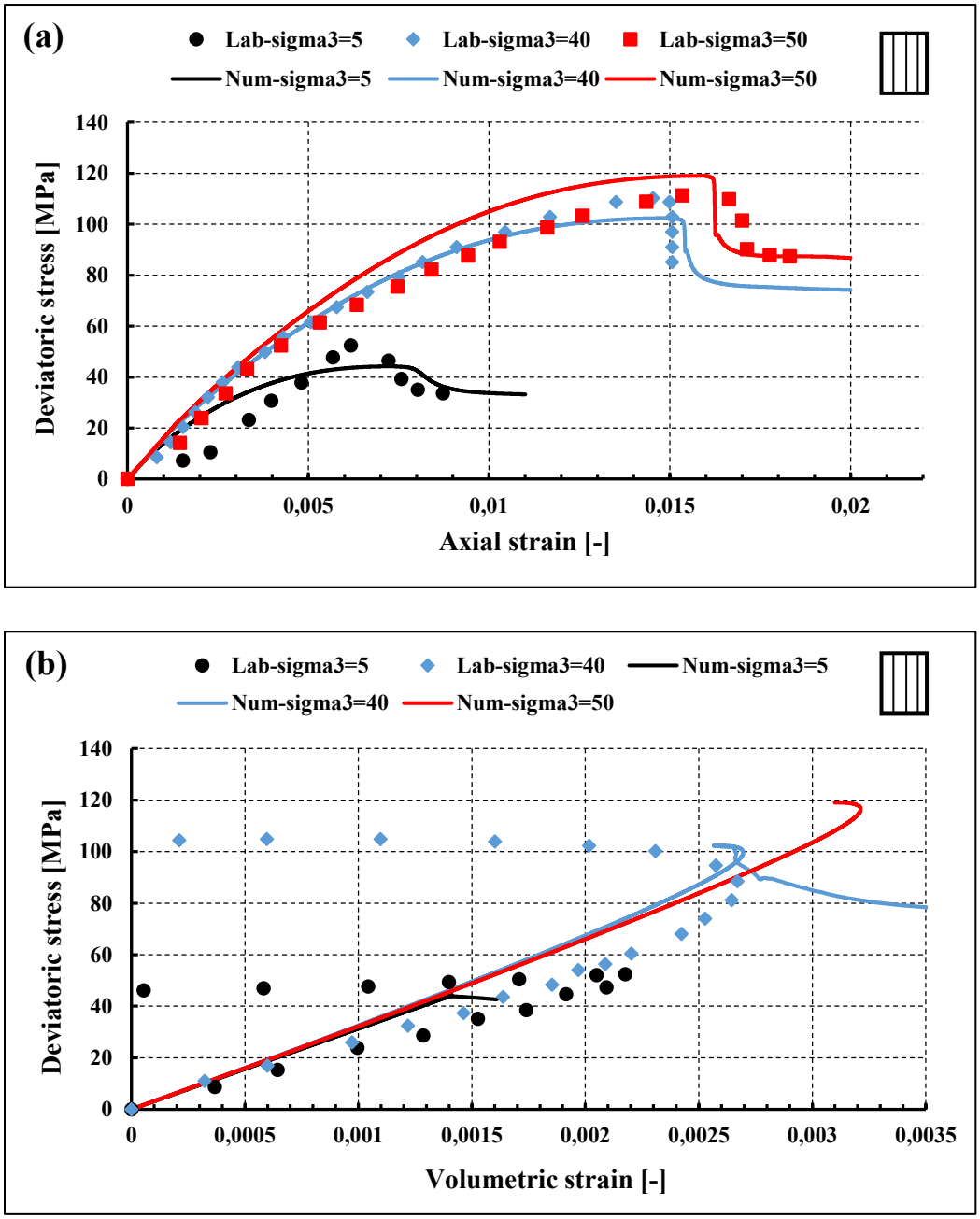

Fig. 4-9 Numerical and lab results for loading parallel to bedding (α = 90°, σ_3 = 5, 40 and 50 MPa): (a) deviatoric stress vs. axial strain, (b) deviatoric stress vs. volumetric strain

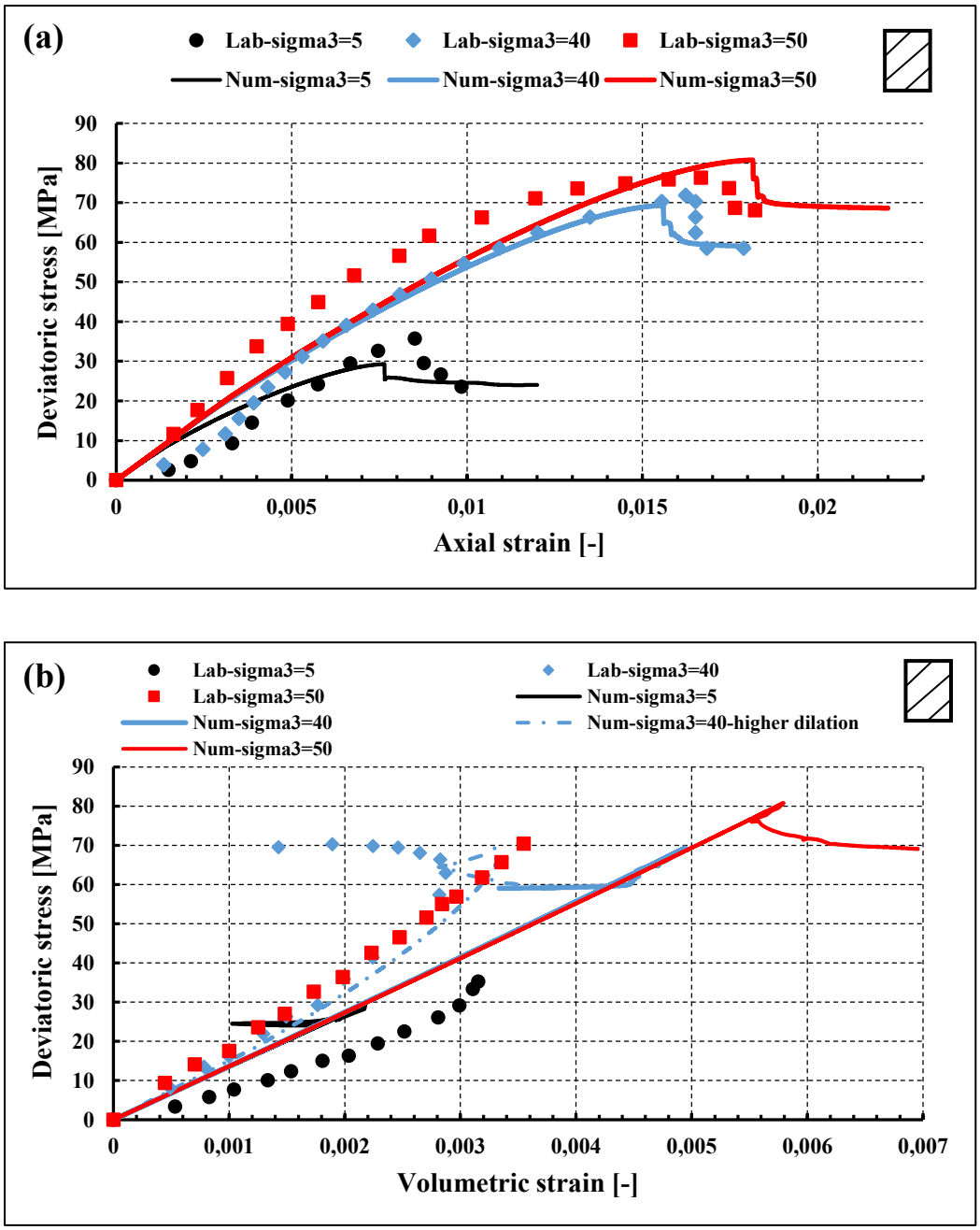

Fig. 4-10 Numerical and lab results for loading inclined to bedding ($\alpha = 45^{o}$, $\sigma_3 = 5$, 40 and 50 MPa): (a) deviatoric stress vs. axial strain, (b) deviatoric stress vs. volumetric strain

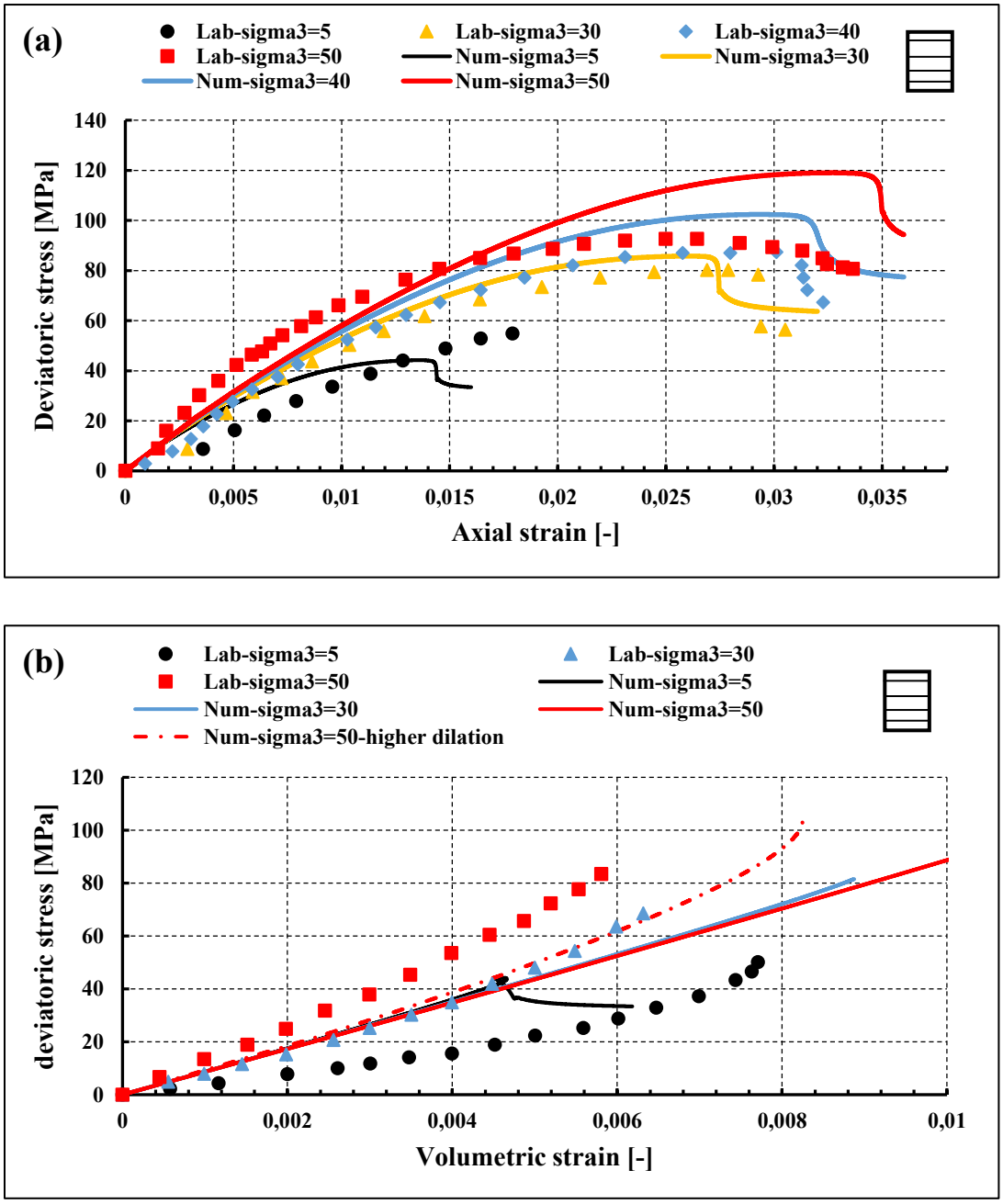

Fig. 4-11 Numerical and lab results for loading perpendicular to bedding (α = 0°, σ_3 = 5, 40 and 50 MPa): (a) deviatoric stress vs. axial strain, (b) deviatoric stress vs. volumetric strain

Analyzing the deviatoric stress versus axial strain for $\alpha = 0^o$ and 90^o reveals that strength anisotropy is not well reproduced by the proposed Transubi model. It should be noticed that the numerical prediction for samples at lower applied pressure (e.g. $\sigma_3 = 5$ MPa) underestimates the strength for $\alpha = 0^o$ and 90^o. Therefore, a bilinear definition of the yield surface for the rock matrix of the Tournemire shale is recommended for both, lower and higher applied stresses.

Finally, it can be stated that observed failure of samples with inclined bedding in the lab is in close agreement to the simulations (Fig. 4-10a). However, the initial nonlinear phases for $\sigma_3 = 5$ and 30 MPa was neglected by the simulations. The observed failure modes are identical with those investigated by Niandou et al. (1997): shear failure in the rock matrix for samples with $\alpha = 0^o$ and 90^o and sliding along the bedding planes for sample with $\alpha = 45^o$.

4.3. Opalinus clay

Similar to the Tournemire shale, Opalinus clay from the underground rock laboratory (URL) located in Mont-Terri (Switzerland) exhibits significant anisotropy in strength and stiffness as a transverse isotropic rock. The anisotropy can be explained by preferred orientation of the clay minerals which form 40 – 70 wt.% of its mineralogical composition (Loon et al. 2008). Salager, Nuth and Laloui (2010) stated that a constitutive model of the Opalinus clay should consider (i) elastic modulus on the inherent planes of anisotropy in a proper way, and (ii) pre- yield hardening or post-yield softening as observed by Olalla, Martin and Saez (1999), Corkum (2006) and Popp and Salzer (2007) taken into account stress induced anisotropy and loading angle.

Updated mechanical properties of the Opalinus clay could be found in (Bock 2009; Lisjak, Grasselli and Vietor 2014; Bossart et al. 2017). Unlike the stress-strain behavior of the Opalinus clay reported by many scholars (e.g. Popp and Salzer 2007; Olalla, Martin and Saez 1999; Corkum and Martin 2004), Salager, Nuth and Laloui (2010) documented post- yielding hardening which is not considered in this work. The uniaxial compressive strength $UCS_{\perp}$ in loading direction normal to the bedding planes ($\alpha = 0^o$) is higher than $UCS_{//}$ parallel to the bedding planes ($\alpha = 90^o$) (Bock 2009; Lisjak, Grasselli and Vietor 2014). In contrast, Popp and Salzer (2007) investigated the Opalinus clay strength under different applied confining pressures showing that $UCS_{//} < UCS_{\perp}$. Fig. 4-12 shows proposed strength parameters for rock matrix provided by Bock (2009) and Thöny (2014) and for the bedding planes by Popp and Salzer (2007). The rock matrix itself does not show any anisotropy.

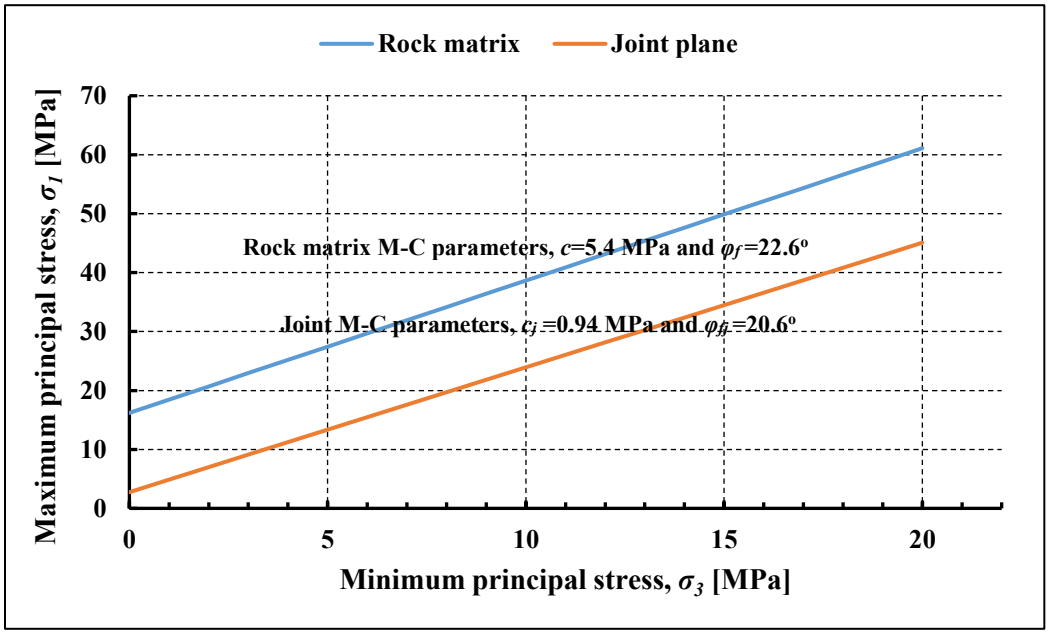

Fig. 4-12 Proposed strength envelops for Opalinus clay accoding to Bock (2009), Thöny (2014) and Popp and Salzer (2007)

Investigations of the sensitivity of the elastic modulus of Opalinus clay in respect to the applied confining pressure are documented for instance by Corkum (2006) and Naumann et al. (2007). A slight dependency of the elastic modulus on the applied confining pressure (σ_3) has been found. Since the value of the elastic modulus is relatively constant between σ_3 = 2 – 10 MPa, which represents the in-situ stress level at Mont Terri, Bock (2009) suggested to use constant elastic modulus. Recently, new drained triaxial lab testing confirmed a relation between the applied confining stress and the measured Young's moduli for P- and S-samples (Favero et al. 2018). Generally, the elastic modulus measured parallel to bedding planes ($E_{//}$, P-samples) is higher than perpendicular to the bedding plans ($E_{\perp}$, S-samples). As shown in Fig. 4-13, the undrained elastic anisotropy ratio $k = E_{//} / E_{\perp}$, is commonly between 3 and 4 (Thöny 2014; Lisjak et al. 2014; Bock 2009). k is decreasing at higher confinement, k is about 1.5 for $\sigma_3 \geq 10$ MPa (Favero et al. 2018). Two different Young's moduli have been identified for the Opalinus clay: the ordinary Young's modulus (E) deduced from cyclic loading tests (loading-unloading-reloading) and the secant or tangent Young's modulus ($E_{t\text{-}50}$ or $E_{0.2\%}$) determined at 50% UCS or after 0.2% of the axial strain

(Bock 2009; Corkum 2006). Usually, E is significantly greater than $E_{t\text{-}50}$. Various values of Young's modulus for different orientations (P- and S- samples) are shown in Fig. 4-13.

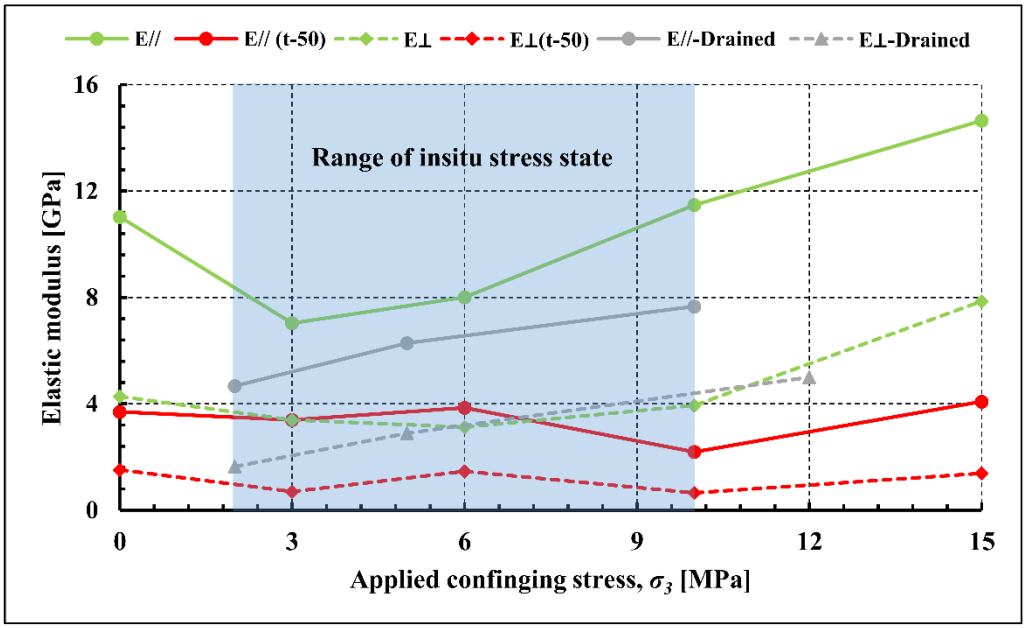

Fig. 4-13 Range of measured Young's moduli for P- and S-samples of Opalinus clay; drained values under saturated conditions and confining stress [σ_3 = 2 – 10 MPa], after Bock 2009 and Favero et al. 2018.

4.3.1. Parameters identification and bi-linear behavior

Based on the published experimental lab testing such as uniaxial compressive tests, triaxial compressive tests, tensile tests and direct shear tests (Olalla, Martin and Saez 1999; Rummel and Weber 2007; Popp and Salzer 2007; Konietzky and te Kamp 2004; Naumann, Hunsche and Schulze 2007; Amann et al. 2011; Amann et al. 2017), the mechanical behavior of Opalinus clay cannot be approximated by a simple linear Mohr-Coulomb failure criterion for rock matrix and bedding planes as shown in Fig. 4-12. Bock (2009) stated that the failure mode at lower applied confinement (< 5 MPa) is a combination of axial fractures with local shear fractures and/or spalling, while shear failure is observed at higher confining pressures. Thus, a non-linear M-C envelop should be considered for the mechanical behavior of the Opalinus clay. The strength parameters for a bi-linear constitutive law are given in Table 4-3, Fig. 4-14 and Fig. 4-15 (Konietzky, Blümling and te Kamp 2003; Bock 2009; Popp and Salzer 2007; Thöny 2014).

Table 4-3 Bi-linear peak and residual M-C strength parameters for rock matrix and bedding planes for Opalinus clay (Konietzky, Blümling and te Kamp 2003; Popp and Salzer 2007; Thöny 2014; Bock 2009)

Rock matrix				σ^t [MPa]	**Joint plane**				σ^t_j [MPa]
Peak values					***Peak values***				
First surface ***(< 3 MPa)***		*Second surface* ***(> 3 MPa)***			*First surface* ***(< 1 MPa)***		*Second surface* ***(< 1 MPa)***		
c_1	φ_{f1}	c_2	φ_{f2}	1.2	c_{j1}	φ_{fj1}	c_{j2}	φ_{fj2}	0.4
3.5	35	6.5	20		0.6	29	0.96	21	
Residual values					***Residual values***				
First surface		*Second surface*			*First surface*		*Second surface*		
c_1^{res}	φ_{f1}^{res}	c_2^{res}	φ_{f2}^{res}		c_{j1}^{res}	φ_{fj1}^{res}	c_{j2}^{res}	φ_{fj2}^{res}	
1.5	35	3.2	20		0.3	26	0.6	18	

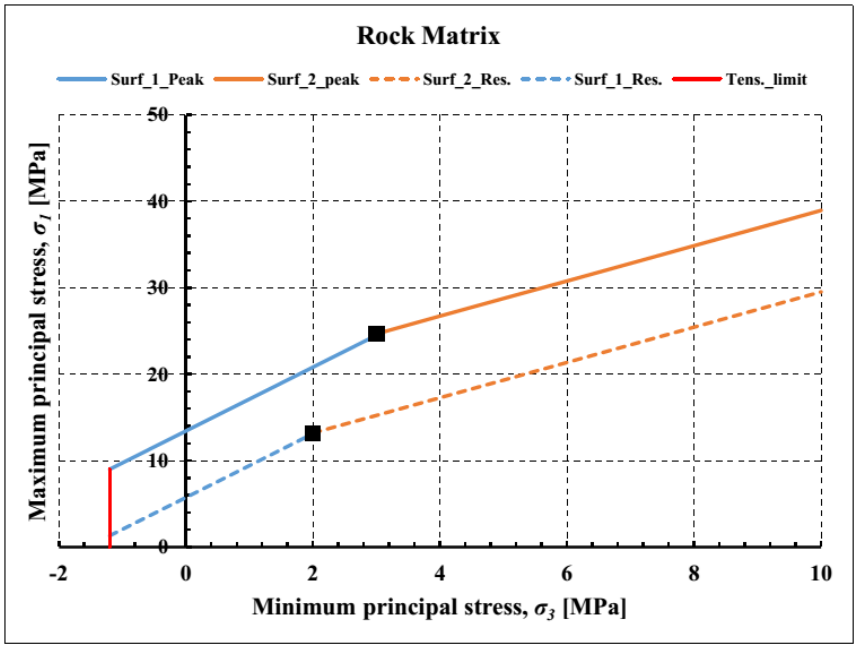

Fig. 4-14 Bi-linear M-C strength envelopes for rock matrix of Opalinus clay

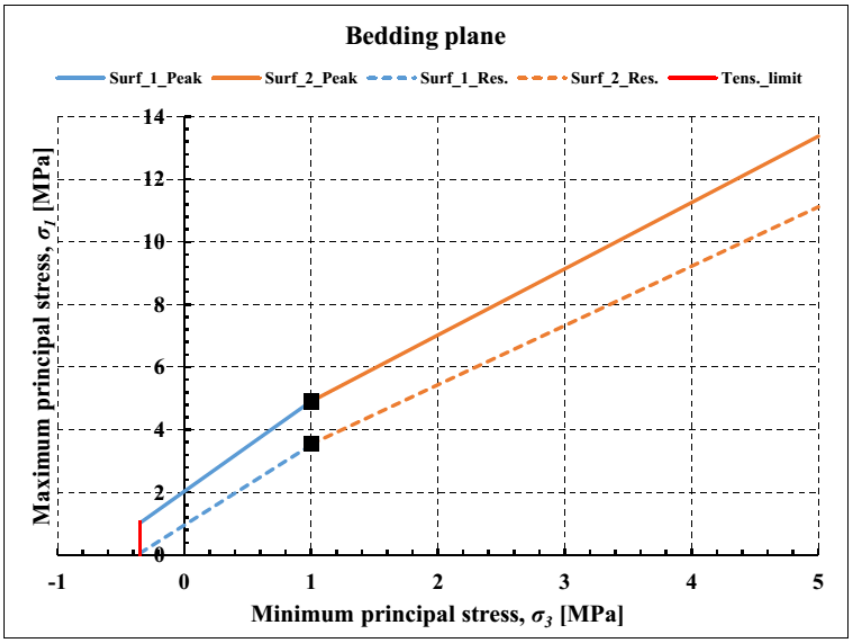

Fig. 4-15 Bi-linear M-C strength parameters for bedding planes of Oplainus clay

The work by Popp and Salzer (2007) focused on the bedding planes dilation angle assuming a relatively high value of 25° for low confinement (< 1 MPa) which decreases exponentially to values close to 0° for higher confining pressure (> 2 MPa). They analyzed the dilatancy for both, the rock matrix and the bedding planes via the comparison between numerical simulation results, triaxial lab testing and direct shear tests.

4.3.3. Mobilization of strength parameters

Similar to the mobilization procedure described for Tournemire shale in chapter 4.2.3, the analytical functions (Eq. 5.2 – 5.6) for pre-yield hardening and post-yield softening are applied also for the Opalinus clay. The mobilization is considered for cohesion and friction angle while tensile strength and dilation angle are constant. It is assumed that elastic parameters are not sensitive to the applied confining pressure, thus the plastic strain depends completely on the bedding plane orientation. Fig. 4-16 and Fig. 4-17 present the mobilization of the strength parameters for both rock matrix and bedding planes, respectively.

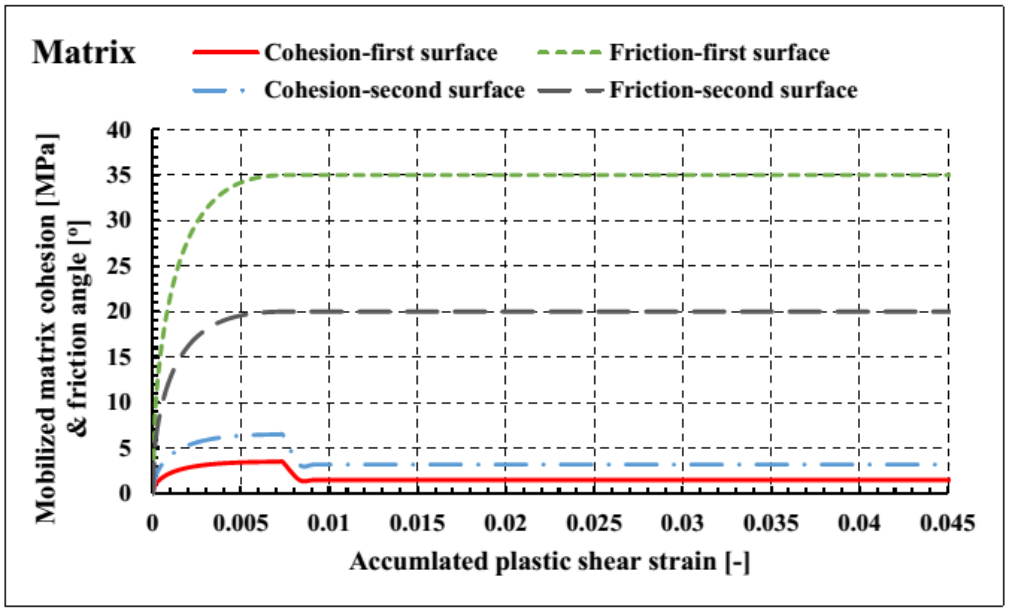

Fig. 4-16 Mobilization of strength parameters (cohesion and friction angle) for Opalinus clay for rock matrix.

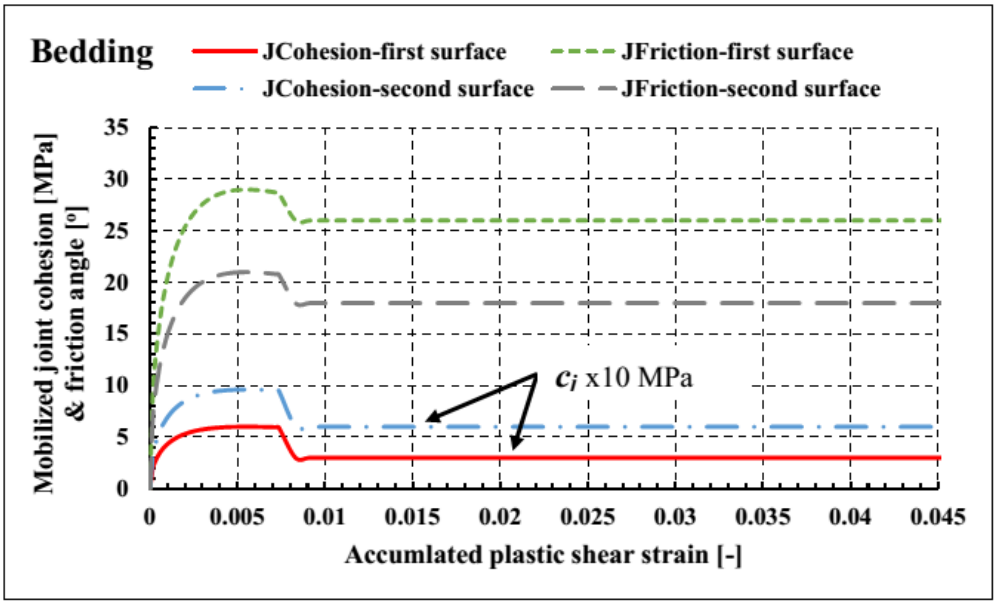

Fig. 4-17 Mobilization of strength parameters (cohesion and friction angle) for Opalinus clay for bedding planes.

The plotted strength mobilization functions are used within the following section to simulate the triaxial and the direct shear tests conducted on Opalinus clay by Popp and Salzer (2007).

4.3.4. Numerical simulation of triaxial tests

The numerical simulation of triaxial compression tests conducted on Opalinus clay by Popp and Salzer (2007) is performed using the proposed Transubi model and applying the strength parameters given in Table 4-3, Fig. 4-14 and Fig. 4-15. The simulations utilize the mobilization of these strength parameters as discussed previously. The elastic parameters are given in Table 4-4 (Bock 2009; Lisjak, Grasselli and Vietor 2014).

Table 4-4 Elastic parameters for Opalinus clay

E [GPa]	E' [GPa]	ν [-]	ν' [-]	G' [GPa]
10.5	3.0	0.35	0.25	2.0

Constant values are assumed for the dilation angles: $\psi_1 = 7^o$ and $\psi_2 = 5^o$ for rock matrix. Literature does not provide values for the dilation angle of the rock matrix, but the volumetric dilatancy was investigated via triaxial lab tests with different orientation of bedding planes to loading directions (Bock 2001; Popp and Salzer 2007). Without a detailed explanation Thöny (2014) proposed relatively high values for the dilation angle for rock matrix and bedding planes: 32° and 19°, respectively. On the other side, the dilation angle was considered as 2/3 of the friction angle which varies with the loading angle (α) (i.e. $\psi_{min} = 10^o$ (for orientation $\alpha = 40^o$) and $\psi_{max} = 15^o$ (for orientation $\alpha = 90^o$)) (Nguyen and Le 2015). As the proposed constitutive model considers hardening and softening in the pre- and post-yielding phase, the numerical results are highly sensitive to any variation of the dilation angles.

Fig. 4-18 presents that simulation results show a good agreement with lab data obtained from triaxial compression tests. As previously mentioned, the Transubi model considers no strength anisotropy for the rock matrix, thus the computed strength of the rock matrix for the same confining pressure (σ_3) is independent on the sample orientation. However, the model is able to simulate the stiffness anisotropy as well as pre-yielding hardening and post-yielding softening, especially for S-samples. On the other hand, the plastic strain of Opalinus clay shows dependency on the bedding plane orientation. As shown in Fig. 4-18 for P-samples, the simulation displays

excessive hardening in the pre-yielding region. Generally, the Opalinus clay shows pronounced strain softening for P-samples especially at higher confinement. On the contrary, a brittle plastic behavior is adapted for S-samples as explained by Popp and Salzer (2007). The dilatancy of P- and S- samples during the triaxial tests is shown in Fig. 4-19.

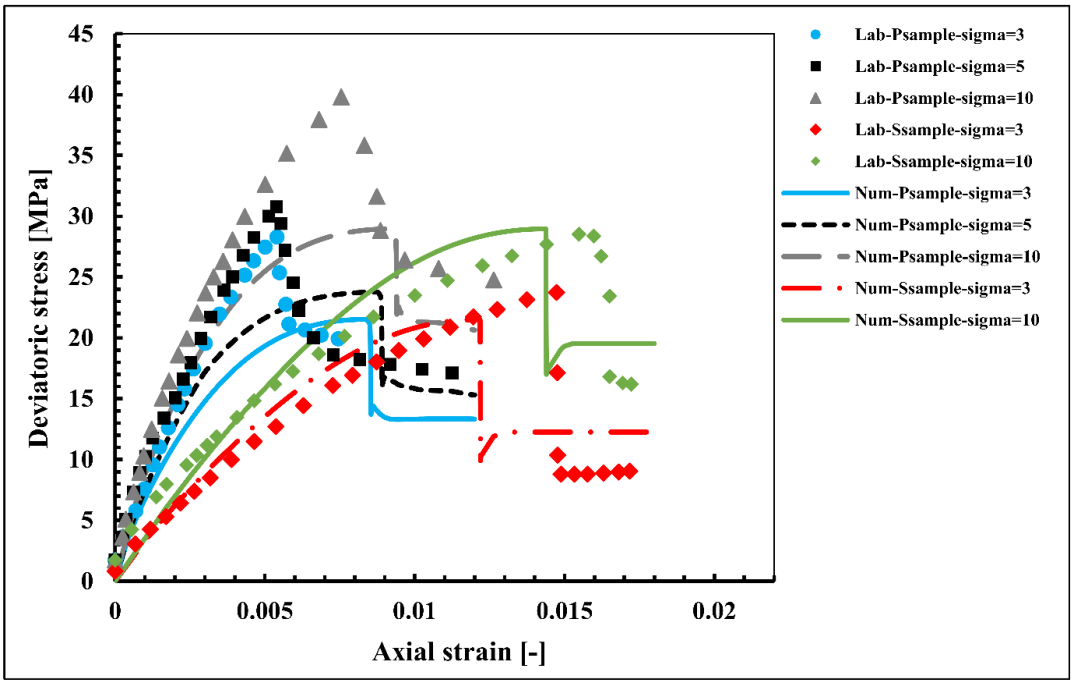

Fig. 4-18 Numerical and lab results of triaxial tests (P- and S-samples)

The volumetric strain shows significant variations in behavior and magnitude for different loading directions. Hatzor and Heyman (1997) confirmed that applied confining pressure and bedding plane orientation play a significant role in dilation performance. Loading in direction perpendicular to the bedding planes (i.e. S-sample, $\alpha = 0^{o}$) produces higher dilation than loading parallel to bedding (i.e. P-sample, $\alpha = 90^{o}$) (Hatzor and Heyman 1997; Bonnelye et al. 2017). A numerical example has been introduced by Zhao and Cai (2010) in which an elastic-perfect-plastic M-C rock sample is subjected to (i) fixed confining pressure and different dilation angles (Fig. 4-20a), and (ii) different confining pressures with constant dilation angle (Fig. 4-20b).

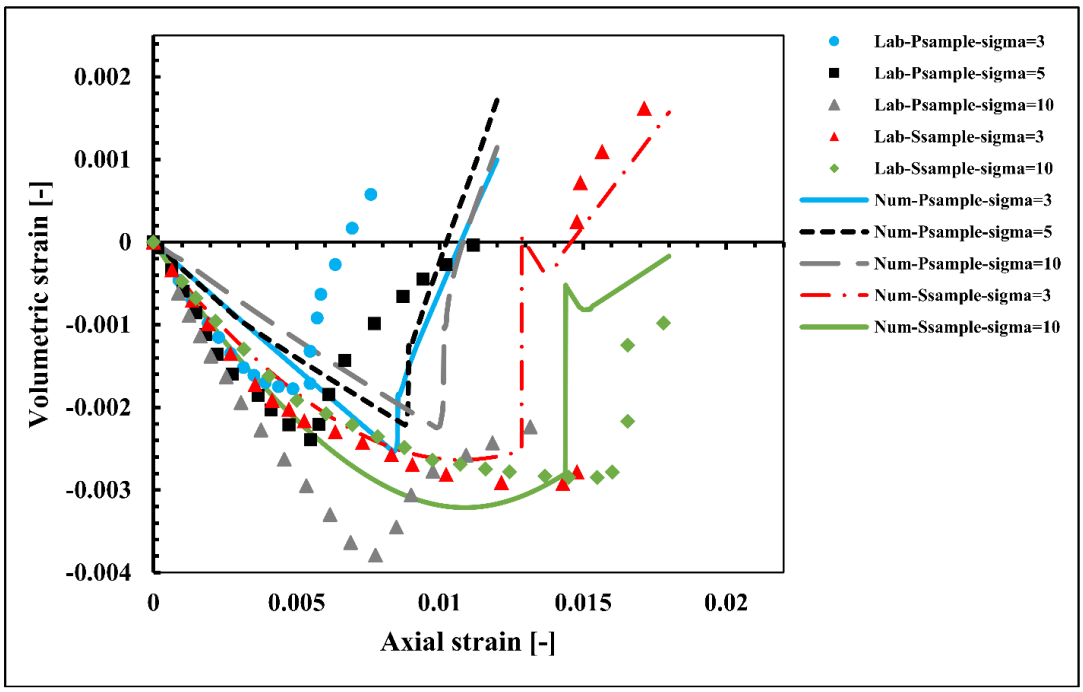

Fig. 4-19 Numerical and lab results of the observed dilatancy of P- and S-sample during triaxial lab tests

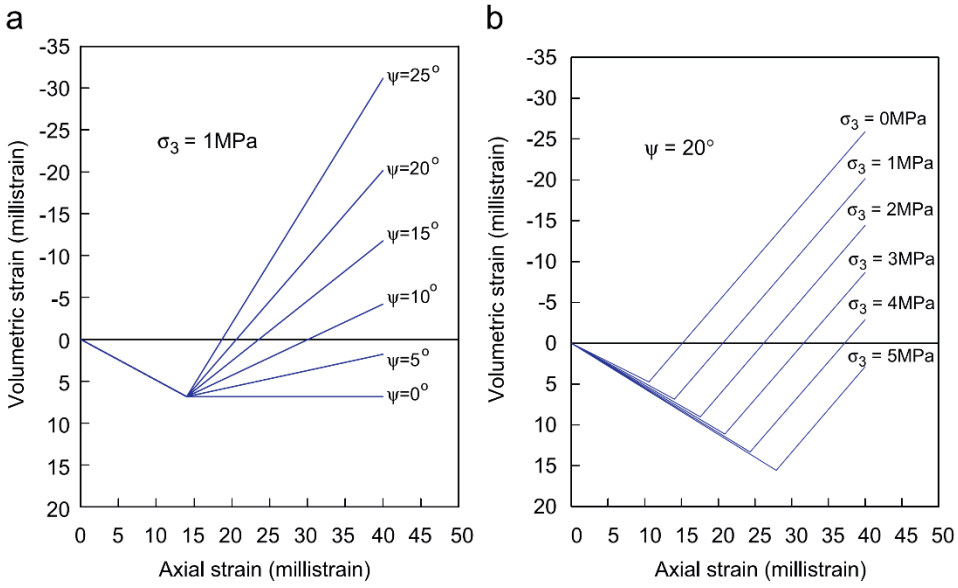

Fig. 4-20 Volumetric vs. axial strain for rock samples with (a) different constant dilation angles (σ_3 =1 MPa), and (b) subjected to different confining stresses (ψ=20°) (simulations by Zhao and Cai 2010).

Based on the lab datasets given by Popp and Salzer (2007), the volumetric strain behavior with loading direction perpendicular to the bedding planes ($\alpha = 0^o$) fits with the curves given in Fig. 4-20. Generally, rock samples ($\alpha = 0^o$) for different confinement indicate a fixed pre-yielding slope which confirms constant elastic properties.

Unlike the behavior captured at rock samples with loading normal to bedding ($\alpha = 0^o$), a remarkable contrast is found in the volumetric strain for loading direction parallel to bedding (P-sample, $\alpha = 90^o$). Applying constant dilation angles (e.g. $\psi_1 = 7^o$ and $\psi_2 = 5^o$) does not lead to proper volumetric strain results. Hatzor and Heyman (1997) stated that increasing confining pressure could cause either decreasing dilation or increasing elastic modulus (as observed by Corkum (2006) and Bock (2009)) or decreasing Poisson's ratio (Favero et al. 2018). Because constant elastic properties are used in the proposed model, this behavior cannot be duplicated. According to Bonnelye et al. (2017) bedding plane dip angle is not the only variable causing the dilation variations but also the dip direction as documented in Fig. 4-21.

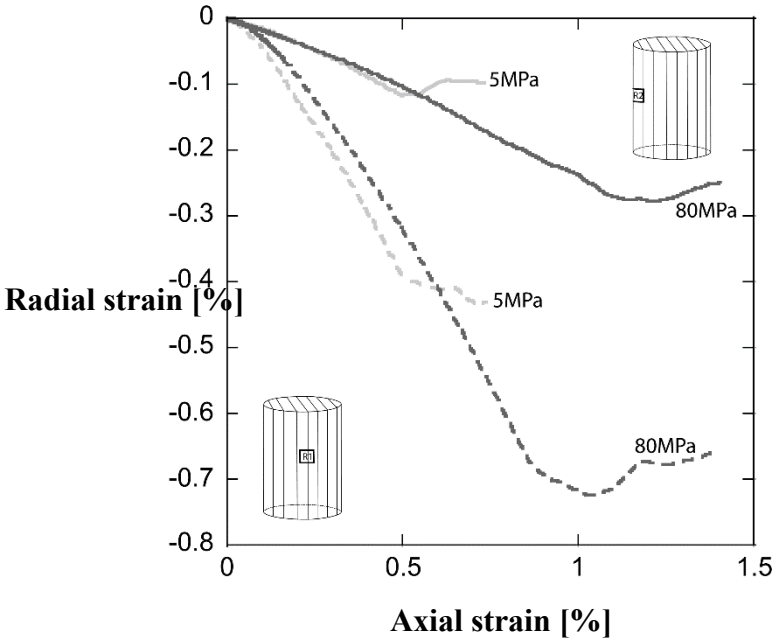

Fig. 4-21 Radial vs. axial strain as a function of the locations of gauges R1 (dashed lines) and R2 (solid lines) for loading parallel to bedding planes ($\alpha = 90^o$) and confining pressures of 5 and 80 MPa (Bonnelye et al. 2017).

By applying a dilation angle nearly similar to the angle proposed by Nguyen and Le (2015) for P-sample (i.e. $\psi_2 = 12^o$), the numerical simulation shows closer agreement with lab results for confinement $\sigma_3 = 10$ MPa (Fig. 4-22). However, such excessive decrease in volume for clay rocks

in general and Opalinus clay in particular is usually not observed (Amann et al. 2011; Wild et al. 2015; Favero et al. 2018)). Also, Nguyen and Le (2015) stated that P-sample dilation is overestimated. As shown in Fig. 4-22, the computed maximum volumetric strain using $\psi_2 = 5^o$ equals -0.0022 which closely fits the measurements provided by Bock (2001) with -0.0021. The difference in values given by Bock (2001) and Popp and Salzer (2007) could reflect the influence of bedding plane dip direction. Dilatancy starts at peak stress and continues up to failure. This finding is consistent for S-samples (Popp and Salzer 2007; Naumann et al. 2007; Nguyen and Le 2015). However, for P-sample, it is far from experimental observations (Fig. 4-19).

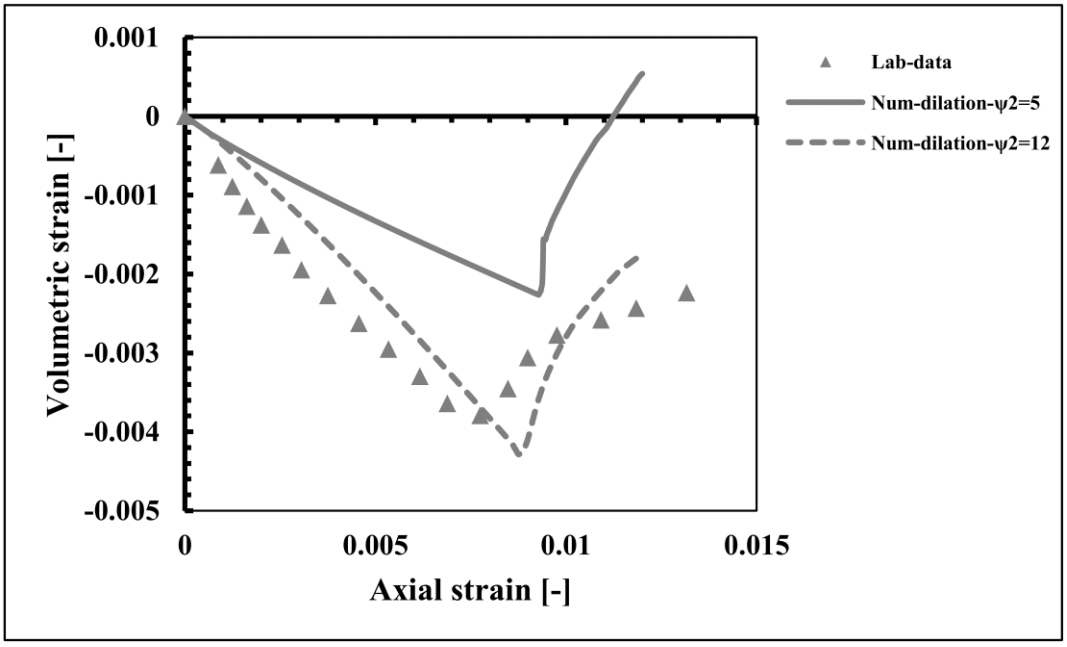

Fig. 4-22 Numerical and lab results of volumeritic strain of P-sample (σ_3 = 10 MPa) applying different dilation angles

4.3.5. Numerical simulation of direct shear tests

This part documents numerical simulations of direct shear tests conducted on Opalinus clay in the lab by Popp and Salzer (2007). Samples are horizontally bedded blocks with dimension w = 200 mm and h = 100 mm (see Fig. 4-23) subjected to different normal stresses (σ_n = 0.5, 1, 3 and 4 MPa). The entire test procedure is explained in details by Popp and Salzer (2007) showing also the influence of the displacement rates.

As shown in Fig. 4-23, the numerical simulation is based on a 2-dimensional model with same size of the sample (0.2 m x 0.1 m) discretized into 40 x 20 zones in x- and y- direction, respectively. This model is adjusted from the shear test example found as example 3.5 in FLAC manual (Itasca 2016). A constant vertical stress (σ_{yy}) is applied while two different horizontal stresses (σ_{xx} and σ_{zz}) are initiated and their values are similar to the applied vertical stress. Afterward, a fixed horizontal displacement is applied on the upper boundary in the positive x-direction. Different 8 points located on the upper boundary of the sample are assigned as history points to record the displacements in both x- and y-directions by which the dilation and the shear displacements could be plotted.

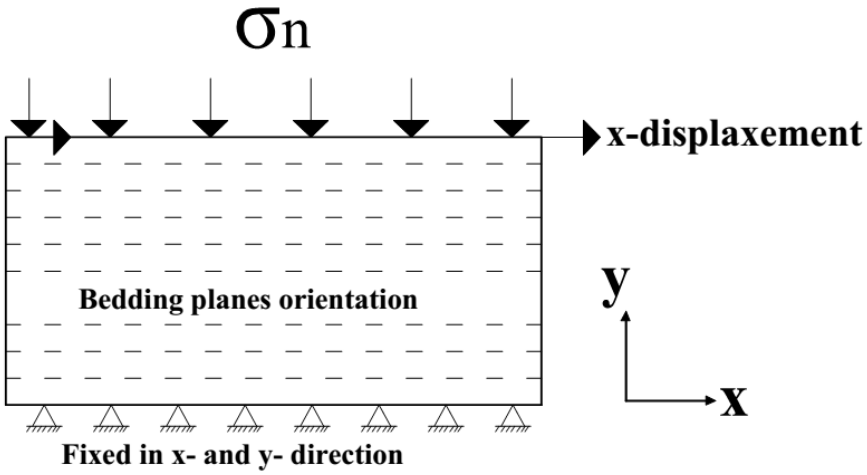

Fig. 4-23 Sketch of the numerical direct shear test

Elastic and strength properties of the rock matrix and the bedding planes of the Opalinus clay are identified previously, however the dilation angle of the bedding planes is not yet assigned. According to Popp and Salzer (2007), the value of the dilation angle depends on the applied normal stress, for $\sigma_n \leq 1$ MPa: $\psi_j \geq 10^o$. On the other side, the dilation angle exponentially decreases for $\sigma_n \geq 1$ MPa and reaches almost zero ($\psi_j \approx 0^o$) at σ_n = 5 MPa. Fig. 4-24 and Fig. 4-25 show a comparisons between lab and numerical simulation results.

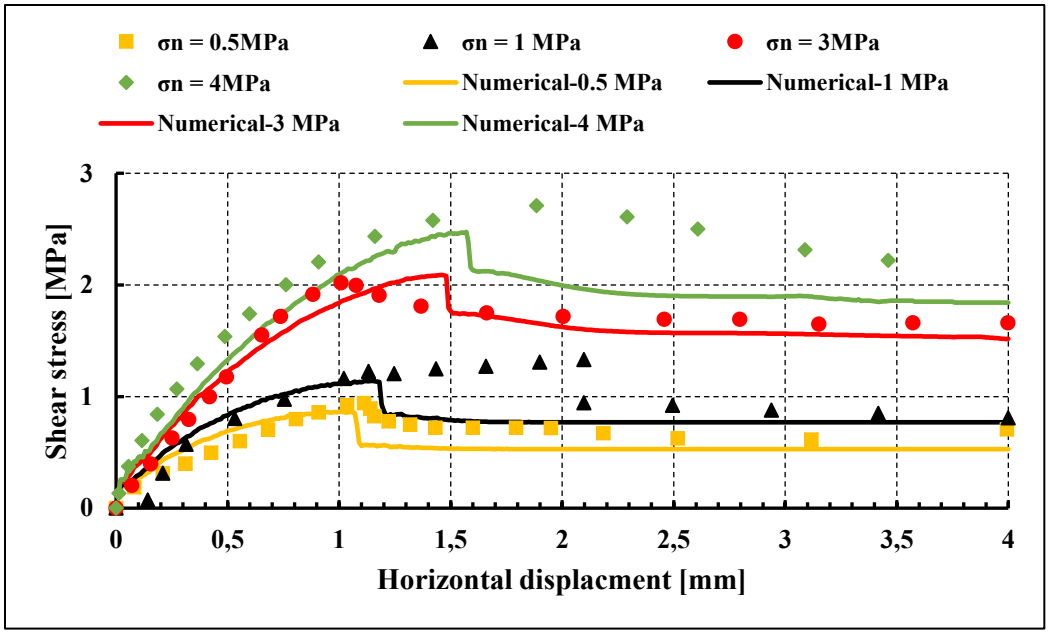

Fig. 4-24 Shear stress vs. shear displacement for various normal stresses

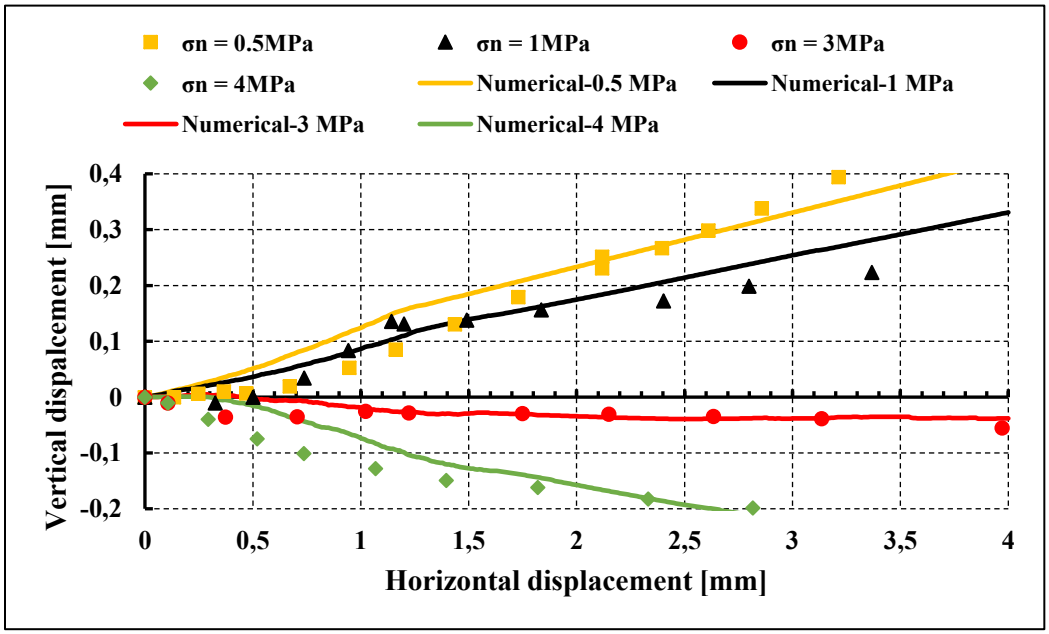

Fig. 4-25 Dilatancy (i.e. vertical displacement) vs. shear displacement for various normal stresses.

The applied dilation angles for bedding planes are defined according to the observation given by Popp and Salzer (2007) in which the values are measured using the dilatancy curves. As already explained, a bi-linear M-C failure criterion is used to describe the behaviors of the rock matrix and the bedding planes. The intersection between these two shear surfaces is assigned at σ_3 = 1 MPa where the dilation angle decreases significantly as well, see Fig. 4-26.

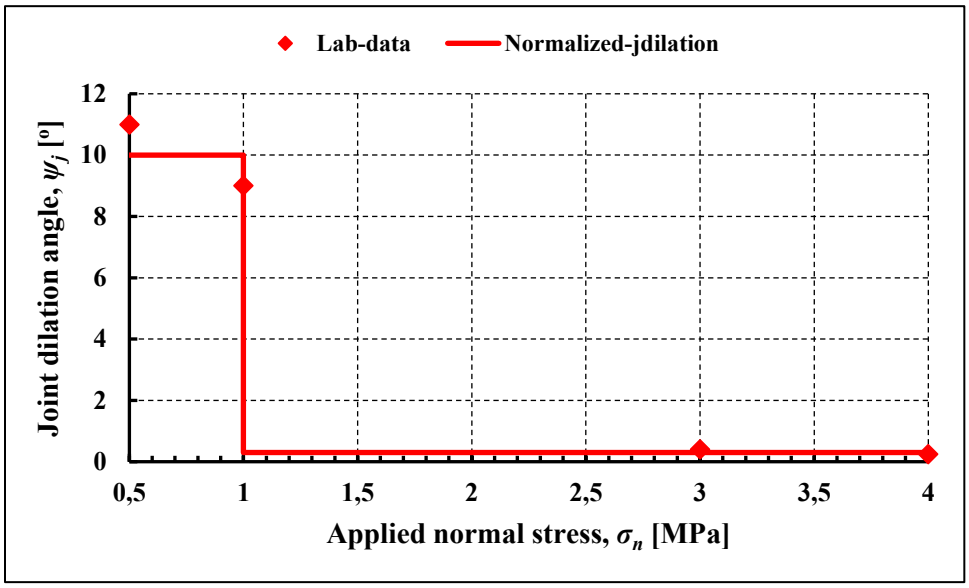

Fig. 4-26 Normalized applied joint dilation angle vs. the observed lab values.

Compared with lab data, the Transubi model using the bi-linear yield surfaces is able to simulate the direct shear test conducted on horizontally bedded Opalinus clay samples. Although this simulation - in respect to the bedding planes - shows significant difference in behavior under low normal stress (≤ 1 MPa), in practice considering in-situ stress states between 2 to 10 MPa, the applied yield surface is linear and follows the second yield surface (σ_3 >1 MPa).

4.4. Conclusions

This chapter introduced numerical simulations of lab tests conducted on inherent anisotropic rocks: Tournemire shale and Opalinus clay. As illustrated, both rocks behave as transverse isotropic materials which possess anisotropy in strength and stiffness. For Tournemire shale, the triaxial compression tests done by Niandou (1994) were simulated using the Transubi model which is able to capture the pre-yield hardening and the post-yield softening. The mobilization of the strength

parameters for the Tournemire shale show relation to plastic strain, deformation modulus, volumetric strain, applied confining pressure and strength in respect to loading direction.

On the other hand, Transubi model utilizes bilinear yield surfaces for both, the rock matrix and the bedding planes. Similar to the Tournemire shale, the Opalinus clay behaves non-linear in the pre- and post-yield regions, thus the mobilization of the strength parameters starts from the first stages of loading. Unlike the Tournemire shale, there is not dependency of the plastic strain on the confining pressure for Opalinus clay. Triaxial and direct shear tests carried out by Popp and Salzer (2007) have been numerically simulated and results show good agreement with the lab datasets. Dilation angles for rock matrix and bedding planes show high variability in respect to loading direction and applied confining pressure.

To sum up, the Transubi constitutive model is able to model the stiffness and strength anisotropy for bedded argillaceous rocks and predicts in good agreement with lab tests the stress – strain behavior. However, it does not include stress dependent elastic modulus or rock matrix strength anisotropy. Also, the simulation results show significant influence of the assigned dilation angle which should be carefully assigned.

5. Loading and unloading of transverse isotropic rock block with circular hole: lab test and numerical simulation

5.1. Introduction

Transverse isotropic elastic constants have a significant influence on the plastic zone around excavated openings (Tonon 2000). To investigate this phenomenon a special laboratory test has been designed using a transverse isotropic slate rock block containing a circular opening. A one-sided partial faced cyclic loading is applied on the sample while the opening perimeter was continuously observed using a special optical observation method. Later, this test was simulated using different constitutive models: anisotropic elastic model, ubiquitous joint model and Transubi model.

5.2. Evaluation of previous numerical studies

The improvement of computational methods has given deeper insight into the behavior of openings in transverse isotropic rocks, e.g. by introduction of stress-dependent deformation modulus (Corkum 2006), the evolution of the EDZ based on continuum modelling (Wang et al. 2009) or finite discrete element modelling (Lisjak et al. 2014). A review is summarized in Table 5-1 focusing on the stress-strain behavior around openings in transverse isotropic rock masses.

Wang and Huang (2014) analyzed the deformations around a tunnel based on the enhanced strain hardening/softening ubiquitous joint model considering up to three joint sets. The assigned parameters of the joint planes are fixed to all included joint sets. Later, Agharazi (2013) and Chang (2017) developed an equivalent continuum multi-joint ubiquitous joint model based on elastic-perfect-plastic theory. Based on the FEM code RFPA, Tang et al. (1998), Wang et al. (2009); Jia and Tang (2008) and Wang et al. (2012) modelled not only the influence of stiffness and strength anisotropy, but also the effect of rock heterogeneity on the growth of the EDZ around unlined openings of different geometries. Wang et al. (2012) studied in detail the failure modes around a circular hole driven into an interlayered rock based on experimental investigations by Tien et al. (2006). Using the FEM code Phase2 (Rocscience, 2011), a tunnel excavation in a stratified rock mass was investigated by Fortsakis et al. (2012). In contrast to the elastic study by Lisjak et al. (2015) based on the same software, Fortsakis et al. (2012) used a generalized Hoek–Brown constitutive law based on the GSI-Index where dominant discontinuities were explicitly modelled by the nonlinear Barton–Bandis failure criterion. Similar, a tunnel in dipping layered formation

was investigated by Li et al. (2013) using the FDM code FLAC3D (Itasca, 2016). Here, for the rock matrix the isotropic Mohr–Coulomb law was used while the dipping layering was modelled explicitly by interface elements. Another continuum based approach with strength and stiffness anisotropy is available in the FEM code PLAXIS (Plaxis, 2016). Simanjuntak et al. (2014) used this 2-dimensional elasto-plastic model in which the rock matrix behaves elastic while the joint planes react elasto-plastic. Full elasto-plastic numerical simulations based on continuum based constitutive models are presented by François et al. (2014) in which a cross-anisotropic strain hardening/softening constitutive model is applied to simulate the deformations and plastic zone around unlined openings. All previous mentioned numerical studies considered symmetrical loading conditions. Liu et al. (2017) conducted centrifugal model tests and corresponding numerical simulations for a shallow unlined opening excavated in an interlayered inclined rock mass in which the applied loading on the opening is unsymmetrical. A comparative study provided by Riahi and Curran (2009) considers the response of a circular hole excavated in a layered rock with layers oriented in an out-of-plane direction by using a Cosserat equivalent continuum elasto-plastic model. The results were compared with those obtained by the DEM code 3DEC. Regarding the discontinuum based models, a recent numerical study about the failure mechanisms of horizontal boreholes in transversely isotropic rock mass utilizing the particle flow code PFC^{2D} by Jia et al. (2017) has to be mentioned. The failure modes around a horizontal borehole considering different bedding inclinations have been investigated and compared with numerical analysis by Wang et al. (2012). The hybrid finite discrete element method (FDEM) combines continuum mechanics principles with DEM algorithms to simulate the progressive failure and the spontaneous nucleation and propagation of cracks in an explicit manner within the rock mass (Lisjak and Grasselli 2014; Lisjak et al. 2014; Lisjak et al. 2015).

Table 5-1 Summary of selected recent numerical studies of a tunnel in layered rock mass

Reference	No. of joint/interface sets	Strength anisotropy	Stiffness anisotropy	Type of used software	Captured failure modes	remarks
(Azadeh Riahi and Curran 2009)	One joint set, spacing considered	Yes	Yes, as equivalent continuum	FEM	Sliding on joints, failure through rock matrix and flexural layer bending	3D Cosserat-based constitutive model
(Wang and Huang 2014)	Three joint sets, spacing included	Yes	Yes, as equivalent continuum	FLAC	Sliding on joints, failure through rock matrix	Joint properties are fixed for the different sets
(Wang et al. 2012)	One joint set, interlayered rock type	Yes	Yes, as transverse isotropic stiffness matrix	RFPA	Sliding on joints, failure through rock matrix and cracking	Interlayered elastic properties are explicitly defined
(Liu et al. 2017)	One inclined joint set, interlayered rock type	Yes	Yes	ANSYS	Sidewall failure with increasing acceleration	Centrifugal test
(Fortsakis et al. 2012)	One dominant discontinuity set	Yes, but rock matrix behaves as "pseudo-isotropic" material	Yes	Phase2D	Sliding on joints and deflections of internal rock mass	Beam theory
(Jia et al. 2017)	One inherent joint set	Yes	Yes	PFC2D	Sliding on joints, failure through rock matrix; collapsed zone is simulated	Different applied horizontal stresses
(Simanjuntak et al. 2014)	One inherent joint set	Yes	Yes	Plaxis	Sliding on joints	Rock matrix is elastic
(François et al. 2014)	One inherent joint set	Yes	Yes, as transverse isotropic stiffness matrix	LAGAMINE FEM	Sliding on joints, failure through rock matrix and shear banding	HM-coupling
(Lisjak et al. 2014)	One inherent joint set	Yes	Yes	Y-Geo FEM/DEM	Shearing through intact matrix, bedding plane delamination and axial splitting	EDZ formation process in horizontal bedded rock mass
(A Lisjak et al. 2015)	One inherent joint set	No	Yes	Phase2D	Elastic deformations	Underestimation of deformation around the hole
(Li et al. 2013)	Isotropic rock with five interface element layers	Yes, at the interfaces	No	FLAC3D/ANSYS interface	Sliding on joints, failure through rock matrix	Effect of dipping layers on the construction process

5.3. Experimental Model Setup

The experiment was conducted on a slate block with inherent planes of anisotropy (horizontal bedding). The tested block had the dimensions (height x width x thickness) of 249.03 x 250.75 x 39.27 mm. A circular hole with radius (r) of 23.33 mm was drilled in the middle of the rock block. Boundary conditions are illustrated in Fig. 5-1. Note that, the loading on the plate was not applied on the entire face, and the model sides were not fixed. Applying such load on a partial side of the sample was suggested due to the capacity of the testing machine (i.e. maximum stress which could be generated using the entire boundary is 100 MPa) which is lower than the estimated compressive strength of the sample (σ_c = 142 MPa).

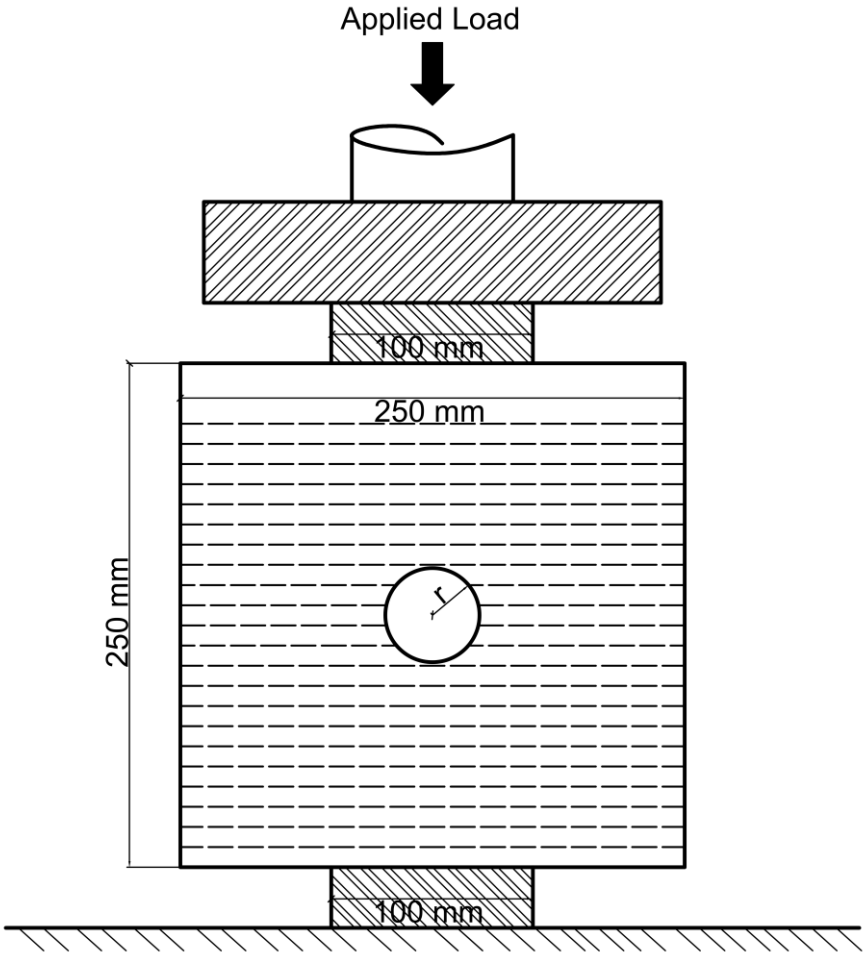

Fig. 5-1 Simplified sketch of the lab test settings

5.3.1. Loading pattern and deformation monitoring system

A pseudo static cyclic load was applied at the sample with a displacement velocity of 0.05 mm/min which results in a measured vertical force of approximately 0.12 kN/sec. The loading (F_y) history is shown in Fig. 5-2. The load is increased in stages up to: 100 kN, 150 kN, 200 kN, 250 kN, 350 kN and 400 kN. Once the peak load was reached, the specimen was unloaded to 10 kN with the same loading speed.

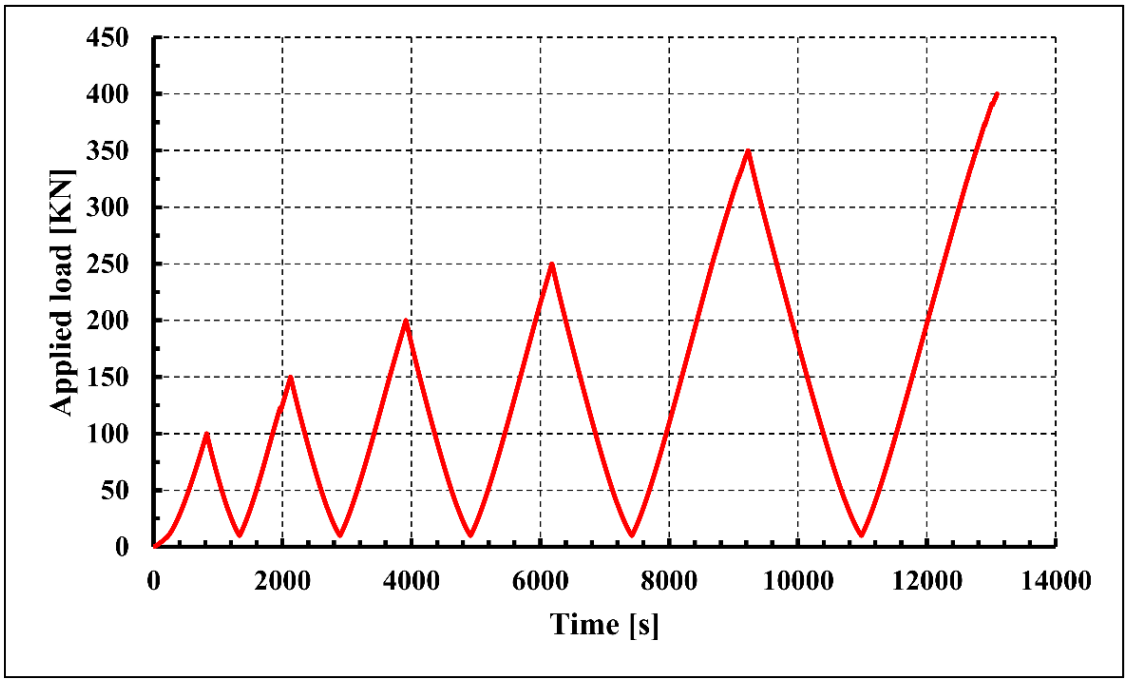

Fig. 5-2 Vertical load (F_y) vs. time with applied loading velocity of 0.05 mm/min

The cyclic loading was applied until the sample failed. Vertical load was measured directly by the load measuring cell. The initial loading until 100 kN shows a strong non-linear behavior (see Fig. 5-2) caused by the initial setting of the interface between the sample and the loading platens and will not be considered further in the simulation. The real time deformation behavior along the perimeter of the hole was observed in detail using a high precision optical multi-point and profile measurement device. Up to 16 points can be measured simultaneously with an accuracy of about 2 µm for each measurement point. The measurement technique is based on a 2D image projected on a complementary metal–oxide–semiconductor [CMOS] receiver. The optical system uses a green LED. Telecentric lenses apply uniform LED light onto the target. This light projects an

image on the CMOS. The experimental test setting is shown in Fig. 5-3.a. A closer view of the contour of the circular hole before and after the experiment is shown in Fig. 5-3.b.

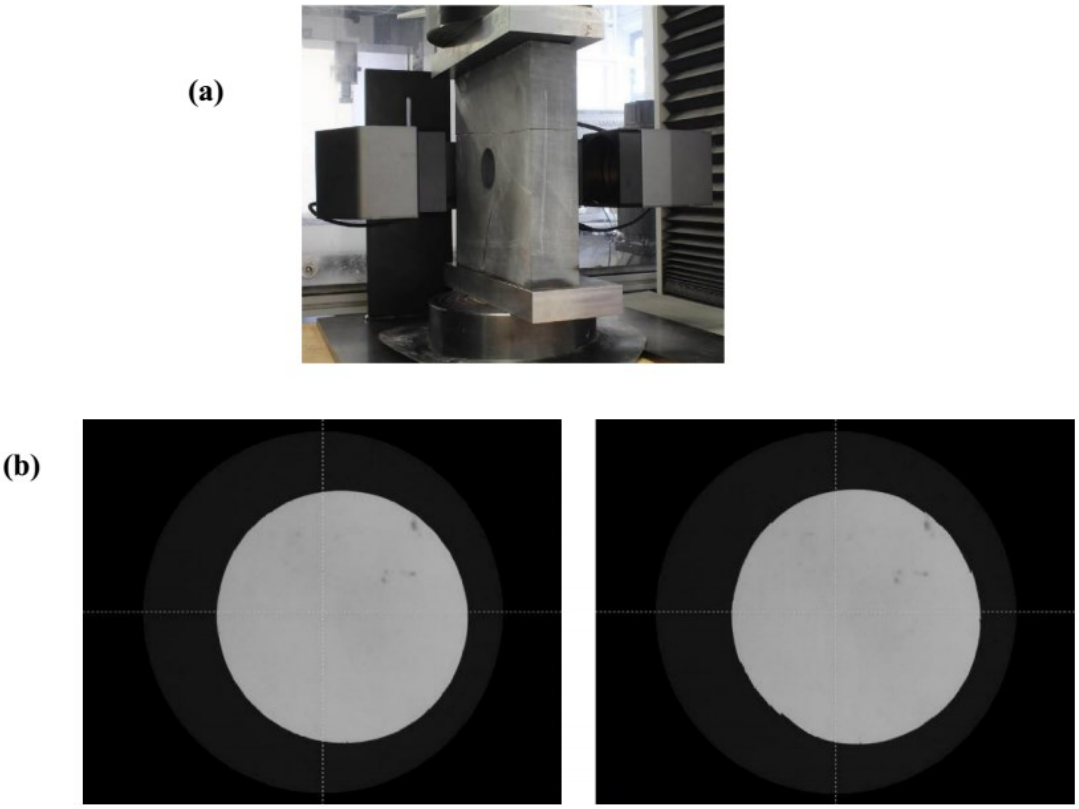

Fig. 5-3 Observation system: (a) Exemplary photo of optical deformation observation system, and (b) Detailed view of the circular opening (left: before loading; right: after the experiment).

5.3.2. Observation results

During the experiment the absolute position of several points along the perimeter was determined every second. As axisymmetric behavior was assumed, the observation was carried out only on one quarter of the perimeter (α = 0° to 90°), see Fig. 5-4.

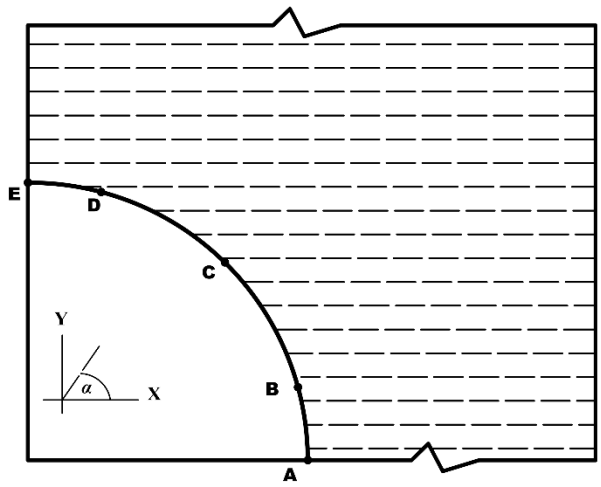

Point no.	Point code	α [°]
1	A	0°
2	B	15°
3	C	45°
4	D	75°
5	E	90°

Fig. 5-4 Locations and angular positions of the observation points

The observed radial deformations of the observations points are shown in Fig. 5-5. The displacements of points D and E (i.e. from $\alpha = 90^o$ to 75°, called crown) are mainly directed toward the center of the hole. For the sidewall, i.e. the springline region according to Hefny and Lo (1999), the behavior should be somewhat different. The radial deformations in the region from point A to point B (i.e. $0^o < \alpha < 15^o$) are nearly constant with only very minor fluctuations. Starting from the loading cycle at $t \approx 9250$ s, the radial deformation pattern significantly changed. This can be best observed in the graphs for points A, B and C in Fig. 5-5 and can be interpreted as an indication of yielding and fracturing occurring along the perimeter.

As previously discussed, the first loading cycle shows pronounced non-linearity which is not considered in the simulation. Thus, the initial point was shifted to the point in time of 800 sec. The variation of the radial deformation confirms an elastic behavior for the first loading cycles, while plastic effects start at 9250 sec (applied load ≈ 315 KN). This is indicated by notable deviations in the radial displacements at point C (i.e. α = 45°). Furthermore, it is observed that the radial deformation at various observation points shows significant softening, especially at points A, B and C, once the plastic behavior has been initiated.

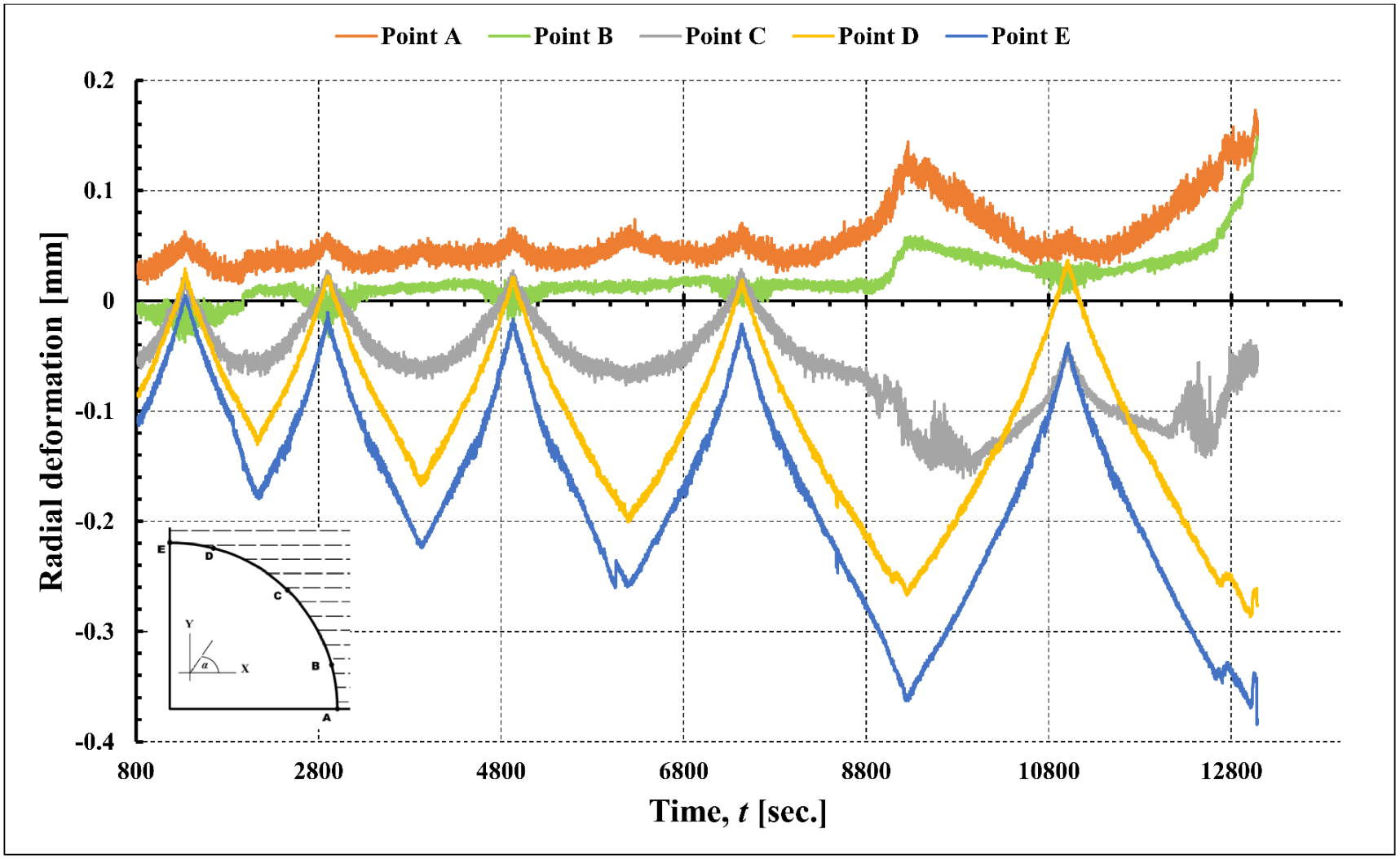

Fig. 5-5 Radial displacements versus time for observation points (minus sign indicates movement toward the centre of the hole)

During the cyclic loading with increasing amplitude, elastic and plastic deformations are observed. In particular, sample 5 shows significant anisotropic behavior not only in strength, but also in stiffness. The deformation behavior for the crown region is significantly different from that in the sidewall region. In other words, for the same applied stress interval ($\Delta\sigma$) a unique strain value ($\Delta\varepsilon$) is not expected for the different observed points along the perimeter, as explained in Fig. 5-6.

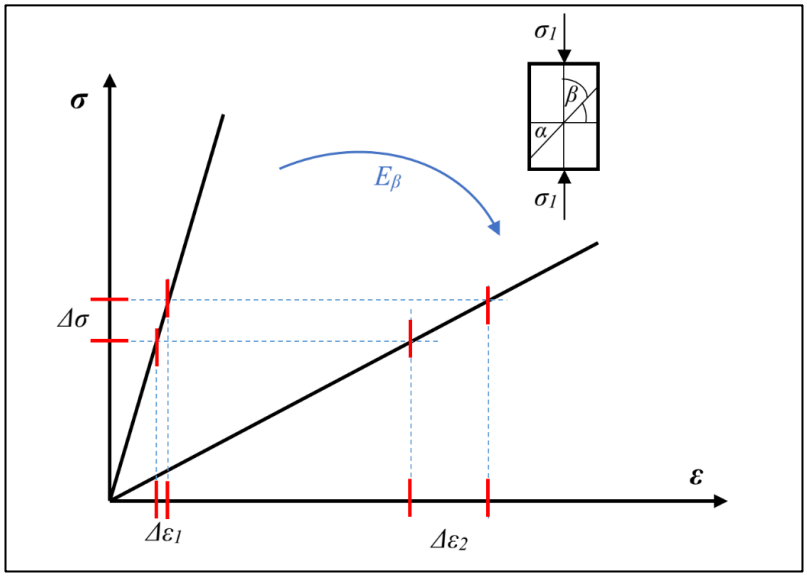

Fig. 5-6 Schematic illustration showing the effect of the stiffness anisotropy, after (Niandou 1994)

For transverse isotropic rock with inclined inherent plane of isotropy with angle β, Pei (2008) introduced Eq. 5.1 to interpret the anisotropic Young's modulus E_β for Chichibu green schist tested by Mogi (2006) based on the work of Amadei (1983).

$$\frac{1}{E_\beta}=\frac{\cos^2\beta}{E}+\frac{\sin^2\beta}{E'}+\frac{\sin^2(2\beta)}{4}\left(\frac{1}{E}+\frac{1}{E'}\right) \qquad (5.1)$$

E and E' are the Young's moduli in direction parallel and normal to the inherent anisotropy plane. The elastic anisotropy of inherent laminated rocks could be quantified by an index defined in Eq. 5.2 according to Amadei et al. (1987).

$$k=\frac{E}{E'} \qquad (5.2)$$

The value of k for most anisotropic rocks is usually between 1 to 4 (Lisjak et al. 2014), which fits well with the experimental testing for shale samples by Gholami and Rasouli (2014). Also,

the conducted experiments on Yeoncheon schist performed by Park and Min (2015) show that elastic stiffness anisotropy is app. 4.

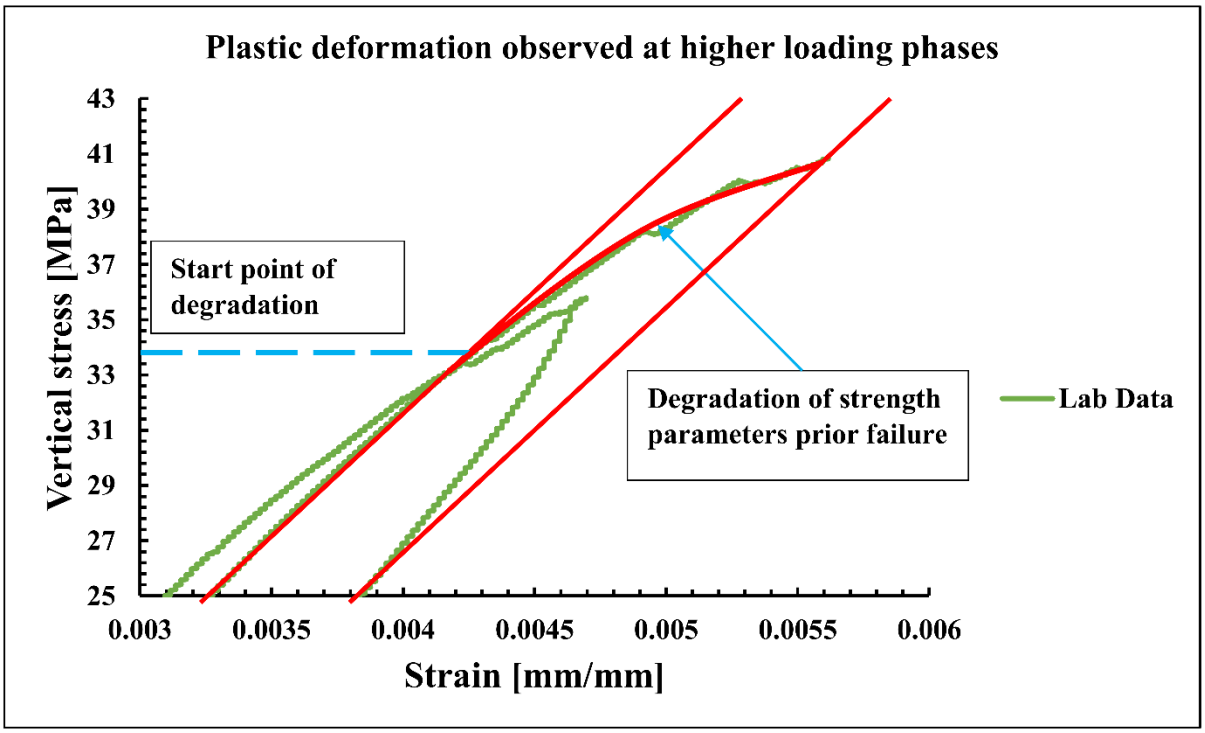

Fig. 5-7 Stress-strain curve of the tested sample at higher loading stages till failure point.

There is a noticeable change in the inclination of the stress-strain curve at the higher loading levels as documented in Fig. 5-7. This feature can be explained by the plasticity theory considering residual or softening parameters (Zhang et al. 2012; Cui et al. 2017). Consequently, the numerical simulation of such lab test needs the consideration of strength anisotropy and stiffness anisotropy which demands the framework of an anisotropic elasto-plastic constitutive model with strain softening.

5.4. Material parameters

The tested roof slate from the Sauerland region in the west of Germany is a fine grained slate with remarkable anisotropy (Braun, 2012; Brenne et al., 2014). The mechanical anisotropy of this slate has been investigated by Braun (2012) via uniaxial tests with orientation intervals of 15°. Berwanger and Helms (1993) performed loading tests on samples with three different orientations (β = 0°, 45° and 90°). Mechanical investigations of the same shale type have been performed by Haumann (2016) with different loading angles (β = 0°, 30° and 90°). On the other hand, material parameters were obtained from lab testing conducted on Mayen Mosel-Slate by (Tan et al. 2015; Dinh 2011). This slate has similar mechanical behavior as the tested slate (strain softening behavior). Fig. 5-8 shows the uniaxial compressive strength (UCS) and elastic modulus (E) for different loading angles (β) including the error bars for the UCS lab values.

The ratio of the elastic anisotropy, defined in Eq. 5.2, equals 3.55 (19.5/5.5) which indicates a very high stiffness anisotropy.

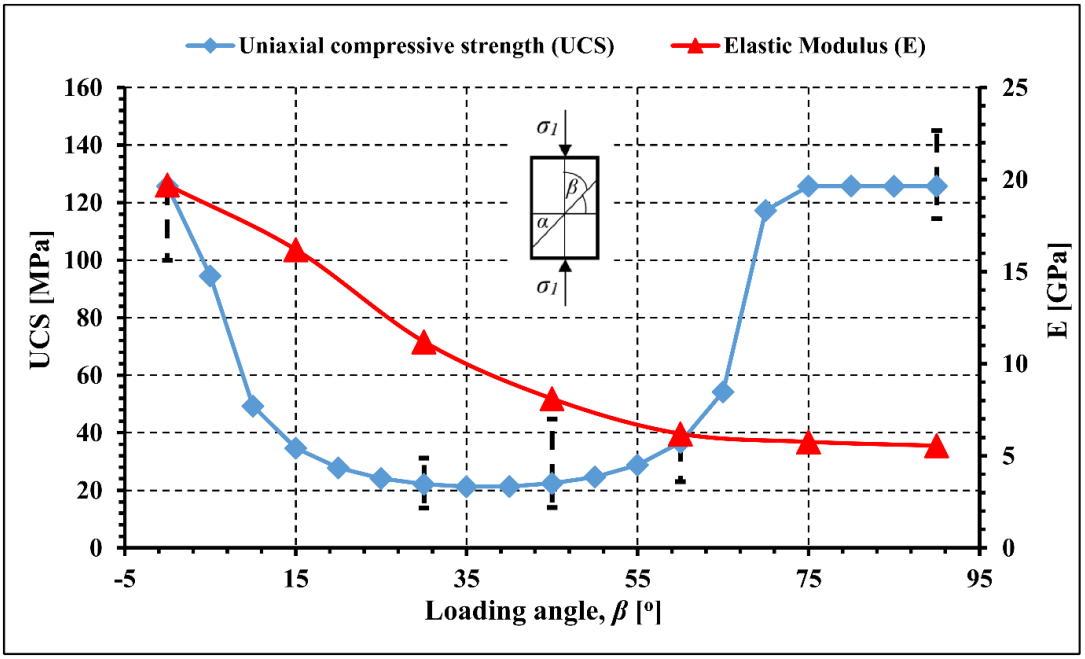

Fig. 5-8 Plotted numerical values of UCS incl. error bars and the numerical elastic modulus (E) vs. the loading angle (β), after Brenne et al. (2014) and Haumann (2016)

According to Ramamurthy (1993) and based on the data shown in Fig. 5-8, the strength anisotropy Rc varies between 2.5 and 6. For this slate, Rc covers a range between 6 to 9 which indicates a very high anisotropy in strength. Within this paper it is assumed that Rc equals 5.9 (125.7/21.3) as σ_{min} is found at $\beta = 30^{o}$. The numerical simulation of the uniaxial compressive strength shows the following pattern: concave upwards [$\beta = 10^{o} - 60^{o}$] referring to sliding failure mode and shoulder type for non-sliding failure mode [$\beta = 0^{o}, 75^{o} - 90^{o}$]. Average value of UCS for both shoulders is no equal according to lab results: UCS_{90} is about 135 MPa and UCS_{0} is about 110 MPa (Fig. 5-8).

The input properties used in the numerical simulations are averaged based on previous testing (Braun 2012; Berwanger and Helms 1993; Haumann 2016). Missing properties have been reasonably assumed and were calibrated in the numerical models. The finally assigned properties are summarized in Table 5-2. The behavior of the tested slate is assumed to be elasto -plastic with softening for rock matrix and joint plane. For the rock matrix, softening for cohesion, friction angle and tensile strength is proposed, while the softening for joint plane is implemented only for the shear parameters (c_j and ϕ_{fj}).

Table 5-2 Mechanical input parameters for numerical simulations

Parameter	Value
Bulk density, ρ [kg/m^3]	2760
Elastic components	
E [GPa]	19.5
E' [GPa]	5.5
ν [-]	0.1
ν' [-]	0.05
G' [GPa]	3.5
Rock matrix	
σ^t [MPa]	12.5
c [MPa]	23.5
φ_f [°]	49
$\sigma^{t,res}$ [MPa]	9.5
c^{res} [MPa]	19
φ_f^{res} [°]	45
ψ [°]	10
Joint planes	
σ_j^t [MPa]	4.0
c_j [MPa]	8.0
φ_{fj} [°]	16
c_j^{res} [MPa]	4.0
φ_{fj}^{res} [°]	15
ψ_j [°]	0
Angle of inclination, α [°]	0

The tensile strength of the rock matrix (σ^t) is about 10% of the defined maximum UCS as shown in Fig. 5-8. The maximum UCS on the bedding planes varies between 14 to 45 MPa. Thus, the applied values for the joint plane tensile strength (σ_j^t) is 4.0 MPa, which is almost 13% of the average UCS observed at $\beta = 45^o$ (Fig. 5-8). Generally, it is found from literature that there is a remarkable variation in the measured properties of tested slates, therefore most of the assigned parameters in Table 5-2 have been checked by numerical back analysis.

As previously mentioned, slight softening behavior is noticed for the slates in the post yielding region. The mobilization of the strength parameters for rock matrix and the joint plane are defined manually in respect to the plastic strain (i.e. e^p). Fig. 5-9 shows the applied mobilization of the strength parameters. The strength mobilization functions were calibrated to duplicate the same degradation as shown in Fig. 5-7.

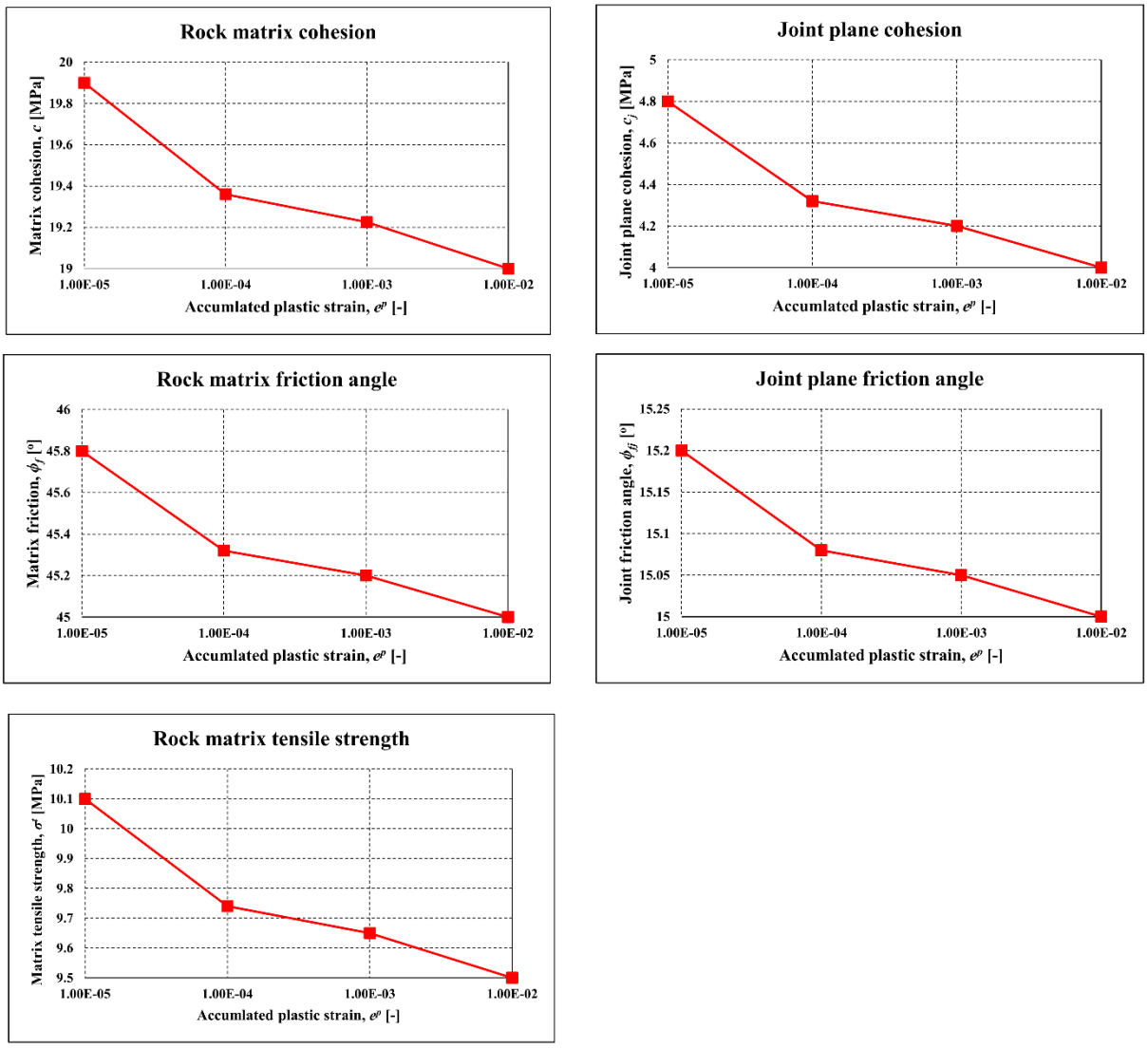

Fig. 5-9 Mobilization of the strength parameters for matrix and joint versus plastic strain

5.5. Numerical simulations

5.5.1. Model setup

Different constitutive models are used to duplicate the lab experiment: the developed constitutive model (Transubi), the transverse isotropic elastic model (Elastic) and the original ubiquitous joint model (Ubi model). This comparison documents the capability of the Transubi model to overcome some problems of different existing anisotropic constitutive models to reproduce the lab measurements.

Model geometry and loading pattern (Fig. 5-1 and Fig. 5-2) as well as the mesh (Fig. 5-10) for simulations using different constitutive models are identical. A full model with circular hole is chosen. The grid is formed by radial zoning with square outer boundaries. The model consists of 7200 (60 x 120) trapezoid-shaped zones. The mesh is coarse at the boundaries and very fine

close to the hole. The hole perimeter is discretized into 120 equal segment (gridpoint very 3°). Moreover, the radial mesh structure allows a detailed observation of the deformation acting on the perimeter. In order to simulate the incremental load on both sides of the sample, velocity in the y-direction is applied along the location of both loading plates, see Fig. 5-1.

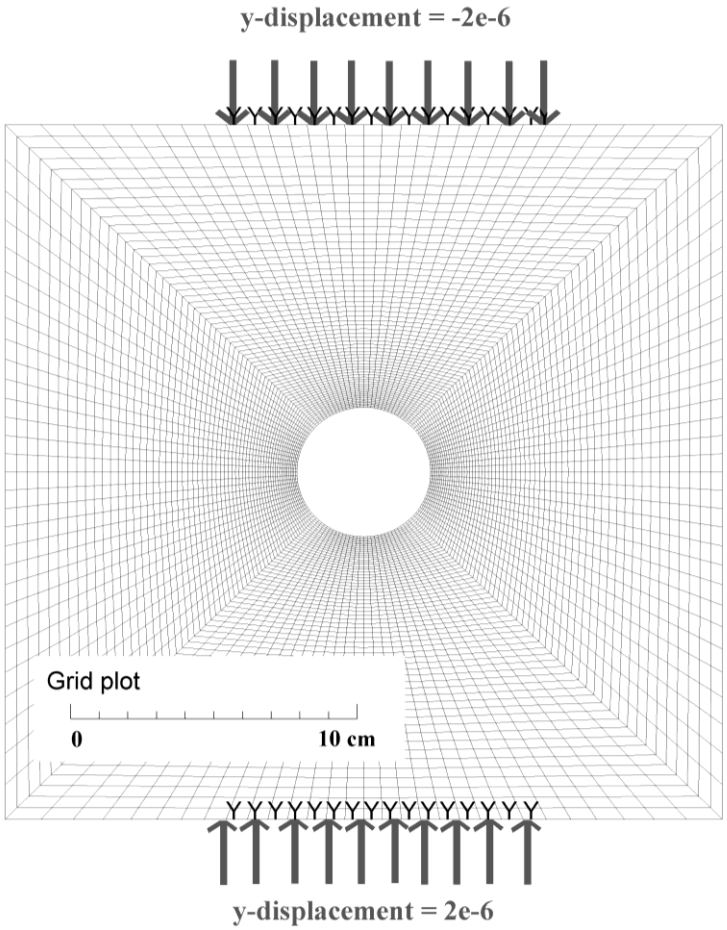

Fig. 5-10 Numerical model set-up incl. boundary conditions

For the simulation with the Transubi model, material parameters given in Table 5-2 are used. For the pure transverse isotropic elastic simulations only the elastic parameters are used. For the ubiquitous joint model average values are used for Young's modulus (E = 15.5 GPa) and Poisson ratio (ν = 0.1), otherwise plastic parameters according to Table 5-2 are used. Different history points (same as in the experiments, see Fig. 5-4) were placed at the perimeter of the opening in order to record the displacements. All the loading and unloading phases performed in the experiment were duplicated by the numerical modeling. The relatively large calculation time required by the Transubi model (4 times greater than using the ubiquitous joint model) is due to the complexity of the used constitutive model. Fig. 5-11 shows the vertical applied stress

versus the axial strain for the lab data and different modeling approaches. Simulation results are given based on the model shown in Fig. 5-10. The mechanical parameters are presented in Table 5-2 and the applied mobilization for the strength parameters of the Transubi simulation is shown in Fig. 5-9.

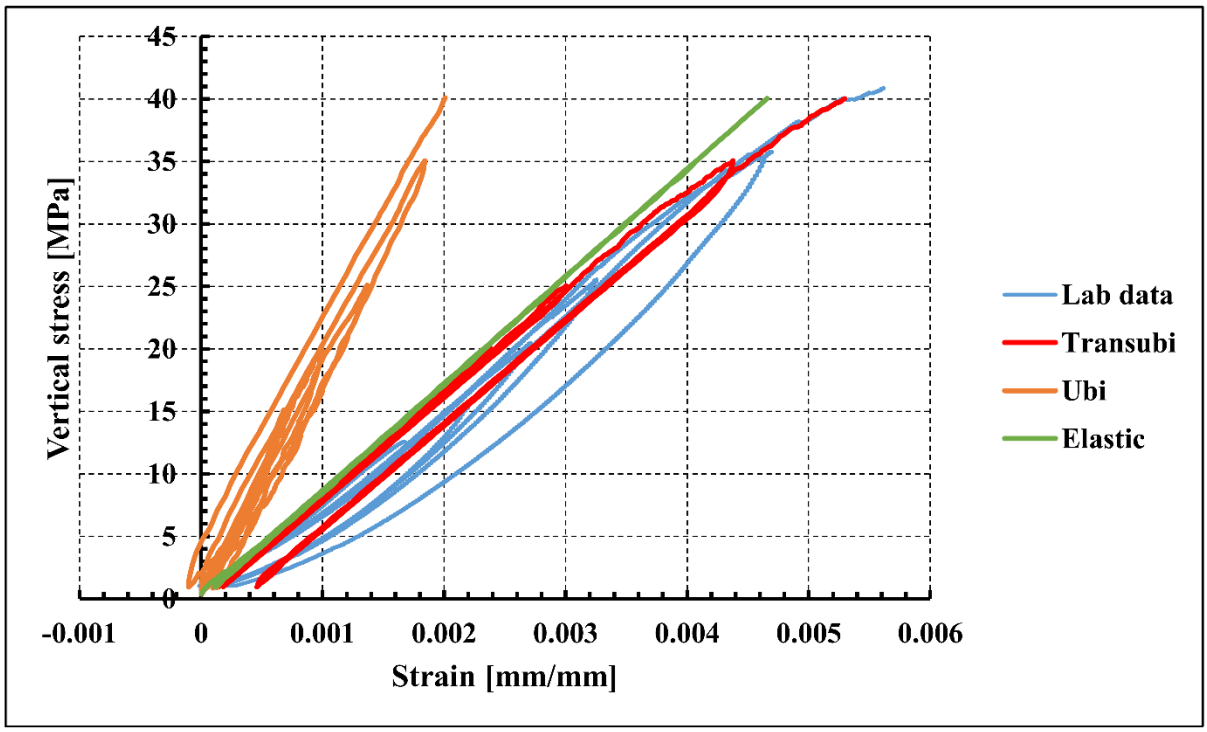

Fig. 5-11 Vertical stress versus axial strain of the tested sample: numerical simulations using Transubi, Elastic and Ubi models vs. lab data

5.5.2. Simulation of strength and stiffness anisotropy

Fig. 5-12 and Fig. 5-13 present the comparison between the numerical simulation results and the lab experiments for 5 observation points located along the periphery of the circular hole. As expected, the Ubi model tends to overestimate the radial deformation for the sidewall region: points A, B and C (i.e. $\alpha = 0^o - 45^o$) (Fig. 5-12). The numerical simulation using the Transubi model is able to duplicate both, the elastic and plastic deformations observed during the lab experiment. The elastic stiffness anisotropy is responsible for a remarkable change in the behavior of the radial deformations (Δr) at each observation point. On the other hand, the plastic behavior has been also captured by the numerical simulation which begins in the fifth loading cycle at around $F_y = 315$ kN (i.e. after time = 8800 sec of loading, Fig. 5-2). As shown in Fig. 5-12, the transition from expansion to contraction of the opening diameter begins at point C (i.e. $\alpha = 45^o$) which could not be captured by the Ubi model as well. Furthermore, the

radial deformations at the crown, points D and E, are underestimated by the Ubi model in reference to the lab observations (Fig. 5-13).

On the other side, the elastic anisotropic model is able to duplicate the general trend detected during the lab test. However, the elastic approach leads to a significant underestimation of the final displacement values and cannot show the progressive deformations due to the yielding of the sample at last loading stages. During the cyclic loading significant yielding occurs especially close to the boundary of the opening which is responsible for the sample failure and remarkable increase in radial deformations. In general, the numerical simulation using the Transubi model is able to predict the final displacements along the opening's perimeter and the overall trend of radial deformation during all phases of loading and unloading. Within the last unloading path, a significant distortion in the radial deformation is noticed which marks the formation of a main crack, noticed at point C (Fig. 5-12). The numerical simulation explains this distortion by sudden loss of the rock strength (tensile and shear). Generally, the Transubi model can capture the strength and stiffness anisotropy based on the elasto-plastic theory quite well, whereas both, the Ubi and transverse-isotropic model show significant deviations from the lab observations because they only consider one type of anisotropy, either stiffness or strength anisotropy.

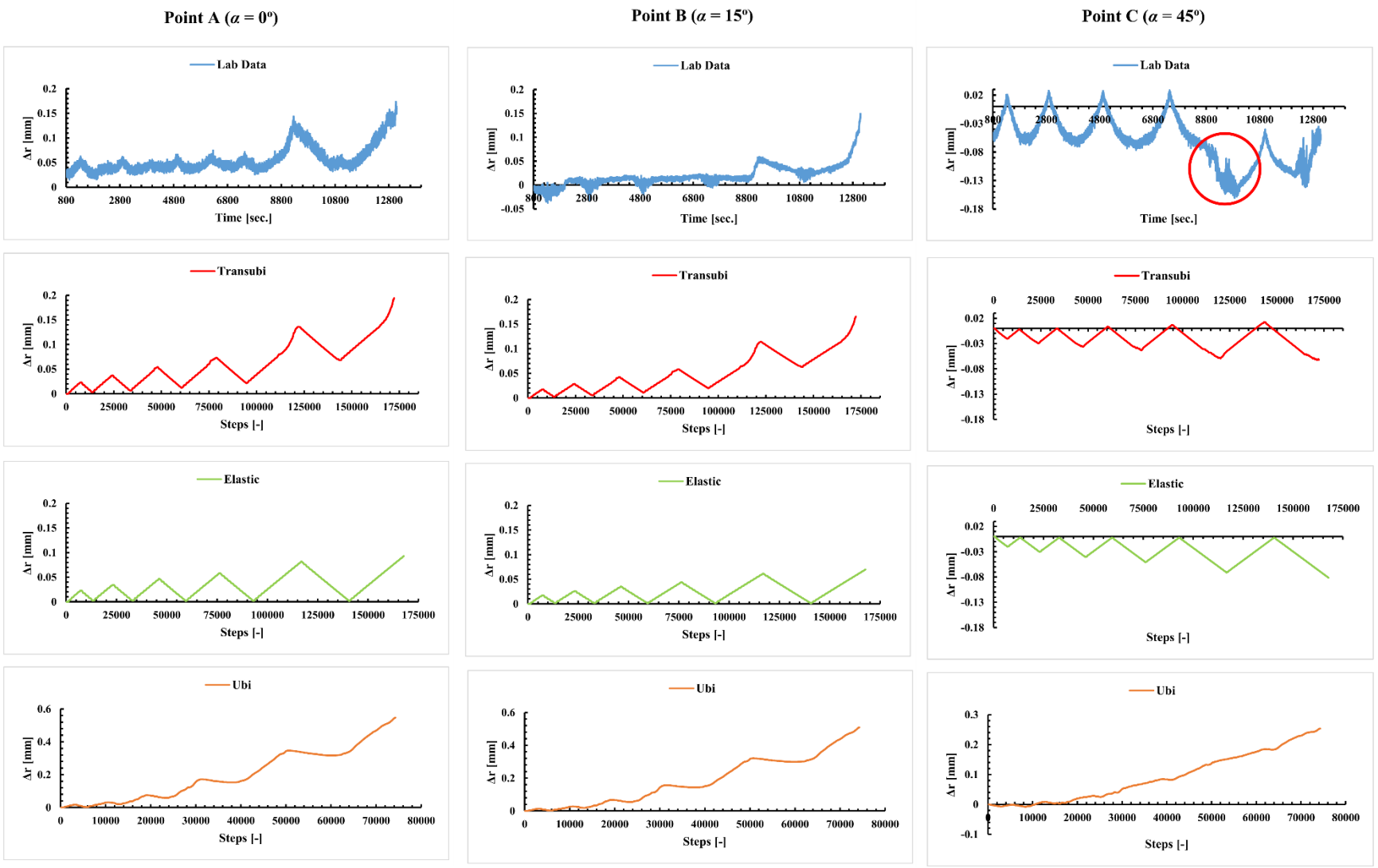

Fig. 5-12 Comparison of the radial deformation evolution (Transubi, Elastic and Ubi models) vs. lab data for 3 observation points A, B and C. At point C, there is an excessive failure notice during lab test (circled in red).

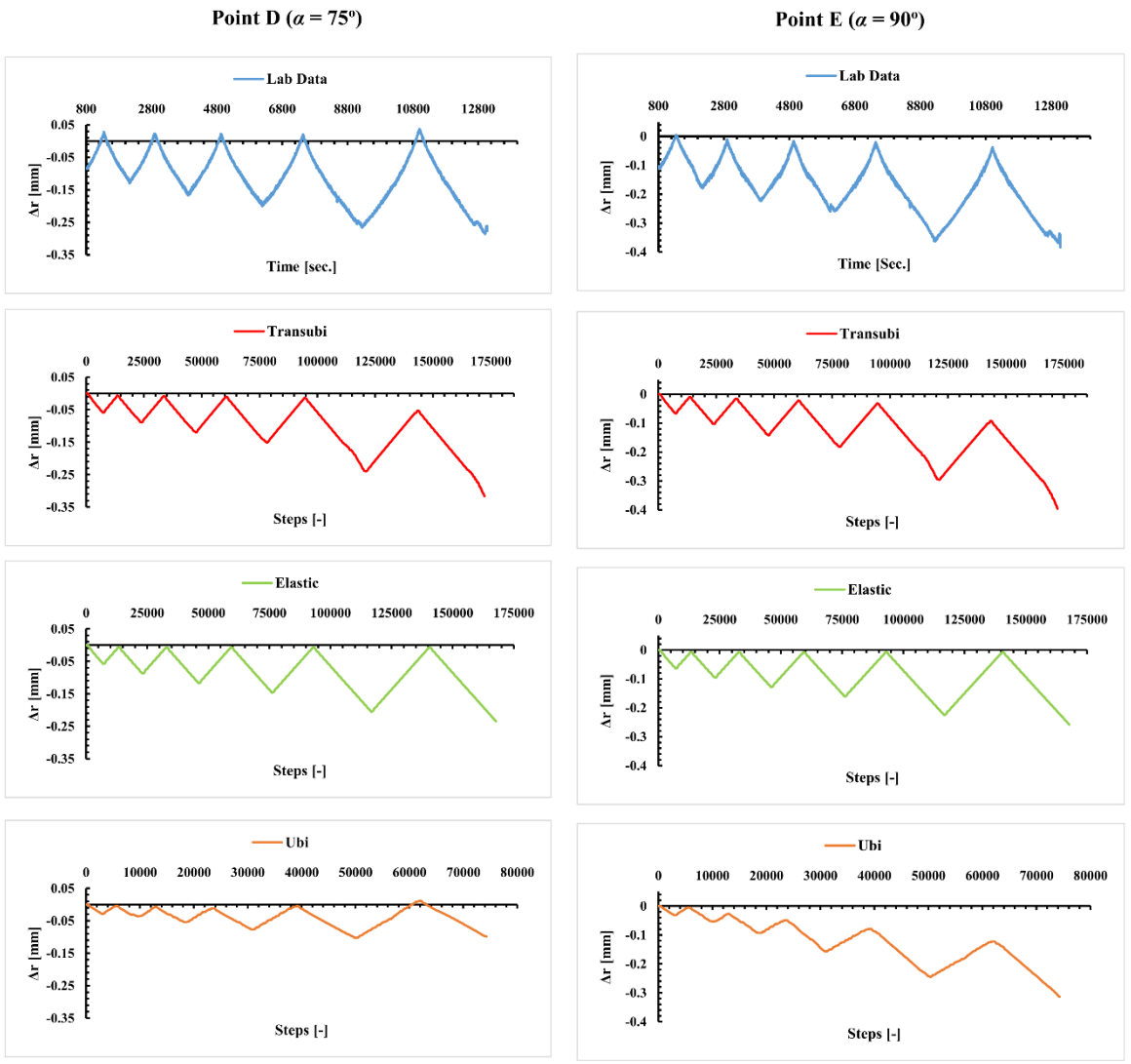

Fig. 5-13 Comparison of the radial deformation evolution (Transubi, Elastic and Ubi models) vs. lab data for 2 observation points D and E.

The final radial displacements along the opening perimeter for different constitutive models are shown in Fig. 5-14 in comparison with the lab data. Both, the Transubi and the linear elastic models show much better agreement with the lab test data compared to the Ubi model. However, a severe under-prediction is observed (at points B and C) using the transverse-isotropic elastic model: maximum expansion of sidewalls of +0.093 mm (total difference of -42% compared to lab measurements) and an average contraction at the crown with about -0.258 mm (total difference of -33% compared to lab measurements). At the side wall, the Ubi model overestimates the expansion of the hole. The predicted deformation by the Ubi model at $\alpha = 0^{o}$ is about three times the value predicted by the Transubi model and the value measured in the lab, although a relative high elastic modulus has been given (i.e. greater than average). This overestimation in the sidewall deformation is due to the elastic isotropic assumption (i.e. $E_{//} = 19.5$ MPa and $E_{\perp} = 5.5$ MPa while given E value for Ubi = 15.5 MPa). The transition zone where the hole deformation switches from expansion to contraction is predicted quite well by the Transubi and elastic model ($\alpha \approx 30^{o}$ - 35^{o}). The numerical simulation using the Ubi model underestimates the contraction due to the lack of stiffness anisotropy.

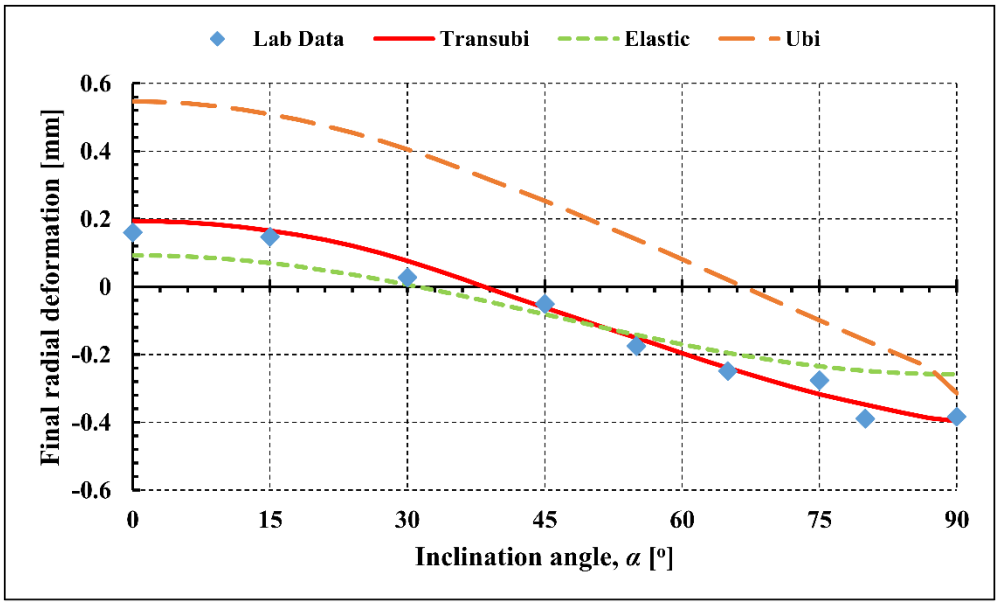

Fig. 5-14 Final radial deformation versus angle of inclination α: numerical simulations and experimental measurement (+: expansion of hole)

According to Fig. 5-15, the total displacement pattern for both Transubi (Fig. 5-15.a) and linear elastic model (Fig. 5-15.b) is sand-clock shaped, similar to the findings by Lisjak et al. (2014). The maximum displacements occur at the crown, while the displacements reach their minimum at the sidewalls due to two reasons: (i) the local perturbation in the stress field near to the hole, and (ii) the elastic anisotropy (i.e. elastic modulus normal to loading direction is greater than parallel to loading). On the other side, the Ubi model tends to overestimate the displacements at the sidewalls (Fig. 5-15.c).

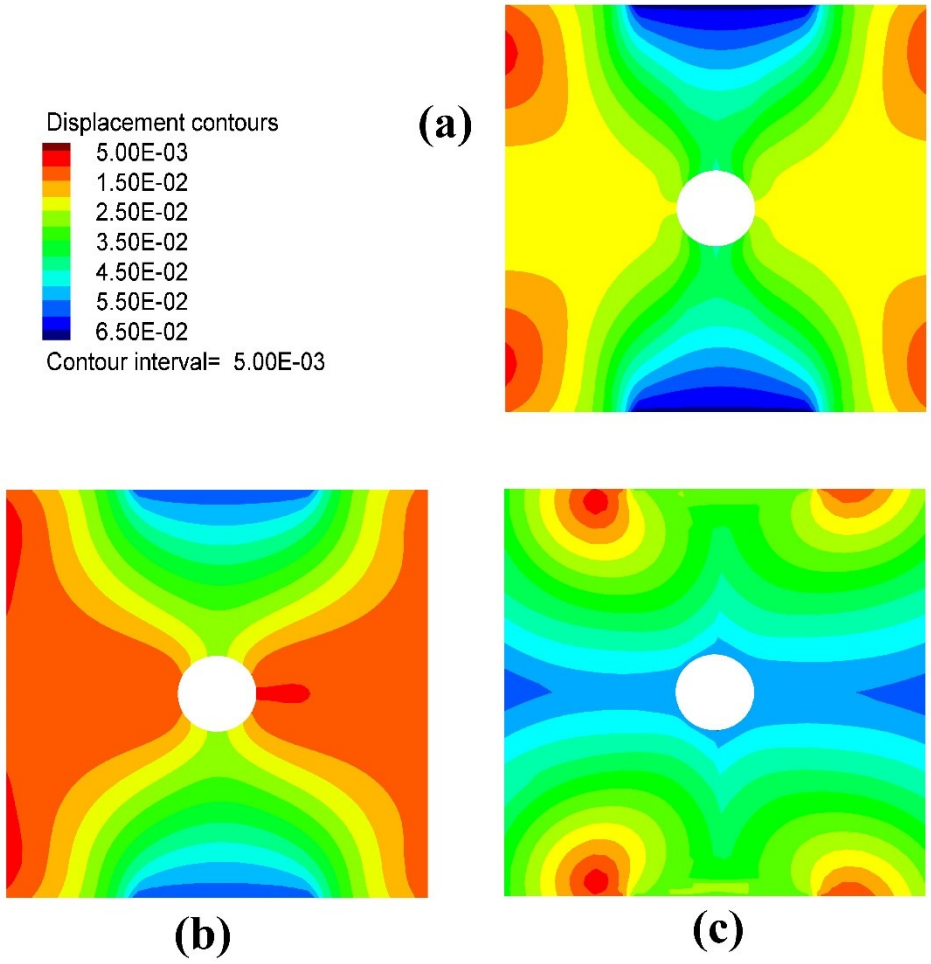

Fig. 5-15 Final total displacement contours [cm]: (a) Transubi model, (b) linear elastic transverse-isotropic model, and (c) Ubi model.

5.5.3. Failure modes detected during elasto-plastic simulations

Three different loading stages are used to compare the generated failure modes in detail for the Transubi and Ubi model (F_y = 150 kN, 350 kN and final load stage 400 kN). Based on the lab

observations, there are two different types of failure noticed around the opening during the test. Damage starts with tensile fracture propagation at the crown (i.e. point E) followed by mixed-mode cracking in zigzag form: tensile cracking interrupted by shear failure along the schistosity planes. Fig. 5-16 shows the progress of the RM failure at the end of the second loading stage (i.e. $F_y \approx 150$ KN) around the hole (invert and crown points) for Transubi and Ubi models.

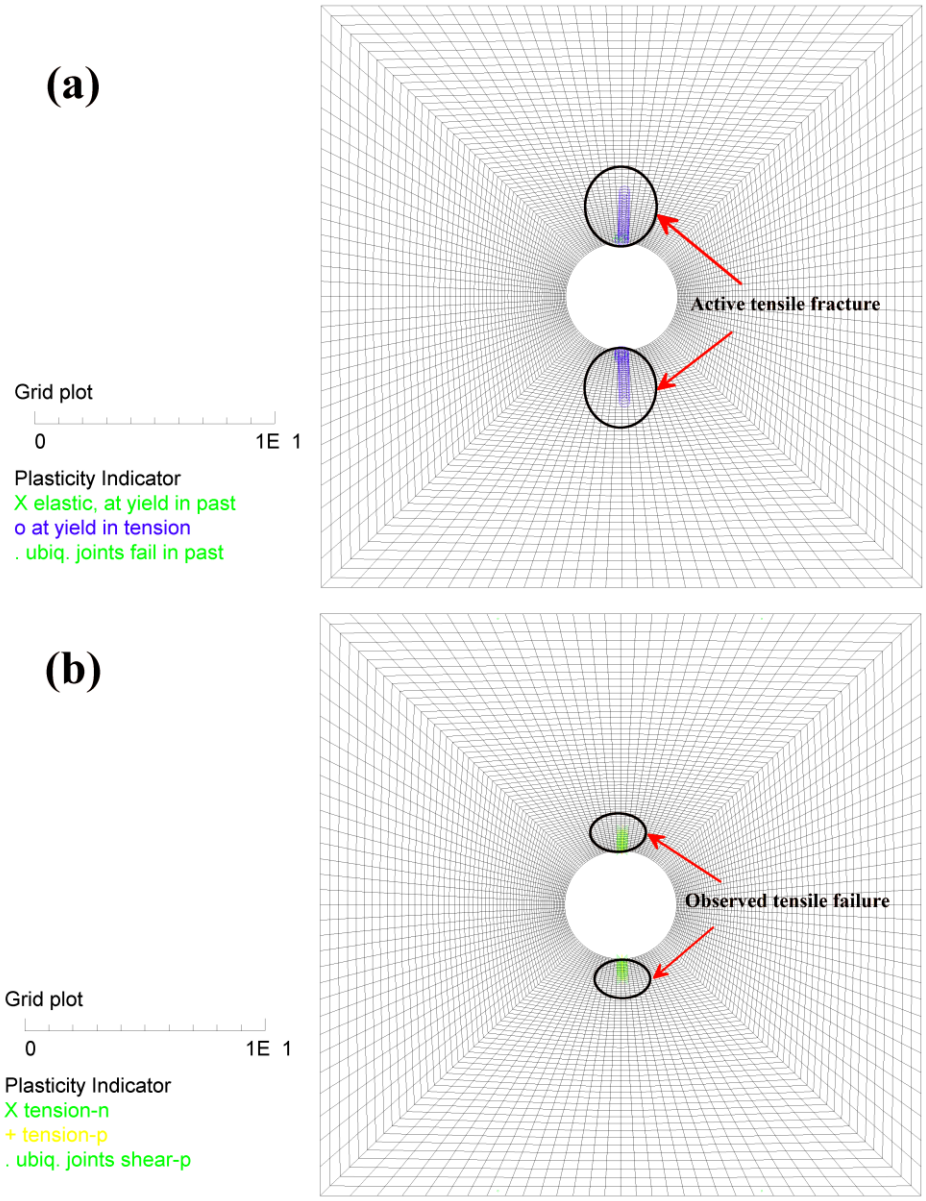

Fig. 5-16 Plasticity indicators at the end of the second loading stage (F_y = 150 KN) showing the development of the rock matrix tensile failure at the crown region for (a) Ubi model and (b) Transubi model (grid plotted in cm).

With increasing applied load, the yield zone around the hole has extended. As noticed in Fig. 5-5, the measurements of the radial displacement have been disturbed at $F_y \approx 327$ KN especially at point C (i.e. $\alpha \approx 45^o$). The lab observations show that the main fracture is continuously growing, but slightly deviated towards the corners of the slate block. Also, different fractures have been noticed at the corners (i.e. $15^o < \alpha < 65^o$) as indication of shear failure which fits with the numerical simulations using the Transubi model (Fig. 5-17). In contrast, the Ubi model predicts more or less only one single vertical tensile fracture.

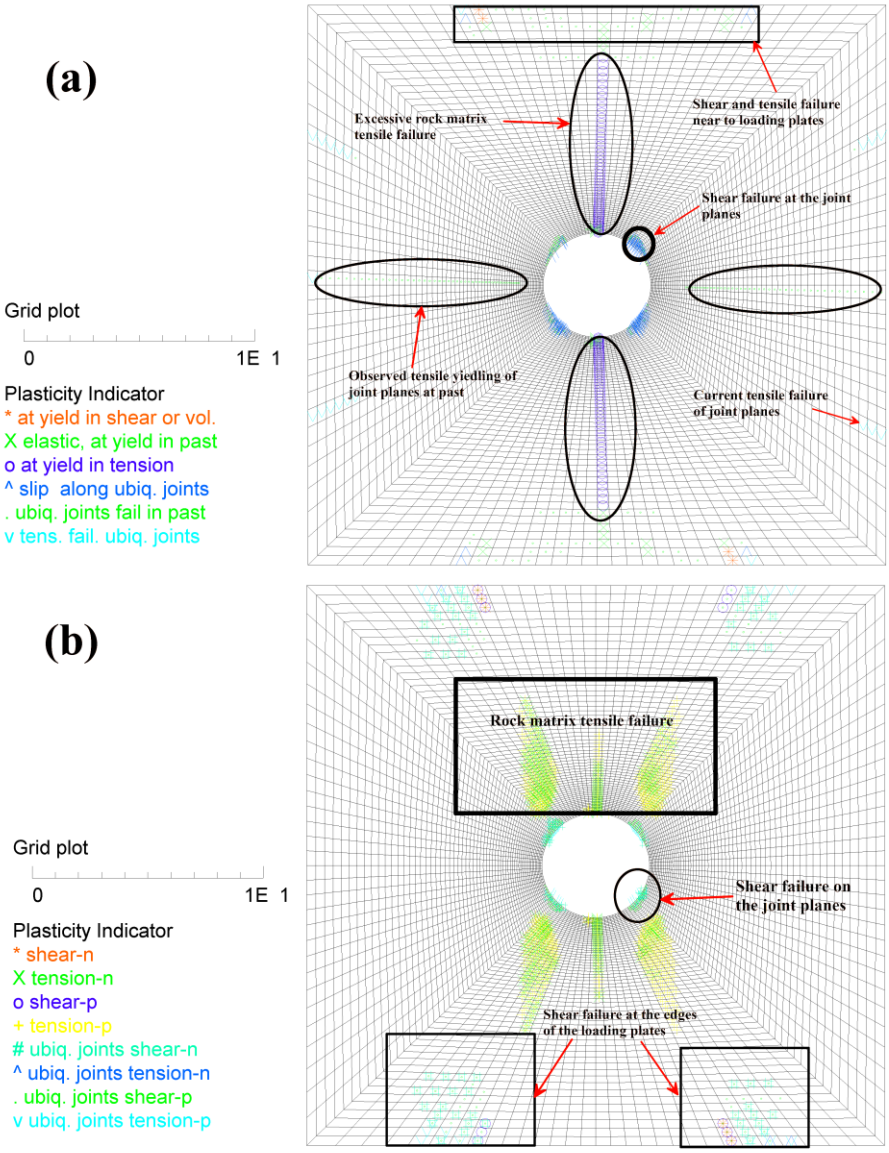

Fig. 5-17 Plasticity indicators at the end of the fifth loading stage ($F_y = 350$ KN) showing the development of the failure modes for (a) Ubi model and (b) Transubi model (grid plotted in cm).

In general, the Transubi model can duplicate the main damage features observed during the lab test (compare the lab observations shown in Fig. 5-20 and Fig. 5-19 against Fig. 5-16, Fig. 5-17 and Fig. 5-18), which is not the case for the Ubi model. However, a continuum-based modelling technique cannot capture the fracture mechanisms in detail. Therefore, discontinuum-based approaches are recommended if fracture evolution should be investigated in detail.

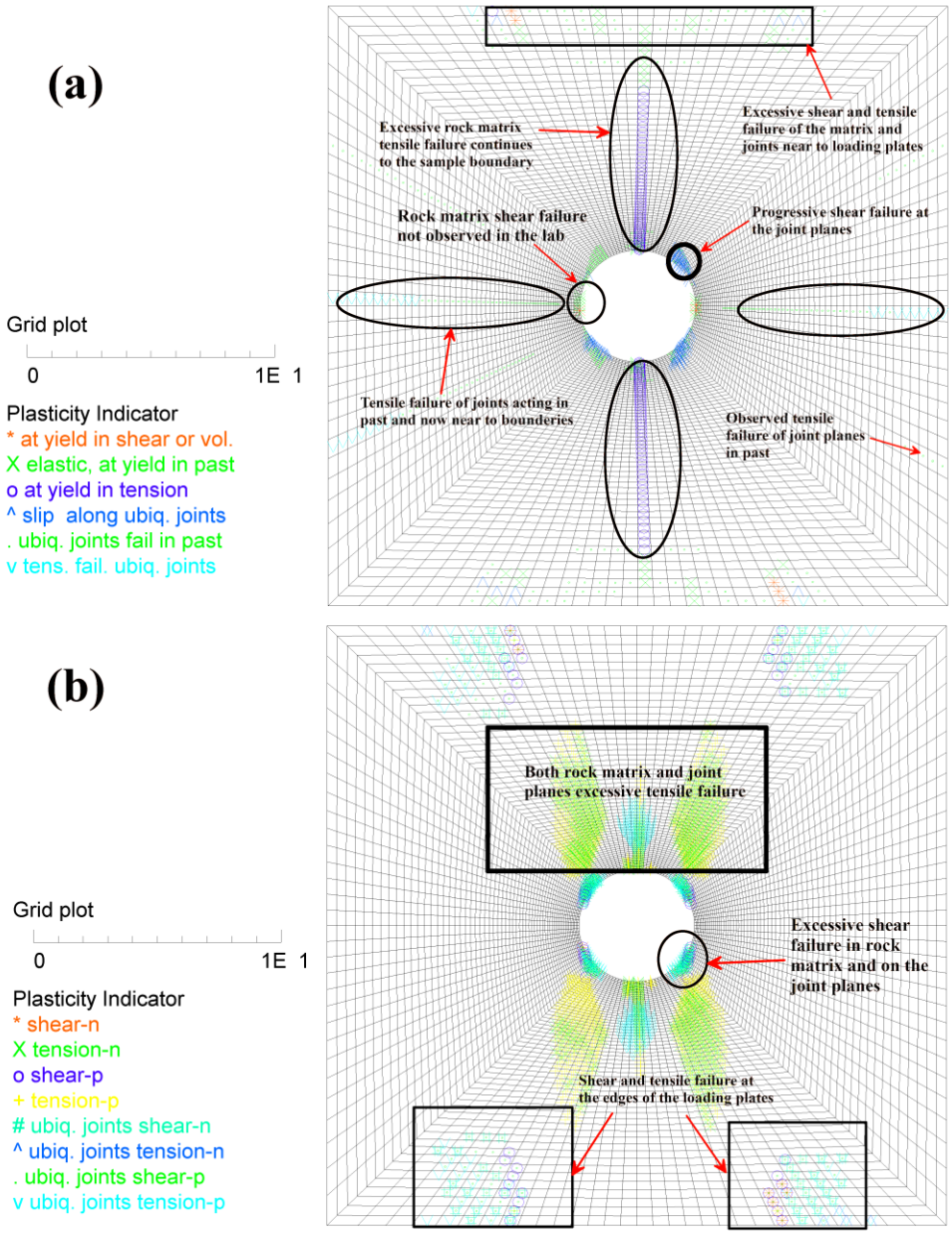

Fig. 5-18 Plasticity indicators at final loading stage (F_y = 400 KN) showing the development of the failure modes around the opening for (a) Ubi model and (b) Transubi model (grid plotted in cm).

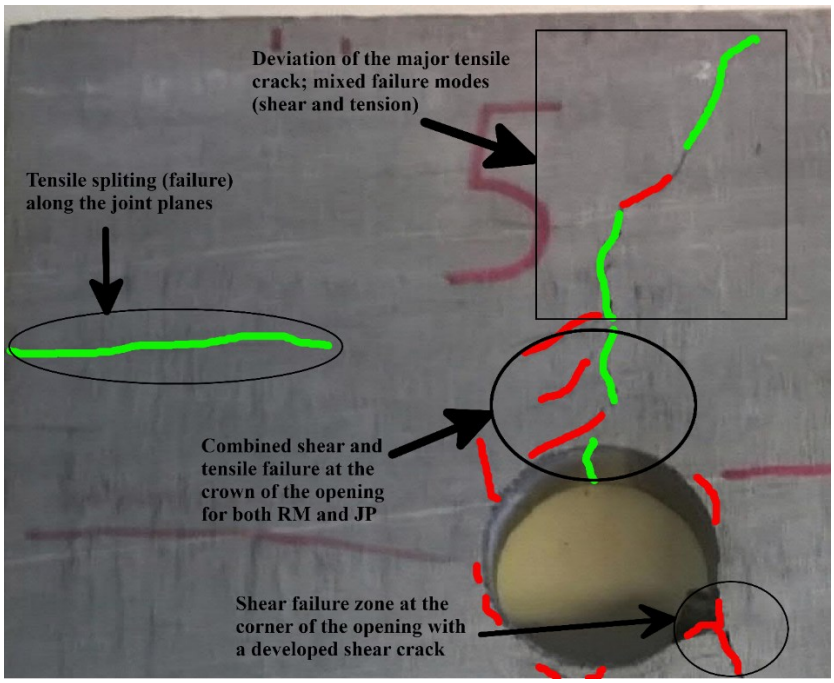

Fig. 5-19 Sample front side: fracture pattern observed around the opening at the end of the test. Red lines correspond the shear (inclined) cracks and green ones represent the tensile (splitting) cracks.

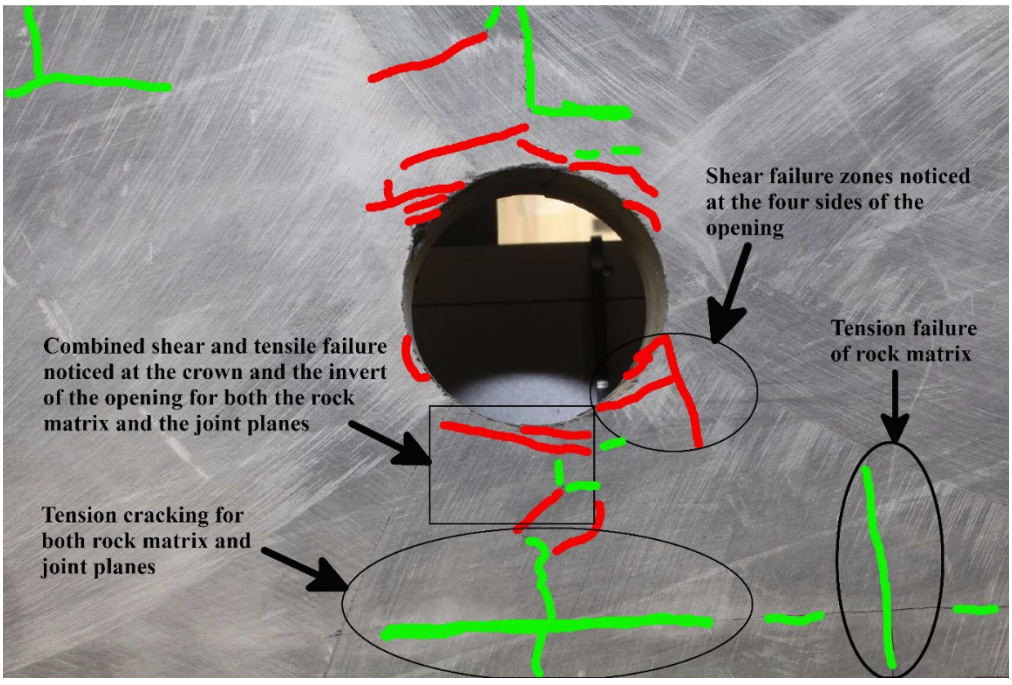

Fig. 5-20 Sample back side: fracture pattern observed around the opening at the end of the test. Red lines correspond the shear (inclined) cracks and green ones represent the tensile (splitting) cracks.

5.6. Conclusions

Different elastic and elasto-plastic constitutive models were applied to back analyze a lab test (slate block with hole under quasi-static cyclic loading up to failure). It is shown, that both - stiffness and strength anisotropy – have to be considered to reproduce the observed deformation and damage behavior. A pure transverse elastic model is able to reproduce the general trends, but is not able to duplicate the non-linearites at higher load levels or accumulated damage and consequently under-predicts the displacements. Elasto-plastic models without considering the elastic stiffness anisotropy are unable to reproduce the significant anisotropic deformation behavior, which can even lead to a wrong prediction of deformation trends. The proposed Transubi model covers stiffness as well as strength anisotropy and has shown good agreement with the lab results in a quantitative and qualitative manner.

At different loading stages, the evolution of the failure around the circular opening displays variations between the Transubi and the Ubi models. The Transubi model can simulate the main failure pattern detected within the experiment. This is only true to some extend for Ubi model. Nevertheless, discontinuum-based approaches are better suited to simulate fracture propagation in detail.

6. Mechanical response of excavations in Opalinus clay

6.1. Introduction

Based on the mechanical behavior of the Opalinus clay described in chapter 4, deformations around a tunnel excavated in Opalinus clay are analyzed by numerical simulations. This tunnel is driven in a shaly facies formation of Opalinus clay in an URL. Short-term stability of the tunnel is considered as part of a long-term research project (Full-scale Emplacement (FE) experiment). The numerical simulation considers a shotcrete-supported 3-m diameter tunnel. The deformational behavior is compared with data from in-situ measurements (Lisjak et al. 2015). The tunnel is excavated steadily, while the lining is installed in certain steps. The FE tunnel was equipped with differed instrumentation providing several data sets. The model considers pore pressure, but water flow is not allowed. A sensitivity analysis is conducted to study both, the influence of grid structure and the effect of sudden excavation on the displacements and the pore pressure development around the tunnel.

6.2. Tunneling in strain softened rock mass

The difficulty associated with strain softened rock masses is that these materials are defined as highly deformable and they behave as low-modulus medium (Duncan Fama 1993). During tunnel excavation, the strength parameters would gradually drop to their residual values at the tunnel periphery causing a weakness zone around the formed opening (Ranjbarnia et al. 2015). Fig. 6-1 illustrates the responses of a circular tunnel driven in elasto-plastic media under hydrostatic in-situ stress (Cui et al. 2017). As indicated in Fig. 6-1.b, the slope of the decreasing part of the stress-strain curve (i.e. the softening rate) plays the most significant role for the stability of the tunnel walls (Egger 2000). Based on the softening rate, the evolution of the residual zone is identified and therefore the critical time to install the tunnel support system is obtained. The higher the softening rate the higher the required support pressure, as indicated in Fig. 6-2 (Egger 2000).

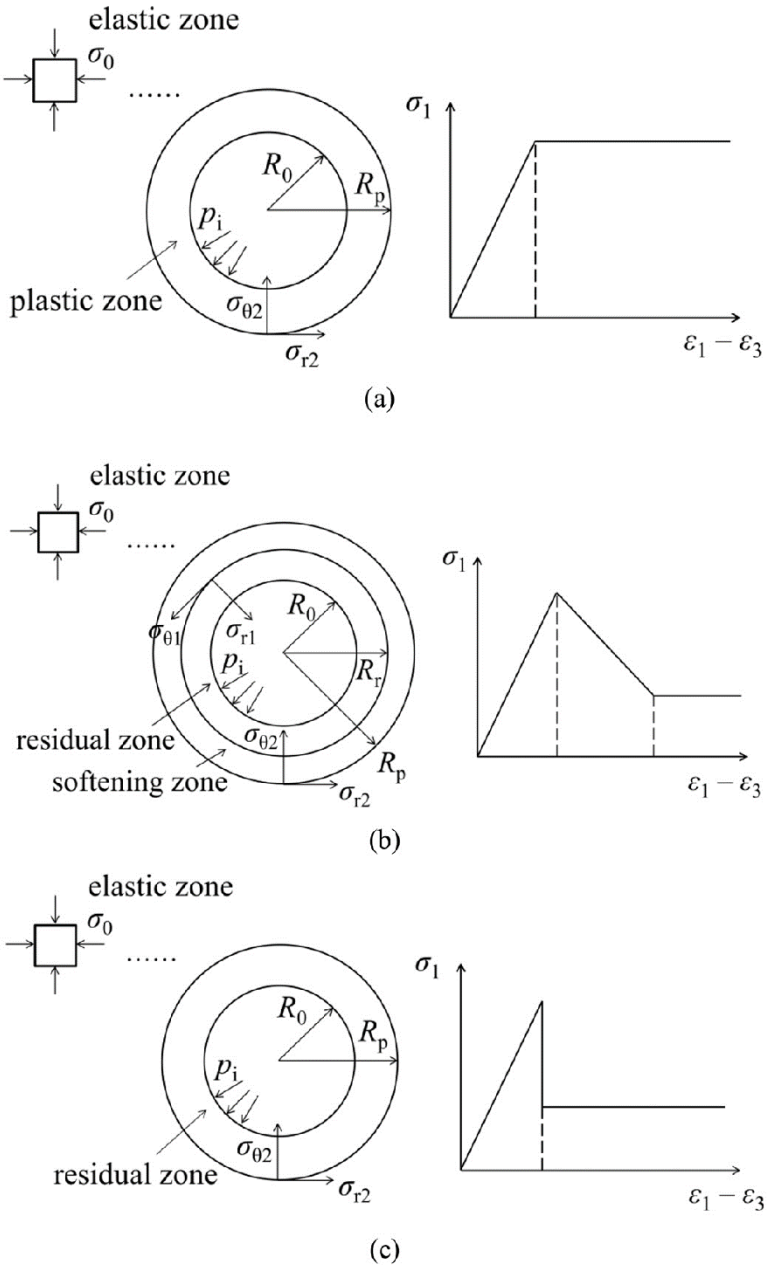

Fig. 6-1: Schematic illustration of formed weakness zones around a circular opening in (a) linear elastic, (b) plastic strain softening, and (c) brittle plastic materials under hydrostatic institu stress conditions (Cui et al. 2017).

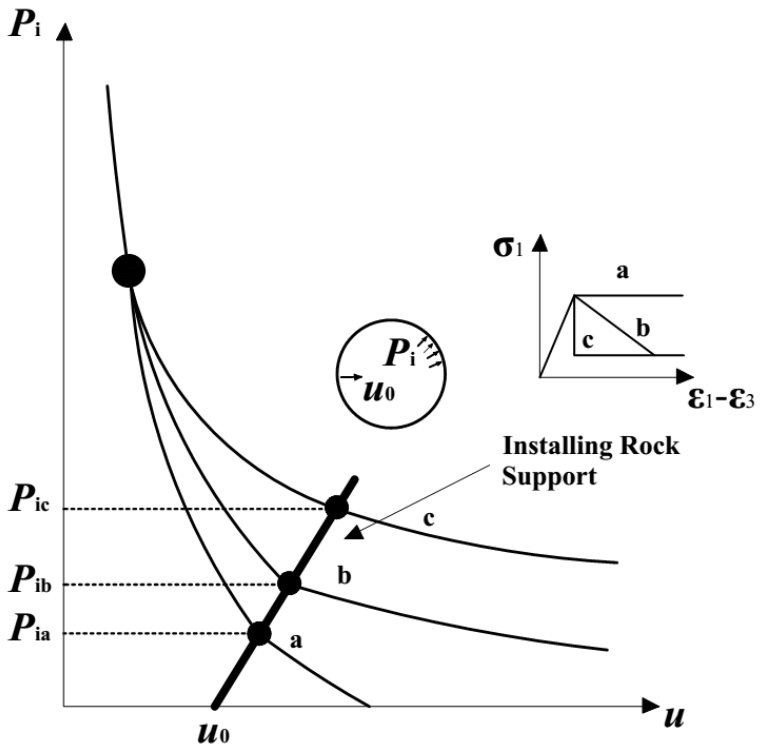

Fig. 6-2 Ground reaction curves for three different types of rocks: (a) perfect plastic, (b) strain softening, and (c) brittle plastic materials (Egger 2000). u_0 is the initial radial displacement before support installation.

Once the internal pressure (P_i) approaches its critical value (i.e. P_{ia}, P_{ib} and P_{ic}) as indicated in Fig. 6-2, the EDZ is extended by forming a failure zone with radius R_p as shown in Fig. 6-1 (Alonso et al. 2003). According to the rock mass behavior, the critical internal pressure value is obtained which is defined as the minimum value of pressure required to prevent the formation of the EDZ. Generally, the formation of the EDZ or the so called yield zone does not mean that the excavated opening would collapse, since the rock mass still has a considerable strength (Duncan Fama 1993; Alonso et al. 2003). Thus, it is important to define the critical strains and critical support pressures of the softened rock mass. Different analytical and numerical attempts were presented to analyze circular tunnels excavated in either H-B or M-C strain softened materials (e.g. Cui et al. 2017; Ranjbarnia, Fahimifar and Oreste 2015). Most solutions are based on isotropic, continuous, and initially elastic rock mass which delimits those solutions for more complex conditions.

In practice, tunnels are excavated in anisotropic in-situ stress conditions which affect the formation of the EDZ zone. Besides that, the occurrence of different discontinuities (e.g. the bedding planes

and inherent anisotropy planes) within the excavated rock mass play a significant role for the development of such yielding zones. Apart of the in-situ stress anisotropy, the bedding planes could influence greatly the direction of the formation of the EDZ. Theoretical scenarios of the formation of the EDZ around tunnels or boreholes have been later confirmed by field observations in the URL Mont Terri as presented in Fig. 6-3 (Wermeille and Bossart 1999).

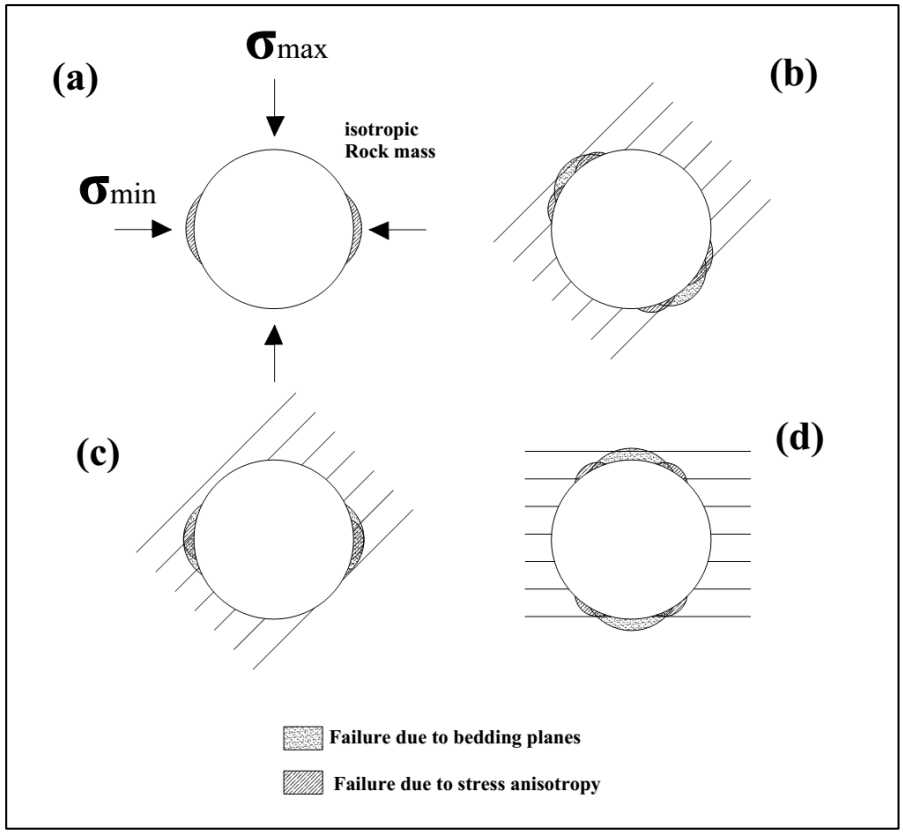

Fig. 6-3 Schematic showing different scenarios of EDZ formation around circular opening: (a) excavated vertically in isotropic rock matrix, (b) excavated verically in bedded rock mass inclined with angle of 45°, (c) excavated horizontally in bedded rock mass inclined with angle of 45°, and (d) excavated horizontally in bedded rock mass inclined with angle of 0°, modified after (Wermeille and Bossart 1999).

Thus, it is difficult to provide an analytical solution to predict the extension of the EDZ in a strain softening rock mass especially under complicated stress conditions and pronounced strength anisotropy. The trend is to solve such cases numerically to improved predictions of rock mass response and to provide a sound basis for a suitable support system. Also, the numerical back-analysis based on field measurements (e.g. extensometers and topological survey) is important for further applications or operations in similar rock masses.

The considered short-term stability analysis has been described as brittle and therefore the EDZ evolution takes place immediately (Marschall et al. 2017). A review of numerical simulations which are used to capture the short-term response of the rock mass around openings and the EDZ process is presented by Lisjak et al. (2015). Short-term response is defined within the duration between the construction stages to a few days after installation of the support system or based on the numerical terminology that the model has reached the equilibrium state. The aforementioned review is updated in this chapter and up-to-date modelling studies are summarized in Table 6-1. The inserted new studies are either released after the publication by Lisjak et al. (2015) or mechanical models for both, drained and undrained rock masses. Blümling and Konietzky (2003) introduced a bi-linear elasto-plastic strain hardening/softening ubiquitous joint model (Subiquitous model) for Opalinus clay. Similarly, the mine-by experiment located in shaly-facies Opalinus clay of Mont Terri underground rock laboratory was evaluated by using the Subiquitous model in FLAC3D without considering the stiffness anisotropy by (Thöny 2014). The proposed Transubi model is considered as an update of these trials to apply both: strength and stiffness anisotropy.

Table 6-1 Updated summary of EDZ simulations for openings in Opalinus clay, after (Lisjak et al. 2015)

Study	**Modeling code**	**Dimensions**	**Anisotropy**		**Constitutive models**
			Stiffness	**Strength**	
Martin and Lanyon (2003)	Boundary element-based 3D program, Examine^{3D}	3D	No	No	Linear elastic
Konietzky, Blümling, and te Kamp (2003) and Blümling and Konietzky (2003)*	FLAC3D	3D	No	Yes	Bi-linear elasto plastic strain hardening ubiquitous joint model
Corkum and Martin (2004)	2D finite element program, Phase2	2D	No	No	Linear elastic
					Elasto-plastic
					Elastic-brittle-plastic
Konietzky and te Kamp (2004) and Konietzky and te Kamp (2006)	FLAC 3D	3D	Yes	Yes	Elasto-plastic with ubiquitous joints
Corkum and Martin (2007)	FLAC 3D	3D	No	No	Linear elastic
				No	Elasto-plastic
				No	Nonlinear stress-dependent modulus elasto plastic model (SDM)
				Yes	Ubiquitous joint model
Stefanizzi, Barla, and Kaiser (2007)	Finite/discrete element code, ELFEN	2D	No	No	Elasto-plastic with the concept of “strain-driven” fractures
Popp and Salzer (2007) and Popp, Salzer, and Minkley (2008)	UDEC	2D	No	Yes	Elasto-plastic with explicit joints
Yong, Kaiser, and Loew (2010)	Phase2	2D	Yes	No	Linear elastic with continuous joints
			Yes	Yes	Elasto-plastic with continuous joints*
	3DEC	3D	No	No	Linear elastic with joints

Yong, Kaiser, and Loew (2013)	FLAC3D	3D	Yes	No	Elastic anisotropic continuum model
Thöny (2014)*	FLAC3D	3D	Yes	No	Linear elastic
			No	Yes	Bi-linear elasto plastic strain hardening/softening ubiquitous joint model
Lisjak et al. (2015)	Phase2	2D	Yes	No	Linear elastic
	Hybrid finite-discrete element code, Y-Geo	2D	Yes	Yes	Linear elastic with cohesive elements
Le and Nguyen (2015)*	Finite element software, COMSOL Multiphysics	3D	Yes	Yes	Elasto-plastic strain hardening/softening with implicit joints.
Lisjak et al. (2016)*	Hybrid finite-discrete element code, Y-Geo	2D	Yes	Yes	Linear elastic with cohesive elements and explicit pre-existing discontinuity

* Newly added studies of excavations in Opalinus clay.

6.3. Short-term stability analysis of the excavation of FE niche

As Opalinus clay is considered as host rock for the deep geological repositories for radioactive waste in Switzerland, the Full-scale Emplacement (FE) Experiment was initiated mainly to investigate Thermo-Hydro-Mechanical (THM) coupled effects. Full description and procedure of this experiment is given by Müller et al. (2017). The experiment consists of a 50-m long full face excavated tunnel starting from the FE cavern/niche (Fig. 6-4).

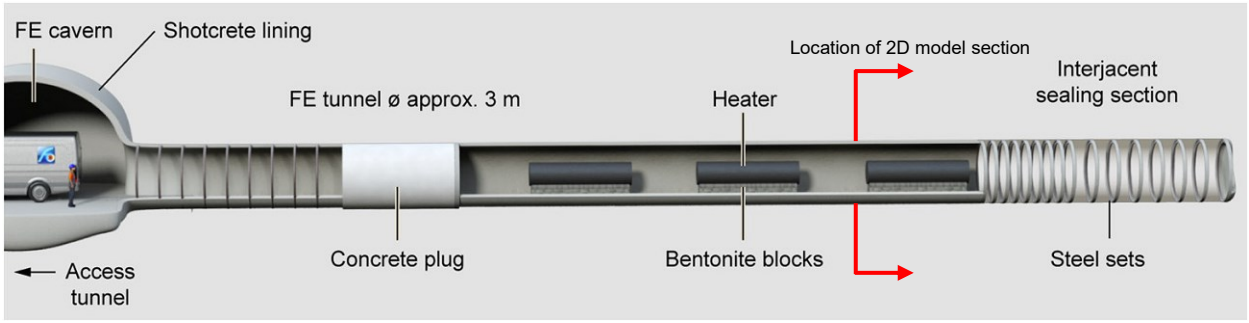

Fig. 6-4 General layout of the FE experiment (Müller et al. 2017).

The short-term analysis of the EDZ is found in (Lisjak et al. 2015), while the general long-term response is described in (Lanyon et al. 2014). This study considers only the short-term behavior.

6.3.1. Site layout and monitoring systems

The Opalinus clay in Mont Terri is categorized into three different formations: (i) sand, (ii) a carbonate-rich, sandy facies, and (iii) a shaly facies. The FE tunnel is excavated at an azimuth of 242° from North, approximately parallel to the strike of the bedding, and is entirely located within the shaly facies formation (Fig. 6-5). The construction of the FE tunnel was accomplished between April 2012 and July 2012. The excavation method was a combination of pneumatically hammering and roadheader (Lisjak et al. 2015; Müller et al. 2017). The excavation sequence was that the remotely controlled excavator equipped with the pneumatic hammer was used for the tunnel profiling, while the roadheader was adjusting the profile. Unlike the simulation, the tunnel invert was excavated as flat section rather than the original circular section.

Such excavation method did not result in a perfect circular profile (diameter is between 2.7 to 3.0 m including lining). However, the simulated section without lining is set to 3.0 m assuming smooth

walls. In practice, this irregularity of the surface caused problems with lining adhesion and therefore shear and bending forces in the lining.

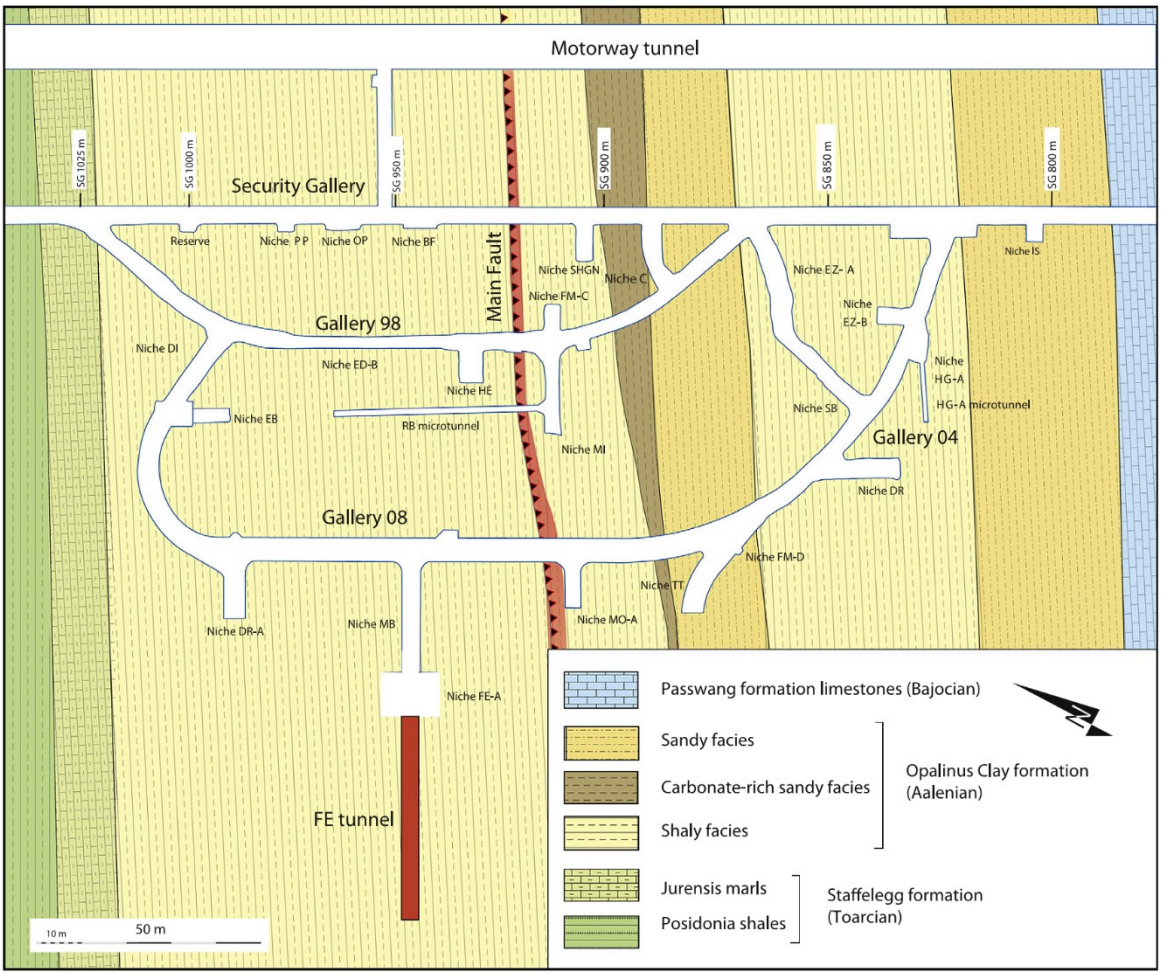

Fig. 6-5 Geological map of the Mont Terri underground rock laboratory, FE tunnel is highlighted in red, (Lisjak et al. 2015).

The support system of this tunnel varied along the tunnel. At the access section from 0 to 9 meter depth, a combination of shotcrete with steel arches is used. With advance of the tunnel and immediately after the excavation, mesh reinforced shotcrete with a minor thickness ranging between 16 and 24 cm was applied from 9 to 38 m depth. The targeted 2-dimensional section is located in the region supported with a 16-cm shotcrete at 28 m depth approximately, see Fig. 6-4. For the rest of the tunnel from 38 to 50 m depth, steel arches with wire meshing are used. The various support systems are summarized in Table 6-2. During the construction of the tunnel, high

convergence rates are observed at section depths TM9 – TM18 m and TM18 – TM38 m. Here invert failed and renovation was required. Thus, a new support system has been installed in the section from TM9 to TM 38 as specified in Table 6-2. The 2-dimensional numerical simulation at TM28 considers only the shotcrete with thickness 16 cm as a support system for the modelled section.

Table 6-2 Summary of support systems used along FE tunnel, after (Lanyon et al. 2014 and Lisjak et al. 2015)

Section depth [m]	**Support system**	**Notes**
TM0 – TM9	Steel sets (0.5 – 1 m spacing) + shotcrete with thickness 19 cm	Recording the minimum convergence rates
TM9 – TM18	Shotcrete with thickness 24 cm	From 12.30 – 18.3 m depth; extra 22 mm diameter and 2.5 m long fibreglass solid bolts with axial spacing = 1.5 m are installed
TM18 – TM38	Shotcrete with thickness 16 cm	From 19.8 – 37.8 m depth; extra 32 mm diameter and 7.5 m long hollow steel bolts in the right side wall with axial spacing = 1.5 m are installed
TM38 – TM50	Steel arches (0.5 – 1 m spacing) + wire mesh	The convergence rate is similar to the access section.

As described in Fig. 6-6, an extensive monitoring system has been installed along the tunnel axis and at the targeted section point TM28. In order to monitor the rock mass response, the entire tunnel has been divided into 10 convergence sections (C0 … to ... C9). At each of them 5 to 7 geodetic monitoring reflectors are installed to record the deformations. Also, five radial extensometers were installed from the tunnel walls each with four displacement sensors and a length of 6 m. Two sections, E1 and E2, are used to continuously record radial measurements of ground movements around the FE tunnel. At each section, extensometers BFEC-01 and BFEC-02, have been installed parallel (inclined with angle = 30^{o}) and perpendicular to the bedding planes (inclined with angle = 120^{o}), respectively.

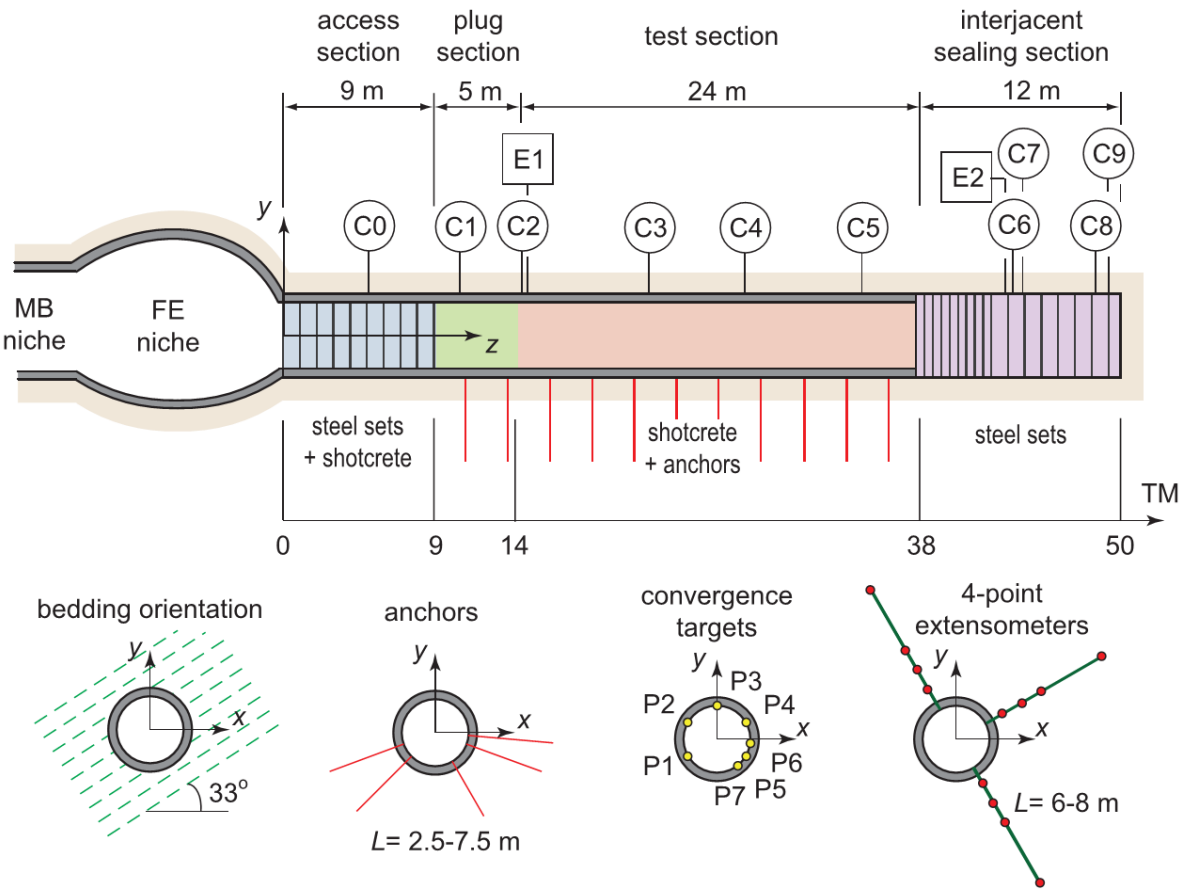

Fig. 6-6 Schematic of simplified longitudinal section showing different support sections, convergence measurement sections (C0 – C9) and location of radial extensometers (E1 and E2) installed during tunnel construction, (adapted from Lisjak et al. 2015)

As previously indicated, the modelled section is located within the convergence measurement sections C3 (TM21.8), C4 (TM27.6) and C5 (TM34.3) at which the supporting system is shotcrete with thickness of 16 cm, no anchors were considered. The 2-dimensional section is approximately at the middle of the tunnel (app. TM28), also it is positioned nearly intermediate between the location of the radial extensometers (E1 and E2). Two 45-m long inclinometers have been installed to continuously monitor the vertical displacements above the crown of the FE-tunnel. The two inclinometers (BFEA-10 and BFEA-11) were nearly parallel to the tunnel axis and drilled directly from the FE cavern prior to the excavation. The position of both inclinometers measured from the tunnel axis at the studied section (TM28) is app. 2.6 m.

The pore pressures in the near- and far-field were monitored before, during and after the excavation. Six boreholes (BFEA-02 to BFEA-07) were installed from the FE niche/cavern. Six measuring points were fixed along each borehole. A visualization of the installed boreholes and the inclinometers is shown in Fig. 6-7. Note that the recording points were located starting from point TM20 till nearly TM40 in such a way that the i6 intervals are the closest to the FE cavern wall and the i1 intervals are furthest from the gallery wall (Lanyon et al. 2014).

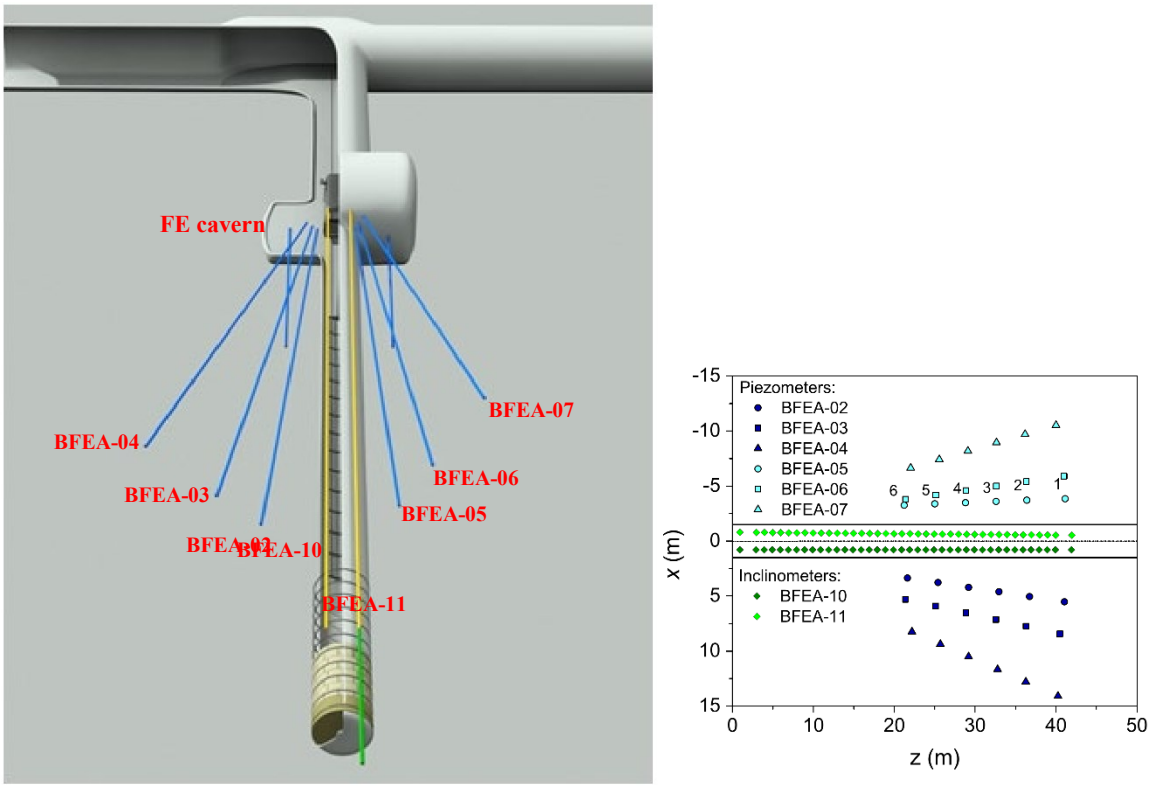

(a) **(b)**

Fig. 6-7 Arrangement of installed inclinometers and borehole array in (a) 3D (adapted from Lanyon et al. 2014) , and (b) top view (adapted from Lisjak et al. 2015)

6.3.2. Model description, in-situ stress field and assigned parameters

The numerical model considers a 3 m diameter circular hole centered in a 50 m x 50 m square domain. A radial mesh is defined by polar coordinates around the opening. This mesh maximizes the model efficiency by providing refinement in the region close to the excavation in order to capture the formation of the EDZ. On the other side, the mesh is quite coarse close to the outer

boundaries where no plasticity is expected which reduces the runtime significantly (Fig. 6-8). The built-up mesh consists of 12.800 elements. The minimum length of elements on the opening perimeter is 0.06 m and the element size is graded toward the borders until it reaches 1.25 m adjacent to the outer boundaries. A sensitivity analysis in respect to mesh performance is presented in section 6.6.4.

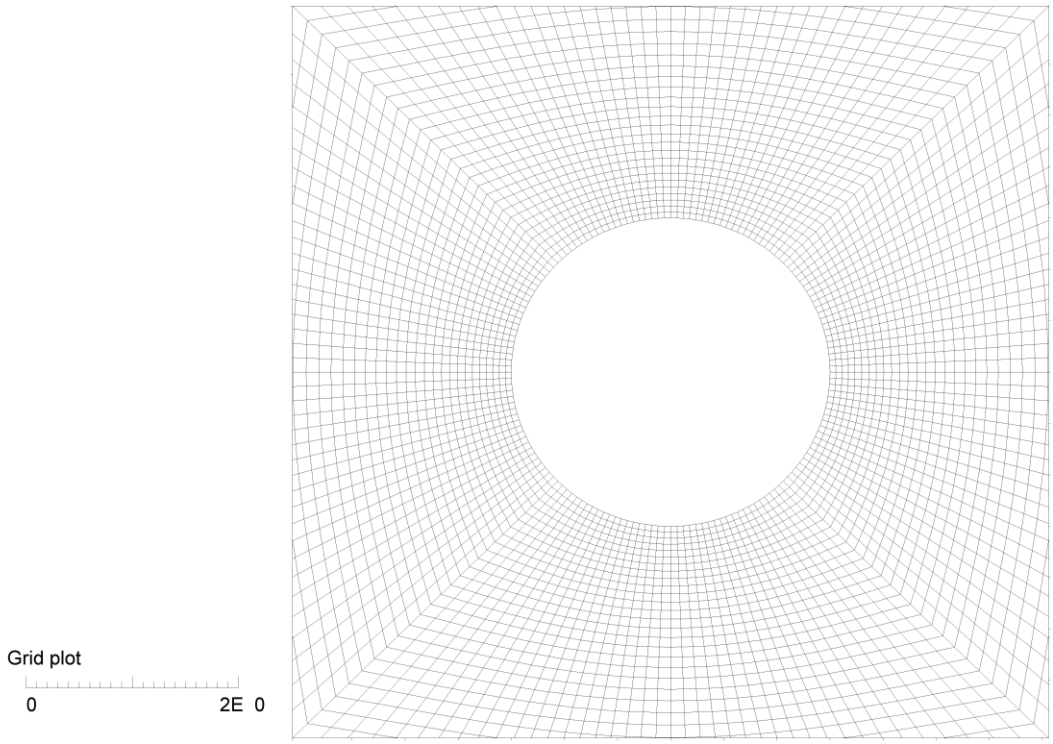

Fig. 6-8 Mesh geometry [m] near to the tunnel, 10 m x 10 m total model size.

Model size was chosen in such a way that boundary effects are negligible. At the outer boundary stresses are applied according to Table 6-3. Unlike the numerical simulation reported by Lisjak et al. (2015), three orthogonal stress components (σ_{xx}, σ_{yy} and σ_{zz}) are applied. As the model for a tunnel section is a plane strain one, the third stress component (σ_{zz}) could not be vanished. Lisjak et al. (2015) analyzed previous studies regarding the in-situ stress state at Mont Terri. Field investigations using borehole breakouts were provided by Wermeille and Bossart (1999). Martin and Lanyon (2003) presented a numerical back-analyses of these measurements. In this context, another 3-dimensional numerical model was obtained showing that the minimum component of the in-situ stress (σ_3) and the out-of-plane component (σ_{zz}) have some uncertainty and should be re-evaluated. Finally, Bock (2009) concluded that the insitu stress values are between 2 to 10 MPa.

On the other side, the measured undisturbed pore pressure (σ_{pp}) around the FE tunnel is 2 MPa (Lanyon et al. 2014). Finally, the in-situ stress tensor is defined as given in Table 6-3.

Table 6-3 Applied in-situ stresses in the numerical model.

Component	σ_{xx} [MPa]	σ_{yy} [MPa]	σ_{zz} [MPa]	σ_{pp} [MPa]
Magnitude	4.5	6.5	2.5	2

The Transubi model is applied for the whole domain, assuming inclined bedding planes with angle (α) = 35° based on the reported observations (Lisjak et al. 2015; Lanyon et al. 2014; Müller et al. 2017) and the field investigations (Jaeggi et al. 2012).

Table 6-4 Mechanical properties of Opalinus clay applied to numerical simulations (Lisjak, Grasselli, and Vietor 2014; Bock 2009)

Parameter	**Value**
Bulk density, ρ [kg/m^3]	2330
Elastic components	
E [GPa]	3.8
E' [GPa]	1.3
ν [-]	0.35
ν' [-]	0.28
G' [GPa]	0.9
Rock matrix	
σ^t [MPa]	1.0
First surface	
c [MPa]	2.0
φ_f [°]	28
c^{res} [MPa]	1.5
φ_f^{res} [°]	20
ψ [°]	5
Second surface	
c [MPa]	3.0
φ_f [°]	20
c^{res} [MPa]	2.0
φ_f^{res} [°]	12
ψ [°]	7
Bedding planes	
σ_j^t [MPa]	0.3
c_j [MPa]	0.8
φ_{fj} [°]	20
c_j^{res} [MPa]	0.4
φ_{fj}^{res} [°]	12
ψ_j [°]	0
Angle of inclination, α [°]	35

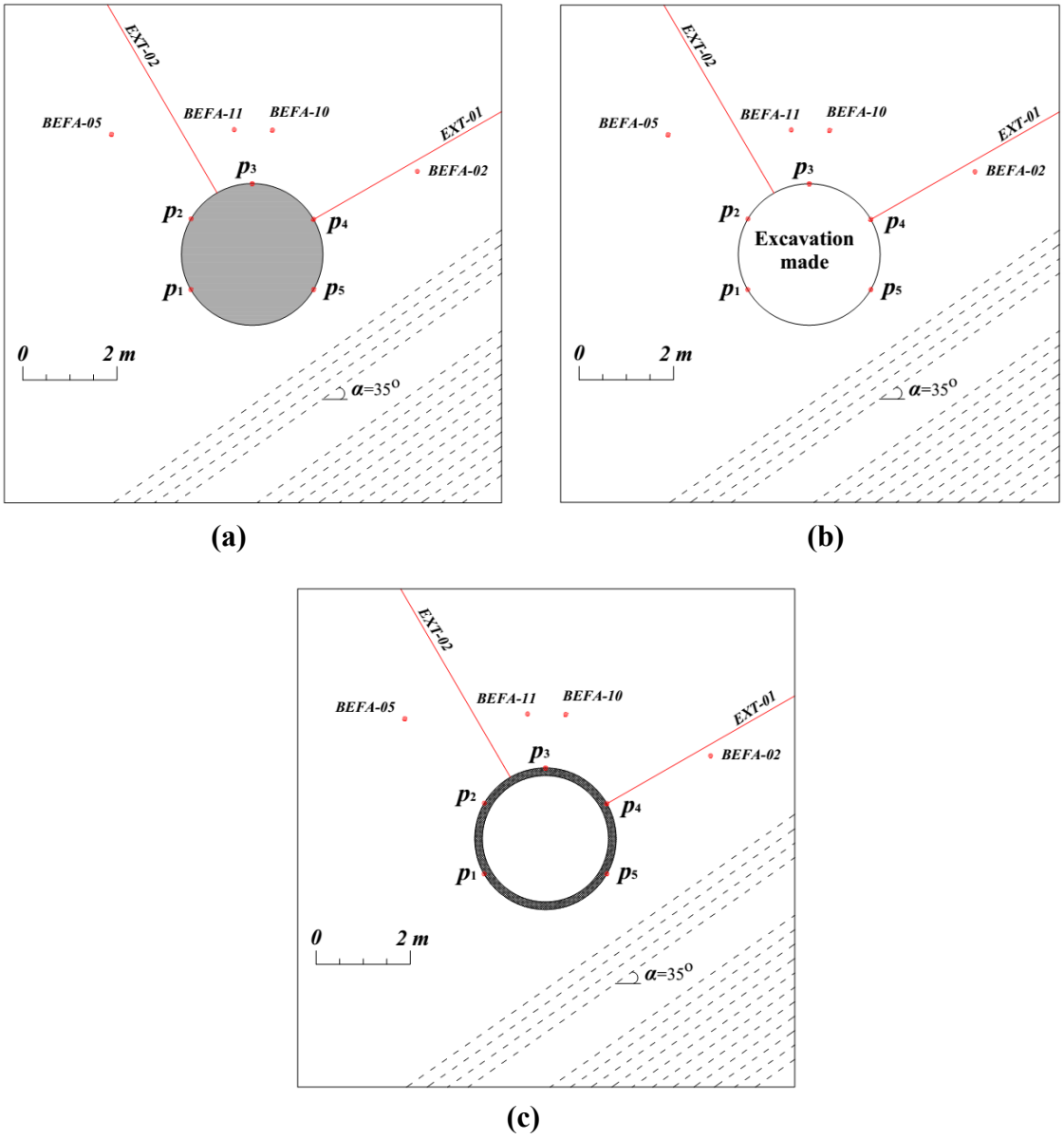

Fig. 6-9 Main stages of the simulation (a) pre-excavation stage including installation of history points and primary stress state, (b) excavation phase, gradual reduction of traction on the tunnel surface until a prescribed factor is reached, and (c) applying liner support and bringing model to equilibrium .

The mechanical properties of Opalinus clay obtained in section 4.3 are updated in which the applied pre-yielding region is linear elastic with no hardening to investigate the propagation of the plastic state around the hole, elastic components are determined after (Lisjak, Grasselli and Vietor 2014; Lisjak et al. 2015), see Table 6-4. Also, the strength parameters have been slightly reduced based on the design recommendations provided by Bock (2009). Softening (brittle-plastic) is still

applied in the post yielding region. The rock matrix is described as bilinear M-C, while for the bedding planes a linear M-C model with tension cut-off is used.

The second stage (Fig. 6-9.b) simulates the relaxation procedure at which the forces at the tunnel wall are incrementally decreased up to a prescribed value. The analysis of the ground reaction curve of the FE-tunnel shows that approximately 50 % convergence occurred before the shotcrete installation. This required a relaxation of 95% (i.e. relaxation factor = 0.05). This value is significantly close to the value suggested by Lisjak et al. (2015). Thus, applied relaxation along the tunnel perimeter from 0 % to 95 % is implemented, whereas the convergences, deformations and pore pressure are continuously recorded around the excavation, see Fig. 6-10.

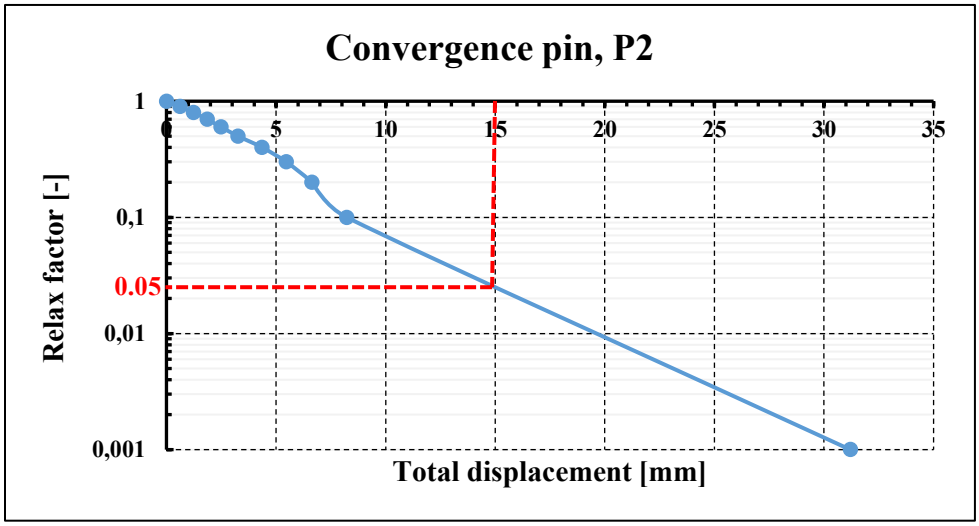

Fig. 6-10 Ground response curve for convergence point P2, almost 50% total displacement occurs at relaxation factor = 0.05 (Relaxation = 95%)

The third and the final stage (Fig. 6-9.c) is the support installation as a liner shotcrete with perfect adhesion. The nodes on the tunnel perimeter are marked, and then the shotcrete segments were applied between each marked node. In FLAC, the logic of structure installation follows the plane-stress formulation. Thus, the given Young's modulus should be altered to be compatible with plane-strain. The applied shotcrete is linear elastic with homogeneous properties. Parameters are given in Table 6-5. After the installation of the shotcrete, the model is brought to equilibrium allowing the complete relaxation (100% relaxation).

Table 6-5 Mechanical properties of installed shotcrete

Parameter	**Young's modulus*** [GPa]	**Thickness** [m]	**Moment of Inertia**, I [m^4]	**Poison ratio**, ν [-]
value	10	0.16	2.73E-4	0.2

* The given value is adjusted for plane-strain case to 10.4 MPa.

Concerning the value of the Young's modulus for the shotcrete, there is no clear data of the applied shotcrete installed prior to the invert renovation in 2015 (Müller et al. 2017). Because the short-term behavior is considered, the assumed stiffness for shotcrete was adjusted for the age of 1 to 7 days (Bryne 2014; Neuner et al. 2017). The assumed values agree with the parametric study in respect to the displacements at pin P2 and the variation of the shotcrete stiffness (Lisjak 2013). Similar, the displacements at pin P3 are recorded prior and after the support installation (relaxation = 95%) assuming two applied Young's modulus for the shotcrete (Fig. 6-11). Very high value is assumed for the shotcrete stiffness (E = 5 GPa) similar to the applied properties of shotcrete in (Itasca 2016) showing no produced displacements. On the other hand, low modulus (E = 10 MPa) is given similar to the value obtained by Lisjak et al. (2015) and Table 6-5 indicating that there is large tunnel convergence consistent with the measured values in-situ.

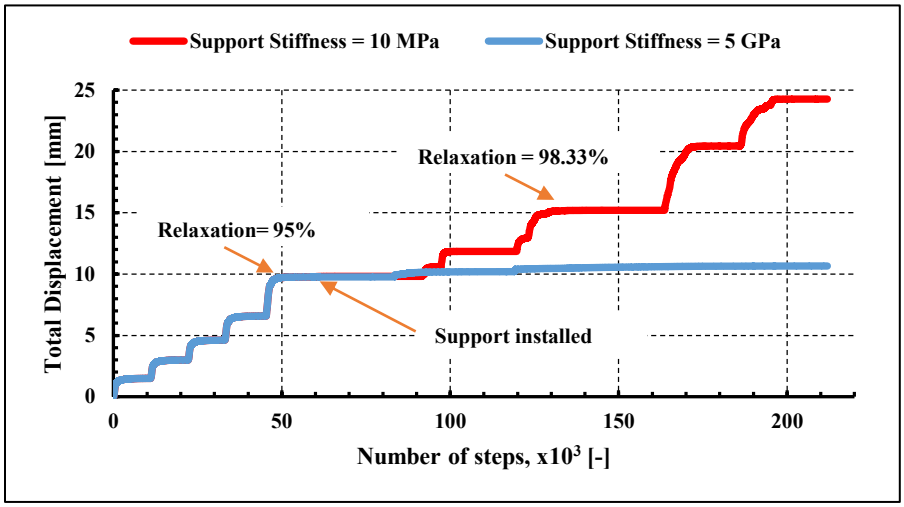

Fig. 6-11 Influence of applied support stiffness on the evolution of the total displacements at convergence pin P3, support installed at relaxation = 95%

The histories of the recorded total displacements versus the normalized distance between the measuring sections and the excavation face for three convergence sections C3, C4 and C5 located in the tunnel part lined with 16 cm thick shotcrete are shown in Fig. 6-12. The described model procedure is applied (a) without consideration of the pore pressure in chapter 6.3.3 and (b) with consideration of a homogenous initial pore pressure and fully saturated rock mass in chapter 6.3.4. Both cases use the Transubi model and the undrained Opalinus clay properties shown in Table 6-4. As the simulations aim at the short-term analysis, no fluid flow is allowed (undrained conditions).

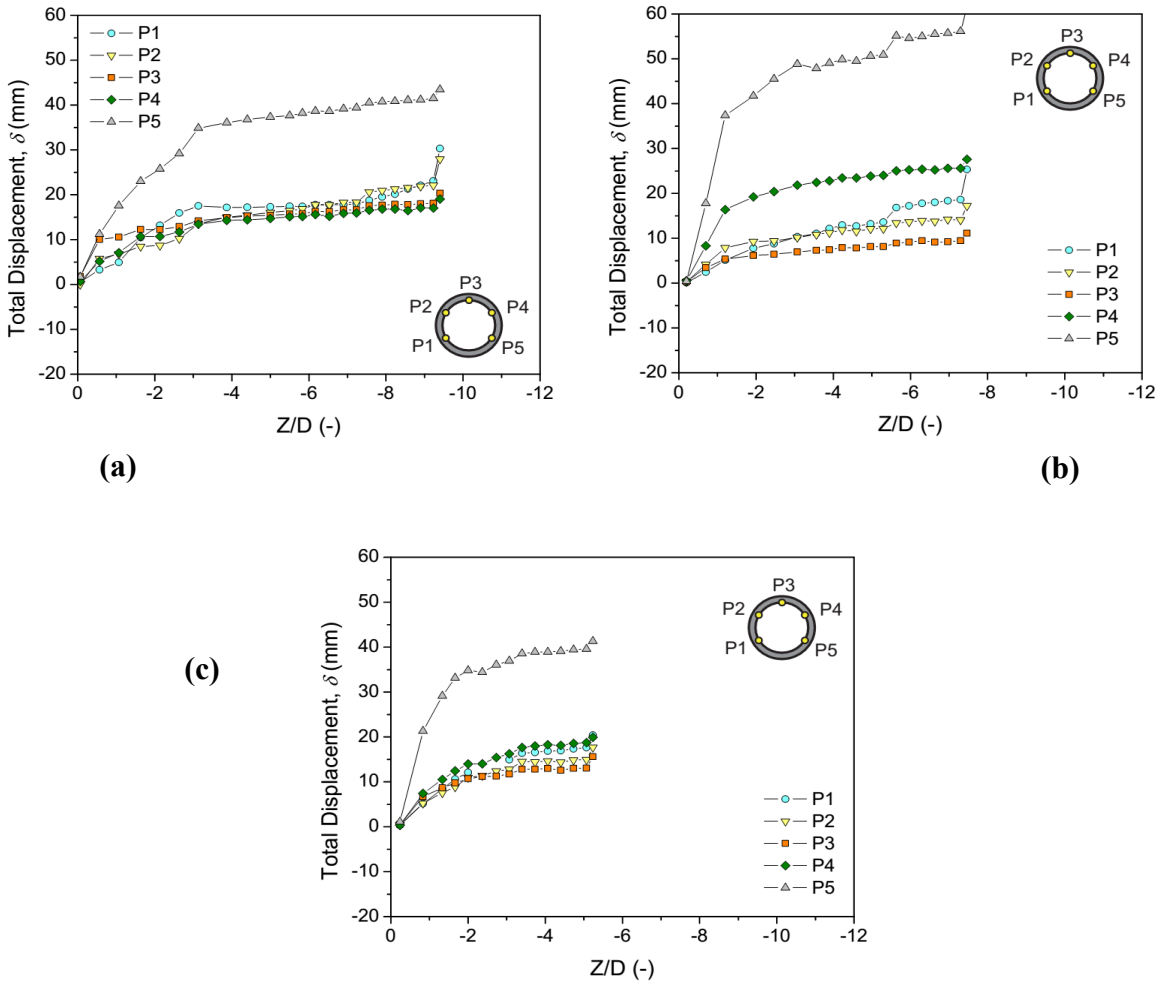

Fig. 6-12 Normalized recorded tunnel wall total displacements at five pins P1, P2, P3, P4 and P5 as function of distance between the measuring section and the excavation face (Z/D), Z is the distance from the tunnel face and D is the tunnel diameter, for convergence sections (a) C3 at TM21.8, (b) C4 at TM27.6, and (c) C5 TM34.3, (Lisjak 2013).

6.3.3. Mechanical simulation: no pore pressure considered

During the simulation, histories of x- and y-displacement components according to the locations of the inclinometers, the extensometers and the convergence pins are recorded. Therefore, the total development of the tunnel convergences and the deformation field around the opening can be reproduced and plotted. Neglecting the measured values before installation of the support, the comparison between the simulated displacements at the pins and the field measurements recorded at convergence sections (C3, C4 and C5) are found in Fig. 6-13.

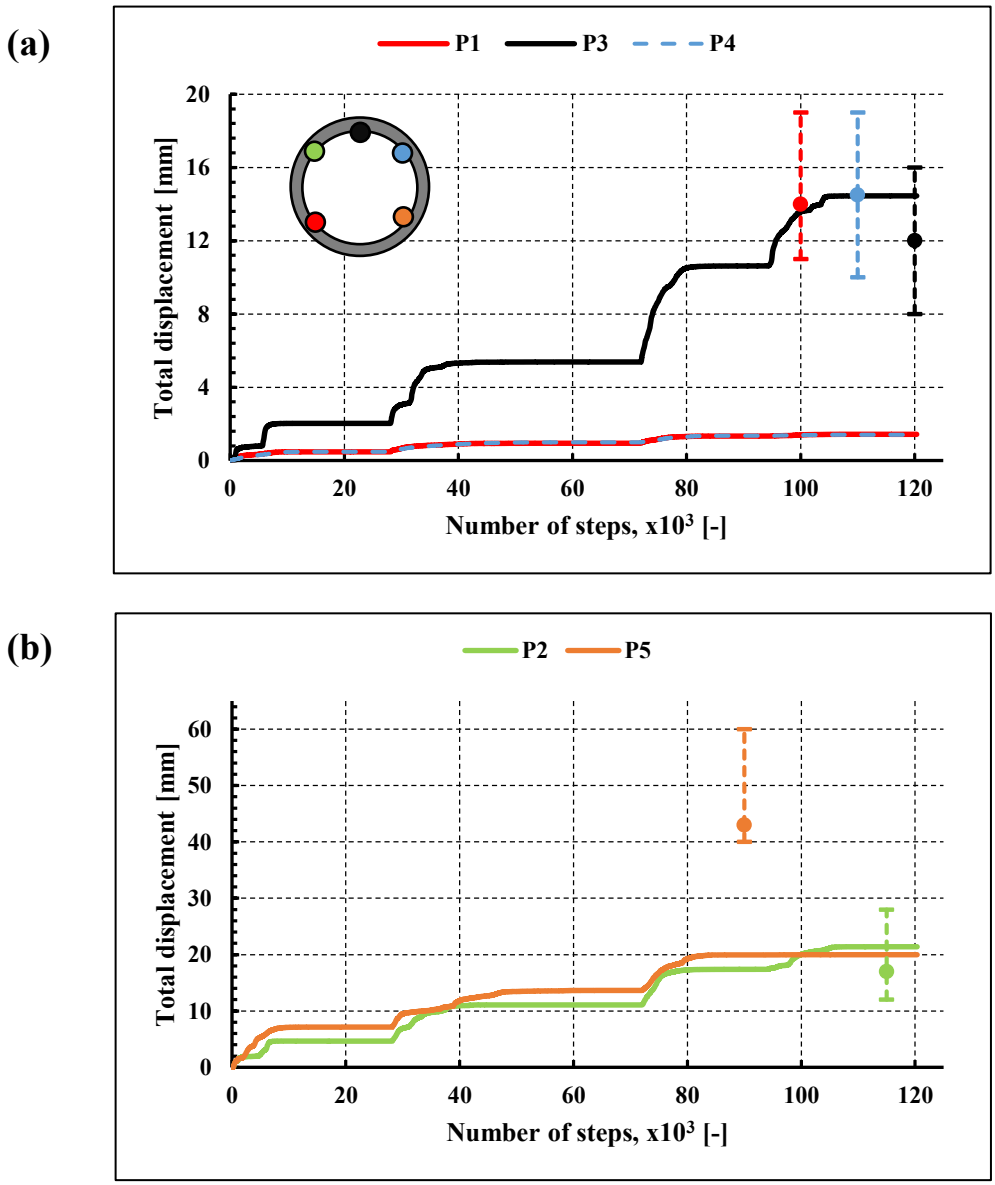

Fig. 6-13 Normalized computed total displacements of tunnel wall compared to average in-situ measurements at convergence pins (a) P1, P3 and P4, and (b) P2 and P5

The computed total displacements show that the proposed numerical model produces symmetric behavior, although the field measurements exhibit asymmetric deformation behavior especially for P5 and P2. Total displacements at P1 and P4 are overall identical and under-predicted by about 9 mm indicating another failure mode. The insitu observed behavior cannot be captured by the proposed continuum-based model. Lisjak et al. (2015) found the same result concerning P1 and P4 as well. Also, the displacements at P5 are underestimated by approximately 20 mm. To explain this, different potential reasons have to be mentioned. The convergence pin P5 is located near to the base of the north-east wall in a region where tectonic fault planes associated with a fault zone present from 14.5 m onwards in the FE cavern exist (Lanyon et al. 2014). Detailed geological mapping of excavation face of FE-tunnel is found in (Jaeggi et al. 2012). Additionally, P5 was near to the sharp edges formed due to the installed flat slap at the invert producing concentration of the deviatoric stresses. In contrast, the model assumed a perfect circular profile without slap in the invert and perfect adhesion of the shotcrete.

On the other hand, the predicted displacements at P3 and P2 are in good agreement with the average in-situ measurements. Notable deformations are generated in P2 because of the shear and tensile failure on bedding planes. The shear zone formed near to P2 influences the deformation field at the tunnel crown, where P3 is located. The evolution of the fractures simulated by Lisjak et al. (2015) confirms an excessive fracturing after the support activation at the crown and the invert associated to the local shear zones at P2 and P5. In order to enhance the understanding of the deformational behavior acting on the tunnel walls, convergences have been recorded between the pin points. The total displacements at each pin are analyzed in the direction of the target convergence line (Fig. 6-14). Computed convergences at lines P1-P3, P5-P3, P2-P5 and P2-P4 are in close agreement with the average field results. The convergence line P1-P4 is under-predicated with value 20 mm which is close to the computed value of the linear elastic analysis performed by Lisjak et al. (2015). Values for convergence line P1-P5 are underestimated by about 40 mm. Similar results were found by Lisjak et al. (2015) where P1-P4 and P1-P5 were under-predicted by approximately 13 and 30 mm, respectively.

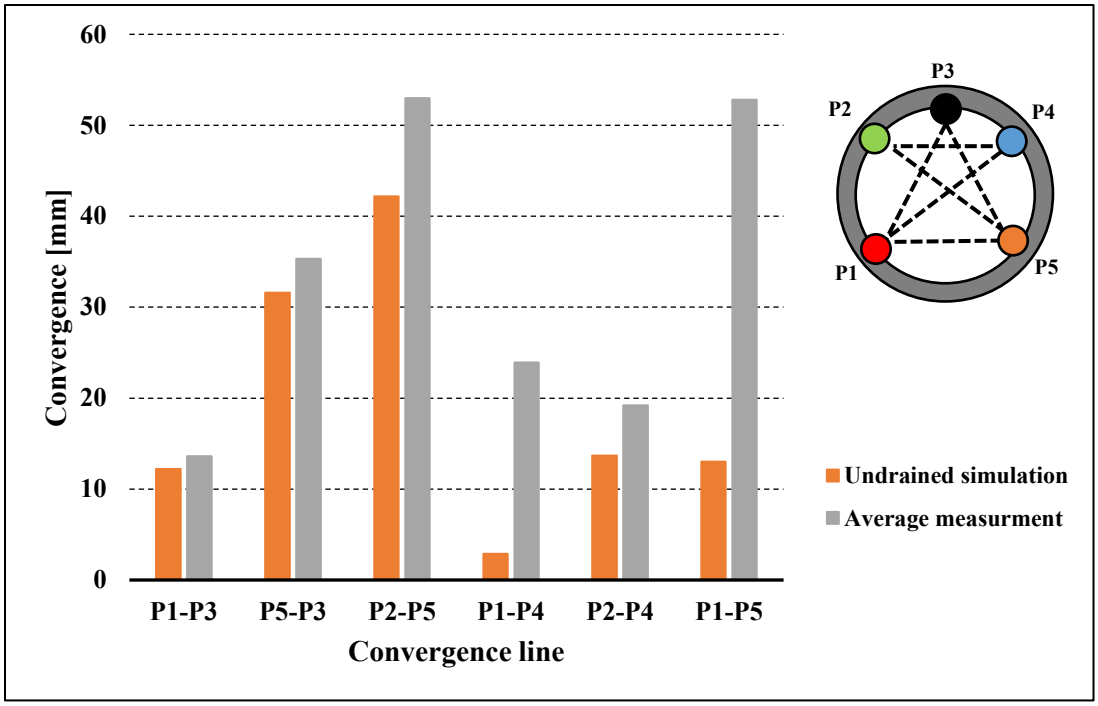

Fig. 6-14 Comparison between the computed convergencs and the average field measurements

The evolution of the vertical displacements is plotted in Fig. 6-15. Two points are located at the same positions of the inclinometers BEFA-10 and BEFA-11, see Fig. 6-9. The recorded vertical deflection is consistent with the analysis presented by Lisjak et al. (2015) in which the recorded vertical displacements at equilibrium were 8 and 10 mm for BEFA-10 and BEFA-11, respectively. On the contrary, the average insitu vertical deflection measured by the inclinometers between TM9 and TM38 is about 21.5 mm shows significant deviation from the numerical simulation results. The insitu value is obtained by considering the displacements recorded at a given section when the excavation face is approximately 9 m away. Such difference could be the consequence of the selection of the 2-dimensional instead of 3-dimensional analysis. Applying different supporting systems along the tunnel axis without consideration the time dependency will lead to irregular values for the measured vertical deflections along the installed inclinometers (BEFA-10 and BEFA-11). As shown in Fig. 6-15, the average measured vertical displacements recorded at the excavation face at TM28 at inclinometers BEFA-10 and BEFA-11 are 4.7 and 9 mm, respectively, which is in close agreement with the numerical simulation results.

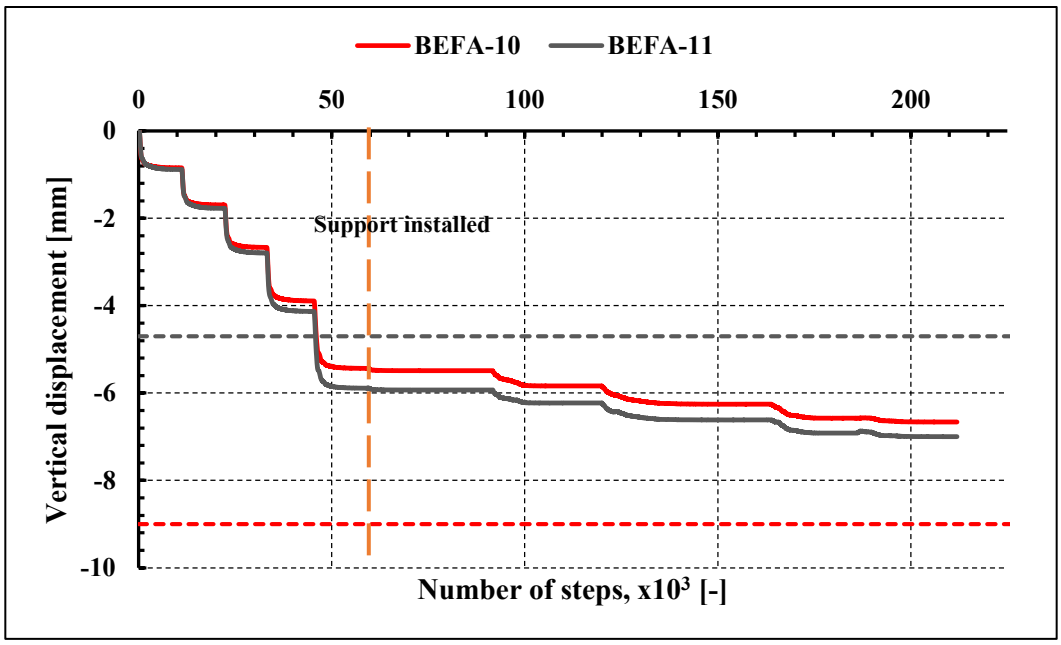

Fig. 6-15 Computed vertical displacements at two history points located at the positions of BEFA-10 and BEFA-11. Doted lines indicate the measured vertical deflections for BEFA-10 and BEFA-11 recorded at the excavation face at TM28.

EXT-01 and EXT-02 are 6 m long extensometers which were installed in orthogonal configuration in order to quantitatively describe the propagation of the EDZ. Fig. 6-16 presents short-term radial displacements for both extensometers at TM14.6 (section E1, Fig. 6-6) (Lisjak et al. 2015). For EXT-01, the measured radial displacements show gradual reduction, almost linear from 2.6 to 0 mm indicating less yielding in direction parallel to bedding planes in a good agreement with the field observations shown in Fig. 6-3.c (Wermeille and Bossart 1999). Conversely, the radial displacements at EXT-02 show a drop in measurements at the region between 1 to 3 m away from the tunnel perimeter which characterizes the extent of the EDZ. Fig. 6-17 shows the computed radial displacements parallel and perpendicular to the bedding planes at equilibrium. The difference between measured and computed values is not rational, Lisjak et al. (2015) stated in such context that a limited share of the radial displacements have been captured by the installed radial extensometers EXT-01 and EXT-02. In addition, it could be concluded that the radial deformations at E1 section (TM14.6) for different support system could be different than the deformations at this section. Generally, both measured and computed results share the same characteristic: radial deformations at EXT-02 are higher than those at EXT-01. The propagation of the EDZ is presented in Fig. 6-18 showing polar symmetric shape and maximum extend in direction perpendicular to the bedding plane (P2 and P5) at about 2.7 m from the tunnel wall.

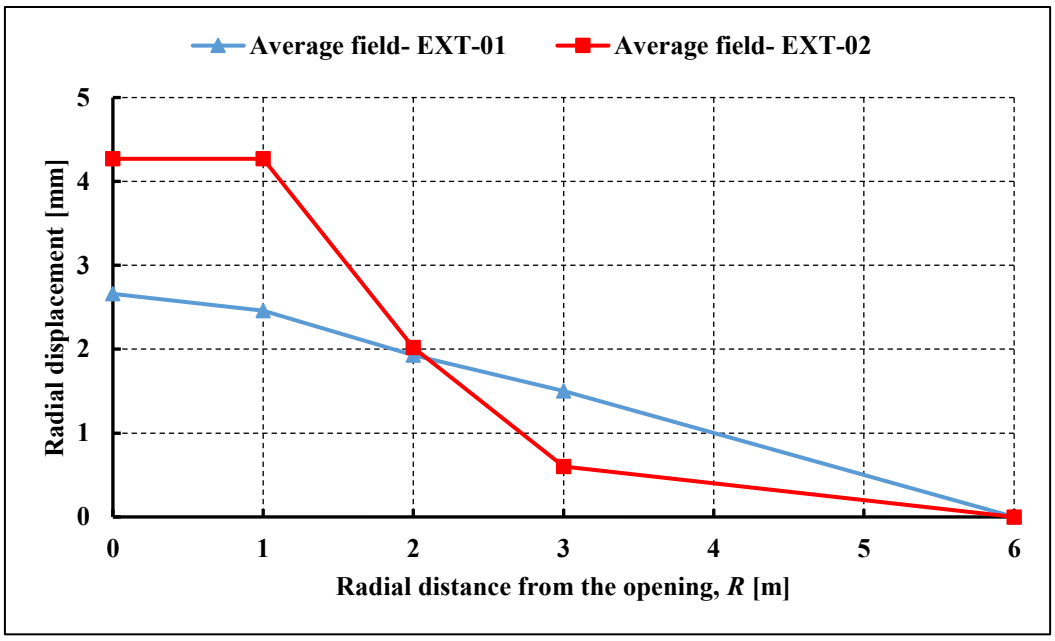

Fig. 6-16 Measured short-term radial displacements at TM14.6 section assuming a zero value at R = 6 m (Lisjak et al. 2015)

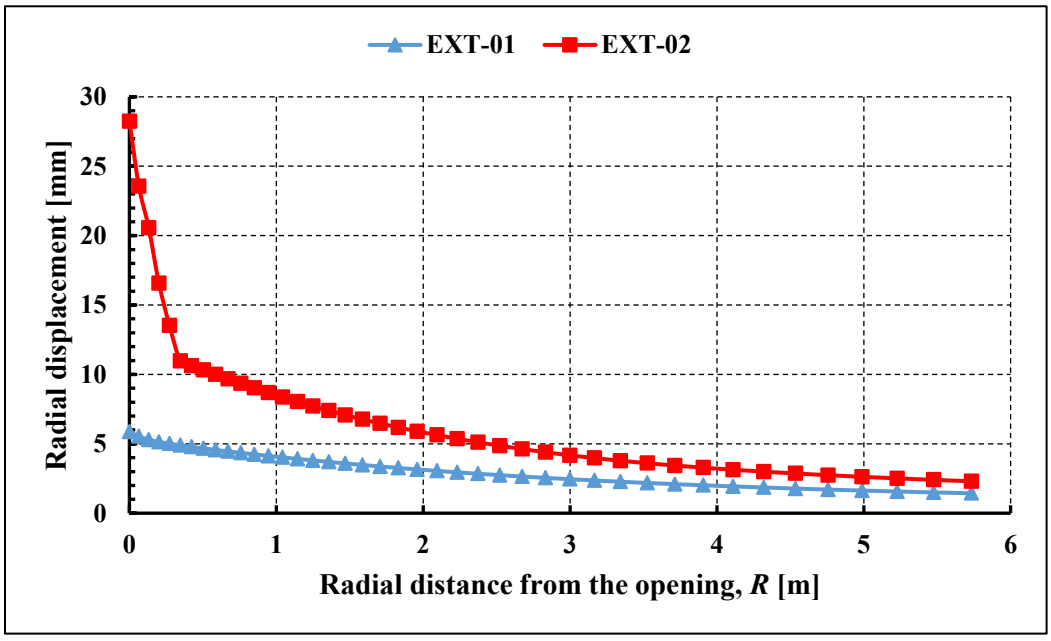

Fig. 6-17 Normalized computed radial displacement at equilliprium along two lines corresponding to the installed extensometers shown in Fig. 6-9

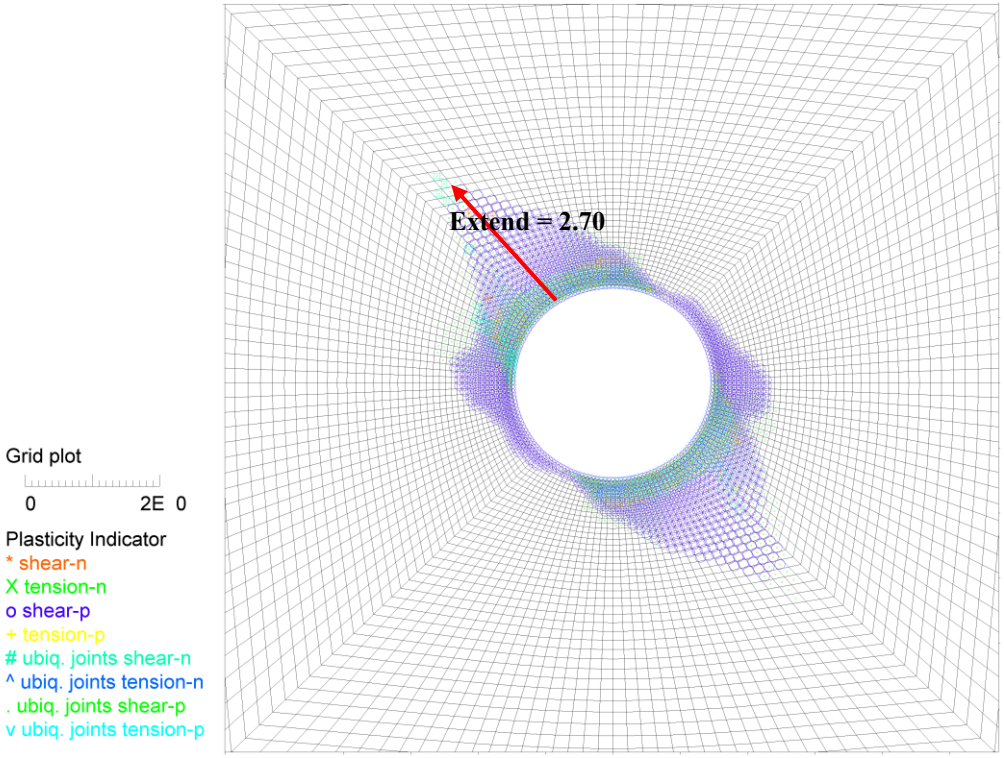

Fig. 6-18 Plasticity indicators showing the formed EDZ at equiliprium state, 10 m x 10 m model size.

6.3.4. Mechanical generation of pore pressure – No flow

For short-term mechanical analysis, the simulation time is shorter than the characteristic time of the coupled diffusion process. Thus, the discussed numerical simulation in this part consists of the undrained mechanical response combined with the generation of pore pressure change.

The properties of the Opalinus clay given in Table 6-4 are applied in the simulation, whereas 100% saturation and porosity of 0.5 are assumed for all model runs. The initial pore pressure is set to 2 MPa (Table 6-3). The assigned fluid bulk modulus equals 1 GPa which is considered as a realistic value. Fig. 6-19 shows the comparison between numerical results and average field measurements as well as the finally evaluated displacements from the mechanical simulations without consideration of the pore pressure (section 6.3.3, Fig. 6-13).

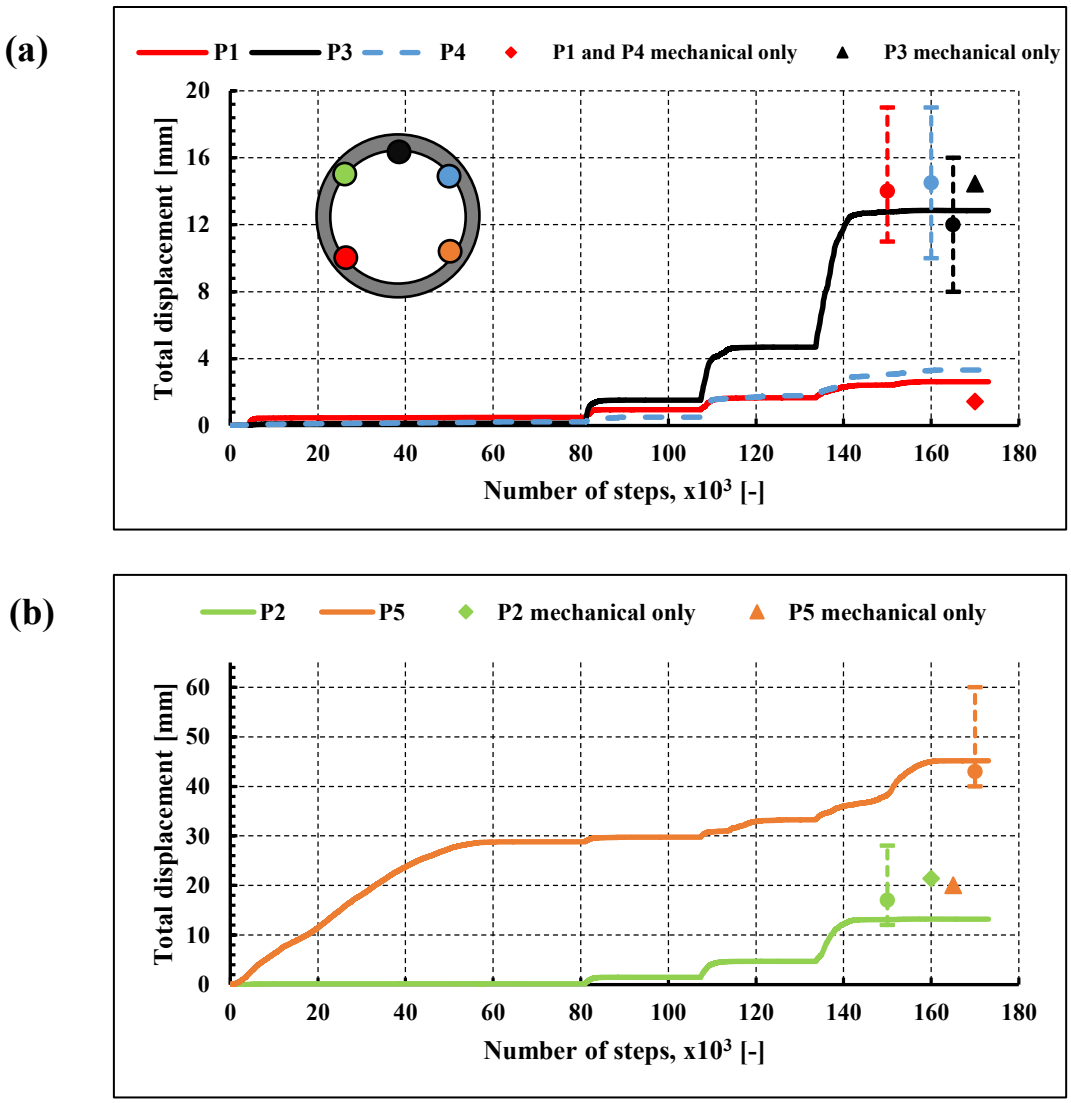

Fig. 6-19 Normalized computed total displacements of tunnel wall compared to the average in-situ measurements at convergence pins (a) P1, P3 and P4, and (b) P2 and P5. Displacements computed from the mechanical simulation without pore pressure consideration are also plotted.

As noticed from Fig. 6-19, the overall behavior of the total displacements for points P1, P2, P3 and P4 after the support installation are quite similar. During the application of the relaxation from 95% to 98.33% at step no. 80.000, displacements are triggered until equilibrium is reached. Compared with simulation results shown in chapter 6.3.3, the computed displacements at points P1 and P4 are higher than predicted previously. At P1, the developed displacements are increased by 87%, while the percentage is even higher for P4 and equals 137%. Such jumping in the values of the computed total displacements for P1 and P4 indicate that the hydraulic coupling plays a

major role. Nevertheless, the computed values are still unsatisfactory compared with the insitu measurements with an average difference of about 7 mm. Although the simulations achieved reasonable predictions for the displacements at P2 and P3, the computed values are lower than those estimated by the pure mechanical simulations without pore pressure consideration. The drop in the computed values for P2 and P3 is 38% and 11%, respectively.

On the other hand, the behavior at pin P5 is totally different than those recorded at the other points. The jump in the displacements values starts directly after the support activation until equilibrium is reached producing a difference in the computed total displacements of approximately 30 mm. Afterward, the system stabilizes up to the point when relaxation (98.33%) is applied at step 80.000. At equilibrium, the computed displacement recorded at P5 is about 45 mm which is in good agreement with the average measured values. For the interpretation of the deformational behavior at P5, the hydro-mechanical interaction should be taken into account. Thus, at this region, the hydro-mechanical coupling is essential to enhance the understanding of this displacement jump at P5 at the moment before and after the support installation. As shown in Fig. 6-20, before the shotcrete installation, the saturation is redistributed around the hole showing decreasing values (≈ 93.5%) in the direction perpendicular to the bedding planes (P2-P5 line). Such reduction in saturation is combined with increasing in the displacements at points P2 and P5 (≈ 20.7 mm). Until this moment, there is no jump in displacement values at P5.

Afterward, the model is brought to equilibrium after installation of the shotcrete. At the end of the simulation (relaxation = 100 %), significant drop in saturation near point P5 (≈ 0 %) occurred which is responsible for the notable jump in the total displacement values in this region due to the generated heave (Fig. 6-21). Excessive upward displacements (y-displacements) were induced (≈ 65 mm) at the tunnel perimeter because of the buoyancy effect: water level tries to raise again to re-saturate region near to P5. Also, the saturation slightly decreased at P2 region to approximately 90%. As remarked, the saturation levels at areas near to P1 and P4 show no change. On the other hand, such high value in displacements near the tunnel invert could cause the breakage of the shotcrete as reported by Müller et al. (2017). Generally, this explanation could be the main contributor to the relatively high measured displacement values at P5 besides the other reasons mentioned previously in 6.3.3 such as: disturbed tectonic fault planes located near to pin P5 and temporary flat slap placed at the invert forming sharp edges (Lanyon et al. 2014; Lisjak et al. 2015).

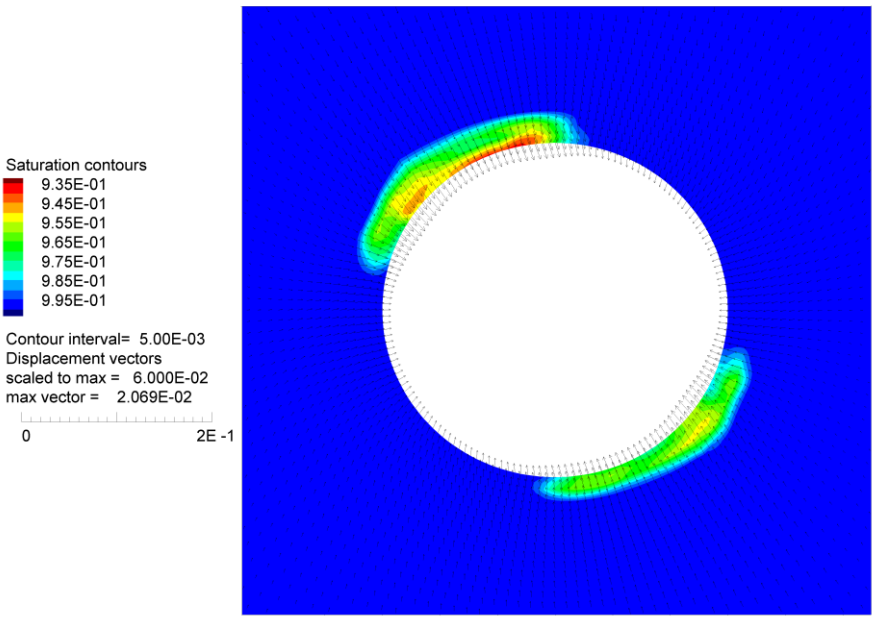

Fig. 6-20 Saturation around the circular opening before support activation (relaxation = 95%) and total displacement vectors showing polar symmetry, maximum displacement values at P2 and P5 with 20.7 mm

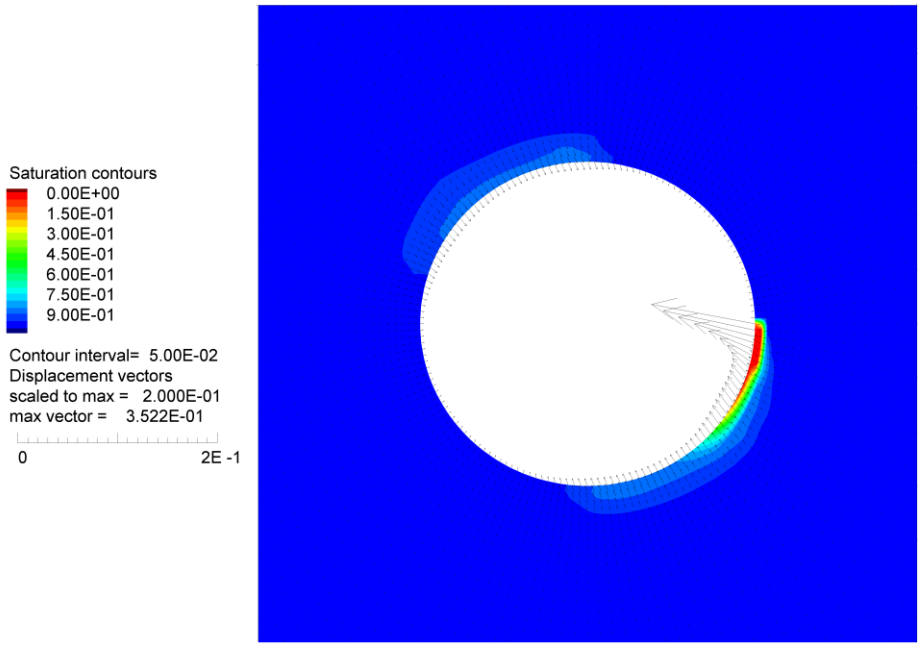

Fig. 6-21 Evolution of saturation at the end of the simulation at equillibrum state, showing drop of saturation near to P5. Excessive total displacement value near to P5 with average value of 65 mm, near to P2 the developed displacements are comparably low. At line P1-P4 displacements reach the minimum.

The computed relative displacements between pin points are compared with the results from undrained numerical simulations and the average field results (Fig. 6-22). Convergences at lines P1-P3 and P2-P4 are quite equal to the computed values using the mechanical only simulation and are also close to the measured values. For lines P5-P3 and P2-P5, the computed values are almost similar, however the predicted convergence at P5-P3 is over-estimated by about 20 mm. There is perfect agreement with in-situ measurements for the computed displacements along P2-P5 ≈ 55 mm. Noticeable improvement in the predicted convergences for lines P1-P4 and P1-P5 was achieved in reference to previous simulation results in which the computed values are under-predicted by 18 and 24 mm, respectively. In general, the numerical simulations considering pore pressure changes result in slightly better prediction of tunnel wall convergences compared to those without hydro-mechanical coupling.

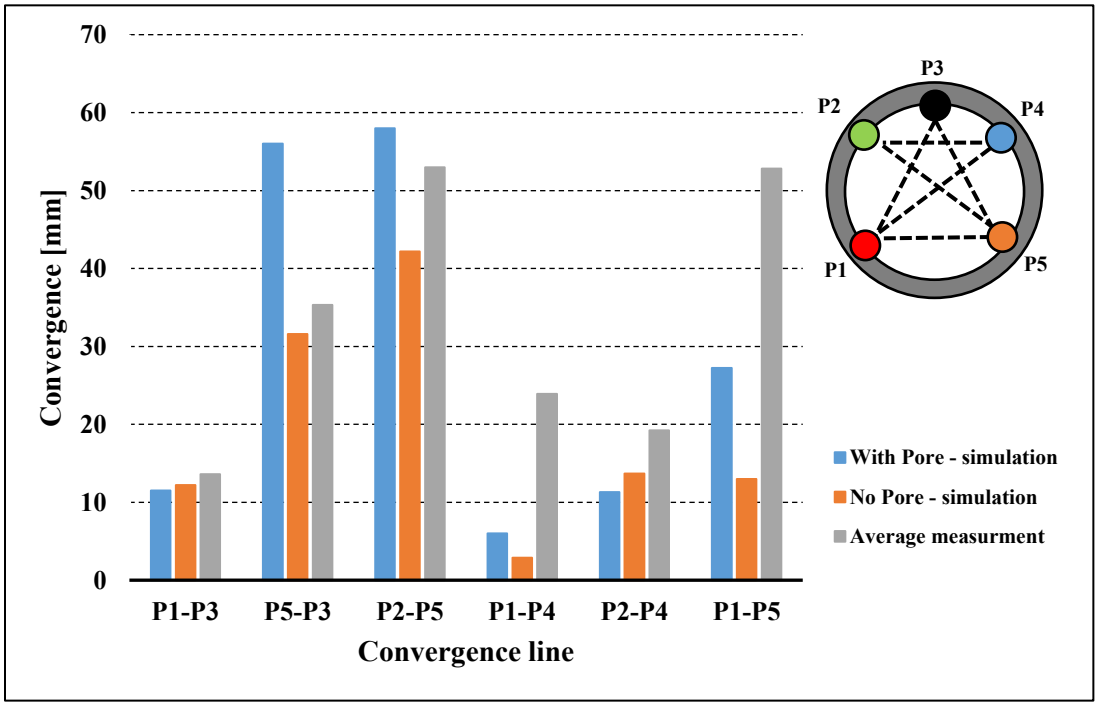

Fig. 6-22 Comparison between the computed convergencs and average measurment, convergence lines are visualized in the legend

The evolution of the vertical displacements is shown in Fig. 6-23. The obtained vertical displacements for BEFA-10 is 8.15 mm while it is about 8.5 mm for BEFA-11 which is consistent with the analysis presented by Lisjak et al. (2015). Also the computed final vertical deflections for

BEFA-10 and BEFA-11 at equilibrium are in close agreement with the field measurements. The predicted displacements are close to the average measured values at TM28 for inclinometers BEFA-10 and BEFA-11 which are 4.7 and 9 mm, respectively. On the other hand, the predicted values in this simulation are increased compared to the mechanical simulation considering no pore pressure for BEFA-10 and BEFA-11 by 22% and 21.6%, respectively. This indicates the effect of pore pressure on the evolution of the vertical deflection and settlement in general. There is still obvious deviation between the predicted vertical displacements and the average in-situ vertical deflection measured by the inclinometers between TM9 and TM38 considering the displacement recorded at a given section when the excavation face is approximately 9 m away. The corresponding value is about 21.5 mm. As previously mentioned, such underestimation of the vertical deflections could be a result of the selection of the 2-dimensional instead of 3-dimensional analysis, applying different supporting systems along the tunnel axis, and not considering the time dependency.

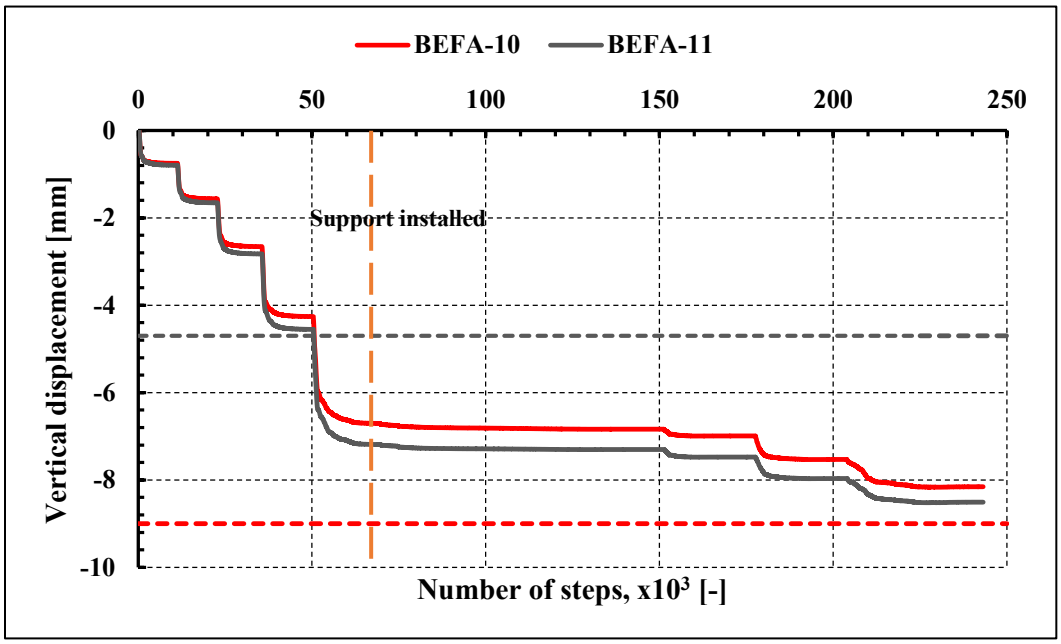

Fig. 6-23 Computed vertical displacements at locations BEFA-10 and BEFA-11 until equilibrium. Doted lines indicate the measured vertical deflections for BEFA-10 and BEFA-11 recorded at the excavation face at TM28.

Regarding the radial displacements, Fig. 6-24 shows the computed values parallel and perpendicular to the bedding planes at equilibrium. Compared to the measured radial displacements in Fig. 6-16 and the predicted values for pure mechanical simulations (Fig. 6-17),

the radial deformations at EXT-02 are still higher than those at EXT-01. Although the predicted displacements at EXT-01 are greater than those for pure mechanical simulation shown in Fig. 6-17, an increase in radial displacement by about 100% near to the tunnel perimeter (at pin P4) is observed. In general, the behavior of the radial displacements between the two simulation methodologies is similar to the Finite/Discrete Element modelling conducted by Lisjak et al. (2015). To visualize the EDZ, the plasticity zones are plotted in Fig. 6-25 showing polar symmetry, similar to the formed EDZ for the mechanical simulation without consideration of pore pressure (Fig. 6-18). The extension of the plastified zones around the opening is larger in case the pore water pressure is considered. The maximum extension of the EDZ is found in direction perpendicular to the bedding plane (P2 and P5) with about 3.5 m from the tunnel wall, while the extension in direction of the sidewalls reaches only 2.5 m.

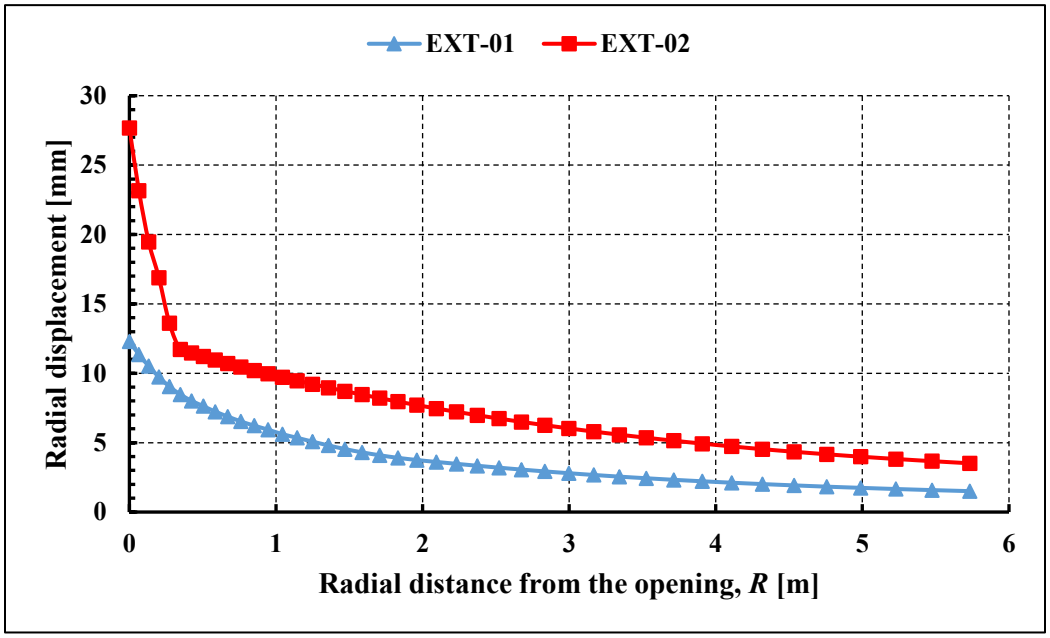

Fig. 6-24 Normalized computed radial displacements at equilliprium along two lines corresponding to the installed extensometers shown in Fig. 6-9

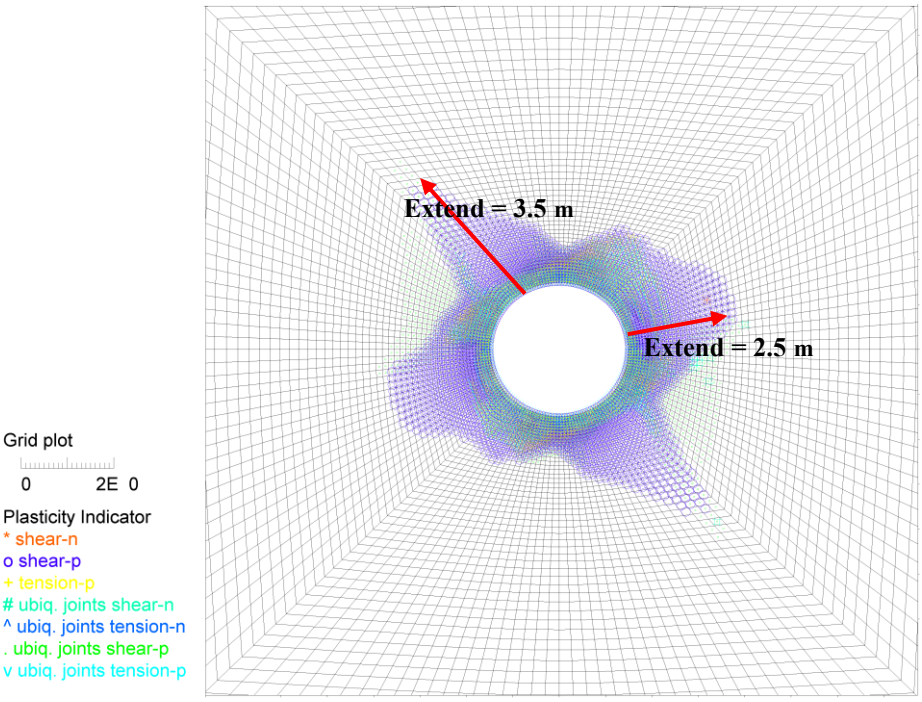

Fig. 6-25 Plasticity indicators showing the extension of the EDZ at equilibrium, 10 m x 10 m model size.

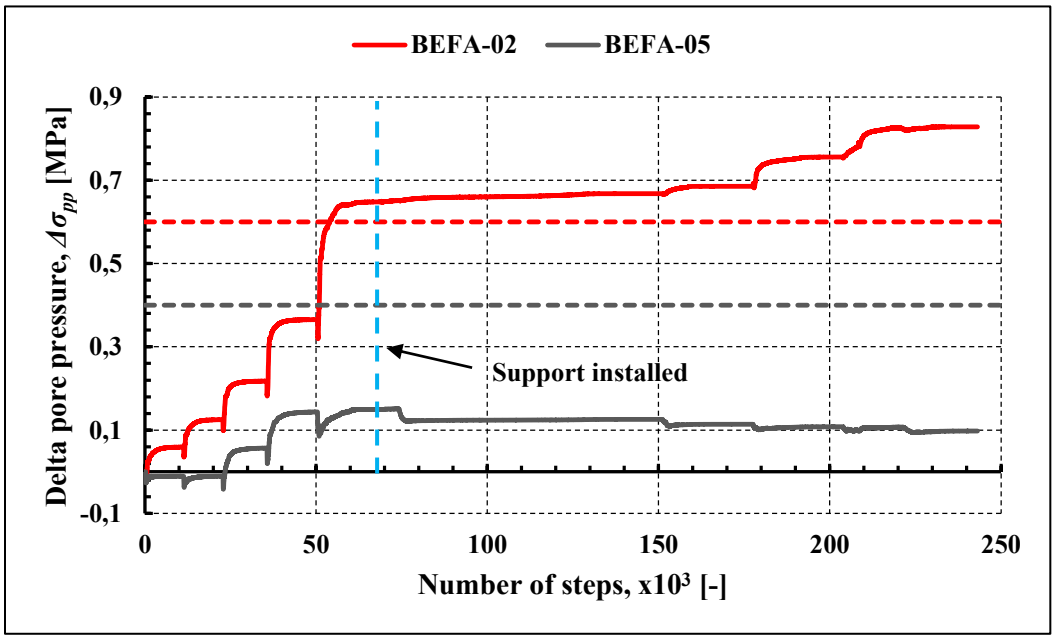

Fig. 6-26 Computed pore pressure change $\Delta\sigma_{pp}$ at locations of boreholes BEFA-02 (parallel to bedding planes) and BEFA-05 (perpendicular to bedding planes) until equilibrium state. Doted lines indicate the maximum measured $\Delta\sigma_{pp}$ at interval midpoints i5 and i4 (BEFA-02 and BEFA-05) recorded close to section TM28.

The computed pore pressures close to the opening are compared with those values measured along the installed boreholes BEFA-02 and BEFA-05 (Fig. 6-9). Two history points were positioned at the same location to record the pore pressure change during the calculation. The location at approximately TM28 close to the installed piezometer interval midpoints i5 and i4 (Fig. 6-7.b) was used. The applied simulation methodology cannot duplicate the variation of pore pressure with real time, thus the computed pore pressures are compared to the maximum average field measurements. Mostly, the hydraulic behavior shows pressure rise as the face is approached followed by a subsequent pressure fall and recovery (Lanyon et al. 2014). Fig. 6-26 shows the variation of the computed pore pressures change at history points located at BEFA-02 and BEFA-05 versus the average insitu results.

Like the field observations, the numerical simulations capture an obvious difference between the pore pressure in direction parallel to bedding planes and the values normal to the bedding planes. The recorded pore pressures parallel to bedding are greater than those in the orthogonal direction which could be explained by the mechanical deformations during the excavation. While the relaxation was applied, regions parallel to bedding planes are less deformed than regions perpendicular to the bedding. As the porosity was assumed constant, the change in pore pressure is mainly a direct consequence of the induced volumetric strains (Fig. 6-27). In conclusion, more detailed time dependent fully coupled hydro-mechanical simulation is required to better model this issue.

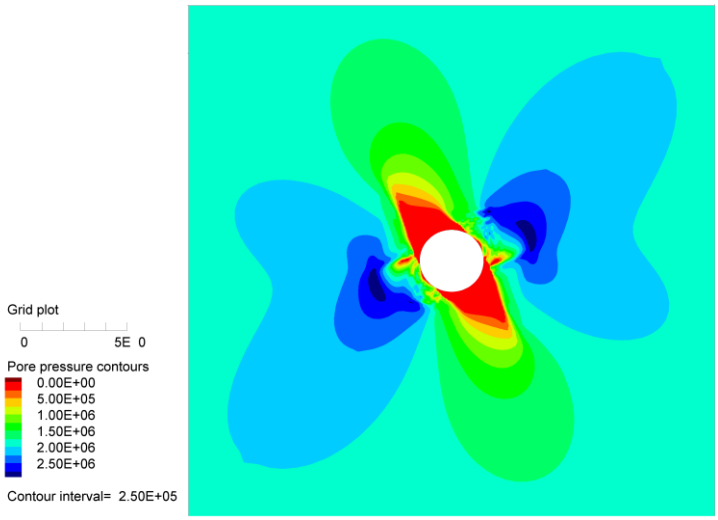

Fig. 6-27 Pore water pressure distribution around excavation at equilibrium showing high pressure values in regions parallel to bedding planes and low pressures perpendicular to the bedding.

6.4. Sensitivity analysis

Usually, strain-softened material behavior is grid dependent due to localization in which the deformation concentrate forming so-called “shear bands”. Thus, sensitivity analysis is performed to investigate the stability of the unlined hole assuming instantaneous excavation with different grid sizes, orientation and inhomogeneity. On the other hand, the simulations presented in sections 6.3.3 and 6.3.4 follow the gradual excavation methodology to minimize the inertial reaction. Another common way assuming that the excavation is made at once will be applied and compared to the results of the simulations considering pore pressure as described in section 6.3.4.

6.4.1. Mesh sensitivity

In case of plasticity grid size and the mesh orientation have remarkable influence on the localization, especially the shear band evolution. Different orthogonal grids – coarse (60 x 60 zones) and fine (140 x 140 zones) – are constructed and used to model instantaneous creation of a circular opening (no relaxation applied, no lining). Same mechanical properties and constitutive model are applied. The localization of shear strain at equilibrium is compared for both grid structures (Fig. 6-28 and Fig. 6-29).

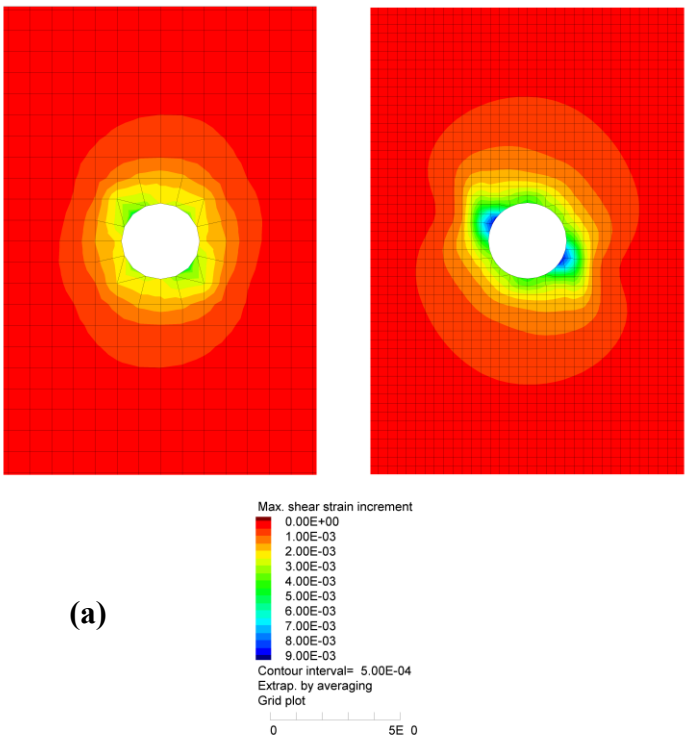

Fig. 6-28 Maximum shear strain at equilliprium (detail with dimension 12 x 18 m) (a) coarse mesh 60 x 60 zones and (b) fine mesh 140 x 140 zones

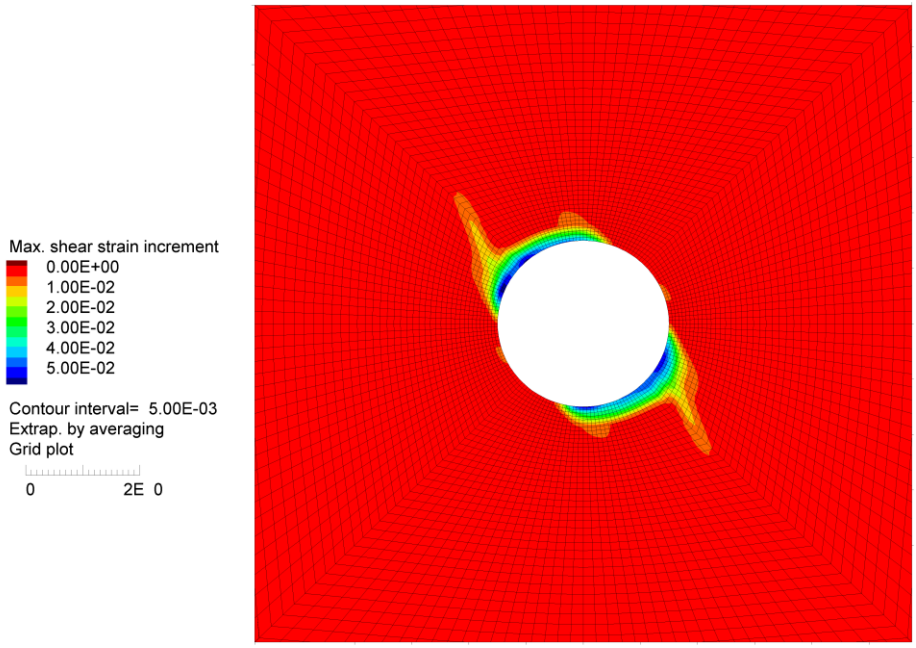

Fig. 6-29 Maximum shear strain (detail with dimension 12 x 18 m of the original grid).

As depicted from Fig. 6-28 and Fig. 6-29, grid structure and orientation have great influence on the developed maximum shear strain. In the coarse grid (Fig. 6-28.a) the shear strain localization can hardly be recognized. The radial mesh with high resolution as used for the mechanical simulations documented in sections 6.3.3 and 6.3.4 shows much better localization effects (Fig. 6-29). This simple mesh study documents, that mesh-independency is not realized. Therefore, calibration is performed and only valid for specified mesh size and structure. This restriction can be avoided if internal length scale parameter would be integrated into the constitutive model.

6.4.2. Effect of sudden excavation on pore pressure

Grid and material properties for the simulation are the same as given in chapter 6.3.4. The difference between gradual and sudden excavation with simultaneously installation of lining is investigated. Fig. 6-30 and Fig. 6-31 indicate that the differences between both modelling methodologies are small. The produced total displacements for gradual relaxation are slightly higher than for suddenly excavated openings especially at sidewalls and at right hand side of the opening where pin P5 is located, see also Fig. 6-21. Otherwise the evolution of the pore water pressure is almost identical for both excavation methodologies. However, the suddenly excavated model indicates higher pore pressure in direction parallel to the bedding planes (σ_{pp} = 3 MPa). Such similarity in results between both models can be explained by the explicit time-marching

calculation scheme of FLAC. The used timestep is always very small to assure that the nonlinear response due to the unloading follows a valid physical way.

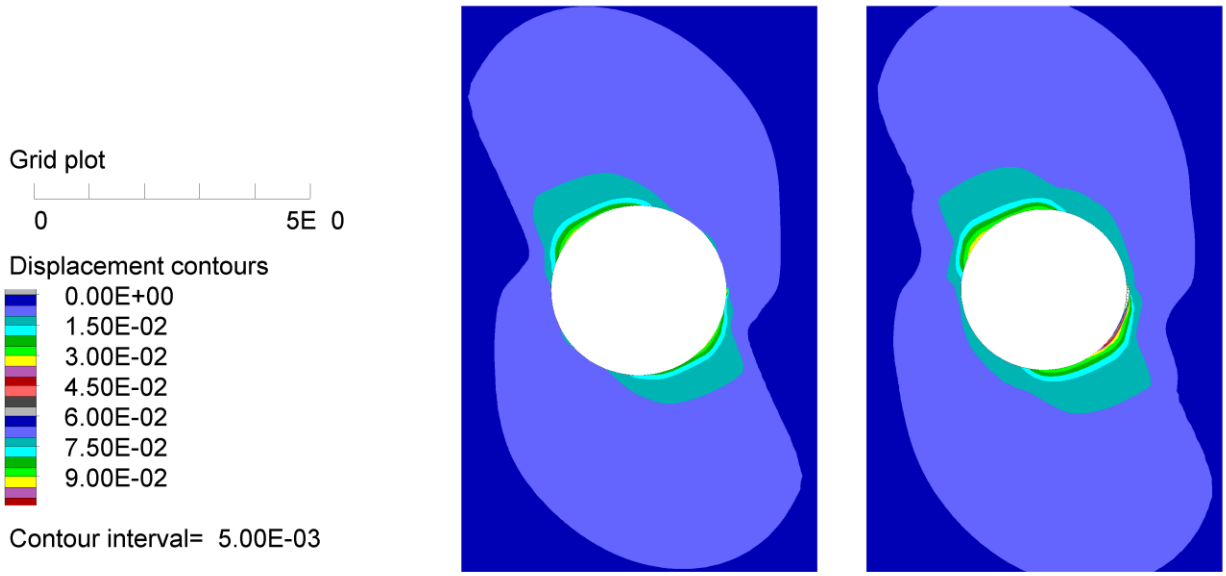

Fig. 6-30 Total displacements around the circular opening at equilliprium for (a) sudden excavation and (b) gradual excavation.

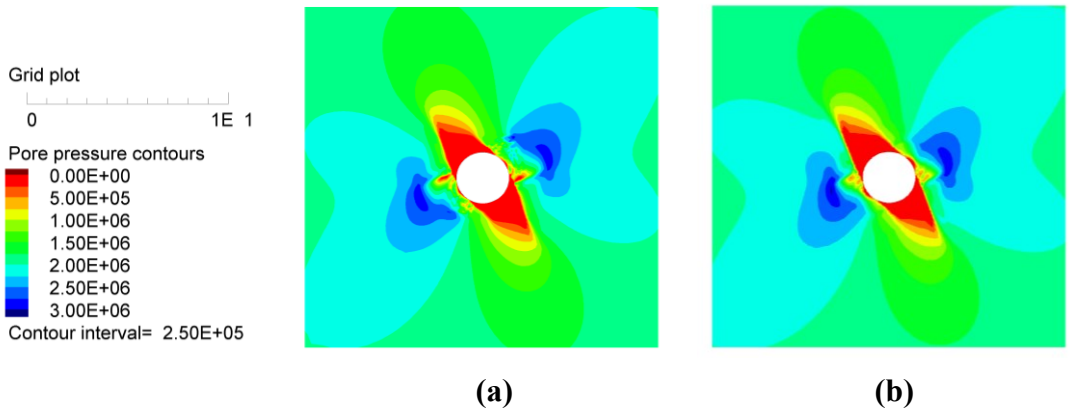

Fig. 6-31 Evolution of pore pressure around opening at equilliprium for (a) sudden excavation and (b) gradual excavation

6.5. Conclusion

The short-term deformation behavior of a 3 m diameter tunnel excavated as part of the long term experiment called "Full-scale Emplacement (FE)" is simulated. The tunnel was excavated in shaly facies Opalinus clay and its axis is parallel to the bedding planes with dip angle ($\alpha = 33^o - 40^o$). The tunnel length is 50 m in which 4 different support systems have been used. The studied section was at 28 m depth from the tunnel portal and supported by a 16 cm thick shotcrete layer.

Owing to the mentioned excavation sequence by Müller et al. (2017) and the insitu measurements (Lisjak et al. 2015), gradual excavation was used for the numerical simulation of the tunnel. The support system was installed after 50% of computed convergences. The undrained mechanical simulations without consideration of pore water pressure showed good agreements with the FDEM analysis performed by Lisjak et al. (2015). On the other hand, simulations considering the pore water pressure as a function of volumetric strain was carried out and resulted in even better results compared to the field data. Generally, the simulated EDZ is in close agreement compared to numerical studies and field observations.

Finally, a sensitivity analysis in respect to grid dependency and excavation sequence was executed. For strain softened material like Opalinus clay, grid structure and resolution play an important role. Strain localization and formation of shear bands are highly grid dependent. Best results are found for radial symmetric grid. Also, different excavation methodologies have been applied: sudden and gradual excavations. The effect of these excavation method was analyzed in terms of displacements and generated pore water pressure around the excavation. It was found that both methodologies showed only minor differences.

7. Ubiquitous joint model based on the Hoek-Brown failure criterion

7.1. Introduction

The development of appropriate constitutive models is one of the key issues for reliable predictions in rock mechanics and rock engineering. Salager et al. (2013) emphasize the importance to fully capture the stress-strain behavior of anisotropic rocks and also the current limitations of various anisotropic rock failure criteria. The directional variation of strength for rocks has been experimentally verified under different loading conditions (i.e. under uniaxial or triaxial compression) by many researchers (e.g. Jaeger 1960; Donath 1964; Hoek 1964; Walsh and Brace 1964; Chenevert and Gatlin 1965; McLamore and Gray 1967; Horino and Ellickson 1970; Attewell and Sandford 1974; Brown et al. 1977; Ramamurthy et al. 1993; Niandou et al. 1997; Duveau and Shao 1998; Saroglou and Tsiambaos 2008). A full assessment of the mechanical anisotropy of inherent anisotropic rocks was provided by Fereidooni et al. (2016), especially considering cohesion and friction angle. Within this thesis, the term 'inherent anisotropic rock' means transverse isotopic fabric rock like slate or shale. However, most of those studies are empirical and only applicable for specific rocks under certain loading conditions.

For transverse isotropic rocks, the directional variation of the strength has been extensively studied (Ramamurthy 1993; Tien and Kuo 2001; Ramamurthy and Arora 1994; Bagheripour et al. 2011), see Fig. 7-1. Jaeger (1960) and Donath (1964) have only considered the potential of sliding failure on the joint and did not consider the non-sliding failure, which leads to an U-shaped failure criterion as shown in Fig. 7-1.a. Later, this approach has been extended based on the Mohr-Coulomb failure criterion to include also non-sliding failure resulting in a shoulder-shaped failure criterion (Jaeger and Cook 1979). For uniaxial compressive loading the shoulder-shaped curve gives equal strength values for both sides of the non-sliding failure area. Most of the experimental studies show maximum strength at $\beta = 90^{o}$ (β is the angle between the main loading direction and orientation of anisotropy plane). The minimum strength is noticed at $\beta = 30^{o} - 45^{o}$ (Tien and Kuo 2001). However, as shown in Fig. 7-1.b, the strength at both shoulders is not equal if confining pressure acts. The third typical failure type valid for rock with more than one joint set is undulatory or wavy shaped, as shown in Fig. 7-1.c. Usually the directional strength variation is a function of

both, the degree of the strength anisotropy and the value of the confining pressure (Nasseri, Rao and Ramamurthy 1997). In case of rocks with higher degree of anisotropy, it is likely that the strength variation follows the U-shoulder shape or the abstracted shape given in Fig. 7-1.d (Duveau and Shao 1998).

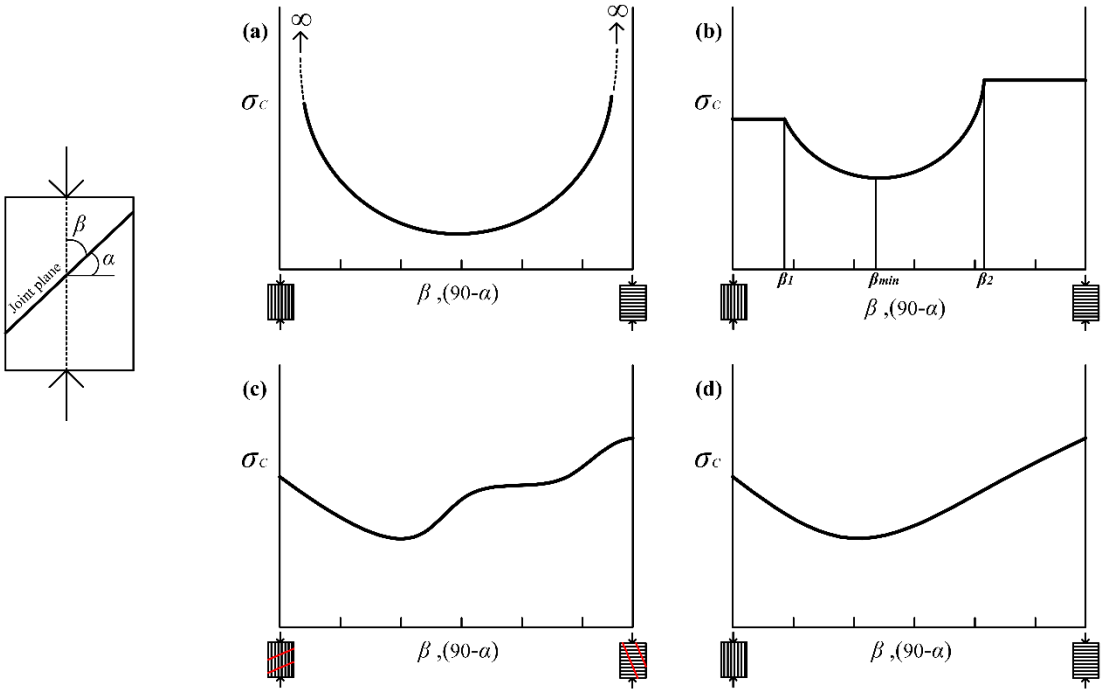

Fig. 7-1 Schematics showing the compressive strength anisotropy vs. angle β (a) Jaeger's definition – U-shape, (b) Extended Jaeger's solution – shoulder-shape (Duveau and Shao 1998), (c) Wavy or undulatory type, and (d) simplified or abstracted shape (Nasseri, Rao and Ramamurthy 1997).

The failure modes of inherent anisotropic rocks under uniaxial and various triaxial stress conditions have been discussed extensively by different scholars (Donath 1964; McLamore and Gray 1967; Niandou et al. 1997). Ambrose (2014) utilized CT scanning and thin sections of the Bossier shale to investigate the failure modes under different confinement. All of these investigations showed that failure modes can be categorized into two different types. On the one hand, failure through the rock matrix, also called "non-sliding mode", is observed. The analytical solution of Jaeger and Cook (1979) assumes that the rock matrix strength is a constant value, but experiments showed different strength values for the matrix depending on loading angle β. McLamore and Gray (1967) introduced a simple function to explain the variation of the matrix strength in dependence on the angle β. In a similar way Duveau and Shao (1998) combined the

non-linear Barton failure criterion with the analytical solution of Jaeger and Cook (1979) to adjust the variability of the strength in the non-sliding region. On the other hand, failure along the inherent planes of weakness, also called "sliding-mode" can occur. Such mode was successfully explained already by Jaeger (1960) and therefore it is included in different solutions to describe the strength behavior of anisotropic rocks. The explained failure modes of inherent anisotropic rocks are similar to those found for artificial interlayered materials documented by Tien and Kuo (2001) and Tien et al. (2006). However, the scope of this chapter is the strength anisotropy of rocks possessing a natural single set of anisotropic planes, i.e. schistose, bedded, foliated and laminated rocks. The weakness planes of such rocks cannot explicitly considered in either analytical or numerical solutions because those planes are found everywhere within the rock and therefore they are called "ubiquitous joints" (Wang and Huang 2009).

7.2. Anisotropy of Hoek-Brown failure criterion

The Hoek-Brown (H-B) failure criterion is an empirical formulation which is governed by three material parameters: m, s and σ_{ci}. The rock parameter s refers to the quality of the rock: for intact rock (s=1) and for crushed pieces (0 < s < 1). Thus, the corresponding equation can be written as follows:

$$\sigma_1 = \sigma_3 + \sigma_{ci}\left(m_i \frac{\sigma_3}{\sigma_{ci}} + 1\right)^{0.5} \qquad (7.1)$$

Where, σ_1 and σ_3 are the maximum and minimum principal stresses. σ_{ci} is the uniaxial compressive strength of the intact rock matrix and m_i is a material parameter which expresses the interlocking and friction between the particles (Hoek and Brown 1980). In case of transverse isotropic rocks, it was found that both, σ_{ci} and m_i are dependent on the orientation of the applied loading to the orientation of the anisotropy plane. The consideration of the anisotropic strength characteristics using the H-B failure criterion can be performed by direct or indirect modifications. Direct modification means that a factor or a parameter is added into the original formulation to account for the strength anisotropy while keeping the material parameters constant in terms of their orientation (Bagheripour et al. 2011; Ismael et al. 2014; Saroglou and Tsiambaos 2008). Indirect modification means that empirical functions are used to modify the material parameters (m_i or s or both) according to the orientation angle (Colak and Unlu 2004; Hoek and Brown 1980). Eq. 7.2 shows the indirect formulation of anisotropic H-B criterion.

$$\sigma_1 = \sigma_3 + \sigma_{c\beta}(m_\beta \frac{\sigma_3}{\sigma_{c\beta}} + 1)^{0.5} \qquad (7.2)$$

Most of these modifications of the H-B failure criterion are empirically formulated and work exclusively for the tested rocks and cannot be generalized. An overview about the latest direct and indirect anisotropic H-B failure criteria have been provided by Ismael et al. (2015) and Shi et al. (2016).

This chapter focuses on the indirect approach to provide an anisotropic H-B based constitutive model. The approach is known as composed failure criterion or discontinues failure criterion according to Duveau et al. (1998), in which two different failure criteria are merged to describe both, the sliding and the non-sliding modes of failure.

The pioneering work in this context is those by Hoek (1983) who assumed that the strength of the rock matrix follows the isotropic H-B failure criterion and for the joint planes the Jaeger solution for a single plane of weakness is adopted. Later, Amadei and Savage (1989) proposed a multiaxial composed failure criterion in which the isotropic H-B failure criterion is used for the intact rock matrix (i.e. $s = 1$, m_i and σ_{ci} are constants), while the Coulomb criterion with complete tension cut-off is applied for the joints. This approach has the advantage to consider the complete triaxial stress state, whereas the original H-B failure criterion considers only the minimum and maximum components. However, the shortcomings of this model are: the failure in the rock matrix is still isotropic and the tensile strength of the joint is restricted to zero.

Another composed failure criterion for transverse isotropic rocks in which the joint is represented by Jaeger's weakness failure plane modified by a degradation of cohesion and friction angle according to the orientation (Tien and Kuo 2001). For the matrix failure an empirical maximum axial strain criterion derived from the H-B failure criterion is used. The strength of the rock matrix is dependent on the orientation as two empirical parameters (k and n) were introduced by which the strength of the rock matrix is controlled. This criterion was successfully tested at several uniaxial and triaxial lab data and showed good agreement. However, this criterion cannot explain the severe change of the curvature at points where the failure is changing from non-sliding to sliding. Also, there is a difficulty regarding the determination of the anisotropy parameter (n) which plays a critical role in the non-sliding failure region.

Furthermore, Lee and Pietruszczak (2008) proposed a three-dimensional H-B failure criterion based on the critical plane approach (CPA) published earlier by Pietruszczak and Mroz (2001).

The matrix strength is anisotropic with directional parameters (m_β and s_β) utilizing distribution functions for both parameters, while the sliding failure mode is described by a local form of the H-B criterion in terms of traction components on the plane. In principle, this approach computes the failure under consideration of the orientation. This model incorporates the effect of the intermediate principal stress as well. Compared to the lab results from Martinsburg slate (Donath 1964), the simulation results show good agreement in relation to the sliding failure, but there is some discrepancy regarding the strength predication of the rock matrix, especially at β=15°. Also, the applied compressive strength is a constant value.

Recently, the H-B failure criterion has been extended by Lee et al. (2012) to consider the inherent strength anisotropy based on the microstructure-tensor approach proposed by Pietruszczak and Mroz (2000). The uniaxial compressive strength is supposed to be orientation dependent while the rock parameter m_i is constant. The intermediate principal stress σ_2 is also considered in that work. The simulation results show the noticeable effect of σ_2 on the formation of the failure planes. On the other hand, this failure criterion could not duplicate the post failure behavior or the orientation dependency of m_i.

Generally, all the above discussed H-B model variants are only failure criteria and do not provide a full description of the stress-strain relations for anisotropic rocks. Therefore, this chapter introduces a complete constitutive model (i.e. elastic-perfect-plastic in terms of classical plasticity theory) consisting of two combined approaches to describe both failure modes of inherent laminated rocks. For the sliding failure mode along the inherent anisotropy planes, the ubiquitous joint approach (Ubi) is adopted. On the other hand, the modified H-B criterion is used to capture the failure in the rock matrix. In the anisotropic constitutive model, the rock parameter m_i is a function of β by using the distribution function given by Lee and Pietruszczak (2008).

7.3. Proposed H-B model framework (*Jhoek model*)

The developed constitutive model is the result of combining two different approaches to describe the non-sliding and the sliding failure modes. The non-sliding failure mode is described according to the adjusted H-B failure criterion and the sliding mode follows the ubiquitous joint approach. Below the newly developed model is called “Jointed Hoek-Brown constitutive model” (Jhoek model) which is qualified to capture the strength anisotropy and to simulate the full stress-strain behavior.

7.3.1. The H-B Model for rock matrix

The Jhoek model is quite similar to the Mhoek model in (Itasca 2016) and it is considered as an alternative version of the Hoek-Brown constitutive model based on the work of Cundall et al. (2003). The Mhoek model includes a tensile yield criterion and allows to specify a dilation angle. Compared to the Hoek model, the Mhoek model provides a simplified and suitable flow rule for both, tensile and compressive regions. The simplicity of the Mhoek model is based on a continuous approximation of the non-linear H-B failure criterion by the linear Mohr-Coulomb failure surface. This approximation is defined as tangent at the H-B failure envelope for the current acting σ_3 value, as shown in Fig. 7-2.a. In case of tensile stress, the tangential M-C line at $\sigma_3 = 0$ is extended and intersects with the vertical line at $\sigma_3 = -s*\sigma_{ci}/m_b$, which works as tension cut-off part as shown in Fig. 7-2.b. The yield surface of the Mhoek model uses the general formulation of the H-B failure criterion according to Eq. 7.3.

$$\sigma_1 = \sigma_3 + \sigma_{ci}(m_b \frac{\sigma_3}{\sigma_{ci}} + s)^a \tag{7.3}$$

For the current stress level σ_3, a linear approximation of the M-C failure criterion is performed:

$$\sigma_1 = \sigma_3 N_{\phi a} + 2c_a \sqrt{N_{\phi a}} \tag{7.4}$$

$$N_{\phi a} = \frac{1+\sin\phi_a}{1-\sin\phi_a} \tag{7.5}$$

where; c_a and ϕ_a are the apparent cohesion and friction angle, respectively. Actual cohesion and friction values for each timestep are evaluated using the following equations:

$$\phi_a = 2\tan^{-1}\sqrt{N_{\phi a}} - 90^o \tag{7.6}$$

$$c_a = \frac{\sigma_a^{ucs}}{2\sqrt{N_{\phi a}}} \tag{7.7}$$

The values of the parameters $N_{\phi a}$ and σ_a^{ucs} are numerically computed based on the assigned H-B parameters and the current value of σ_3.

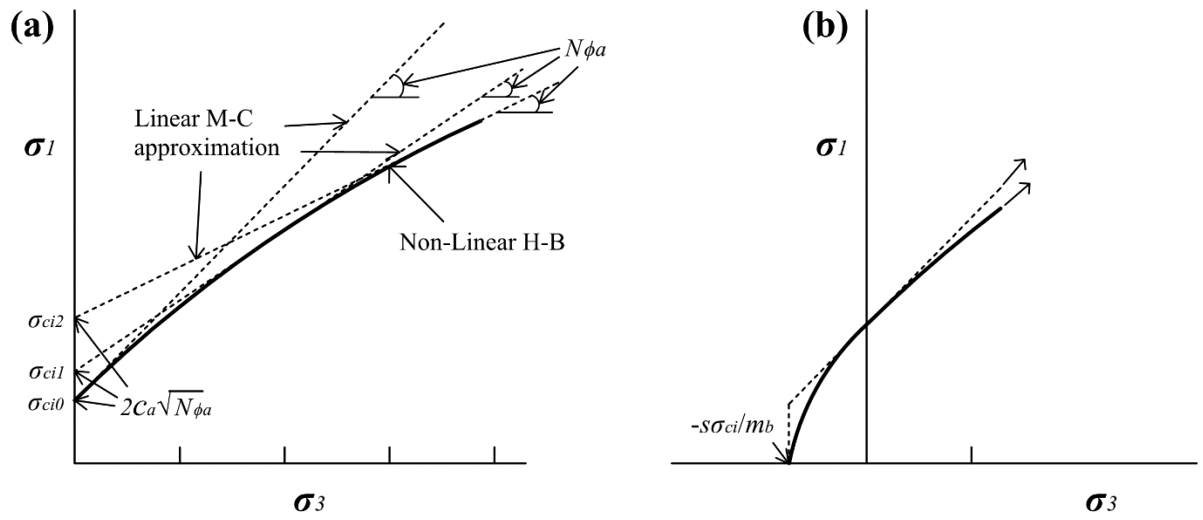

Fig. 7-2 Sketch of failure envelope (a) linear approximation of non-linear H-B yield surface at any applied σ_3 and (b) tension cut-off part, after (Itasca 2016).

The original Mhoek model is altered to simulate the failure in the rock matrix in which the H-B parameters *s* is 1.0 and *a* equals 0.5 assuming the rock matrix is totally intact. The rock parameter m_b is orientation dependent (becomes m_β) and its value is determined either by lab testing or values from the distribution function which is discussed later in section 7.3. Based on this modification, the numerically computed M-C parameters depend on both, the orientation of the inherent anisotropy planes and the confining pressure. Also, the uniaxial compressive strength σ_{ci} is orientation dependent (i.e. $\sigma_{ci\beta}$). For simplification, the proposed model however requires only the values of σ_{ci} at β=0° and β=90°. Thus, the governing failure criterion can be written as follows:

$$\sigma_{1\beta} = \sigma_3 + \sigma_{ci,\beta=0}\left(m_\beta \frac{\sigma_3}{\sigma_{ci,\beta=0}} + 1\right)^{0.5} \quad \text{for } 0 \le \beta < \beta_{\min} \tag{7.8a}$$

$$\sigma_{1\beta} = \sigma_3 + \sigma_{ci,\beta=90}\left(m_\beta \frac{\sigma_3}{\sigma_{ci,\beta=90}} + 1\right)^{0.5} \quad \text{for } \beta_{\min} \le \beta < 90 \tag{7.8b}$$

This modified H-B failure criterion works well for the strength prediction of anisotropic rocks, especially for regions ($0^o \le \beta \le \beta_1$) and ($\beta_2 \le \beta \le 90^o$), see Fig. 7-1.b. This goes beyond the modified analytical solution by Jaeger and Cook (1979) and the Ubi model found in FLAC (Itasca 2016) in which the strength parameters are constant as the rock matrix is considered as isotropic. The variation of the rock parameter m_β with orientation guarantees the anisotropy in strength in the rock matrix.

7.3.2. The ubiquitous joint approach

Similar to the work of Tien and Kuo (2001) and the Ubi model, the proposed Jhoek model uses the superposition principle to transfer the global stress state to the local stress state according to the orientation of the inherent anisotropic planes. The converted stress state allows to test for sliding along those planes. Normal and shear stresses acting on those planes are considered. The applied failure criterion is a shear strength criterion. The joint plane strength depends on the assigned parameters: joint cohesion (c_j) and joint friction angle (ϕ_j). From Eq. 7.9, the strength is orientation dependent and reaches its minimum value at β_{min} (Fereidooni et al. 2016; Hu et al. 2013). The failure criterion can be expressed considering the confinement as follows:

$$\sigma_{1\beta} = \sigma_3 + \frac{2c_j + \sigma_3 \tan\phi_j}{(1 - \tan\phi_j \tan\beta)\sin 2\beta} \quad \text{for } \beta_1 \le \beta < \beta_2 \qquad (7.9)$$

Assigning the strength parameters is described in detail previously in Tien and Kuo (2001). However, the proposed model demands the quantification of additional parameters, such as: tensile strength and dilation angle of the joints.

7.3.3. Orientation dependency of parameter m_β

As has been mentioned before, the rock parameter m_β is orientation-dependent which needs assignment for each β. However, it is not applicable to evaluate this parameter for each β or for small intervals such as ($\Delta\beta = 5^o$ or 10^o). Thus, it is logical to normalize the values of m_β by a spatial distribution function based on the proposed technique by Lee and Pietruszczak (2008). This approach has been conducted for the spatial variation of the friction angle and cohesion of transverse isotropic rocks. As mentioned in (Lee and Pietruszczak 2015), the exponential spatial distribution function proposed in (Lee and Pietruszczak 2008) is more suitable for higher degrees of anisotropy than the polynomial approximation given by Pietruszczak and Mroz (2001). In this work, the utilized function from Lee and Pietruszczak (2008) is altered considering the loading angle β instead of using the orientation angle α or dip angle which is defined as the angle between the bedding plane and the horizontal axis, see Fig. 7-1. As $\beta = 90^o - \alpha$, $\cos^2\alpha$ is modified to $\sin^2\beta$. This recent research utilizes explicitly (i.e. not implicitly included into the Jhoek model) the special distribution function which normalizes the values of m_β according to the orientation β. The spatial distribution function consists of two wings: the left wing distributes the m_β values from m_0 to m_{min}, while the right wing is for the values between m_{min} and m_{90}. The following equation explains the implementation of the spatial distribution function:

$$m_\beta = a_1 + a_2 Exp[\Omega_0(1-3\sin^2\beta)] \quad (7.10)$$

where Ω_0 is the principal coefficient of the second order tensors describing the spatial distribution ($\Omega_0 = \Omega_{11} = \Omega_{33}$). The assigned value for Ω_0 has a great influence on the distribution of m_β and offers three different values (- 0.1, - 1.0 and - 5.0). The direction independent coefficients (a_1 and a_2) could be determined as follows:

$$a_1 = \frac{m_{\max} Exp[-2\Omega_0] - m_{\min} Exp[\lambda\Omega_0]}{Exp[-2\Omega_0] - Exp[\lambda\Omega_0]} \quad (7.11a)$$

$$a_2 = \frac{m_{\min} - m_{\max}}{Exp[-2\Omega_0] - Exp[\lambda\Omega_0]} \quad (7.11b)$$

$$\lambda = 1-3\sin^2\beta^* \quad (7.11c)$$

Similar to Lee and Pietruszczak (2008), the constant λ is evaluated based on the assigned β^* of 70°. The presented spatial distribution formulation of m_β could be applied for both wings as specified previously. In case of the left wing (m_0 to m_{min}), the value of m_{max} could be assumed as m_0. On the other hand, the value of m_{max} could be assumed as m_{90} for the right wing. The value of Ω_0 could not be the same for both wings and depends on the best fit of the distribution with the lab test results. However, in this work a single value of Ω_0 is assumed for both wings. m_{min} refers to the minimum value of m_β, and is assumed to be at β = 30° or 45°. This distribution function provides a non-symmetric polynomial normalization of the rock parameter m_β along β assuming that the values of m_{max} are found at β = 0° and 90°. Although this assumption is hypothetically satisfactory for anisotropic rocks, the real practicing with anisotropic rocks shows different behavior: the maximum value is sometimes found at $\beta \neq 0°$ or 90° (Colak and Unlu 2004).

The applicability of this formulation is tested on some inherent anisotropic rocks from the literature to normalize m_β values (Table 7-1). The triaxial lab test data were processed to evaluate the value of m_i for different orientation β using RocLab (Rocscience 2011b). RocLab 4.0 (Rocscience 2016) is a specific tool to perform a regression to get the parameters m_i and σ_{ci} for certain strength data sets while s is set to 1 as the tests are conducted on intact rocks and not on a rock mass.

Table 7-1: Spatial distribution of m_β deduced from rock sample data

Rock type	m_{90}	m_0	m_{min}	β_{min}	$\Omega_{0\text{-}Best}$ [Omega]
Martinsburg Slate (Donath 1964)	14.22	11.54	1.1	30°	-0.1
Angers Schist (Duveau et al. 1998)	10.74	14.86	1.65	30°	-0.1
Austin Slate (McLamore and Gray 1967)	5.72	6.56	2.54	40°	-0.1 or -1.0
Green River Shale I (McLamore and Gray 1967)	6.99	6.7	6.2	30°	-5.0
Penrhyn slate (Attewell and Sandford 1974)	9.9*	8.81	3.07** or 2.48	60°** or 30°	-0.1
Tournemire Shale (Niandou et al. 1997)	4.33	4.5	2.65	30°	-1.0 or -5.0

** Most references stated that m_{90}=6.23. However according to the analysis of the triaxial lab data of Penrhyn slate from* (Pei 2008) *a value of m_{90}=9.9 is obtained. This value fits well with the RocData 4.0 plots* (Rocscience 2016). *Also, the ratio of the variation of m_β values follows the ratio from* (Saroglou and Tsiambaos 2008b). *** The best selected value of β_{min} is at $\beta = 60^o$, although at $\beta = 60^o$ it is not the lowest value of m_i.*

As shown in Fig. 7-3, the spatial distribution function gives an approximation of the values of m with the orientation according to parameters given in Table 7-1. However, the lab results show some slight misfit to this distribution as there are values greater than the values at m_0 and m_{90}. Also, this distribution function overestimates slightly the m_β value for β = 45° – 75°. Moreover, the dependency of the distribution on the applied value of Ω_0 is quite strong. A parametric study on Ω_0 was conducted by Lee and Pietruszczak (2008) which revealed a great influence of the selected Ω_0 value on the shape of the H-B failure criterion envelope for different applied confinements especially for rock matrix failure.

As shown in Fig. 7-3, the determination of Ω_0 plays a significant role for the shape of the spatial distribution function (m_β). Thus, it is recommended to perform a calibration of Ω_0 against experimental data to get the best fit. The greater the anisotropy, the greater the fluctuation of the spatial distribution function and therefore the greater the value of Ω_0. For example, the Green River shale I which possesses low strength anisotropy according to Ramamurthy strength anisotropy classification Ramamurthy (1993) (i.e. Rc = 1.4) Ω_0 is -5.0 (very low). However, for high to very

high anisotropic rocks such as: Martinsburg slate with Rc value > 8 or Penrhyn slate with Rc value ≈ 4.85 the value of Ω_0 is -0.1 (very high).

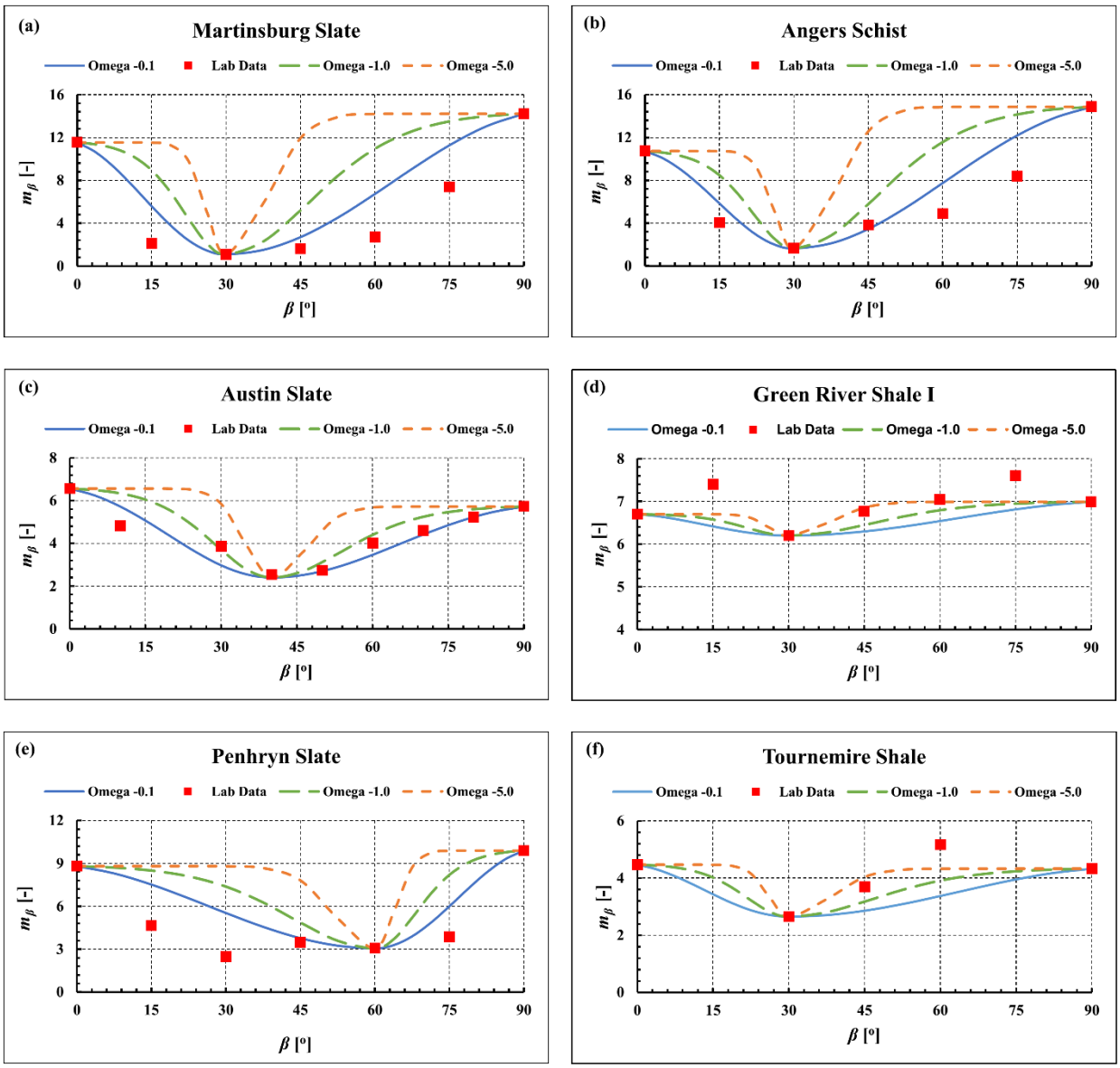

Fig. 7-3 Spatial distribution of parameter m for various anisotropic rock samples with different applied Ω_0 values.

7.4. Model implementation

This part contains a detailed description of the implementation of the developed constitutive model, which consists of two distinct parts: one for the rock matrix by applying the non-linear modified H-B failure criterion and the other which is a ubiquitous joint approach.

7.4.1. Model parameters

The model can be used with associated or non-associated flow rule for the rock matrix similar to the original model Mhoek (Itasca 2016). Table 7-2 specifies the required model parameters. As shown in Table 7-2, new parameters in the Jhoek model compared to the Mhoek model are: m_β, σ_{ci0} and σ_{ci90} for the rock matrix as well as all parameters for the joints.

Table 7-2 Parameters for Jhoek model.

Rock matrix parameters	**Joint plane parameters**
- Young's modulus and Poisson ratio, - Dilation angle, - Defined tensile strength (Fig. 7-2.b and Eq. 7.12), - Uniaxial compressive strength (σ_{ci0} or σ_{ci90}), according to Eq. 7.8, - Rock parameter (m_β).	- Inclination angle (α) = 90 – loading angle (β), - Joint friction angle (ϕ_j), - Joint cohesion (c_j), - Joint dilation angle (ψ_j), - Joint tensile strength (σ_j^t).

Generally, the selection of the rock matrix dilation angle value is dependent on the applied confinement as the dilation decreases with increasing confining pressure (Ribacchi 2000). In the proposed model, the rock matrix dilation angle could be assigned as a constant value or as a pre-defined fraction of the numerically computed apparent friction angle ϕ_a, as given by Eq.7.6. For excellent to very good quality rock, the value is estimated as $\psi = \phi/4$ (Alejano and Alonso 2005; Hoek and Brown 1997). Generally, by increasing the applied confinement, the H-B failure envelop is softened and therefore the computed apparent friction angle decreases (Eberhardt 2012). Thus, the best way to assign the rock matrix dilation angle is to use a fraction of the friction angle. The variability of the dilation angle against the applied confinement is extensively discussed as well (Zhao and Cai 2010). Moreover, the defined maximum tensile strength is dependent on the specified uniaxial compressive strength and (m_β) value as follows:

$$\sigma^t = \sigma_{ci(0 \text{ or } 90)} \Big/ m_\beta \qquad (7.12)$$

The joint plane parameters friction angle ϕ_j and cohesion c_j should be determined experimentally based on the procedure proposed by Tien and Kuo (2001). Unlike the joint definition by Barton (2013), the M-C approximation of the joint behavior requires the assignment of joint cohesion and tensile strength as well. For the ubiquitous joint model, the assigned joint dilation has not such a noticeable effect as the pre-yield phase exhibits no plasticity and the post failure behavior is perfect

plastic. Consequently, the assigned value for ψ_j is between 0° and 10°. The maximum value for the joint tensile strength is estimated according to (Itasca 2016) as follows:

$$\sigma_j^{\,t} = {c_j}\Big/{\tan\phi_j} \tag{7.13}$$

In general, the inserted values of friction angle, cohesion and dilation for the inherent joint planes do not follow Barton's definitions of rock joints and particularly those for natural joints in rock masses. The joint parameters are usually back-analyzed by numerical simulations or obtained from in-situ measurements. Although the estimation of these parameters does not follow a defined strategy, it is very important to conduct a sensitivity analysis especially in respect to the scale-effect and the applied boundary conditions (Alejano and Alonso 2005).

7.4.2. Implementation sequence

After assigning of model parameters, the numerical calculation sequences starts with testing if the stress state violates the failure envelop. At each step as shown in Fig. 7-4, the failure conditions for both, the rock matrix and the joint plane have to be tested. For the rock matrix, the applied stress state is transformed into the principal state at which the H-B yield surface is defined (see Eq. 7.8). As already mentioned, the non-linear H-B failure envelop is approximated by a tangent linear M-C yield surface at the current applied σ_3 and the M-C rock parameters are evaluated from the assigned H-B rock parameters. If the principal stress state violates the yield surface a correction for the plastic state is required to bring the stress state back to the defined M-C yield surface. For simplicity perfect plasticity is assumed, although in reality rock exhibits ductility and softening.

After handling the plasticity for the rock matrix, the resulting stress state is examined in respect to the sliding failure mode on the joint plane. Thus, the global stress state should be transformed to the predefined local coordinates of this joint plane. Based on the defined M-C yield surface, the failure conditions are tested for either shear or tension. At the local stress state, the plastic corrections are numerically computed and then the stress state is transformed back to the global system. As the stepping in FLAC is an explicit time scheme and the used timestep is always smaller than the critical time step, violation of the yield surface is avoided after the correction, that means at the end of each calculation step.

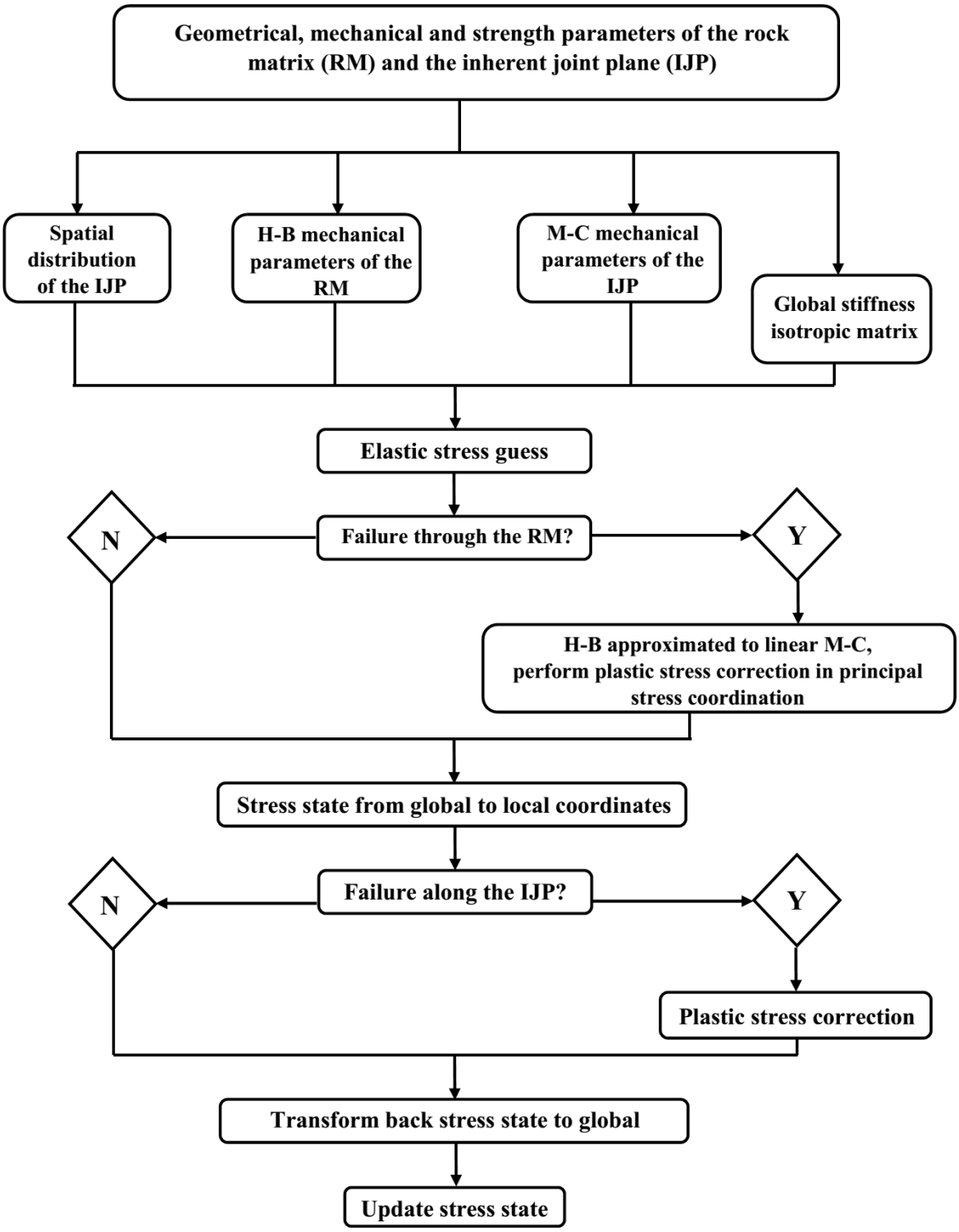

Fig. 7-4 Flowchart for each calculation step of the Jhoek constitutive model.

As illustrated, the stress state is tested first for the non-sliding failure mode and later for the sliding failure mode of the joint plane. As shown in Fig. 7-5, the formed yield surfaces depend on the value of β. For higher confining stresses and when the friction angle of the joint is larger than the friction angle of the rock matrix. As shown in Fig. 7-5.b, the linear M-C failure surface of the joint plane intersects with the H-B failure envelope at higher confinement σ_3. Thus, a complex yield surface is formed describing that sliding failure along the joints occurs as long as σ_3 is lower as at the intersection point, while at higher confinement the sliding failure mode turns into the non-sliding mode of failure.

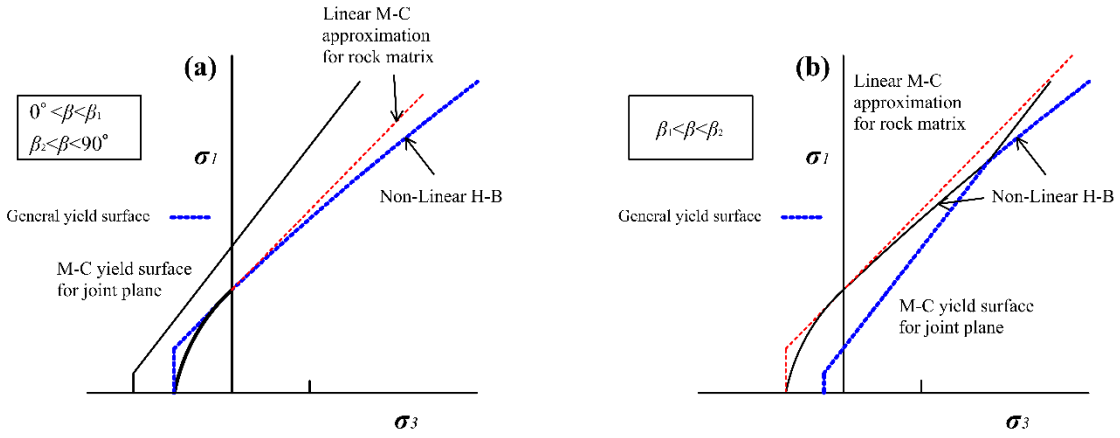

Fig. 7-5 Yield surfaces for (a) failure through rock matrix: non-sliding failure mode, and (b) sliding along the inherent joint planes.

7.5. Validation of the model

Various simulations using different lab data have been conducted to check the applicability of the Jhoek model to simulate the mechanical behavior of inherent anisotropic rocks. The validation of the Jhoek model involves the gneiss B (Saroglou and Tsiambaos 2008) at different loading orientations and a study of the strength anisotropy for several rock samples. Also, simulations of true triaxial tests are used to illustrate the behavior of this model under different values of principal stresses.

7.5.1. Failure envelops for gneiss at different loading angle

The tested gneiss B (Saroglou and Tsiambaos 2008) is an inherent anisotropic rock because it is rich in foliation planes due to the presence of long particles within the fabric (Ismael et al. 2014; Saroglou and Tsiambaos 2008). Triaxial tests with various confining pressures and at different orientation angles regarding the foliation planes and the main loading direction were performed. The given data are not sufficient for the proposed Jhoek model as there are no data about the inherent joint planes. Therefore, the remaining data concerning the joint planes are taken from (Asadi 2016). However, dilation angle and tensile strength are missing. These parameters are assumed reasonably based on previous experience.

Table 7-3 Parameters of gneiss B (Saroglou and Tsiambaos 2008b; Asadi 2016)

Rock matrix parameters							
σ_{c0} [MPa]	σ_{c90} [MPa]	m_0 [-]	m_{30} [-]	m_{45} [-]	m_{90} [-]	ψ [°]	σ^t [MPa]
45.4	85.7	20.4	13.7	9.5	23.2	$\phi_a/4$	2.0
Bedding planes parameters							
c_j [MPa]	ϕ_j [°]	ψ_j [°]	σ^t_j [MPa]				
7.2	33	8	1.7				

The dilation angle of the rock matrix is assumed to be friction angle dependent and the computed friction is a function of the confining stress. The rock matrix tensile strength varies from 2.23 to 3.70 MPa based on Eq. 7.12, but it is fixed here to 2 MPa. Also, the assigned value for the inherent joint plane tensile strength is set to 1.7 MPa in contrast to the computed value according to Eq. 7.13 which gives an unrealistic high value as 11 MPa. The comparison between the lab data for gneiss B at different values of β and the output from the Jhoek model is shown in Fig. 7-6.

It should be noticed that $\beta = 45^o$ mark a transition point at which the failure mode changes from sliding mode to a mixed failure mode, see Fig. 7-7. According to (Niandou et al. 1997; Tien et al. 2006), the mixed failure mode is a combination of rock matrix failure and sliding along the joint planes. This was explained already in Fig. 7-5.b, where the complex yield surface shows an intersection between rock matrix and joint failure planes. Unlike the failure mode at $\beta = 30^o$, for different confinement the yield surface is linear which indicates a sliding failure mode and follows the ubiquitous joint approach.

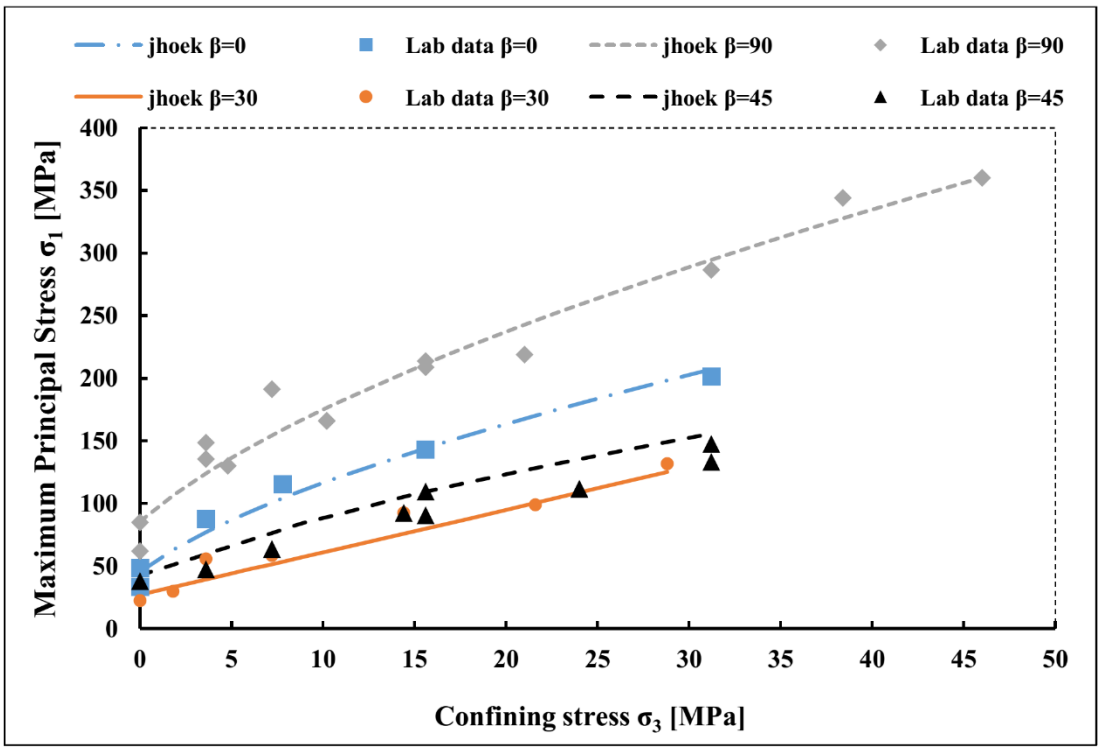

Fig. 7-6 Failure envelops for gneiss B at different β: lab data and Jhoek model.

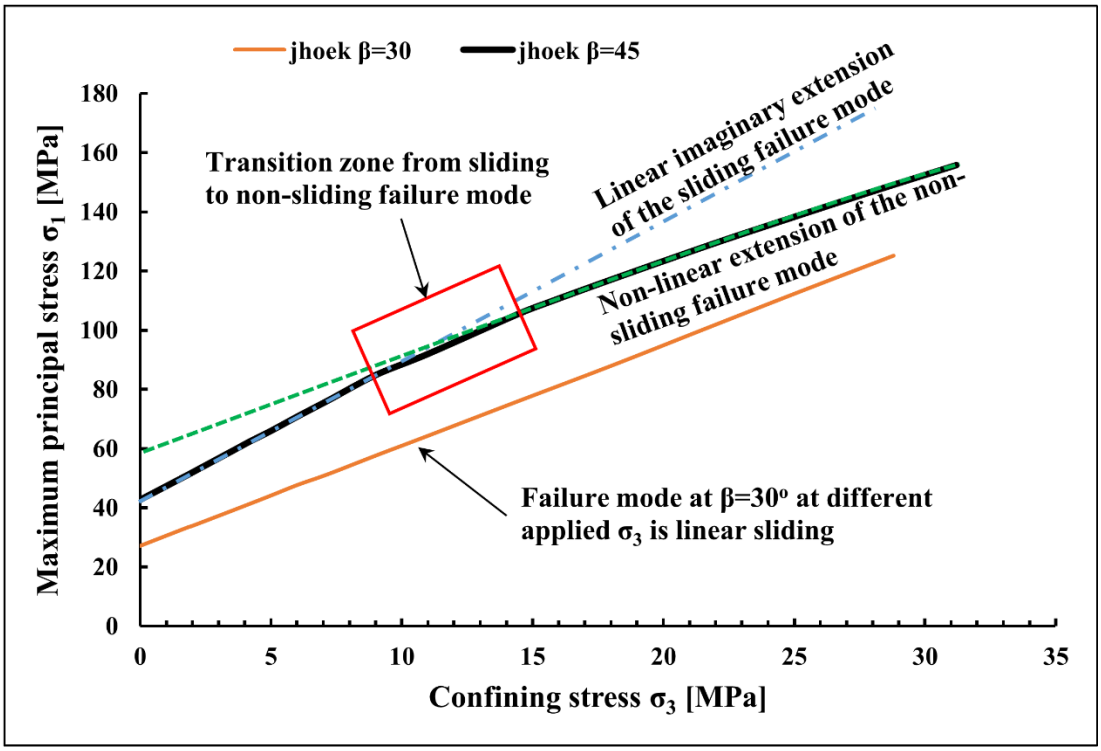

Fig. 7-7 Transition of failure mode from sliding along the inherent joint planes to non-sliding at $\beta = 45^{o}$ under applied $\sigma_3 \approx$ 10-15 MPa.

7.5.2. Strength anisotropy of natural inherent anisotropic rocks

The Jhoek constitutive model is applied to predict the strength for different inherent anisotropic rocks (persistent continuous foliation planes, (Nasseri et al. 1997)) for different orientation angles β and different applied confinement σ_3. In order to predict the mechanical strength for different orientation angles β, the spatial distribution function defined in section 7.3.3 is applied. Therefore, the distributions of parameter m_β shown in Fig. 7-3 are used. The additional required material parameters are given in Table 7-4.

Table 7-4 Assigned parameters for different tested inherent anisotropic rocks (Ambrose 2014; Asadi 2016; Duveau and Shao 1998; Pei 2008; Tien and Kuo 2001)

Rock type	c_j [MPa]	ϕ_j [°]	σ_{c0} [MPa]	σ_{c90} [MPa]	Ω_0
Martinsburg Slate (Donath 1964)	9	21	100	155	-0.1
Angers Schist (Duveau et al. 1998)	4	17	145	165	-0.1
Austin Slate (McLamore and Gray 1967)	31	17	230	195	-0.1
Green River Shale I (McLamore and Gray 1967)	40.5	30	220	200	-5.0
Penrhyn Slate (Attewell and Sandford 1974)	34.3	14	155	175	-0.1
Tournemire Shale (Niandou et al. 1997)	4	36	36	40	-1.0

A comparison between the experimental data and the model results are given in Fig. 7-8 to Fig. 7-13. The lab data are plotted as scattered points while the numerical results are lines, as the assigned $\Delta\beta$ (i.e. = β_{i+1} - β_i) in the numerical simulations for the different anisotropic rock samples is not larger than 7.5°. On the contrary, the lab test data cannot be interpolated for such small intervals of β.

The exhibited shape of the strength variation with orientation angle β fluctuates between shoulder-type and U-type. It is noticed also in (Tien and Kuo 2001), that sliding along the joint is observed according to the single plane of weakness solution of Jaeger. However, there is some fluctuation

regarding the compressive strength in the joint sliding part as shown in Fig. 7-9, Fig. 7-12 and Fig. 7-13. In the region where matrix failure occurs, the modified H-B failure criterion gives a convenient prediction displaying the strength anisotropy with the non-sliding part. According to Eq. 7.8, the predicted σ_1 depends on the assigned values of m_β, $\sigma_{ci\beta}$ and the applied σ_3. For rocks with high variation of m_β: by increasing the value of the applied confining stress, the predicted shape of the failure envelop is different at both shoulders, see Fig. 7-8, Fig. 7-9 and Fig. 7-12. It is observed also and illustrated in Fig. 7-5.b that with increasing confinement a remarkable convergence of the values of β_1 and β_2 is noticed, which indicates a shift from sliding to non-sliding failure at the edges of the U-shaped failure envelope representing sliding on the joint. In agreement with the lab data, there is no significant change of the value of β_{min} at which the value of σ_{1min} is found. Finally, it can be stated, that the proposed constitutive model is able to predict the compressive strength of the tested inherent anisotropic rocks under different applied confining stresses.

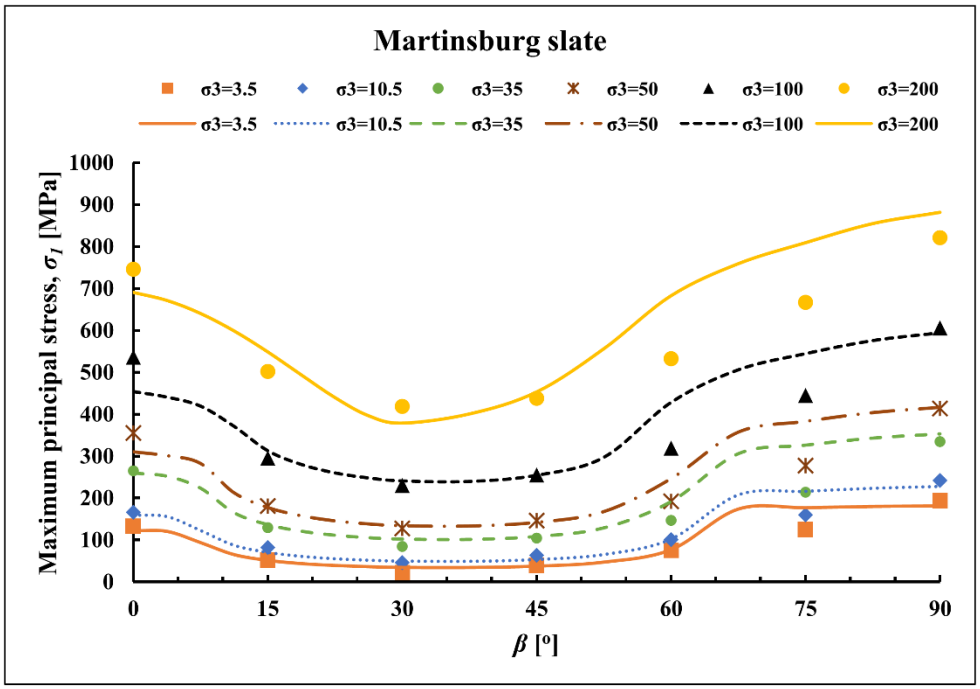

Fig. 7-8 Predicted failure strength by Jhoek model model in comparison with lab results of Martinsburg slate (Donath 1964).

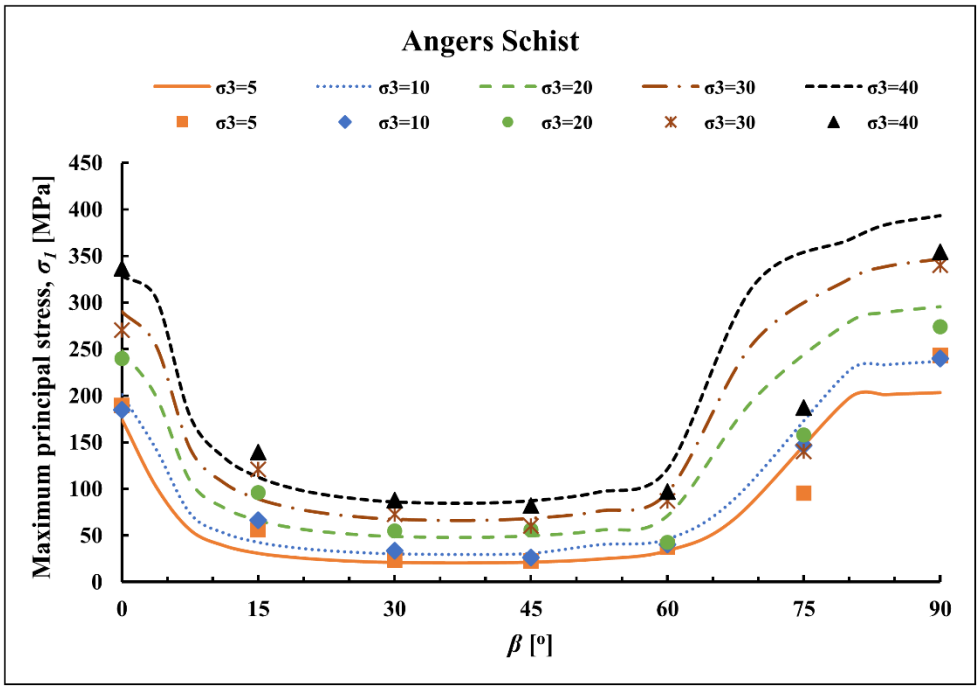

Fig. 7-9 Predicted failure strength by Jhoek model in comparison with lab results of Angers Schist (Duveau and Shao 1998).

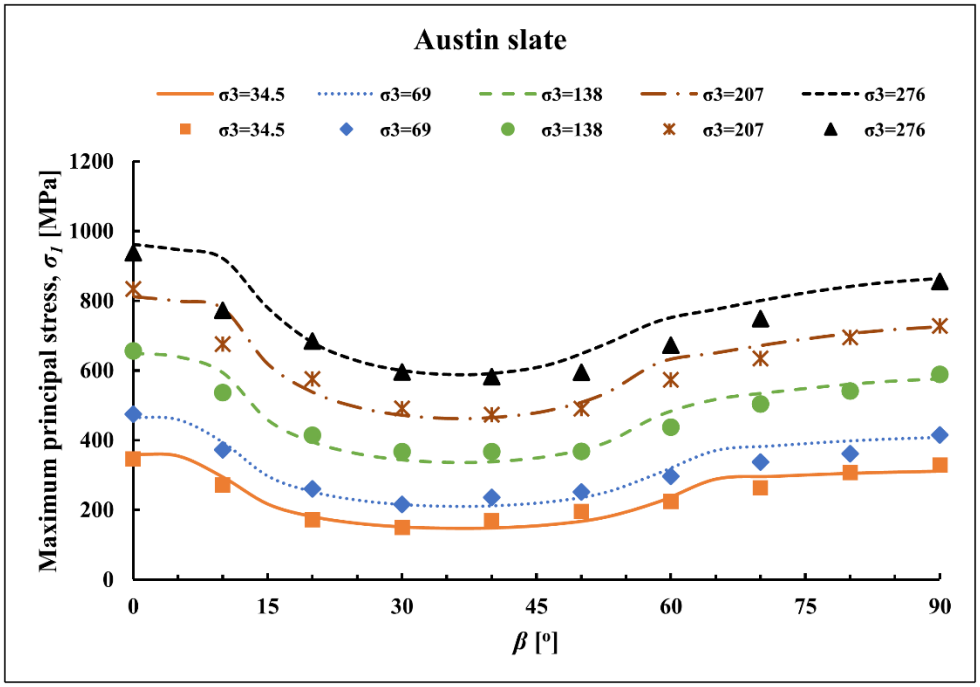

Fig. 7-10 Predicted failure strength by Jhoek model in comparison with lab results of Austin slate (McLamore and Gray 1967).

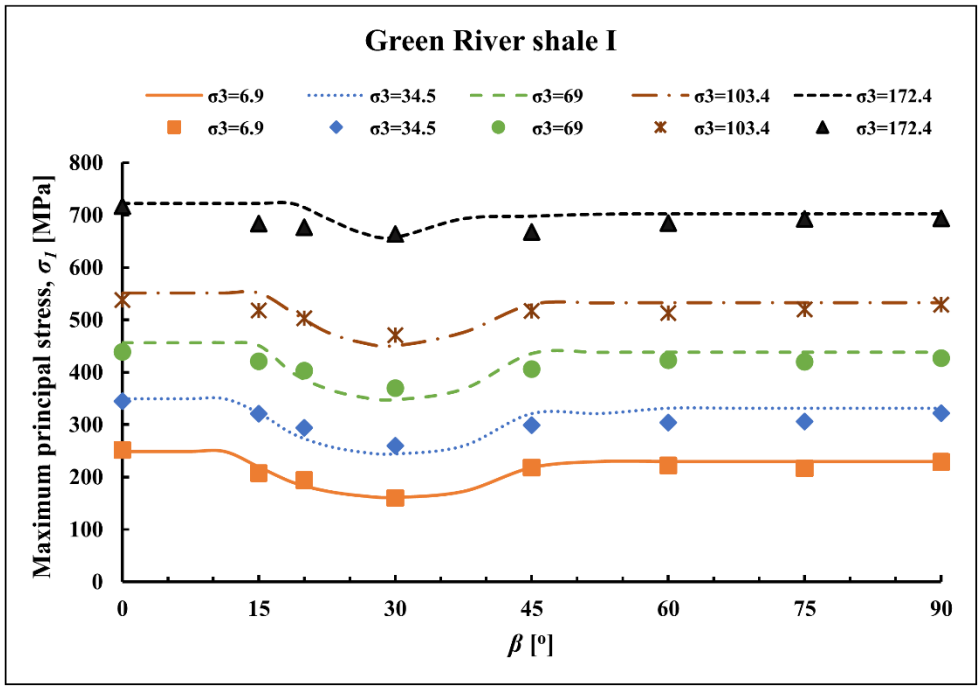

Fig. 7-11 Predicted failure strength by Jhoek model in comparison with lab results of Green River shale I (McLamore and Gray 1967).

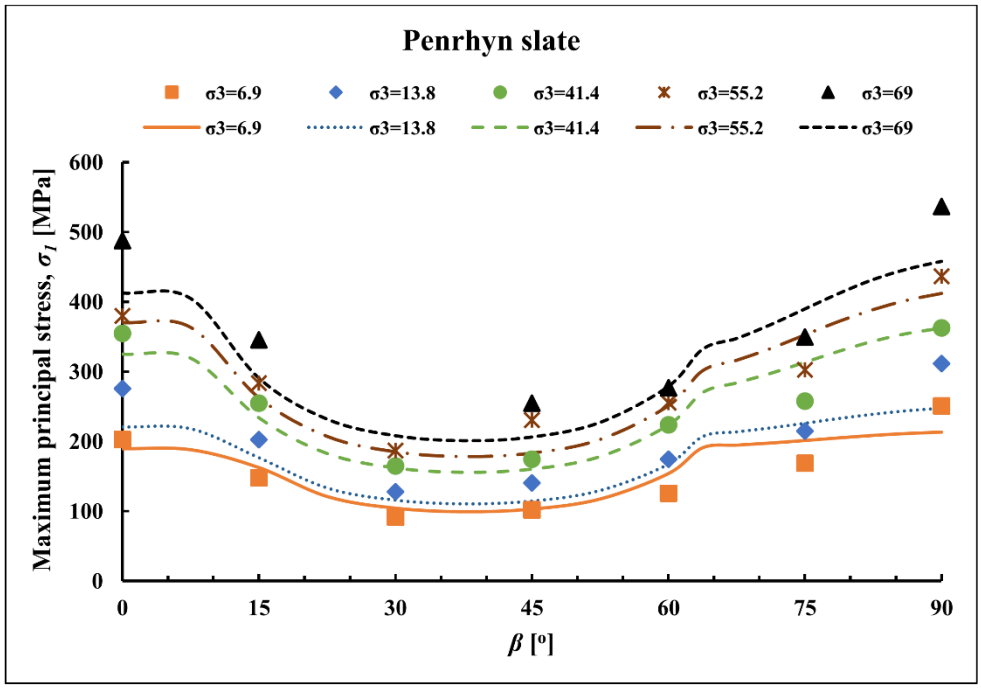

Fig. 7-12 Predicted failure strength by Jhoek model in comparison with lab results of Penrhyn slate (Attewell and Sandford 1974).

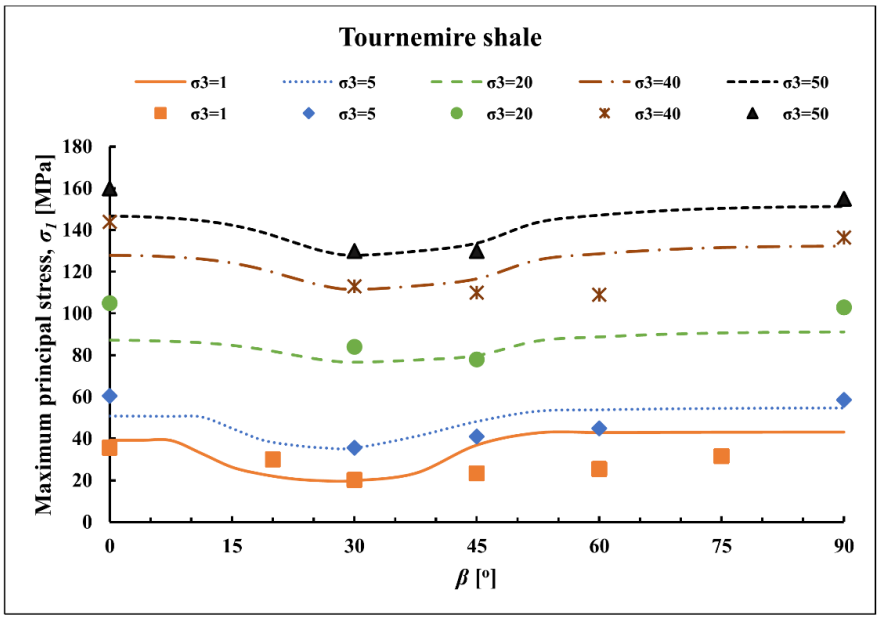

Fig. 7-13 Predicted failure strength by Jhoek model in comparion with lab results of Tournemire shale (Niandou et al. 1997).

7.5.3. True triaxial test and effect of intermediate principal stress

True triaxial tests as proposed by Mogi (1966) allow to apply independently the three principal stresses on a rectangular prismatic specimen. The applied principal stresses can have different values which allows to investigate the influence of the intermediate principal stress. One of the weaknesses of the classical H-B failure criterion is the disregarding of the effect of the intermediate principal stress (σ_2). The proposed Jhoek constitutive model is tested against various values of dip angle *jdip* (i.e. the orientation angle in 2D, α), strike *jdd* and various applied σ_2, while the minimum applied principal stress σ_3 is kept constant. Fig. 7-14 illustrates the test settings.

According to the results presented in previous sections, the Jhoek model shows a remarkable accuracy in predicting the rock strength for different angles β (i.e. $\beta = 90^o - jdip$ or α). In this section, the influence of different values of *jdd* with a fixed value of *jdip* ($\beta = 30^o$) with applying different values of the intermediate principal stress is tested. Based on the experimental investigations on the green foliated Chichibu schist (Mogi et al. 1978; Kwaśniewski and Mogi 1990; Kwaśniewski and Mogi 2000), three different *jdd* orientations have been tested under true triaxial stress conditions. The following cases are considered: (I) strike is parallel to applied σ_2 (i.e. $jdd = 90^o$); (II) strike is 45°, and (III) strike is perpendicular to applied σ_2 (i.e. $jdd = 0^o$). All these cases are applied at fixed value of *jdip* which equals 60°, and the applied σ_3 is fixed to 50 MPa.

The test results are given by Mogi (2006) and Pei (2008), while the green Chichibu schist parameters used in the simulation are presented in Table 7-5.

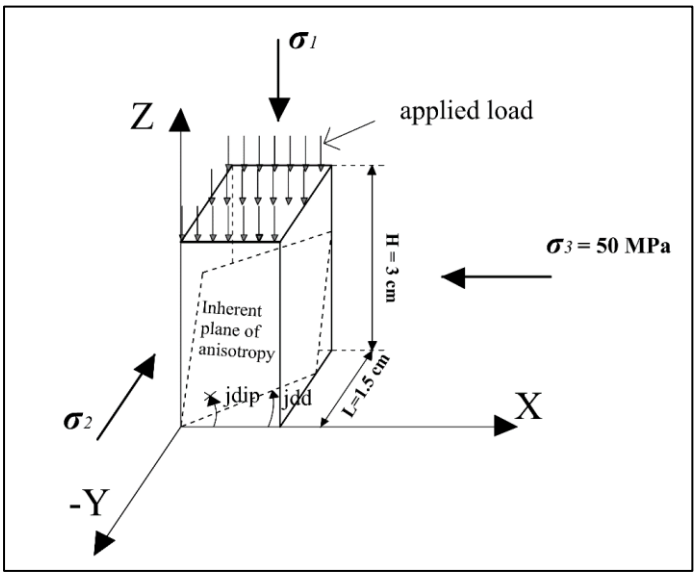

Fig. 7-14 Test setting for simulation of true triaxial experiment using Jhoek model.

Table 7-5 Assigned parameters of the green foliated Chichibu schist, deduced from (Lee and Pietruszczak 2008; Mogi 2006; Pei 2008)

Rock matrix parameters							
Density	***E*** [GPa]	***v*** [-]	σ_{c90} [MPa]	σ_{c0} [MPa]	m_{90} [-]	m_{30} [-]	ψ [°]
2780	31	0.2	150	160	13.5	7.54	10
Bedding planes parameters							
c_j [MPa]	ϕ_j [°]	ψ_j [°]	σ^t_j [MPa]				
17	33	8	0.4				

The values of Young's modulus, Poisson ratio and joint parameters are assigned according to Pei (2008), while other rock matrix parameters are evaluated from the performed conventional triaxial test using (Rocscience 2016) at orientation angle $\beta = 90^o$ (i.e. $jdip = 0^o$). Because there are no data about the strength value at $\beta = 0^o$, σ_{c0} is assumed to be 160 MPa, as it is supposed that it must be greater than σ_{c90}. For Case II, there are two different values of m_{30} assigned to the rock matrix. The applied values for the uniaxial compressive strength and m_{30} for each case are given in Table 7-6.

Table 7-6 Assigned values for rock matrix depending on strike orientation with applied σ_2

Case Number	***jdip/jdd* (i.e. α)** [°]	**β/strike** [°]	σ_{c0} [MPa]	m_β	**σ_2 orientation**
I	60/90	30/parallel	160	7.54*	strike is parallel to applied σ_2
II – m_β similar to I	60/45	30/45	160	7.54	strike is inclined with angle 45° to applied σ_2
II – m_β similar to III***	60/45	30/45	160	13.5	
III	60/0	30/normal	160	13.5**	strike is perpendicular to applied σ_2

** The value of m_β for case I equals the value of m_{30} based on the analysis of Colak and Unlu (2004),*

*** The value of m_β for case III equals the value of m_{90} based on the calibration of conventional triaxial tests using RocLab (Rocscience 2011),*

**** The best fit value of m_β for case II should be similar to the value of Case III, i.e. m_β for case II equals the value of m_{90}. However, the best fit for strength is shown fort m_{30} instead of m_{90}. This could be considered as a shortcoming of the model as there is no representation of the intermediate principal stress, σ_2.*

The results of the numerical simulations using the Jhoek constitutive model in comparison with the lab results for the three cases are shown in Fig. 7-15. In case I, the difference between maximum and minimum principal stress is constant (183 MPa). In this case, σ_2 has no effect due to the following reasons: (i) the shear strength of the joint is considered to be constant, and (ii) the direction of the applied σ_2 is parallel to the strike of the inherent plane of anisotropy and therefore in the direction of the shear traction force.

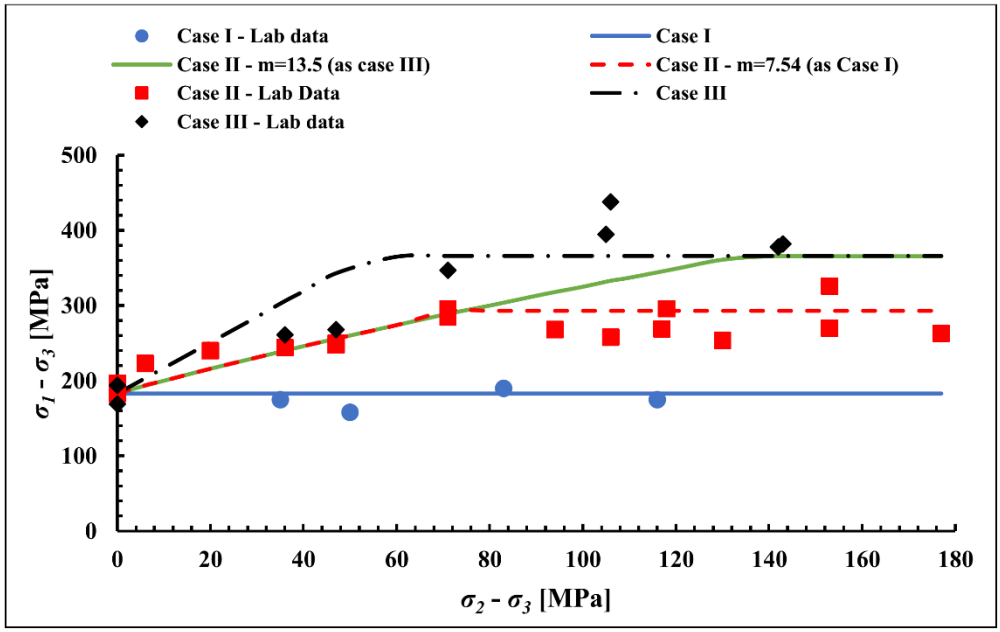

Fig. 7-15 Numerical simulation results for Jhoek model in comparison with lab data from Mogi (2006), σ_3 = 50 MPa.

For case II, in which the strike of the anisotropy plane is 45° in relation to the direction of σ_2, the value of σ_1 varies with increasing applied σ_2. Two different values are assigned for the rock parameter m_β: 7.54 similar to case I and 13.5 similar to case II. The applied σ_2 is decomposed into three traction components: one as normal stress and the two others as shear stresses. The failure mode is sliding along the anisotropy planes, as long as the shear component is larger than the normal traction. For m_β = 13.5, the failure mode is sliding along inherent planes till σ_2 = 190 MPa, then the failure mode becomes non-sliding. The rock matrix strength is similar to this value observed in case III (σ_1 - σ_3 = 366 MPa), as there is no influence of the intermediate principal stress on the rock matrix failure and the assigned value of m_β is fixed for both cases II and III. Generally, the numerical results in this case do not show good agreement with the lab data. Therefore, a different value of m_β is assumed by back analysis to get better correlation with the lab data.

As shown in Fig. 7-15, the sliding mode of failure is observed until (σ_2 = 121 MPa) and then it becomes non-sliding failure mode in the rock matrix for case II with m_β = 7.54. As the value of m_β was reduced by -44%, the yielding limit of the rock matrix decreased to (σ_1 - σ_3 = 396 MPa) which is considered in close range to the obtained lab data. Thus, the numerical simulations for case II assure that the value of m_β in 3-dimentional does not only depend on the *jdip*, the *jdd* plays a significant role as well. Similarly, for case III when the strike of the inherent anisotropic planes are perpendicular to the direction of applied σ_2, a change in the mode of failure happens rapidly in this case (i.e. $\sigma_2 \approx$ 110 MPa). This fits well the numerical findings of Lee and Pietruszczak (2008) and the experimental results of Mogi (2006).

In general, the proposed constitutive Jhoek model is able to capture the effect of the intermediate principal stress for inherent jointed rocks especially for the failure on the joint planes. However, the non-sliding failure mode is not affected by σ_2 because the used H-B yield surface for the rock matrix does not include σ_2 which is a shortcoming of the proposed Jhoek model. Therefore, in the future the rock matrix part in the Jhoek model should be modified to consider σ_2 like proposed in (Zhang 2008; Zhang and Zhu 2007).

7.6 Conclusions

The simulation of the strength anisotropy of rocks based on the H-B failure criterion is still a challenging topic which needs improvements. Different approaches have been presented. However, engineering applications require more comprehensive H-B based constitutive models which are

able to simulate the behavior of naturally laminated rocks. This chapter presented an elastic-perfect plastic constitutive model called Jhoek which combines two yield surfaces: one for describing the anisotropic rock matrix (modified H-B failure criterion) and the ubiquitous joint model duplicating the inherent joints. The anisotropy of the rock matrix is considered by the variation of the H-B parameters m_β, σ_{ci0} and σ_{ci90}. Due to the complication of the plasticity of the H-B failure criterion, the plastic corrections of the rock matrix are based on the linear approximated M-C model. For the normalization of the rock parameter m_β, a spatial distribution function is utilized based on Lee and Pietruszczak (2008).

The developed Jhoek model was successfully tested in reference to different lab experiments. It can predict the failure load for different angles between loading and foliation (β). For the region of sliding failure mode ($\beta = [\beta_1, \beta_2]$), however the failure shows a linear behavior as it reflects the linear M-C failure criterion assigned to the inherent joint planes. The model predictions show a remarkable agreement with lab data for various applied confinements. Also, the effect of the intermediate principal stress σ_2 was duplicated in a correct manner.

Otherwise, the Jhoek model is not able to detect the influence of intermediate principal stress regarding the rock matrix because σ_2 is not yet included in the H-B failure criterion. The proposed model is consistent to the lab results and the introduced examples verify that the Jhoek model can improve numerical predictions or back analysis for more complex engineering applications in naturally inherent anisotropic rocks.

8. Conclusions and recommendations for future work

8.1. Conclusions

In this thesis, stiffness and strength anisotropy behavior of inherent laminated rock masses has been investigated based on numerical simulations and lab tests. The aim of this work was to develop different continuum-based anisotropic constitutive laws able to model the influence of mechanical anisotropy and validate them in reference to lab and in-situ datasets. Different topics have been discussed in this work: continuum-based approaches for anisotropic rocks, different failure and deformation mechanisms in anisotropic rocks, propagation and formation of plastic zones of circular opening in bedded argillaceous rocks and dilatancy of laminated rocks. Overall, the following conclusions can be drawn.

(1) The rock strength is closely related to the direction of the loading with respect to the orientation of inherent planes of weakness. Such planes are formed naturally and found in intact rock samples and rock masses. On other hand, such rocks possess remarkable stiffness anisotropy as well. Different numerical modelling approaches were analyzed considering the computational efficiency and accuracy. Continuum modelling techniques shows high proficiency.

(2) A comprehensive literature review over the recent developed continuum-based constitutive models for inherent anisotropic rocks is presented showing the advantages and limitations of each model.

(3) Different inherent anisotropic rocks, such as bedded argillaceous rocks, possess not only anisotropy in strength and stiffness, but show also non-linearity in their stress-strain behavior. Thus, new bi-linear elasto-plastic transverse isotropic strain hardening/softening model (Transubi model) was developed to capture all these features. Several datasets from uniaxial and triaxial compressive tests were gathered from literature and used to validate the Transubi model and to compare it with existing constitutive models (e.g. Caniso model, ubiquitous joint model).

(4) Both, the elastic and plastic framework of the Transubi model are introduced in detail. Plastic corrections for rock matrix and weak planes showed the influence of the stiffness anisotropy. Thus, this model needs different transformation procedures for stress and strain second order tensors and fourth order stiffness tensor.

(5) The Transubi model has great potential to reproduce the mechanical response of bedded argillaceous rocks such as Tournemire shale or Opalinus clay. The pre-yielding hardening and the post-yielding softening were successfully simulated for both studied rocks. Generally, both rock types show brittle failure mechanisms. Tournemire shale was simulated using single M-C yield surface with tension cut-off, while Opalinus clay was simulated with bi-linear shear yield surface. The dilatancy of both, rock matrix and bedding planes of the Opalinus clay was extensively investigated by the Transubi model giving more realistic values for the dilation angle.

(6) The presence of the inherent bedding planes can be simulated via both continuum and discontinuum approaches. However, for larger scale of applications such as tunnels, discontinuum approaches show limitations in respect to the computational efficiency and upscaling. A special lab experiment of rock block containing a circular hole excavated in transverse isotropic slate and subjected to cyclic loading was conducted to investigate the deformation behavior around the hole. Numerical simulations using the Transubi, the ubiquitous joint and the elastic anisotropic model were calibrated against the lab results showing good agreement between results of measurements and the Transubi model.

(7) Numerical analysis of the short-term mechanical response of Opalinus Clay investigated by field measurements at the FE tunnel excavated at the Mont Terri URL (Switzerland) was conducted. Two simulations were performed: one considered no pore pressure, while the second considered pore pressure under undrained conditions. Comparison between simulations and in-situ data showed that the consideration of pore pressure gives more realistic results.

(8) A sensitivity study was performed in respect to grid dependency and excavation sequence. As the modelled material (Opalinus clay) is considered as strain softened, the deformation results show dependency on grid structure and size. Different mesh configurations are proposed and tested,

with the result, that radial symmetric mesh gives best results. On the other hand, gradual or sudden excavations methodologies lead to only minor differences. However, wall convergences obtained from gradual excavation method shows slightly better agreement with in-situ measurements.

(9) An elasto-perfect plastic constitutive model called Jhoek is presented. This model combines two yield surfaces: one for describing the anisotropic rock matrix (modified H-B failure criterion) and the ubiquitous joint model duplicating the inherent joint sliding mode. The anisotropy of the rock matrix is considered by the variation of the H-B parameters m_β, σ_{ci0} and σ_{ci90}. This model is validated against series of triaxial tests from literature showing good agreement between numerical results and lab data. True triaxial test of the green foliated Chichibu schist is simulated showing that the influence of the intermediate principal stress σ_2 is duplicated in a correct manner.

8.2. Recommendations for future work

(1) Upgrade the proposed Transubi model for 3-dimensional analysis.

This is recommended because (i) axis of principal stress as well as axis of geotechnical construction may be inclined in relation to joint planes and (ii) developed stress states have a pronounced 3-dimensional character like a tunnel face etc.

(2) Extension of the Transubi model by including time-dependent behavior.

The current version of the Transubi model is time-independent and used only for short-term analysis. The consideration of long-term stability (sub-critical crack growth, stress corrosion etc.) or creep effects need an extension.

(3) Incorporation a regularization algorithm into Transubi model

In order to avoid mesh-dependency, it is very important to incorporate an internal length scale parameter as a better regularization procedure.

(4) Performing fully hydro-mechanical coupled simulations.

Further validation of the Transubi model should include fully hydro-mechanical coupled simulations of the pore pressure around the excavated tunnel. For example, the FE-tunnel experiment at Mt. Terri is providing a good case study for such a task.

(5) Experimental investigation of dilation behavior of Opalinus clay

During the numerical investigation of the Opalinus clay, it was found that the dilatancy of the Opalinus clay is sensitive to the orientation of the bedding planes. The reported data from Popp and Salzer (2007) were only interested in the dip angle without mentioning the dip direction of the bedding planes. It is recommended to study this issue as it greatly affects the results of the dilation angles especially for the rock matrix.

(6) Applying Jhoek model in rock engineering

Although the results of the proposed Jhoek model showed consistent agreement to the lab results, it is recommended to apply this model on more complex engineering applications. The introduced examples verified that the Jhoek model can improve numerical predictions for naturally inherent anisotropic rocks. A field study could show the extend and the applicability of this model.

References

Abdi, H., D. Labrie, T. Nguyen, J.D. Barnichon, G. Su, E. Evgin, R. Simon, and M. Fall. 2015. "Laboratory Investigation on the Mechanical Behaviour of Tournemire Argillite." *Canadian Geotechnical Journal* 52 (3). NRC Research Press: 268–82.

Abdi, H, and E Evgin. 2013. "Laboratory Characterization, Modeling, and Numerical Simulation of an Excavation Damaged Zone around Deep Geologic Repositories in Sedimentary Rocks." Ontario, Canada.

Adachi, T, and F Oka. 1995. "An Elasto-Plastic Constitutive Model for Soft Rock with Strain Softening." *Int. J. for Numerical and Analytical Methods in Geomechanics* 19 (4): 233–47.

Adhikary, D. 2010. "Deficiencies in the Ubiquitous Joint Model of Layered Rocks." In *ISRM International Symposium -Rock Mechanics in Civil and Environmental Engineering-EUROCK 2010*, edited by Zhao et al.: 165–68. Lausanne, Switzerland.

Adhikary, D, and A Dyskin. 1997. "A Cosserat Continuum Model for Layered Materials." *Computers and Geotechnics* 20 (1): 15–45.

Adhikary, D, and A Dyskin. 1998. "A Continuum Model of Layered Rock Masses with Non-Associative Joint Plasticity." *Int. J. for Numerical and Analytical Methods in Geomechanics* 22 (4): 245–61.

Adhikary, D, A Dyskin, and R Jewell. 1996. "Numerical Modelling of the Flexural Deformation of Foliated Rock Slopes." *Int. J. of Rock Mechanics and Mining Sciences & Geomechanics Abstracts* 33 (6): 595–606.

Adhikary, D, and H Guo. 2002. "An Orthotropic Cosserat Elasto-Plastic Model for Layered Rocks." *Rock Mechanics and Rock Engineering* 35 (3): 161–70.

Agharazi, A, C Martin, and D Tannant. 2011. "Implementation of an Equivalent Continuum Constitutive Model for Rock Masses with Systematic Joint Sets in FLAC3D." In *Continuum and Distinct Element Continuum Modeling in Geomechanics - the 2nd International FLAC/DEM Symposium*, edited by Stainsbury et al., Paper: 13-06. Melbourne, Australia.

Agharazi, A. 2013. "Development of a 3D Equivalent Continuum Model for Deformation Analysis of Systematically Jointed Rock Masses, PhD Thesis." University of Alberta.

Alehossein, H, and A Korinets. 1999. "Gradient Dependent Plasticity and Finite Difference Method." In *The 5th International Workshop on Bifurcation and Localisation Theory in*

Geomechanics, edited by Muhlhaus et al.: 117–24. Lisse: Balkema.

Alehossein, H, and A Korinets. 2000. "Mesh-Independent Finite Difference Analysis Using Gradient-Dependent Plasticity." *Communications in Numerical Methods in Engineering* 16 (5): 363–75.

Alejano, L, and E Alonso. 2005. "Considerations of the Dilatancy Angle in Rocks and Rock Masses." *Int. J. of Rock Mechanics and Mining Sciences* 42 (4): 481–507.

Allirot, D, and J Boehler. 1979. "Evolution Des Propriétés Mécaniques d'une Roche Stratifiée Sous Pression de Confinement." In *4th Int. Conf. ISRM*, 15. Montreux: Balkema, Rotterdam.

Alonso et al. 2003. "Ground Response Curves for Rock Masses Exhibiting Strain-Softening Behaviour." *Int. J. for Numerical and Analytical Methods in Geomechanics* 27 (13): 1153–85.

Amadei, B. 1983. *Rock Anisotropy and the Theory of Stress Measurements, Lecture Notes in Engineering Series*. 2nd ed. New York: Springer.

Amadei, B. 1996. "Importance of Anisotropy When Estimating and Measuring in Situ Stresses in Rock." *Int. J. of Rock Mechanics and Mining Sciences & Geo. Abstracts*, 33:293–325.

Amadei, B, and W Savage. 1989. "Anisotropic Nature of Jointed Rock Mass Strength." *Journal of Engineering Mechanics* 115 (3): 525–42.

Amadei, B, W Savage, and H Swolfs. 1987. "Gravitational Stresses in Anisotropic Rock Masses." *Int. J. of Rock Mechanics and Mining Sciences & Geo. Abstracts* 24 (1): 5–14.

Amann et al. 2011. "Experimental Study of the Brittle Behavior of Clay Shale in Rapid Unconfined Compression." *Rock Mechanics and Rock Engineering* 44 (4): 415–30.

Amann et al. 2017. "Geomechanical Behaviour of Opalinus Clay at Multiple Scales: Results from Mont Terri Rock Laboratory (Switzerland)." *Swiss Journal of Geosciences* 110 (1): 151–71.

Ambrose, J. 2014. "Failure of Anisotropic Shales under Triaxial Stress Conditions." Imperial College London: Department of Earth Science and Engineering.

Asadi, M. 2016. "Optimized Mamdani Fuzzy Models for Predicting the Strength of Intact Rocks and Anisotropic Rock Masses." *J of Rock Mechanics and Geot. Engineering* 8 (2): 218–24.

Attaia, A, O Vorobiev, and S Walsh. 2015. "Implementation of an Anisotropic Mechanical Model for Shale in Geodyn." Livermore, CA (United States).

Attewell, P, and M Sandford. 1974. "Intrinsic Shear Strength of a Brittle, Anisotropic Rock—I." *Int. J. of Rock Mechanics and Mining Sciences & Geo. Abstracts* 11 (11): 423–30.

Bagheripour et al. 2011. “A Complement to Hoek-Brown Failure Criterion for Strength Prediction in Anisotropic Rock.” *Geomechanics and Engineering* 3 (1): 61–81.

Bahrani, N, and J Hadjigeorgiou. 2018. “Influence of Stope Excavation on Drift Convergence and Support Behavior: Insights from 3D Continuum and Discontinuum Models.” *Rock Mechanics and Rock Engineering*, April: 1–19.

Baraldi et al. 2016. “Continuous and Discrete Strategies for the Modal Analysis of Regular Masonry.” *Int. J. of Solids and Structures* 84: 82–98.

Barnichon, J. 1998. “Finite Element Modelling in Structural and Petroleum Geology.” Université de Liège.

Baron et al. 2005. “Numerical Analysis of Deep-Seated Mass Movements in the Magura Nappe; Flysch Belt of the Western Carpathians (Czech Republic).” *Natural Hazards and Earth System Sciences* 5 (3): 367–74.

Barton, N. 2013. “Shear Strength Criteria for Rock, Rock Joints, Rockfill and Rock Masses: Problems and Some Solutions.” *J. of Rock Mechanics and Geotechnical Engineering* 5 (4).

Berwanger, S, and W. Helms. 1993. “Laboruntersuchung Zur Einaxialen Druckfestigkeit Und Zur Biegesugfestigkeit von Prüfkörpern Des Schiefers Der Grube Felicitas.”

Blümling, P, and H Konietzky. 2003. “Development of an Excavation Disturbed Zone in Claystone (Opalinus Clay).” In *Int. Symposium on Geotechnical Measurements and Modelling, 23-25 September*, edited by Natau et al.: 127–32. Karlsruhe, Germany.

Bobet et al. 2009. “Numerical Models in Discontinuous Media: Review of Advances for Rock Mechanics Applications.” *J. of Geotechnical and Geoenvironmental Engineering* 135 (11): 1547–61..

Bock, H. 2001. “RA Experiment. Rock Mechanics Analyses and Synthesis: Data Report on Rock Mechanics. Technical Report 2000-02. Mont Terri Project.”

Bock, H. 2009. “RA Experiment. Updated Review of the Rock Mechanics Properties of the Opalinus Clay of the Mont Terri URL Based on Laboratory and Field Testing. Technical Report 2008-04. Mont Terri Project.”

Boehler, J, and A Sawczuk. 1977. “On Yielding of Oriented Solids.” *Acta Mechanica* 27 (1): 185–204.

Bonnelye et al. 2017. “Strength Anisotropy of Shales Deformed under Uppermost Crustal Conditions.” *Journal of Geophysical Research: Solid Earth* 122 (1): 110–29.

Bossart et al. 2017. “Mont Terri Rock Laboratory, 20 Years of Research: Introduction, Site Characteristics and Overview of Experiments.” *Swiss Journal of Geosciences* 110 (1): 3–22.

Braun, J. 2012. “Geomechanische Untersuchungen von Dachschiefer Aus Dem Sauerland, Unpublished MSc. Thesis.” Ruhr-Universität Bochum.

Brenne et al. 2014. “Hydraulic Fracturing of a Devonian Slate under Confining Pressure – With Emphasis on Cleavage Inclination.” In *Structures in and on Rock Masses - ISRM Regional Symposium - EUROCK 2014*, edited by Alejano et al.: 1369–73. Vigo, Spain

Brown, E, L Richards, and M. Barr. 1977. “Shear Strength Characteristics of the Delabole Slates.” In *Proceedings of the Conference on Rock Engineering, 4-7 April:* 33–51. Newcastle.

Bryne, L. 2014. “Time Dependent Material Properties of Shotcrete for Hard Rock Tunneling, PhD Thesis.” KTH Royal Institute of Technology, Stockholm, Sweden.

Bye, A, and F Bell. 2001. “Stability Assessment and Slope Design at Sandsloot Open Pit, South Africa.” *Int. J. of Rock Mechanics and Mining Sciences* 38 (3): 449–66.

Cartney, S. 1977. “The Ubiquitous Joint Method.” *Cavern Design at Dinorwic Power Station. Tunnels & Tunneling* 9: 54–57.

Casagrande, A and N Carillo. 1944. “Shear Failure of Anisotropic Materials.” *J. Boston Soc. Civ. Eng.* 31 (4): 78–87.

Casolo, S. 2006. “Macroscopic Modelling of Structured Materials: Relationship between Orthotropic Cosserat Continuum and Rigid Elements.” *Int. J. of Solids and Structures* 43 (3–4): 475–96.

Chang, L. 2017. “Joint Behaviour of Rock Mass, PhD Thesis (In Press).” TU Bergakademie Freiberg.

Chen et al. 2012. “Induced Anisotropic Damage and Plasticity in Initially Anisotropic Sedimentary Rocks.” *Int. J. of Rock Mechanics and Mining Sciences* 51: 13–23.

Chen, S, and G Pande. 1994. “Rheological Model and Finite Element Analysis of Jointed Rock Masses Reinforced by Passive, Fully-Grouted Bolts.” *Int. J. of Rock Mechanics and Mining Sciences & Geo. Abstracts* 31 (3): 273–77.

Chen, S, and P Egger. 1999. “Three Dimensional Elasto-Viscoplastic Finite Element Analysis of Reinforced Rock Masses and Its Application.” *Int. J. for Numerical and Analytical Methods in Geomechanics* 23 (1): 61–78.

Chen, S, C Fu, and S Isam. 2009. “Finite Element Analysis of Jointed Rock Masses Reinforced by

Fully-Grouted Bolts and Shotcrete Lining." *Int. J. of Rock Mechanics and Mining Sciences* 46 (1): 19–30.

Chenevert, M, and C Gatlin. 1965. "Mechanical Anisotropies of Laminated Sedimentary Rocks." *Society of Petroleum Engineers* 5 (1): 67–77.

Colak, K, and T Unlu. 2004. "Effect of Transverse Anisotropy on the Hoek–Brown Strength Parameter 'Mi' for Intact Rocks." *Int. J. of Rock Mechanics and Mining Sciences* 41 (6): 1045–52.

Coli, M, and A Pinzani. 2014. "Tunnelling and Hydrogeological Issues: A Short Review of the Current State of the Art." *Rock Mechanics and Rock Engineering* 47 (3): 839–51.

Corkum, A. 2006. "Non-Linear Behaviour of Opalinus Clay Around Underground Excavations, PhD Thesis" University of Alberta.

Corkum, A, and C Martin. 2004. "Modelling of the Short-Term Behaviour of Opalinus Clay around a Circular Excavation." In *Proceedings of the Canadian Geotechnical Conference*. Quebec City, Canada.

Corkum, A, and C Martin. 2007. "Modelling a Mine-by Test at the Mont Terri Rock Laboratory, Switzerland." *Int. J. of Rock Mechanics and Mining Sciences* 44 (6): 846–59.

Cosserat, E, and F Cosserat. 1909. *Théorie des corps déformables*. Paris: Librairie Scientifique A. Hermann et Fils.

Coulthard, M, and A Dutton. 1988. "Numerical Modelling of Subsidence Induced by Underground Coal Mining." In *The 29th US Symposium on Rock Mechanics (USRMS)*. ARMA.

Crook, A, J Yu, and S Willson. 2002. "Development of an Orthotropic 3D Elastoplastic Material Model for Shale." In *SPE/ISRM Rock Mechanics Conference*.

Cudny, M, and P Vermeer. 2004. "On the Modelling of Anisotropy and Destructuration of Soft Clays within the Multi-Laminate Framework." *Computers and Geotechnics* 31 (1): 1–22.

Cui et al. 2017. "Prediction of Critical Strains and Critical Support Pressures for Circular Tunnel Excavated in Strain-Softening Rock Mass." *Engineering Geology* 224 (June): 43–61.

Cundall, P, C Carranza-torres, and R Hart. 2003. "A New Constitutive Model Based on the Hoek–Brown Criterion." In *The Third International Symposium on FLAC and FLAC3D Numerical Modelling in Geomechanics*, edited by Brummer et al., 17–25. Sudbury, Canada.

Cundall, P, and E Dawson. 1992. "Cosserat Plasticity for Modeling Layered Rock." In *Fractured and Jointed Rock Masses (Proceedings of the ISRM Regional Conference)*, 267–74. Lake

Tahoe: Rotterdam: Balkema.

Davila, J, and W Schubert. 2014. “Rock Layering Influence on Rock Mass Displacements in Tunnelling.” In *8th Asian Rock Mechanics Symposium - Rock Mechanics for Global Issues*, edited by Kaneko and Kodama, 1123–30. Sapporo, Japan.

Dawson, E. 1995. “Micropolar Continuum Models for Jointed Rocks, PhD Thesis.” University of Minnesota, USA.

Detournay, C, G Meng, and P Cundall. 2016. “Development of a Constitutive Model for Columnar Basalt.” In *4th Itasca Symposium on Applied Numerical Modeling in Geomechanics*, edited by Gomes et al., 249–65. Lima, Peru: Itasca International Inc.

Diederichs, M, and P Kaiser. 1999. “Stability of Large Excavations in Laminated Hard Rock Masses: The Voussoir Analogue Revisited.” *Int. J. of Rock Mechanics and Mining Sciences* 36 (1): 97–117.

Donath, F. 1964. “Strength Variation and Deformational Behavior in Anisotropic Rock.” In *State of Stress in the Earth’s Crust*, edited by Judd, 281–98.

Duveau, G, J Shao, and J Henry. 1998. “Assessment of Some Failure Criteria for Strongly Anisotropic Geomaterials.” *Mechanics of Cohesive-Frictional Materials* 3 (1): 1–26.

Duveau, G, and J Shao. 1998. “A Modified Single Plane of Weakness Theory for the Failure of Highly Stratified Rocks.” *Int. J. of Rock Mechanics and Mining Sciences* 35 (6): 807–13.

Eberhardt, E. 2012. “The Hoek-Brown Failure Criterion.” *Rock Mechanics and Rock Engineering* 45 (6): 981–88.

Egger, P. 2000. “Design and Construction Aspects of Deep Tunnels (with Particular Emphasis on Strain Softening Rocks).” *Tunnelling and Underground Space Technology* 15 (4): 403–8.

Fama, D. 1993. “Numerical Modeling of Yield Zones in Weak Rock.” In *Analysis and Design Methods*: 49–75.

Fang et al. 2013. “An Approach for Predicting Stress-Induced Anisotropy around a Borehole.” *Geophysics* 78 (3): D143–50.

Favero, V, A Ferrari, and L Laloui. 2018. “Anisotropic Behaviour of Opalinus Clay Through Consolidated and Drained Triaxial Testing in Saturated Conditions.” *Rock Mechanics and Rock Engineering* 51 (5): 1305–19.

Fereidooni et al. 2016. “Assessment of Inherent Anisotropy and Confining Pressure Influences on Mechanical Behavior of Anisotropic Foliated Rocks Under Triaxial Compression.” *Rock*

Mechanics and Rock Engineering 49 (6): 2155–63.

Forest, S, and R Sievert. 2003. "Elastoviscoplastic Constitutive Frameworks for Generalized Continua." *Acta Mechanica* 160 (1): 71–111.

Fortsakis et al. 2012. "Anisotropic Behaviour of Stratified Rock Masses in Tunnelling." *Engineering Geology* 141 (Supplement C): 74–83.

François et al. 2011. "Development of an Extended Drucker–Prager Hardening Model for Cross-Anisotropy of Soft Rocks." In *2nd International Symposium on Computational Geomechanics (ComGeo II)*, 142–52. Cavtat-Dubrovnik, Croatia.

François et al. 2014. "Hollow Cylinder Tests on Boom Clay: Modelling of Strain Localization in the Anisotropic Excavation Damaged Zone." *Rock Mechanics and Rock Engineering* 47 (1): 71–86.

Fu et al. 2012. "An Elastoplastic Model for Soft Sedimentary Rock Considering Inherent Anisotropy and Confining-Stress Dependency." *Soils and Foundations* 52 (4): 575–89.

Gholami, R, and V Rasouli. 2014. "Mechanical and Elastic Properties of Transversely Isotropic Slate." *Rock Mechanics and Rock Engineering* 47 (5): 1763–73.

Goodman, R. 1967. "Research on Rock Bolt Reinforcement and Integral Lined Tunnels." DTIC Document.

Haghighat et al. 2015. "Numerical Investigation of the Mechanical Behaviour of Tournemire Argillite." In *13th ISRM International Congress of Rock Mechanics*, edited by Hassan et al., Monterial, Canada.

Hakami, E, and N Barton. 1990. "Aperture Measurements and Flow Experiments Using Transparent Replicas of Rock Joints." *Rock Joints*, 383–90.

Hashagen, F, and R de Borst. 2001. "Enhancement of the Hoffman Yield Criterion with an Anisotropic Hardening Model." *Computers & Structures* 79 (6): 637–51.

Hatzor, Y, and E Heyman. 1997. "Dilation of Anisotropic Rock Salt: Evidence from Mount Sedom Diapir." *Journal of Geophysical Research: Solid Earth* 102 (B7): 14853–68.

Haumann, M. 2016. "Modellversuche Zur Bestimmung Des Verformungsverhaltens Eines Kreisförmigen Tunnelquerschnitts Im Geschichteten Gebirge, Unpublished MSc. Thesis." TU Bergakademie Freiberg.

Hefny, A, and K Lo. 1999. "Analytical Solutions for Stresses and Displacements Around Tunnels Driven in Cross-Anisotropic Rocks." *Int. J. Numer. Anal. Meth. Geomech* 23: 161–77.

Hill, R. 1950. *The Mathematical Theory of Plasticity*. Oxford: Oxford University Press.

Hoek, E. 1964. "Fracture of Anisotropic Rock." *Journal of the South African Institute of Mining and Metallurgy* 64 (10): 501–18.

Hoek, E, and E Brown. 1980. "Empirical Strength Criterion for Rock Masses." *Journal of the Geotechnical Engineering Division, ASCE* 106 (GT9, Proc. Paper, 15715): 1013–35.

Hoek, E, and E Brown. 1997. "Practical Estimates of Rock Mass Strength." *Int. J. of Rock Mechanics and Mining Sciences* 34 (8): 1165–86.

Hoek, E. 1983. "Strength of Jointed Rock Masses." *Geotechnique* 23 (3): 187–223.

Hoek, E, and E Brown. 1980. *Underground Excavations in Rock*. 1st ed. London: The Institute of Mining and Metallurgy.

Hoffman, O. 1967. "The Brittle Strength of Orthotropic Materials." *Journal of Composite Materials* 1 (2): 200–206.

Horino, F, and M Ellickson. 1970. "A Method for Estimating Strength of Rock Containing Planes of Weakness." Vol. 7449. US Dept. of Interior, Bureau of Mines.

Hsiung et al. 1995. "Development of Rock Mechanics Properties Database - Progress Report."

Hu et al. 2013. "Modeling of Inherent Anisotropic Behavior of Partially Saturated Clayey Rocks." *Computers and Geotechnics* 48: 29–40.

Hu, Z, and H Tang. 2013. "A Transversely Isotropic Cosserat Continuum Model and Its Numerical Application." In *Geotechnical Special Publication*, 541–48.

Huang, J, and D Griffiths. 2008. "Observations on Return Mapping Algorithms for Piecewise Linear Yield Criteria." *International Journal of Geomechanics* 8 (4): 253–265.

Inks et al. 2014. "Comparison of Marcellus Fracturing Using Azimuthal Seismic Attributes Versus Published Data From Outcrop Studies." *Proceedings of the 2nd Unconventional Resources Technology Conference*, no. 1: 1–19.

Ismael, M, H Imam, and Y El-Shayeb. 2014. "A Simplified Approach to Directly Consider Intact Rock Anisotropy in Hoek-Brown Failure Criterion." *Journal of Rock Mechanics and Geotechnical Engineering* 6 (5): 486–92.

Ismael, M, and H Konietzky. 2017. "Integration of Elastic Stiffness Anisotropy into Ubiquitous Joint Model." In *Symposium of the International Society for Rock Mechanics- Human Activity in Rock Masses - Eurock 2017*, 191:1032–39. Ostrava, Czech Republic.

Ismael et al. 2015. "Extension and Modification of Hoek and Brown Failure Criterion to

Incorporate Anisotropy." In *EUROCK 2015 & 64th Geomechanics Colloquium*, edited by Schubert and Kluckner, 767–72. Salzburg: ÖGG.

ISRM. 1985. "Suggested Method for Determining Point Load Strength." *Int. J. Rock Mech. Min. Sci. & Geomech. Abstr.* 22: 51–60.

Itasca Consulting Group Inc. 2016. "FLAC – Fast Lagranian Analysis of Continua, Constitutive Models Manual." Minneapolis: Itasca Consulting Group Inc.

Jaeger, J. 1960. "Shear Failure of Anisotropic Rocks." *Geological Magazine* 97 (1). Cambridge University Press: 65–72.

Jaeger, J. 1964. *Elasticity, Fracture and Flow*. 2nd ed. New York: Barnes & Noble.

Jaeger, J, and N Cook. 1979. *Fundamental of Rock Mechanics*. 3rd ed. London: Chapman and Hall.

Jaeggi et al. 2012. "FE-C Experiment: Engineering Part of Full-Scale Emplacement Experiment Geological and Structural Mapping of the FE-Tunnel Including a Photogrammetric Method. Unpublished Technical Note TN2012-82."

Jia et al. 2017. "Numerical Simulation of Failure Mechanism of Horizontal Borehole in Transversely Isotropic Shale Gas Reservoirs." *Journal of Natural Gas Science and Engineering* 45 (Supplement C): 65–74.

Jia, P, and C Tang. 2008. "Numerical Study on Failure Mechanism of Tunnel in Jointed Rock Mass." *Tunnelling and Underground Space Technology* 23 (5): 500–507.

Jiang, Q, Y Hu, and W Lai. 2009. "Three-Dimensional Stability Analysis of Stratified Rock Slope Based on Ubiquitous-Joint Model." *Rock and Soil Mechanics* 3: 28.

Jing, L. 2003. "A Review of Techniques, Advances and Outstanding Issues in Numerical Modelling for Rock Mechanics and Rock Engineering." *International Journal of Rock Mechanics and Mining Sciences* 40 (3): 283–353.

Johnson, P, and P Rasolofosaon. 1996. "Nonlinear Elasticity and Stress-Induced Anisotropy in Rock." J. of Geophysical Research - All Series - 101: 3113–24.

Karampinos et al. 2015. "Discrete Element Modelling of the Buckling Phenomenon in Deep Hard Rock Mines." *Int. J. of Rock Mechanics and Mining Sciences* 80: 346–56.

Kazakidis, V, and M Diederichs. 1993. "Understanding Jointed Rock Mass Behaviour Using a Ubiquitous Joint Approach." *Int. J. of Rock Mechanics and Mining Sciences & Geo. Abstracts* 30 (2): 163–72.

Kim et al. 2012. "Anisotropy of Elastic Moduli, P-Wave Velocities, and Thermal Conductivities

of Asan Gneiss, Boryeong Shale, and Yeoncheon Schist in Korea." *Engineering Geology* (147): 68–77.

Kolymbas, D. 2007. "Incompatible Deformation in Rock Mechanics." *Acta Geotechnica* 2 (1): 33–40.

Konietzky, H, P Blümling, and L te Kamp. 2003. "Opalinuston, Felsmechanische Untersuchungen, Nagra Interne Berichte (NIB) 03-08."

Konietzky, H, and L te Kamp. 2004. "Prediction Modelling of Deformations in Future Niches HG-A and EZ-B with FLAC3D. Technical Note 2005-21." Mont Terri Project. St-Ursanne, Switzerland.

Konietzky, H, and L te Kamp. 2006. "EZ-A Experiment. 3D Numerical Modelling: EZ-A Drift Mont Terri. Unpublished Technical Note 2006-50."

Krieg, R, and D Krieg. 1977. "Accuracies of Numerical Solution Methods for the Elastic-Perfectly Plastic Model." *Journal of Pressure Vessel Technology* 99 (4). ASME: 510–15.

Kwaśniewski, M. 1993. *Mechanical Behavior of Anisotropic Rocks*. *Comprehensive Rock Engineering. Vol. 1*.

Kwaśniewski, M, and K Mogi. 1990. "Effect of Intermediate Principal Stress on the Failure of a Foliated Anisotropic Rock." In *Proceedings of Mechanics of Jointed and Foulted Rock*, 407–16. Balkema, Rotterdam.

Kwaśniewski, M, and K Mogi. 2000. "Faulting in an Anisotropic, Schistose Rock Under General Triaxial Compression." In *4th North American Rock Mechanics Symposium, 31 July-3 August*, edited by Girard, Liebman, Breeds, and Doe, 737–46. Seattle, Washington.

Lanyon et al. 2014. "Development and Evolution of the Excavation Damaged Zone (EDZ) in the Opalinus Clay – A Synopsis of the State of Knowledge from Mont Terri, Arbeitsbericht NAB 14-87."

Le, A, and T Nguyen. 2015. "Hydromechanical Response of a Bedded Argillaceous Rock Formation to Excavation and Water Injection." *Canadian Geotechnical Journal* 52 (1): 1–17.

Lee, Y, and S Pietruszczak. 2008. "Application of Critical Plane Approach to the Prediction of Strength Anisotropy in Transversely Isotropic Rock Masses." *Int. J. of Rock Mechanics and Mining Sciences* 45 (4): 513–23.

Lee, Y, and S Pietruszczak. 2015. "Tensile Failure Criterion for Transversely Isotropic Rocks." *Int. J. of Rock Mechanics and Mining Sciences* 79: 205–15.

Lee, Y, S Pietruszczak, and B Choi. 2012. “Failure Criteria for Rocks Based on Smooth Approximations to Mohr – Coulomb and Hoek – Brown Failure Functions.” *Int. J. of Rock Mechanics and Mining Sciences* 56: 146–60.

Lekhnitskii, S. G. 1981. *Theory of Elasticity of an Anisotropic Body*. Moscow: Mir Publishers.

Li et al. 2013. “Bidirectional Construction Process Mechanics for Tunnels in Dipping Layered Formation.” *Tunnelling and Underground Space Technology* 36 (Supplement C): 57–65.

Li et al. 2009. “A New Cosserat-like Constitutive Model for Bedded Salt Rocks.” *Int. J. for Numerical and Analytical Methods in Geomechanics* 33 (15): 1691–1720.

Lisjak et al. 2015. “The Excavation of a Circular Tunnel in a Bedded Argillaceous Rock (Opalinus Clay): Short-Term Rock Mass Response and {FDEM} Numerical Analysis.” *Tunnelling and Underground Space Technology* 45: 227–48.

Lisjak, A, and G Grasselli. 2014. “A Review of Discrete Modeling Techniques for Fracturing Processes in Discontinuous Rock Masses.” *Journal of Rock Mechanics and Geotechnical Engineering* 6 (4): 301–14.

Lisjak, A, G Grasselli, and T Vietor. 2014. “Continuum–discontinuum Analysis of Failure Mechanisms around Unsupported Circular Excavations in Anisotropic Clay Shales.” *Int. J. of Rock Mechanics and Mining Sciences* 65 (Supplement C): 96–115.

Lisjak, A. 2013. “Investigating the Influence of Mechanical Anisotropy on the Fracturing Behaviour of Brittle Clay Shales with Application to Deep Geological Repositories, PhD Thesis.” University of Toronto.

Lisjak et al. 2016. “Hybrid Finite-Discrete Element Simulation of the EDZ Formation and Mechanical Sealing Process Around a Microtunnel in Opalinus Clay.” *Rock Mechanics and Rock Engineering* 49 (5). Springer Vienna: 1849–73.

Liu et al. 2017. “Model Test and Stress Distribution Law of Unsymmetrical Loading Tunnel in Bedding Rock Mass.” *Arabian Journal of Geosciences* 10 (7): 184.

Loon et al. 2008. “Preferred Orientations and Anisotropy in Shales: Callovo-Oxfordian Shale (France) and Opalinus Clay (Switzerland).” *Clays and Clay Minerals* 56 (3). GeoScienceWorld: 285–306.

Manh et al. 2015. “Anisotropic Time-Dependent Modeling of Tunnel Excavation in Squeezing Ground.” *Rock Mechanics and Rock Engineering* 48 (6): 2301–17.

Marschall et al. 2017. “Hydro-Mechanical Evolution of the EDZ as Transport Path for

Radionuclides and Gas: Insights from the Mont Terri Rock Laboratory (Switzerland)." *Swiss Journal of Geosciences* 110 (1): 173–94.

Martin, C, and G Lanyon. 2003. "Measurement of In-Situ Stress in Weak Rocks at Mont Terri Rock Laboratory, Switzerland." *Int. J. of Rock Mechanics and Mining Sciences* 40 (7–8): 1077–88.

Masiani, R, and P Trovalusci. 1996. "Cosserat and Cauchy Materials as Continuum Models of Brick Masonry." *Meccanica* 31 (4): 421–32.

Matsukura, Y, K Hashizume, and C Oguchi. 2002. "Effect of Microstructure and Weathering on the Strength Anisotropy of Porous Rhyolite." *Engineering Geology* 63 (1–2): 39–47.

McLamore, R, and K Gray. 1967. "A Strength Criterion for Anisotropic Rocks Based Upon Experimental Observations." In *Annual Meeting of the American Institute of Mining, Metallurgical, and Petroleum Engineers*, SPE 1721. Los Angeles.

Meyer, R. 2002. "Anisotropy of Sandstone Permeability." *CREWES Reaserch Report* 14: 1–12.

Mindlin, R. 1964. "Micro-Structure in Linear Elasticity." *Archive for Rational Mechanics and Analysis* 16 (1): 51–78.

Mogi, K. 1966. "Some Precise Measurements of Fracture Strength of Rocks under Uniform Compressive Stress." *Rock Mechanics and Engineering Geology* 4 (1): 43–55.

Mogi, K. 2006. *Experimental Rock Mechanics*. London: Taylor & Francis Group.

Mogi, K, M Kwaśniewski, and H Mochizuki. 1978. "Fracture of Anisotropic Rocks under General Triaxial Compression." *Seismological Society of Japan Bulletin* 1 (40): 25.

Mokhtari et al. 2013. "Stress-Dependent Permeability Anisotropy and Wettability of Shale Resources." In *Unconventional Resources Technology Conference, Denver, Colorado, 12-14 August 2013*, 2713–28. Denver, Colorado.

Muhlhaus, H.-B. 1993. *Continuum Models for Layered and Blocky Rock*. *Comprehensive Rock Engineering. Vol. 2*.

Mühlhaus, H.-B, and I Vardoulakis. 1986. "Axially-Symmetric Buckling of the Surface of a Laminated Half Space with Bendinh Stiffness." *Mechanics of Materials* 5 (2): 109–20.

Mühlhaus, H.-B. 1995. "A Relative Gradient Model for Laminated Materials." In *Continuum Models for Materials with Microstructure*, 451–82. Wiley Series in Materials, Modelling, and Computation.

Mühlhaus, H.-B. 1990. "Stress and Couple Stress in a Layered Half Plane with Surface Loading."

Int. J. for Numerical and Analytical Methods in Geomechanics 14 (8): 545–63.

Müller et al. 2017. "Implementation of the Full-Scale Emplacement (FE) Experiment at the Mont Terri Rock Laboratory." *Swiss Journal of Geosciences* 110 (1): 287–306.

Nakai, T, and Y Mihara. 1984. "A New Mechanical Quantity for Soils and Its Application to Elastoplastic Constitutive Models." *Soils and Foundations* 24 (2): 82–94.

Nasseri, M, K Rao, and T Ramamurthy. 1997. "Failure Mechanism in Schistose Rocks." *Int. J. of Rock Mechanics and Mining Sciences* 34 (3): 219.

Naumann, M, U Hunsche, and O Schulze. 2007. "Experimental Investigations on Anisotropy in Dilatancy, Failure and Creep of Opalinus Clay." *Physics and Chemistry of the Earth, Parts A/B/C* 32 (8–14): 889–95.

Neuner et al. 2017. "Time-Dependent Material Properties of Shotcrete: Experimental and Numerical Study." *Materials* 10 (12): 1067.

Nguyen, T, and A Le. 2015. "Development of a Constitutive Model for a Bedded Argillaceous Rock from Triaxial and True Triaxial Tests." *Canadian Geotechnical Journal* 52 (8): 1072–86.

Nguyen, Van Manh. 2013. *Static and Dynamic Behaviour of Joints in Schistose Rock : Lab Testing and Numerical Simulation, PhD Thesis*. TU Bergakademie Freiberg: Institut fuer Geotechnik.

Niandou, H. 1994. "Etude Du Comportement Rheologiques et Modelisation de l'argilite de Tournemire. Application a La Stabilite Des Ouvrages Souterrains, These de Doctorat." USTL Lille, France.

Niandou et al. 1997. "Laboratory Investigation of the Mechanical Behaviour of Tournemire Shale." *Int. J. of Rock Mechanics and Mining Sciences* 34 (1): 3–16.

Nova, R. 1986a. "An Extended Cam Clay Model for Soft Anisotropic Rocks." *Computers and Geotechnics* 2 (2): 69–88.

Nova, R. 1986b. "Soil Models as a Basis for Modelling the Behaviour of Geophysical Materials." *Acta Mechanica* 64 (1): 31–44.

Oda, M. 1993. "Inherent and Induced Anisotropy in Plasticity Theory of Granular Soils." *Mechanics of Materials* 16 (1): 35–45.

Oda, M, and H Nakayama. 1989. "Yield Function for Soil with Anisotropic Fabric." *Journal of Engineering Mechanics* 115 (1): 89–104.

Oka et al. 2002. "Anisotropic Behavior of Soft Sedimentary Rock and a Constitutive Model." *Soils*

and Foundations 42 (5): 59–70.

Olalla, C, M Martin, and J Saez. 1999. "ED-B Experiment: Geotechnical Laboratory Testing on Opalinus Clay Rock Samples, Tech. Rep. TN98-57, Mont Terri Project."

Ortiz, M, and J Simo. 1986. "An Analysis of a New Class of Integration Algorithms for Elastoplastic Constitutive Relations." *Int. J. for Numerical Methods in Engineering* 23 (3): 353–66.

Owen, D, and E Hinton. 1980. *Finite Element in Plasticity: Theory and Practice*. 6th ed. Swansea.

Pande, G, and K Sharma. 1983. "Multi-Laminate Model of Clays—a Numerical Evaluation of the Influence of Rotation of the Principal Stress Axes." *Int. J. for Numerical and Analytical Methods in Geomechanics* 7 (4): 397–418.

Pande, G, and M Yamada. 1994. "The Multilaminate Framework of Models for Rock and Soil Masses." In *The International Workshop on Application of Computational Mechanics in Geotechnical Engineering*, edited by Vargas, 107–23. Rio de Janeiro: Balkema, Rotterdam.

Pariseau, W. 1968. "Plasticity Theory For Anisotropic Rocks And Soil." In *The 10th U.S. Symposium on Rock Mechanics (USRMS)*. Austin, Texas: ARMA.

Park, B, and K Min. 2015. "Bonded-Particle Discrete Element Modeling of Mechanical Behavior of Transversely Isotropic Rock." *Int. J. of Rock Mechanics and Mining Sciences* 76: 243–55.

Pei, J. 2008. "Strength of Transversely Isotropic Rocks, PhD Thesis." Massachusetts Institute of Technology.

Pietruszczak, S, J Jiang, and F Mirza. 1988. "An Elastoplastic Constitutive Model for Concrete." *Int. J. of Solids and Structures* 24 (7): 705–22.

Pietruszczak, S, D Lydzba, and J Shao. 2002. "Modelling of Inherent Anisotropy in Sedimentary Rocks." *Int. J. of Solids and Structures* 39 (3): 637–48.

Pietruszczak, S, and Z Mroz. 2000. "Formulation of Anisotropic Failure Criteria Incorporating a Microstructure Tensor." *Computers and Geotechnics* 26 (2): 105–12.

Pietruszczak, S, and Z Mroz. 2001. "On Failure Criteria for Anisotropic Cohesive-Frictional Materials." *Int. J. for Numerical and Analytical Methods in Geomechanics* 25 (5).: 509–24.

Pietruszczak, S, and G Pande. 1987. "Multi-Laminate Framework of Soil Models—plasticity Formulation." *Int. J. for Numerical and Analytical Methods in Geomechanics* 11 (6): 651–58.

Pietruszczak, S, and G Pande. 2001. "Description of Soil Anisotropy Based on Multi-Laminate Framework." *Int. J. for Numerical and Analytical Methods in Geomechanics* 25 (2): 197–206.

Pietruszczak, S, and R Ushaksaraei. 2003. “Description of Inelastic Behaviour of Structural Masonry.” *Int. J. of Solids and Structures* 40 (15): 4003–19.

plaxis. 2016. “PLAXIS 2D: Material Models Manual.”

Popp, T, and K Salzer. 2007. “HE-D Experiment: Influence of Bedding Planes (IfG) - Final Report, Technical Report 2007-04.”

Popp, T, K Salzer, and W Minkley. 2008. “Influence of Bedding Planes to EDZ-Evolution and the Coupled HM Properties of Opalinus Clay.” *Physics and Chemistry of the Earth, Parts A/B/C* 33 (January): S374–87.

Rahmati, E. 2016. “Numerical Assessment of Caprock Integrity in SAGD Operations Considering Mechanical Anisotropic Behavior of Shale Layers, , PhD Thesis.” University of Alberta.

Ramamurthy, T. 1993. “Strength and Modulus Responses of Anisotropic Rocks.” *Comprehensive Rock Engineering* 1. Pergamon Press, Oxford: 313–29.

Ramamurthy, T, and V Arora. 1994. “Strength Predictions for Jointed Rocks in Confined and Unconfined States.” *Int. J. of Rock Mechanics and Mining Sciences And* 31 (1): 9–22.

Ramamurthy, T, G Rao, and J Singh. 1993. “Engineering Behaviour of Phyllites.” *Engineering Geology* 33 (3): 209–25.

Ranjbarnia, M, A Fahimifar, and P Oreste. 2015. “Analysis of Non-Linear Strain-Softening Behaviour around Tunnels.” *Proceedings of the Institution of Civil Engineers - Geotechnical Engineering* 168 (1): 16–30.

Riahi, A, J Curran, and H Bidhendi. 2009. “Buckling Analysis of 3D Layered Structures Using a Cosserat Continuum Approach.” *Computers and Geotechnics* 36 (7): 1101–12.

Riahi, A. 2008. “3D Finite Element Cosserat Continuum Simulation of Layered Geomaterials, PhD Thesis.” University of Toronto.

Riahi, A, and J Curran. 2009. “Full 3D Finite Element Cosserat Formulation with Application in Layered Structures.” *Applied Mathematical Modelling* 33 (8): 3450–64.

Riahi, A, and J Curran. 2008. “Application of Cosserat Continuum Approach in the Finite Element Shear Strength Reduction Analysis of Jointed Rock Slopes.”

Ribacchi, R. 2000. “Mechanical Tests on Pervasively Jointed Rock Material: Insight into Rock Mass Behaviour.” *Rock Mechanics and Rock Engineering* 33 (4): 243–66.

Rocscience Inc. 2016. “RocData.” Toronto.

Rocscience Inc. 2011a. “Phase2. 2D Finite Element Program for Stress Analysis and Support

Design Around Excavations in Soil and Rock."

Rocscience Inc. 2011b. "RocLab, Ver. 1.032." Toronto, Ontario, Canada.

Roosta et al. 2006. "Rock Joint Modeling Using a Visco-Plastic Multilaminate Model at Constant Normal Load Condition." *Geotechnical and Geological Engineering* 24 (5): 1449.

Rummel, F, and U Weber. 2007. "Rock Mechanics Analyses (RA) Experiment: Results of Uniaxial and Triaxial Tests on Opalinus Clay Samples, Unpublished Mont Terri Technical Note 2005-57, Mont Terri Project, Switzerland."

Sainsbury, B, and D Sainsbury. 2017. "Practical Use of the Ubiquitous-Joint Constitutive Model for the Simulation of Anisotropic Rock Masses." *Rock Mechanics and Rock Engineering*, 1–22.

Sainsbury, B, M Pierce, and D Mas Ivars. 2008. "Simulation of Rock Mass Strength Anisotropy and Scale Effects Using a Ubiquitous Joint Rock Mass (UJRM) Model." In *Continuum and Distinct Element Numerical Modeling in Geo-Engineering*, edited by Hart et al: 06-02. Anchorage, Alaska: Itasca.

Salager, S, M Nuth, and L Laloui. 2010. "Anisotropic Features of the Mechanical Behaviour of Opalinus Clay." In *Rock Mechanics in Civil and Environmental Engineering- ISRM International Symposium - EUROCK 2010*, edited by Zhao et al. Lausanne, Switzerland.

Salager et al. 2013. "Constitutive Analysis of the Mechanical Anisotropy of Opalinus Clay." *Acta Geotechnica* 8 (2): 137–54.

Salerno, G, and G de Felice. 2009. "Continuum Modeling of Periodic Brickwork." *Int. J. of Solids and Structures* 46 (5): 1251–67.

Sánchez et al. 2008. "Multilaminate and Microplane Models: Same Principles and Different Solutions for Constitutive Behaviour of Geomaterials." In *12th International Conference on Computer Methods and Advances in Geomechanics 2008*, 2:911–19.

Saroglou, H, and G Tsiambaos. 2008. "A Modified Hoek-Brown Failure Criterion for Anisotropic Intact Rock." *Int. J. of Rock Mechanics and Mining Sciences* 45 (2): 223–34.

Saroglou, H, and G Tsiambaos. 2007. "Classification of Anisotropic Rocks." In *11th Congress of the International Society for Rock Mechanics*, edited by Sousa: 191–96.

Schlegel, R, H Konietzky, and K Rautenstrauch. 2005. "Mathematische Beschreibung von Mauerwerk Unter Statischer Und Dynamischer Beanspruchung Im Rahmen Der Diskontinuumsmechanik Mit Hilfe Der Distinkt-Element-Methode." *Mauerwerk* 9 (4): 143–

51.

Schoenberg M, and F Muir. 1989. “A Calculus for Finely Layered Anisotropic Media.” *Geophysics* 54(5): 581–89.

Schweiger et al. 2009. “A Multilaminate Framework for Modelling Induced and Inherent Anisotropy of Soils.” *Géotechnique* 59 (2): 87–101.

Semnani et al. 2016. “Thermoplasticity and Strain Localization in Transversely Isotropic Materials Based on Anisotropic Critical State Plasticity.” *Int. J. for Numerical and Analytical Methods in Geomechanics* 40 (18): 2423–49.

Shao, J, D Kondo, and S Ikogou. 1994. “Stress-Induced Microcracking in Rock and Its Influence on Wellbore Stability Analysis.” *Int. J. of Rock Mechanics and Mining Sciences & Geomechanics Abstracts* 31 (2): 149–55.

Sheorey, P. 1997. *Empirical Rock Failure Criteria*. Taylor & Francis.

Shi et al. 2016. “Modified Hoek--Brown Failure Criterion for Anisotropic Rocks.” *Environmental Earth Sciences* 75 (11): 995.

Simanjuntak et al. 2014. “Pressure Tunnels in Non-Uniform in Situ Stress Conditions.” *Tunnelling and Underground Space Technology* 42 (Supplement C): 227–36.

Sitharam, T, V Maji, and A Verma. 2007. “Practical Equivalent Continuum Model for Simulation of Jointed Rock Mass Using FLAC3D.” *Int. J. of Geomechanics* 7 (5): 389–95.

Sitharam T, A Verma, V Maji. 2005. “Equivalent Continuum Analyses of Jointed Rockmass.” *40th U.S. Symposium on Rock Mechanics (USRMS)*. Anchorage, Alaska.

Søreide, O, B Bostrøm, and P Horsrud. 2008. “Borehole Stability Simulations of an HPHT Field Using Anisotropic Shale Modeling.” In *Proceedings of the ARMA Conference*, ARMA-09-185. Asheville, North Carolina: ARMA.

Stefanizzi, S, G Barla, and P Kaiser. 2007. “Numerical Modeling of Strain Driven Fractures around Tunnels in Layered Rock Masses.” In *11th Congress of the International Society for Rock Mechanics*, edited by Sousa et al.: 971–74. Lisbon, Portugal.

Sulem, J, and M Cerrolaza. 2000. “Slope Stability Analysis In Blocky Rock.” In *ISRM International Symposium*. Melbourne, Australia.

Sulem, J, and H-B. Mühlhaus. 1997. “A Continuum Model for Periodic Two-Dimensional Block Structures.” *Mechanics of Cohesive-Frictional Materials* 2 (1): 31–46.

Tang et al. 1998. “A New Approach to Numerical Method of Modelling Geological Processes and

Rock Engineering Problems — Continuum to Discontinuum and Linearity to Nonlinearity." *Engineering Geology* 49 (3): 207–14.

Tang, C. 1997. "Numerical Simulation of Progressive Rock Failure and Associated Seismicity." *Int. J. of Rock Mechanics and Mining Sciences* 34 (2): 249–61.

Thöny, R. 2014. "Geomechanical Analysis of Excavation-Induced Rock Mass Behavior of Faulted Opalinus Clay at the Mont Terri Underground Rock Laboratory (Switzerland)." ETH-Zürich.

Tien, M, and M Kuo. 2001. "A Failure Criterion for Transversely Isotropic Rocks." *Int. J. of Rock Mechanics and Mining Sciences* 38 (3): 399–412.

Tien et al. 2006. "An Experimental Investigation of the Failure Mechanism of Simulated Transversely Isotropic Rocks." *Int. J. of Rock Mech. and Mining Sciences* 43 (8): 1163–81.

Tonon, F. 2000. *Three-Dimensional Modeling of Underground Excavations and Estimation of Boundary Conditions in Rock with Fabric*. University of Colorado.

Tsai, S, and E Wu. 1971. "A General Theory of Strength for Anisotropic Materials." *Journal of Composite Materials* 5 (1): 58–80.

Tsidzi, K. 1986. "A Quantitative Petrofabric Characterization." *Bull. Int. Assoc. Eng. Geol.* 33: 3–12.

Tsidzi, K. 1990. "The Influence of Foliation on Point Load Strength Anisotropy of Foliated Rocks." *Engineering Geology* 29 (1): 49–58.

Ullemeyer et al. 2006. "Experimental and Texture-Derived P-Wave Anisotropy of Principal Rocks from the TRANSALP Traverse: An Aid for the Interpretation of Seismic Field Data." *Tectonophysics* 414 (1–4): 97–116.

Van Hise. 1896. "Deformation of Rocks.: III. Cleavage and Fissility." *The Journal of Geology* 4 (4): 449–83.

Vermeer, P, and de Borst. 1984. "Non-Associated Plasticity for Soils, Concrete and Rock." *HERON* 29 (3). Delft University of Technology: 3–64.

von Dinh, Q. 2011. *Brazilian Test on Anisotropic Rocks – Laboratory Experiment , Numerical Simulation and Interpretation, PhD Thesis*. TU Bergakademie Freiberg: Institut für Geotechnik.

Walhlstrom. 1973. *Tunnelling in Rock*. 1st ed. Amsterdam: Elsevier.

Walsh, J, and W Brace. 1964. "A Fracture Criterion for Brittle Anisotropic Rock." *Journal of Geophysical Research* 69 (16): 3449–56.

Walton et al. 2015. “A Laboratory-Testing-Based Study on the Strength, Deformability, and Dilatancy of Carbonate Rocks at Low Confinement.” *Rock Mechanics and Rock Engineering* 48 (3): 941–58.

Wang et al. 2009. “Modeling the Effects of Heterogeneity and Anisotropy on the Excavation Damaged/Disturbed Zone (EDZ).” *Rock Mechanics and Rock Engineering* 42 (2): 229–58.

Wang et al. 2012. “Numerical Simulation of the Failure Mechanism of Circular Tunnels in Transversely Isotropic Rock Masses.” *Tunnelling and Underground Space Technology* 32 (Supplement C): 231–44.

Wang, T, and T Huang. 2011. “Numerical Simulation on Anisotropic Squeezing Phenomenon of New Guanyin Tunnel.” *Journal of GeoEngineering* 6 (3): 125–33.

Wang, T, and T Huang. 2014. “Anisotropic Deformation of a Circular Tunnel Excavated in a Rock Mass Containing Sets of Ubiquitous Joints: Theory Analysis and Numerical Modeling.” *Rock Mechanics and Rock Engineering* 47 (2): 643–57.

Wang, T, and T Huang. 2009. “A Constitutive Model for the Deformation of a Rock Mass Containing Sets of Ubiquitous Joints.” *Int. J. of Rock Mechanics and Mining Sciences* 46 (3): 521–30.

Wang, Y, N Kessler, and F Santarelli. 1993. “Stress-Induced Anisotropy and Loading Path Effects on Borehole Responses.” *Int. J. of Rock Mechanics and Mining Sciences & Geo. Abstracts* 30 (7): 1367–70.

Wang, Z. 2002. “Seismic Anisotropy in Sedimentary Rocks, Part 1: A Single-plug Laboratory Method.” *GEOPHYSICS* 67 (5). Society of Exploration Geophysicists: 1415–22.

Wermeille, S, and P Bossart. 1999. “Insitu Stresses in the Mont Terri Region: Data Compilation, Technical Report 99-02.”

Wild et al. 2015. “Dilatancy of Clay Shales and Its Impact on Pore Pressure Evolution and Effective Stress for Different Triaxial Stress Paths.” *49th U.S. Rock Mechanics/Geomechanics Symposium*. San Francisco, California.

Wittke, W. 1990. *Rock Mechanics: Theory and Applications with Case Histories*. Springer.

Wu, B, and J Hudson. 1991. “Stress-Induced Anisotropy In Rock And Its Influence On Wellbore Stability.” In *The 32nd U.S. Symposium on Rock Mechanics (USRMS), 10-12 July, Rock Mechanics as a Multidisciplinary Science*, edited by Rogier, 941–50. Norman, Oklahoma.

Xin-pu, S, Z Mroz, and X Bing-ye. 2001. “Constitutive Theory of Plasticity Coupled with

Orthotropic Damage for Geomaterials." *Applied Mathematics and Mechanics* 22 (9): 1028–34.

Xu et al. 2013. "An Elasto-Plastic Model and Its Return Mapping Scheme for Anisotropic Rocks." In *Constitutive Modeling of Geomaterials: Advances and New Applications*, edited by Qiang et al.: 371–80. Berlin, Heidelberg.

Yong, S, P Kaiser, and S Loew. 2010. "Influence of Tectonic Shears on Tunnel-Induced Fracturing." *Int. J. of Rock Mechanics and Mining Sciences* 47 (6): 894–907.

Yong, S, P Kaiser, and S Loew. 2013. "Rock Mass Response Ahead of an Advancing Face in Faulted Shale." *Int. J. of Rock Mechanics and Mining Sciences* 60 (June): 301–11.

Yun-mei et al. 1984. "Failure Modes of Openings in a Steeply Bedded Rock Mass." *Rock Mechanics and Rock Engineering* 17 (2): 113–19.

Zhang et al. 2005. "An Elastoviscoplastic Model for Soft Sedimentary Rock Based on Tij Concept and Subloading Yield Surface." *Soils and Foundations* 45 (1): 65–73.

Zhang L. 2006. "Engineering Properties of Rocks." Edited by John Hudson. *Elsevier Geo-Engineering Book Series* 4: 226–30.

Zhang, L. 2008. "A Generalized Three-Dimensional Hoek-Brown Strength Criterion." *Rock Mechanics and Rock Engineering* 41 (6): 893–915.

Zhang, L, and H Zhu. 2007. "Three-Dimensional Hoek-Brown Strength Criterion for Rocks." *Int. J. Geotech. Geoenv. Eng.* 133 (9): 1128–35.

Zhang, Z, and Q Lei. 2013. "Object-Oriented Modeling for Three-Dimensional Multi-Block Systems." *Computers and Geotechnics* 48: 208–27.

Zhao, X, and M Cai. 2010. "A Mobilized Dilation Angle Model for Rocks." *Int. J. of Rock Mechanics and Mining Sciences* 47 (3): 368–84.

Zhao, X, M Cai, and M Cai. 2010. "Considerations of Rock Dilation on Modeling Failure and Deformation of Hard Rocks—a Case Study of the Mine-by Test Tunnel in Canada." *Journal of Rock Mechanics and Geotechnical Engineering* 2 (4): 338–49.

Zhu et al. 2009. "Improved Ubiquitous-Joint Model and Its Application to Underground Engineering in Layered Rock Masses." *Rock and Soil Mechanics* 10: 45.

Zienkiewicz, O, and G Pande. 1977. "Time-Dependent Multilaminate Model of Rocks—a Numerical Study of Deformation and Failure of Rock Masses." *Int. J. for Numerical and Analytical Methods in Geomechanics* 1 (3): 219–47.

Appendix

Transubi model: FLAC ***keywords***

The "transubi" model can be loaded in FLAC using the following commands:

config cppudm

model load modeltransubi.dll (for FLAC version 8.0)

model transubi

A list of model specific keywords follows:

Elastic parameters for intact rock

density	mass density, ρ [kg/m³]
e1	Young's modulus parallel to the weak plane, E [Pa]
e3	Young's modulus normal to the weak plane, E' [Pa]
g2	Shear modulus normal to the weak plane, G′ [Pa]
nu1	Poisson's ratio in plane, v [-]
nu2	Poisson's ratio cross plane, v' [-]

Mechanical parameters for intact rock

bimatrix	= 0 for matrix linear model (default) = 1 for matrix bilinear model
cohesion	matrix cohesion, c_1 [Pa]
co2	matrix cohesion, c_2 [Pa]
ctable	number of table relating matrix cohesion, c_1, to matrix plastic shear strain
c2table	number of table relating matrix cohesion, c_2, to matrix plastic shear strain
friction	matrix friction angle, ϕ_1 [°]
fr2	matrix friction angle, ϕ_2 [°]
ftable	number of table relating matrix friction, ϕ_1, to matrix plastic shear strain

f2table	number of table relating matrix friction, ϕ_2, to matrix plastic shear strain
dilation	matrix dilation angle, ψ_1 [°]
di2	matrix dilation angle, ψ_2 [°]
dtable	number of table relating matrix dilation, ψ_1, to matrix plastic shear strain
d2table	number of table relating matrix dilation, ψ_2, to matrix plastic shear strain
tension	matrix tension limit, σ^t [Pa]
ttable	number of table relating matrix tension, σ^t, to matrix plastic shear strain

Mechanical parameters for joint plane

bijoint	= 0 for joint linear model (default) = 1 for joint bilinear model
jangle	joint angle taken counterclockwise from the x-axis, α [°]
jcohesion	joint cohesion, c_{j1} [Pa]
jc2	joint cohesion, c_{j2} [Pa]
cjtable	number of table relating joint cohesion, c_{j1}, to joint plastic shear strain
cj2table	number of table relating joint cohesion, c_{j2}, to joint plastic shear strain
jfriction	joint friction angle, ϕ_{j1} [°]
jf2	joint friction angle, ϕ_{j2} [°]
fjtable	number of table relating joint friction, ϕ_{j1}, to joint plastic shear strain
fj2table	number of table relating joint friction, ϕ_{j2}, to joint plastic shear strain
jdilation	joint dilation angle, ψ_{j1} [°]
jdi2	joint dilation angle, ψ_{j2} [°]

djtable	number of table relating joint dilation, ψ_{j1}, to joint plastic shear strain
dj2table	number of table relating joint dilation, ψ_{j2}, to joint plastic shear strain
jtension	joint tension limit, σ^t_j [Pa]
tjtable	number of table relating joint tension, σ^t_j, to joint plastic shear strain

```
;*** small example of input: multi-joint model****
new
config cppudm
model load modeltransubi.dll
g 5 10
        mo transubi
        pro den 2700 e1 10.5e9 e3 3.5e9 g2 1.5e9 nu1 0.35 nu2 0.28
        pro bijoint 1 bimatrix 1
        pro co 4.5e6  fr 34 ten 1.3e6 dila 5
        pro co2 6.5e6  fr2 25 di2 7
        pro jco 0.6e6 jfr 29 jten 0.65e6 jdila 10
        pro jc2 0.96e6  jf2 21 jdi 0
        pro jang 0
end
……
```

Jhoek model: FLAC ***keywords***

The "jhoek" model can be loaded in FLAC using the following commands:

config cppudm

model load modeljhoek.dll (for FLAC version 8.0)

model jhoek

A list of model specific keywords follows:

Parameters for intact rock

Bulk	elastic bulk modulus, K [Pa]
Shear	elastic shear modulus, G [Pa]
density	mass density, ρ [kg/m³]
hbmb	calibrated Hoek-Brown parameter based on given angle, m_β [-]
hbsigci	calibrated Hoek-Brown parameter based on given angle, $\sigma_{ci\beta}$ [Pa] $\sigma_{ci\beta} = \sigma_{ci(0)}$, if β (i.e.: 90-α) $\leq \beta_{min}$ $\sigma_{ci\beta} = \sigma_{ci(90)}$, if β (i.e.: 90-α) $> \beta_{min}$
hb_doption	= 0, means a constant dilation angle specified by **hbpsi** (default) = -1, means associated flow; ψ_c=ϕ_c (current value of friction) =val, means a fraction of friction angle, ϕ_c (ψ_c =val × ϕ_c)
hbpsi	dilation angle, ψ (specified if hb_doption=0)
hb_tension	current value of matrix tension limit, σ^t [pa]

based on the given Hoek-Brown parameters, the following properties can be plotted via FISH:

hb_cohesion	current value of cohesion, c_c [pa]
hb_friction	current value of friction, ϕ_c [°]
hb_dilation	current value of dilation, ψ_c [°]

Parameters for joint plane

jangle	joint angle taken counterclockwise from the x-axis, α [°]
jcohesion	joint cohesion, c_j [Pa]
jfriction	joint friction angle, ϕ_j [°]
jdilation	joint dilation angle, ψ_j [°]

jtension joint tension limit, σ^t_j [Pa]

```
;*** small example of input: multi-joint model****
new
config cppudm
model load modeljhoek.dll
g 5 10
        mo jhoek
        pro dens 2500 bulk 19e9 she 8e9 hbmb 14.86 hbsigci 164.5e6  hb_doption 0.4
        pro jco 4e6 jfr 17 jang 0 jdila 6 jten 0.4e6
end
……
```